# LONG RANGE SURFACE PLASMON BASED BIOSENSOR FOR DENGUE VIRUS DETECTION

WONG WEI RU

FACULTY OF ENGINEERING
UNIVERSITY OF MALAYA
KUALA LUMPUR

2015

# LONG RANGE SURFACE PLASMON BASED BIOSENSOR FOR DENGUE VIRUS DETECTION

**WONG WEI RU**

**THESIS SUBMITTED IN FULFILMENT OF THE REQUIREMENTS FOR THE DEGREE OF DOCTOR OF PHILOSOPHY**

**FACULTY OF ENGINEERING**
**UNIVERSITY OF MALAYA**
**KUALA LUMPUR**

**2015**

# UNIVERSITY OF MALAYA

# ORIGINAL LITERARY WORK DECLARATION

Name of Candidate: **Wong Wei Ru** (I.C/~~Passport~~ No: **880322-04-5120**)

Registration/Matric No: **KHA110062**

Name of Degree: **Doctor of Philosophy**

Title of Project Paper/Research Report/Dissertation/Thesis ("this Work"):

**Long Range Surface Plasmon based Biosensor for Dengue Virus Detection**

Field of Study: **Photonics**

I do solemnly and sincerely declare that:

(1) I am the sole author/writer of this Work;
(2) This Work is original;
(3) Any use of any work in which copyright exists was done by way of fair dealing and for permitted purposes and any excerpt or extract from, or reference to or reproduction of any copyright work has been disclosed expressly and sufficiently and the title of the Work and its authorship have been acknowledged in this Work;
(4) I do not have any actual knowledge nor do I ought reasonably to know that the making of this work constitutes an infringement of any copyright work;
(5) I hereby assign all and every rights in the copyright to this Work to the University of Malaya ("UM"), who henceforth shall be owner of the copyright in this Work and that any reproduction or use in any form or by any means whatsoever is prohibited without the written consent of UM having been first had and obtained;
(6) I am fully aware that if in the course of making this Work I have infringed any copyright whether intentionally or otherwise, I may be subject to legal action or any other action as may be determined by UM.

Candidate's Signature Date: 22 February 2015

Subscribed and solemnly declared before,

Witness's Signature Date:

Name:

Designation:

# ABSTRACT

Dengue, a mosquito-borne disease caused by one of the four dengue virus serotypes, is of major public health interest in over 100 tropical and sub-tropical countries worldwide. Dengue infection causes flu-like symptoms and the severe cases can be fatal. Dengue cannot be reliably distinguished in its early stage using existing laboratory diagnostic techniques. In the absence of specific treatment for or vaccine against this disease, an early diagnosis of dengue infection is extremely important to reduce morbidity and mortality. The study in this thesis aimed to develop a compact, cost-effective, label-free, real-time biosensor based on long-range surface plasmon polariton (LRSPP) waveguides for dengue detection.

Generally, the LRSPP based biosensor consists of thin gold metal waveguides embedded in CYTOP claddings (a fluoropolymer having a refractive index close to that of biologically compatible fluids) with the incorporation of fluidic channels. Several passive elements such as straight waveguides, S-bends, Y-junctions and couplers were designed for different biosensing applications. The detailed fabrication process of the devices using photolithography technique is described.

The sensing performance of straight long-range surface plasmon waveguides was explored theoretically as a function of the metal stripe cross-sectional dimensions and the length of the sensing channel using finite element method (FEM). Three refractive indices of the sensing medium which are slightly below, equal to and slightly above the refractive index of CYTOP were considered. The surface sensitivity and detection limit of the waveguide were evaluated as a function of the adlayer thickness. A trade-off between the insertion loss of the waveguide and the change in insertion loss during sensing was observed.

Prior to biosensing experiments, the long-range surface plasmon waveguide was characterized optically through cut-back measurements, bulk sensing, and protein sensing experiments. The coupling loss and mode power attenuation obtained from the cut-back measurements agreed very well with the theoretical prediction. The sensing index that matches the refractive index of CYTOP produced the highest output power. The experiment with bovine serum albumin (BSA) demonstrated the ability of the LRSPP waveguide to perform (bio)chemical sensing. Besides, the stability of the experimental setup over time was measured in order to establish a stable baseline for subsequent biosensing experiments.

Dengue detection using LRSPP based biosensor was performed using two approaches: direct virus detection (detection of dengue virus antigen) and serological detection (identification of dengue-specific antibodies). The results obtained via serological diagnosis exhibit almost 2-fold higher P/N ratios compared to those collected by conventional immunoglobulin M antibody capture enzyme linked immunosorbent assay (MAC-ELISA). The antigen-based diagnosis also showed comparable results as the conventional method. The detection limit of the biosensor was estimated as $\sim$ 22 pg/mm$^2$. In addition, the reuse of the biosensors was demonstrated by regenerating the sensing surface down to the virus (or antibody) level or down to the bare gold.

In conclusion, the LRSPP based biosensor exhibits potential as the next-generation dengue diagnostic tool at point of care. The sensitivity of the biosensor can be further improved by using phase-dependent structures such as Mach-Zehnder interferometers and Young’s interferometers.

# ABSTRAK

Denggi, penyakit bawaan nyamuk yang disebabkan oleh salah satu daripada empat serotip virus denggi, merupakan isu kesihatan awam penting antara lebih 100 negara-negara tropika dan sub-tropika di seluruh dunia. Jangkitan denggi menyebabkan simptom-simptom seperti selsema dan kes-kes yang tenat boleh membawa maut. Denggi tidak boleh dikenal beza dengan tepat di peringkat awal menggunakan teknik diagnostik makmal yang sedia ada. Dengan ketiadaan rawatan khas atau vaksin terhadap penyakit ini, diagnosis awal jangkitan denggi adalah sangat penting untuk mengurangkan kesakitan dan kematian. Kajian di dalam tesis ini bertujuan untuk menghasilkan biopengesan berasaskan pandu gelombang plasmon permukaan polariton jarak jauh (LRSPP) yang padat, murah, tanpa label dan masa nyata bagi pengesanan denggi.

Secara umumnya, biopengesan berasaskan LRSPP terdiri daripada pandu gelombang emas nipis yang terbenam dalam salutan CYTOP (fluoropolimer yang mempunyai indeks biasan hampir dengan cecair serasi biologi) dengan penggabungan saluran bendalir. Beberapa unsur pasif seperti pandu gelombang lurus, lenturan S, simpang Y dan pengganding telah direka untuk aplikasi biopengesanan yang berbeza. Proses fabrikasi peranti-peranti tersebut yang menggunakan teknik fotolitografi diterangkan dengan terperinci.

Prestasi penderiaan pandu gelombang lurus plasmon permukaan jarak jauh telah diterokai secara teori sebagai fungsi keratan rentas dimensi jalur logam dan panjang saluran bendalir menggunakan kaedah unsur terhingga (FEM). Tiga indeks biasan bagi medium penderiaan yang sedikit di bawah, sama dengan dan sedikit di atas indeks biasan CYTOP telah dipertimbangkan. Kepekaan permukaan dan had pengesanan pandu gelombang telah dinilai sebagai fungsi ketebalan lapisan terjerap. Keseimbangan antara

kehilangan sisipan pandu gelombang dan perubahan dalam kehilangan sisipan semasa penderiaan didapati semasa pengiraan.

Sebelum eksperimen biopengesanan, pandu gelombang plasmon permukaan jarak jauh tersebut dicirikan secara optik melalui pengukuran potong balik, eksperimen penderiaan pukal, dan penderiaan protein. Kehilangan gandingan dan pengecilan kuasa mod yang diperoleh daripada pengukuran potong balik adalah hampir sama dengan ramalan teori. Indeks penderiaan yang sepadan dengan indeks biasan CYTOP menghasilkan kuasa keluaran yang tertinggi. Eksperimen dengan *bovine serum albumin* (BSA) menunjukkan kemampuan pandu gelombang LRSPP untuk menjalankan penderiaan (bio)kimia. Selain itu, kestabilan persediaan eksperimen diukur dalam tempoh masa tertentu bagi membentuk garis pangkal yang stabil untuk eksperimen biopengesanan yang berikutnya.

Pengesanan denggi menggunakan biopengesan berasaskan LRSPP dijalankan melalui dua pendekatan: pengesanan virus secara langsung (pengesanan antigen virus denggi) dan pengesanan serologi (pengenalan antibodi denggi khusus). Keputusan yang diperolehi melalui diagnosis serologi menunjukkan nisbah P/N yang hampir 2 kali ganda daripada keputusan yang didapati daripada konvensional tawanan antibodi imunoglobulin M asai imunoserap terangkai enzim (MAC-ELISA). Diagnosis berdasarkan antigen juga menunjukkan keputusan yang setanding dengan kaedah konvensional. Had pengesanan biopengesan tersebut dianggarkan sebanyak ~22 pg/mm$^2$. Di samping itu, guna semula biopengesan ditunjukkan dengan menjana semula permukaan biopengesan sehingga ke tahap virus (atau antibodi) atau sehingga ke tahap emas terdedah.

Kesimpulannya, biopengesan berasaskan LRSPP menunjukkan potensi sebagai alat diagnostik denggi pada titik penjagaan. Kepekaan biosensor boleh dipertingkatkan dengan menggunakan struktur sandar fasa seperti interferometer Mach-Zehnder dan interferometer Young.

# ACKNOWLEDGEMENTS

I would like to express my appreciation to the following people who supported me throughout this thesis:

My supervisors, Professor Dr Faisal Rafiq Mahamd Adikan at University of Malaya and Professor Dr Pierre Berini at University of Ottawa, for their guidance and motivations throughout my study.

Our medical collaborator, Professor Dr Shamala Devi Sekaran and her team at Medical Microbiology Department, University of Malaya, for their supply of research materials and their expert opinions on the planning of experiments.

Everyone under Professor Berini’s group at University of Ottawa, for having welcomed me as a visiting student and provided continuous support during my stays. Special thanks to Ewa Lisicka, Anthony Olivieri, Alex Krupin, Behnood Ghamsari, and Fan Hui for their technical assistance.

Everyone working in the microfabrication laboratory at University of Carleton, which includes Professor Dr Niall Tait, Rob Vandusen, Angela Mccormick, Rick Adams, Sa’ad Hassan, Norman Fong, and Howard Northfield, for helping me during the fabrication process.

Every member and alumni of the Integrated Lightwave Research Group (ILRG), University of Malaya, for the technical and moral support. Special thanks to Dr Shee Yu Gang, Dr Ghafour Amouzad Mahdiraji, Dr Yeo Kwok Shien, Dr Muhammad Hafiz Abu Bakar, Dr Tee Din Chai, and Seyed Reza Sandoghchi for the guidance and encouragement. Appreciation to the assistance from Nurfathin Mumairah with the administrative work.

My family and friends, for providing unconditional support during my study.

# TABLE OF CONTENTS

# LIST OF FIGURES

# LIST OF TABLES

# LIST OF SYMBOLS AND ABBREVIATIONS

## *Symbols*

° : Degree symbol

Å : Angstrom (1 Å = 0.1 nm)

$\alpha$ : Attenuation constant

$\beta$ : Phase constant

$\gamma$ : Propagation constant

$\varepsilon_r$ : Relative permittivity

$\lambda_0$ : Operating wavelength

$\sigma$ : Standard deviation of the optical output power

$\sigma_{P/N}$ : Error on the positive-to-negative ratio

$\Gamma$ : Surface mass density of the adlayer formed on a waveguide

$\Delta\Gamma_{\min}$ : Smallest detectable change in surface mass density (detection limit)

$\Delta P_{out,\min}$ : Smallest detectable change in output power

$\langle \Gamma_n \rangle$ : Time-averaged surface mass density of the negative control

$\langle \Gamma_p \rangle$ : Time-averaged surface mass density of the positive sample

$\Delta S/\sigma$ : Signal-to-noise ratio

$\partial\alpha_s/\partial a$ : Sensitivity of attenuation constant

$\partial C/\partial a$ : Sensitivity of coupling efficiency

$\partial P_{out}/\partial a$ : Surface sensitivity of the sensor

$\partial T_s/\partial a$ : Surface sensitivity of the sensing channel

$\partial n/\partial c$ : Change in index with analyte concentration

$C$ : Field overlap factor

$C_{dB}$ : Coupling loss

$E_y$ : Transverse electric field component

$L$ : Sensing length

$L_0$ : Length of cladded part of the waveguide

$L_{opt}$ : Optimal sensing length

$P_{inc}$ : Incident power from a single-mode optical fibre

$P_{in,s}$ : Power incident on the sensing waveguide

$P_{out}$ : Output power from the waveguide

$P_{out,s}$ : Output power from the sensing waveguide

$R$ : Radius of curvature

$Re\{\}$ : Real part

$\mathrm{S}$ : Separation between coupler

$\mathrm{T_g}$ : Glass transition temperature

$T_s$ : Transmittance of the sensing channel

$a$ : Adlayer thickness

$a_b$ : Asymmetric mode

$\mathrm{d_{ij}}$ : Distance between ith and jth output waveguides

$\mathrm{n}$ : Refractive index

$n_a$ : Refractive index of the adlayer

$n_c$ : Refractive index of sensing medium

$n_{eff}$ : Effective refractive index

$s_b$ : Symmetric mode

$\mathrm{t}$ : Time

$t$ : Waveguide thickness

$w$ : Waveguide width

## *Abbreviations*

2D : two dimensional

16-MHA : 16-Mercaptohexadecanioc acid

AFM : atomic force microscopy

Au : gold

BC : boundary condition

BSA : bovine serum albumin

CL : coupling length

Cr : chromium

DDI $H_2O$ : distilled/deionized water

DENV : dengue virus

DENV-2 : dengue virus serotype 2

DF : dengue fever

DHF : Dengue Haemorrhagic Fever

DI $H_2O$ : deionized water

DOF : degree of freedom

DUV : deep ultraviolet

EDC : 1-Ethyl-3-(3-dimethylaminopropyl) carbodiimide hydrochloride

ELISA : enzyme linked immunosorbent assay

FEM : finite element method

$H_2O_2$ : hydrogen peroxide

$H_2SO_4$ : sulfuric acid

HF : hydrofluoric acid

HI : hemagglutination inhibition

HMDS : hexamethyldisilazane

IgG : immunoglobulin G

IgM : immunoglobulin M

IL : insertion loss

IPA : 2-isopropanol

IR : infrared

LRSPP : long-range surface plasmon polariton

MAb : monoclonal antibody

MAC-ELISA : immunoglobulin M antibody capture ELISA

MPA : mode power attenuation

MUMPS : MUltifrontal Massively Parallel sparse direct Solver

MZI : Mach–Zehnder interferometer

$N_2$ : nitrogen gas

NHS : N-hydroxysuccinimide sodium salt

NIR : near infrared

NS1 : non-structural 1

$O_2$ : oxygen

OD : optical density

P/N : positive-to-negative ratio

PBS : phosphate buffered saline

PBS/Gly : mixture solution of phosphate buffer saline and glycerol

PDE : partial differential equation

PEC : perfect electric conductor

PM : polarization-maintaining

PMC : perfect magnetic conductor

PML : perfectly matched layer

QCM : quartz crystal microbalance

QoL : quality of life

| | |
|---|---|
| RI | : refractive index |
| RIU | : refractive index unit |
| RNA | : ribonucleic acid |
| RT-PCR | : reverse transcriptase-polymerase chain reaction |
| SAM | : self-assembled monolayer |
| SDS | : sodium dodecyl sulfate |
| Si | : silicon |
| $SiO_2$ | : silicon dioxide |
| SMF | : single-mode fibre |
| SPP | : surface plasmon polariton |
| SPR | : surface plasmon resonance |
| $Ta_2O_5$ | : tantalum pentoxide |
| TM | : transverse magnetic |
| UV | : ultraviolet |

# LIST OF APPENDICES

# CHAPTER 1: INTRODUCTION

## 1.1 Overview

The concept of biosensor was first introduced by Professor Leland C Clark in 1956 (Clark, 1956) and his idea became reality in 1975 when a glucose analyser was successfully launched in the market (Yellow Springs Instruments). Since then, the field of biosensor for various applications such as health care, food and drink, and environmental monitoring has vastly expanded. A biosensor usually consists of two parts: a biological recognition element (e.g. antibodies, proteins, peptides, viruses, microbes, cells and tissues) and a signal transducer. The biological recognition element will interact with the analyte under study and produce a signal which will be transformed by the transducer into another easily-measurable signal.

Among the technologies available for biosensing, optical biosensors have become the primary choice for the detection and characterization of biochemical interaction. Besides being a non-destructive sensing method, optical biosensors are able to perform rapid signal generation and detection. Generally, optical detection is based on the measurement of luminescence, fluorescence, absorbance/reflectance, scattering and refractive index changes. Most of the current optical biosensors are based on the surface plasmon resonance (SPR) technique, a phenomenon that occurs along a metal/dielectric interface when the evanescent wave field excites electrons in the thin metal film resulting in the formation of electron charge density waves (surface plasmons). The research on surface plasmon started when Otto as well as Kretschmann and Raether reported the phenomenon using a prism coupler in late 60s. In the 80s, the Kretschmann prism-based coupler was tested for biosensing (Liedberg, Nylander, & Lunström, 1983). This development has led to the success of the first commercially available optical SPR biosensor by BIACORE (Uppsala, Sweden) in 1990. Over the years, extensive research on plasmonics structures and devices, such as nanoparticles (Kelly, Coronado, Zhao, & Schatz, 2003; Klar *et al.*, 1998; Kottmann, Martin, Smith, & Schultz, 2000; Rechberger *et al.*, 2003) and waveguide interferometers (Bozhevolnyi, Volkov, Devaux, Laluet, & Ebbesen, 2006; Charbonneau *et al.*, 2006; Ditlbacher, Krenn, Schider, Leitner, & Aussenegg, 2002; Drezet *et al.*, 2006; Wang & Wang, 2004) have been done to achieve more sensitive, economical and compact instruments for biosensing. This thesis focusses on long-range surface plasmon polaritons (LRSPPs) based optical waveguide which consists of a thin metal film of finite width embedded in an optically infinite homogeneous dielectric. Despite the higher sensitivity of single-interface SPPs (as implemented in commercial SPR instruments), LRSPPs with greater propagation length produces greater overall sensitivity due to their much longer optical interaction length (Berini, 2008).

## 1.2 Motivations

Dengue is a mosquito-borne disease which can be found in over 100 tropical and subtropical countries around the world. Currently, there are over 3.6 billion people, or more than half of the world’s population, at risk from dengue infection (Beatty *et al.*, 2010). The regions of the world at risk of dengue infection up to year 2013 is shown in Figure 1.1. The disease has spread to a wider geographic range due to global warming and increase in long-distance travel. Every year there are around 390 million dengue infections worldwide (Bhatt *et al.*, 2013). In Malaysia alone, a total of 108,698 dengue cases were reported in 2014, an increase of 151% as compared with 43,346 cases for the previous year and 215 deaths due to dengue were recorded, an increase of 134 % compared to 92 deaths in 2013 (Director General of Health, 2015; World Health Organization Western Pacific Region, 2014).

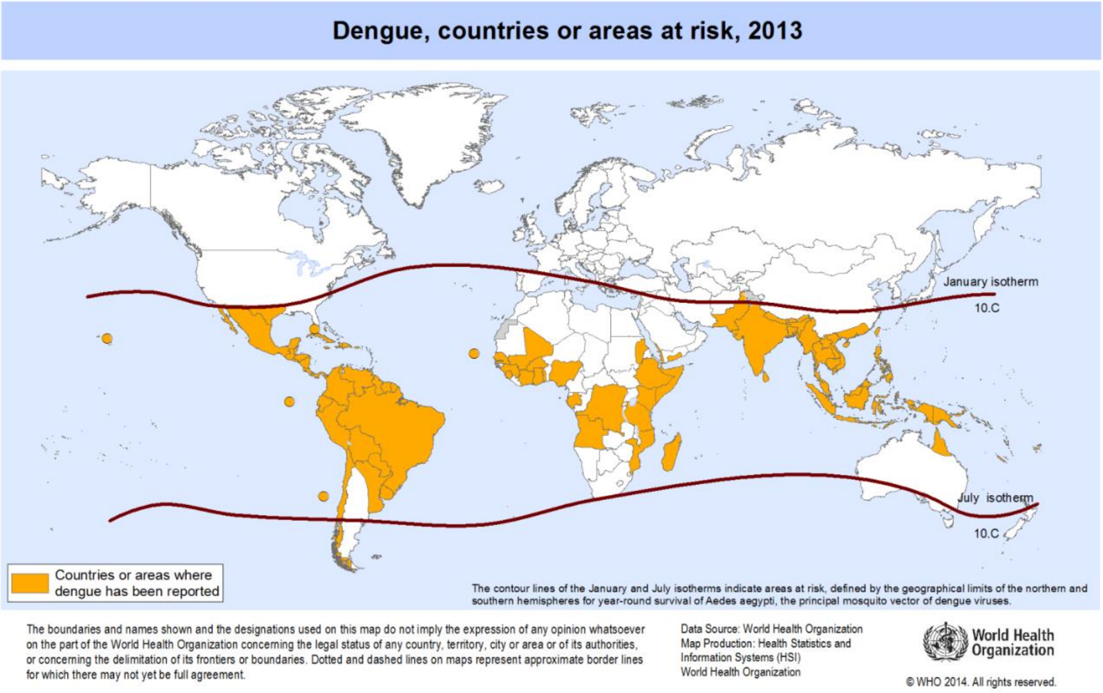

The contour lines of the January and July isotherms indicate areas at risk, defined by the geographical limits of the northern and southern hemispheres for year-round survival of Aedes aegypti, the principal mosquito vector of dengue viruses.

The boundaries and names shown and the designations used on this map do not imply the expression of any opinion whatsoever on the part of the World Health Organization concerning the legal status of any country, territory, city or area or of its authorities, or concerning the delimitation of its frontiers or boundaries. Dotted and dashed lines on maps represent approximate border lines for which there may not yet be full agreement.

Data Source: World Health Organization
Map Production: Health Statistics and Information Systems (HSI)
World Health Organization

© WHO 2014. All rights reserved.

**Figure 1.1: The countries or areas which are at risk of dengue infections as updated in 2013 by World Health Organization (Reproduced, with the permission of the publisher, from World Health Organization, 2014).**

According to a report from collaboration between universities and the Ministry of Health of Malaysia in 2013, the estimated economic burden of dengue is about US$102.25 million per year or approximately US$3.72 per capita (Shepard *et al.*, 2013). A recent study in Malaysia showed that dengue has a considerable impact on social function, vitality, and well-being. At its worst symptoms, dengue causes a 60% lost in quality of life (QoL) (Lum, Suaya, Tan, Sah, & Shepard, 2008). A lot of studies has been done on the the global impact of dengue infections in terms of public health, social and economy (Gubler, 2002; Gubler & Meltzer, 1999; Lee Han *et al.*, 2010; Lum *et al.*, 2008; Shepard *et al.*, 2012; Suaya *et al.*, 2009; Undurraga, Halasa, & Shepard, 2013).

In the absence of specific treatment for or vaccine against this disease, an early diagnosis of dengue infection is extremely important to reduce morbidity and mortality. Generally, current routine laboratory diagnosis techniques are time-consuming, labour-intensive, and expensive. As dengue is mostly endemic in low-resource tropical and developing countries, these lab-based tests are costly and restrict point-of-care diagnosis.

Despite various rapid diagnostic kits available in the market, their sensitivity and specificity are commonly low. Hence, the highly sensitive surface plasmon technique becomes a promising approach to improve the performance of the diagnostic kit. Besides, the development of integrated optics using long range surface plasmon polariton (LRSPP) facilitates the fabrication of a compact and cost-effective biosensor.

Although the research in surface plasmon biosensing started since 1980s, very little work has been done with clinical patient's blood samples. A careful design of the experiment has to be carried out to differentiate the target analyte from the complex blood samples. Therefore, in order to meet the practical situation as a diagnostic tool in pharmaceutical industry, the dengue diagnosis experiments in this thesis will be performed using clinical blood samples.

## 1.3 Objectives

The main objective of this thesis is to develop a long-range surface plasmon polariton (LRSPP) based biosensor for dengue diagnosis. Theoretical and experimental work are combined to investigate the performance of the biosensor. In particular, the scope of this study is as follows:

1. To design and fabricate LRSPP based waveguides for biosensing application;
2. To model and characterize the fabricated device to determine its performance (surface sensitivity and detection limit) and the suitable refractive index of buffer solution for biosensing experiment;
3. To propose suitable surface functionalization approaches for dengue detection;
4. To generate a set of protocols for dengue diagnosis with LRSPP biosensor, which includes the regeneration of the sensor surface and the re-use of the biosensor; and,

5. To analyse and compare the results of the biosensing experiments with existing laboratory technique for dengue diagnosis (“gold standard”).

## 1.4 Thesis Outline

This thesis is comprised of eight chapters, including the current introductory chapter. The contents of each chapter are briefly described as follows:

**Chapter 2** introduces the theoretical background of three main research topics involved in this thesis, which are the dengue disease, surface plasmon principle, and surface functionalization techniques available for the immobilization of biological recognition elements. These studies will provide sufficient fundamental knowledge where the research outcomes are based on.

**Chapter 3** explains the designs of the LRSPP based biosensor and the fabrication process of such devices. The LRSPP based biosensor consists of a thin gold stripe ($t$ ~ 35 nm, $w$ ~ 5 µm) embedded in thick CYTOP claddings (~ 8 µm each). Photolithography technique was used to define various structures (straight waveguides, S bends, couplers, Y-splitters and Mach-Zehnder interferometers) on a silicon wafer.

The surface sensitivity and detection limit of the LRSPP based biosensor were assessed theoretically in **Chapter 4**. Various waveguide dimensions and sensing buffer indices have been modelled to investigate their effects on the performance of a straight LRSPP waveguide as an attenuation-based biosensor.

**Chapter 5** describes the experimental setup and device preparation procedures for the biosensing experiments. Prior to the actual biosensing experiments, the biosensor was characterized through a few experiments, which include cutback measurements, stability test (establishment of baseline for biosensing), bulk sensing and protein sensing.

**Chapter 6** presents the diagnosis of dengue infection through the identification of dengue-specific immunoglobulin M (IgM) antibody in human blood plasma. Two surface functionalization approaches were demonstrated and their results were compared with those collected by conventional IgM Antibody Capture Enzyme Linked Immunosorbent Assay (MAC-ELISA).

In **Chapter 7**, another dengue diagnosis technique which involves the detection of dengue non-structural 1 (NS1) antigen was investigated. The detection of dengue NS1 antigen was first demonstrated using pure NS1 protein. By immobilizing the blood plasma on the sensor surface, both the dengue NS1 antigen and dengue-specific antibodies were detected within a single experiment. The results obtained for the plasma sample agree with those collected by ELISA.

Finally, **Chapter 8** concludes all the important findings in this thesis and explores the possible improvements on the LRSPP based biosensor, which may eventually be commercialized for dengue point-of-care diagnosis.

# CHAPTER 2: LITERATURE REVIEW

This chapter gives a comprehensive review on topics related to the dengue diagnosis using long-range surface plasmon polaritons (LRSPPs). The study starts with the introduction to the dengue disease and its pathogenesis. It continues with an overview of the pros and cons of currently available conventional techniques for dengue diagnosis. We also summarize some of the most relevant work on the development of biosensors for the diagnosis of dengue infections using different transduction mechanisms. Next, we briefly describe the fundamental theory of surface plasmons, an optical sensing technique which this thesis is based on. In particular, we discuss the current technology, LRSPP-based waveguides, and some design considerations for biosensing application. Finally, this chapter ends with a brief description of surface functionalization methods for surface plasmon biosensing. Considering the various strategies available, we focus mainly on the immobilization techniques used in this thesis.

## 2.1 Dengue Fever

Dengue virus (DENV) is a positive single-strand RNA virus of the family *Flaviviridae*, genus *Flavivirus*. It is around 50-nm in diameter enveloped with a lipid bilayer as shown in Figure 2.1 (Matsumura, Stollar, & Schlesinger, 1971). There are four different serotypes of dengue virus, which are DENV-1, DENV-2, DENV-3 and DENV-4. These serotypes cause nearly identical syndromes in humans since they share around 65% of the genome (Guzman, Halstead, *et al.*, 2010). Infection by a dengue serotype provides lifelong immunity against that particular serotype but not the other three serotypes. Subsequent infections by other serotypes may cause severe illness because the virus will activate the immune system to attack it as if it was the first serotype (Halstead, 1988). This results in a more serious form of dengue fever (DF), known as Dengue Haemorrhagic Fever (DHF) and Dengue Shock Syndrome (DSS) which causes fluid loss from the blood vessels. The severe DHF has a rate of fatal cases in patients as high as 44% (Rigau-Pérez *et al.*, 1998).

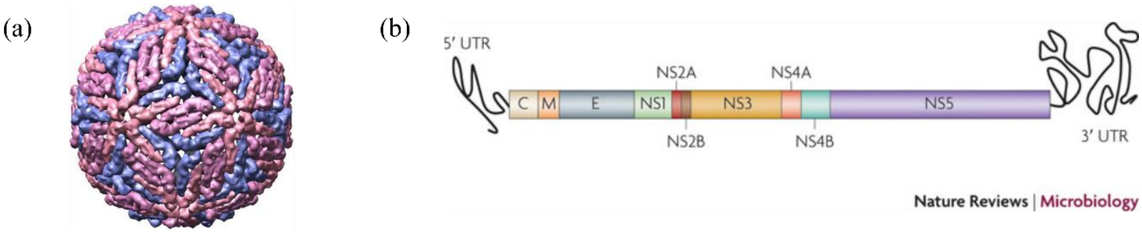

**Figure 2.1: The dengue virus. (a) The dengue virus has a diameter of approximately 50 nm and an electron-dense core surrounded by a lipid membrane. (b) The dengue virus genome that consists of three structural proteins [capsid (C), membrane (M) and envelope (E)] and seven non-structural (NS) proteins [NS1, NS2A, NS2B, NS3, NS4A, NS4B and NS5] (adapted from Kuhn *et al.*, 2002 and Guzman, Halstead, *et al.*, 2010, respectively, with permissions).**

The primary transmission vectors of dengue viruses are the mosquito species, *Aedes aegypti* and *Aedes albopictus*. The virus is transmitted between humans through the bites of infected female mosquitoes. A patient will show symptoms of infection from days 4 - 7 after the mosquito bite and typically these symptoms last for 3 - 10 days (Gubler, 1998). The symptoms caused by dengue infection vary depending on age and immunological status. Most of the dengue infections are asymptomatic or cause mild symptoms such as sudden onset of fever, rashes, nausea, vomiting and diarrhea (Rathakrishnan & Sekaran, 2013). However, 5–10% of patients evolve to severe DHF, which can result in death without proper medical attention (Peeling *et al.*, 2010). Different patterns of antibody responses can be observed in patient’s blood during a first (primary) or subsequent (secondary) dengue infection as illustrated in Figure 2.2. Live virus or viral components (RNA or antigen) can only be detected at the early stage of infection. Immunoglobulin M (IgM) response is typically higher titre and more specific than immunoglobulin G (IgG) during primary dengue infection (World Health Organization and the Special Programme for Research and Training in Tropical Diseases, 2009). In secondary infections, IgG is present from the previous infection and the titre increases dramatically to a value higher than during primary infection. By contrast, IgM is usually at lower titres during secondary infection than in primary infection (Peeling *et al.*, 2010).

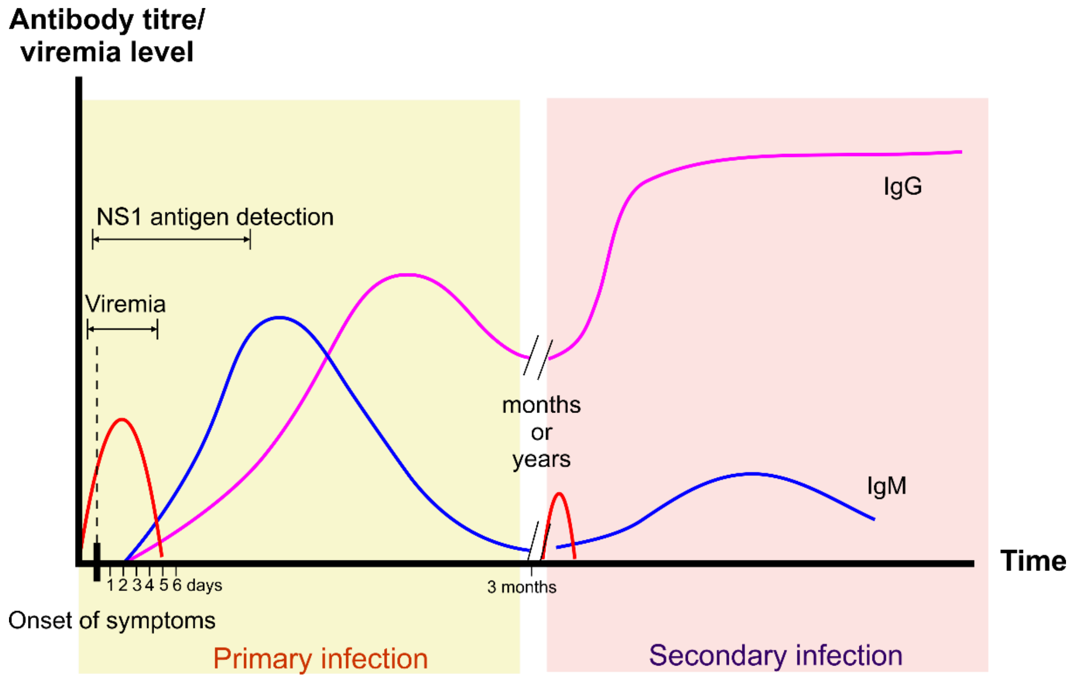

**Figure 2.2: Dengue virus, antigen and antibody responses at different phases of dengue infection (Peeling *et al.*, 2010; Rathakrishnan & Sekaran, 2013; World Health Organization and the Special Programme for Research and Training in Tropical Diseases, 2009).**

Currently, early dengue diagnosis is difficult because dengue cannot be reliably distinguished from several other febrile illnesses and other closely related flaviviruses (such as Yellow Fever, Japanese Encephalitis and West Nile) due to the absence of its pathognomonic clinical features. While a lot of research has been done on dengue pathogenesis, the results remain obscure and controversial. Although there is no specific vaccine or treatment for dengue infection to date, patients may recover if they are clinically well managed following an early diagnosis of the disease. As illustrated in Figure 2.3, two general laboratory methods for the diagnosis of dengue infections are the direct virus detection (viral culture and detection of viral nucleic acid or antigen) and serological detection (identification of dengue-specific antibodies) (Guzman, Halstead, *et al.*, 2010; Peeling *et al.*, 2010; World Health Organization and the Special Programme for Research and Training in Tropical Diseases, 2009).

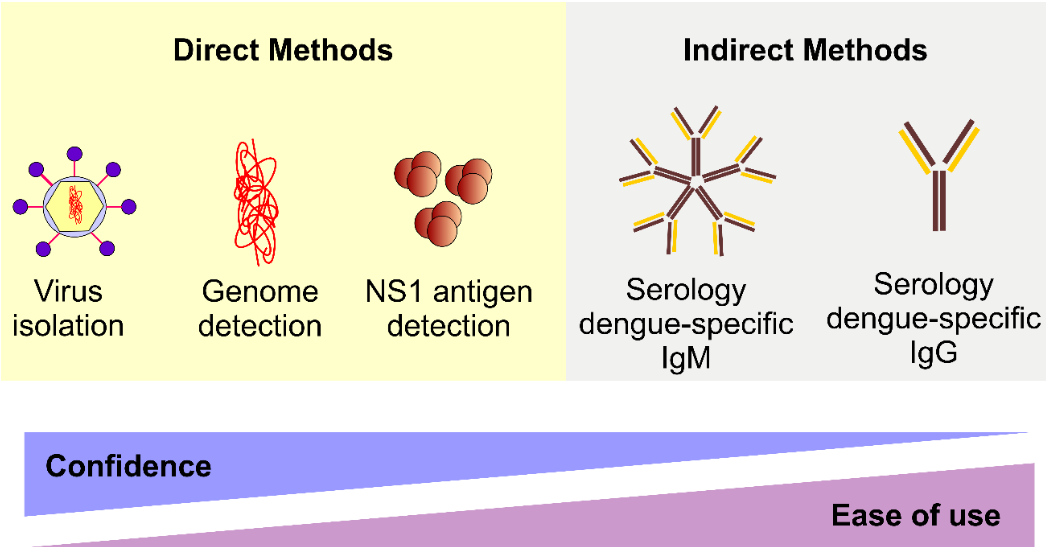

**Figure 2.3: Comparison of laboratory diagnostic tests for dengue infection in terms of confidence in the test results and ease of use of a diagnostic method. There exists an inverse relationship between their confidence and ease of use (adapted from Peeling *et al.*, 2010).**

During the early stage of the disease, live virus or viral components (RNA or antigen) can be detected in serum, plasma, and circulating blood cells 4–5 days after the onset of illness (World Health Organization and the Special Programme for Research and Training in Tropical Diseases, 2009). Isolation of the dengue virus in a cell culture has been a highly sensitive and specific diagnostic test. However, this method usually takes 1-2 weeks and requires expensive cell culture facilities and highly-skilled lab technologists. The non-structural protein 1 (NS1) can be detected in patients up to 9 days after the onset of illness (Alcon *et al.*, 2002). This antigen-based diagnostic test is becoming an important marker in early diagnosis of the disease (Allonso, da Silva Rosa, Coelho, da Costa, Nogueira, Bozza, Santos, *et al.*, 2011). Nevertheless, these direct detection methods are only applicable to patients who seek medical attention 0 - 10 days following the beginning of symptoms but not all are able to be diagnosed within this period. Serological tests are more commonly used especially in dengue epidemic countries due to their ease of use and lower cost as compared to other methods. In general, serological tests involve the capturing of immunoglobulins (IgM, IgG and IgA) produced due to the immune response after dengue infection. These immunoglobulins are mainly specific to the envelope (E) protein in dengue virus. An antibody response is detectable starting from the fifth day of infection up to 2 or 3 months after the onset of symptoms (Centers for Disease Control and Prevention). Serological tests are not limited to the time of collection of blood samples but the presence of immunoglobulins might not be diagnostic of a current illness (Peeling *et al.*, 2010).

Currently, the main routine laboratory tests of dengue infection are reverse transcriptase-polymerase chain reaction (RT-PCR) [to detect dengue RNA genome through amplification] and enzyme linked immunosorbent assay (ELISA) [to measure NS1 protein, dengue-specific IgM or dengue-specific IgG antibodies]. Yet, these lab-based tests are generally costly, especially for low-resource tropical and developing countries where dengue is endemic. They also usually require long assay times and labour-intensive sample processing which restrict point-of-care diagnosis. Taking into consideration the limitations in current diagnostic field, new methodologies and devices aimed at developing biosensors for detection of dengue viruses and dengue antibodies have been reported over the past decades. These biosensors can be classified into their types of transduction mechanisms (Teles, 2011): piezoelectric (quartz crystal microbalance) (Chen *et al.*, 2009; Su, Wu, Chen, Yang, & Tai, 2003; Tai, Lin, Wu, & Chen, 2005; Tai, Lin, Wu, Huang, & Shu, 2006; Wu *et al.*, 2005), optical (surface plasmon resonance (Camara *et al.*, 2013; Jahanshahi, Zalnezhad, Sekaran, & Adikan, 2014; Kumbhat, Sharma, Gehlot, Solanki, & Joshi, 2010; Wong, Krupin, Sekaran, Mahamd Adikan, & Berini, 2014), chemiluminescence (Atias *et al.*, 2009; Baeumner *et al.*, 2002), magnetoresistance (Aytur *et al.*, 2006), fluorescence (Chang *et al.*, 2008; Zaytseva, Montagna, & Baeumner, 2005; Zaytseva, Montagna, Lee, & Baeumner, 2004; Zhang, Bahns, Jin, Divan, & Chen, 2006), photonic crystals (Huang *et al.*, 2008; Mandal *et al.*, 2007; Mateus *et al.*, 2004)), and electrochemical (Andrade *et al.*, 2011; Avelino *et al.*, 2014; I. Cavalcanti *et al.*, 2012; Cavalcanti, Guedes, Sotomayor, Yamanaka, & Dutra, 2012; Cheng *et al.*, 2012; Deng & Toh, 2013; Dias, Gomes-Filho, Silva, & Dutra, 2013; Kwakye, Goral, & Baeumner, 2006; Luna, Oliveira, Nogueira, & Andrade, 2014; Nascimento *et al.*, 2011; Nguyen, Gan, Leo, Finkc, & Toha, 2013; Nguyen *et al.*, 2012; Oliveira, Correia, & Diniz, 2009; Oliveira, Nogueira, Correia, Coelho, & Andrade, 2011; Peh & Li, 2013; Rai *et al.*, 2012; Ribeiro Teles, França dos Prazeres, & de Lima-Filho, 2007; Silva *et al.*, 2014; Souza *et al.*, 2011; Zhang *et al.*, 2010). Among all of the transduction mechanisms, surface plasmon resonance dominates the field of optical biosensing due to good sensor performance (sensitivity, detection limit), ease of microfluidic integration and the availability of good surface chemistries (when gold is used to excite surface plasmon). Surface plasmon exhibits the potential to produce an "ideal" biosensor for dengue diagnosis which is miniaturized, simple to be used, economical, and able to produce confirmative results within short time frame (Rathakrishnan & Sekaran, 2013; Teles, 2011). The advantages and limitations of dengue detection methods are summarized in Table 2.1.

**Table 2.1: Advantages and limitations of dengue detection methods (Darwish, Alias, & Khor, 2015; Law, Ab Mutalib, Chan, & Lee, 2014; Yusof, Ibrahim, Rahman, Adwan, & Harun, 2015).**

| Detection method | Advantages | Limitations |
|---|---|---|
| ELISA | ▪ Easy sample preparation<br>▪ Can handle large number of samples | ▪ Low specificity<br>▪ May result in cross-reactivity with closely related antigens<br>▪ Requires trained personnel<br>▪ Requires labelling of antibodies or antigens |
| RT-PCR | ▪ High sensitivity<br>▪ High specificity<br>▪ Reliable results | ▪ High cost<br>▪ Sophisticated equipment<br>▪ Take ~1 – 2 days |
| Lateral flow immunoassay | ▪ Low cost<br>▪ Easy to operate<br>▪ Sensitive<br>▪ Specific | ▪ Requires labelling of antibodies or antigens |

| | | |
|---|---|---|
| Optical biosensors (e.g. surface plasmon) | ▪ High sensitivity<br>▪ Real-time detection<br>▪ Label-free detection | ▪ Bulky optical components |
| Piezoelectric biosensors (e.g. quartz crystal microbalance) | ▪ High sensitivity<br>▪ Label-free detection<br>▪ Real-time detection | ▪ Inadequate recognition properties in imprinted polymers |
| Electrochemical biosensors | ▪ High sensitivity<br>▪ Simple | ▪ Some requires labelling of target analyte, which is more time-consuming |

## 2.2 Surface Plasmon

Surface plasmon polaritons (SPPs) are transverse magnetic (TM) polarized optical surface waves that propagate along the interface of two media having opposite signs in the real part of their dielectric functions (typically a metal-dielectric interface). Excitation of surface plasmons by prism coupling of light is the most common technique and can be realized with simple and conventional optical components. There are two different configurations used in prism coupled system (Figure 2.4**Error! Reference source not ound.**): Kretschmann (Kretschmann, 1971) and Otto (Otto, 1968).

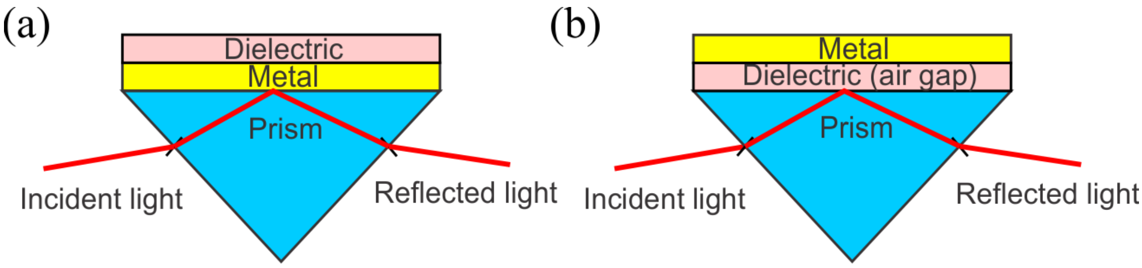

**Figure 2.4: Two configurations used to excite surface plasmon in prism-coupled system. (a) Kretschmann configuration (b) Otto configuration.**

In Otto configuration, there exists a distance (air gap) between the metal and the prism. This configuration is not popular experimentally due to the challenge to control the tiny air gap between the interfaces with precision. The configuration developed by Kretschmann is more commonly used in most SPR instruments due to its ease of construction. In Kretschmann configuration, a thin metal film is deposited on top of a glass prism. The dielectric phase is readily accessible for sensing application. The excitation of surface plasmons occurs at a certain incident angle θ which can be observed as a minimum (dip) in the reflected light intensity. A slight change in the dielectric medium (such as change in refractive index or formation of an adlayer) will cause the angle θ (also known as SPR angle) to change significantly, allowing precise real-time sensing measurement. Plotting the change in θ with time forms the SPR curve known as a sensorgram (Figure 2.5). A typical sensorgram usually consists of three phases (association, steady state and dissociation). Due to the almost-linear relationship between the amount of proteins bound on surface and the SPR signal, binding kinetics can be extracted from the sensorgram to provide quantitative and real-time data (Schasfoort & Tudos, 2008).

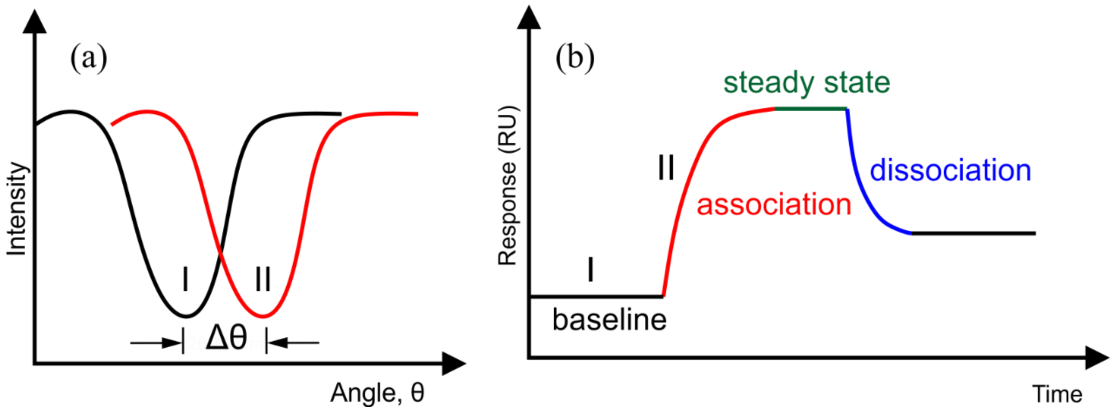

**Figure 2.5: (a) In SPR biosensing, the binding of biomolecules will change the SPR angle θ (from I to II). (b) A sensorgram, which records the change in θ over a period of time, consists of three phases after the biomolecules injection: association, steady state, and dissociation phase.**

Over the past decade, there is a large interest to excite surface plasmons by guided modes of an optical fibre or integrated optical waveguide (Homola, Vaisocherová, Dostálek, & Piliarik, 2005; Jorgenson & Yee, 1993; Lavers & Wilkinson, 1994; Mouvet *et al.*, 1997; Ronot-Trioli, Trouillet, Veillas, & Gagnaire, 1996; Slavík, Homola, Čtyroký, & Brynda, 2001). Waveguide-based SPP devices that use either wavelength or intensity interrogation are preferred to be implemented as sensors because they are compact and enable miniaturization of the sensors. In a metal slab waveguide where a thin metal of thickness $t$ and infinite width is sandwiched between optically semi-infinite dielectrics, there exists two purely bound TM modes. These modes are denoted as symmetric $s_b$ and asymmetric $a_b$ modes, depending on the spatial distribution of their transverse electric field component ($E_y$) across the waveguide (Figure 2.6) (Berini, 2009). The effective index and attenuation of the asymmetric mode decrease as the thickness of the metal film $t$ is increased. The symmetric mode exhibits a lower attenuation than the asymmetric mode. Therefore the symmetric mode is referred as to a long range surface plasmon, while the asymmetric mode is referred as to a short range surface plasmon.

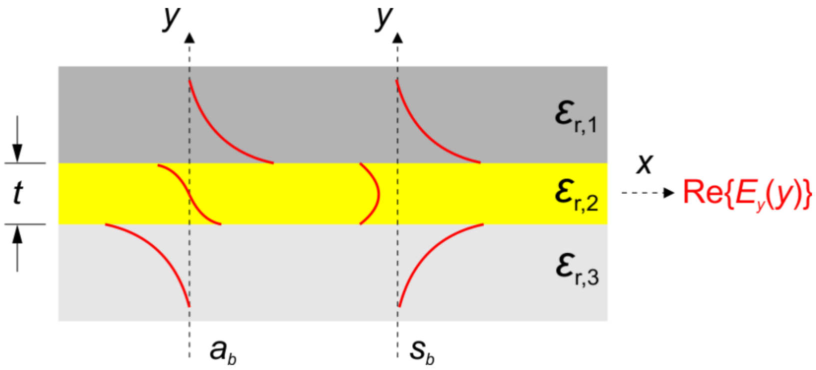

**Figure 2.6: A dielectric-metal-dielectric structure which consists of a thin metal layer ($\varepsilon_{r,2}$) bounded by two dielectric cladding layers ($\varepsilon_{r,1}$, $\varepsilon_{r,3}$). The distributions of the $E_y$ component of the two bound SPP modes ($a_b$ and $s_b$) are shown as red curves. (adapted from Berini, 2009 with permission)**

In this thesis, we restrict our work on long range surface plasmon based biosensor with metal stripe waveguide of finite width $w$. By limiting the metal width of the metal slab structure, a lateral confinement is created and thus enhances the mode spectrum. Berini theoretically studied the bound modes supported by such thin metal stripe structure where the fundamental mode $ss_b^0$ is seen to evolve similarly as the $s_b$ mode in the infinitely wide structure (Berini, 1999). Hence, the $ss_b^0$ mode is also termed as long range surface plasmon polariton (LRSPP). It is more convenient to work with the symmetric structure ($\varepsilon_{r,1} = \varepsilon_{r,3}$ in Figure 2.6) in LRSPP because the mode remains undistorted and non-radiative (purely bound) for a very thin metal film. If $\varepsilon_{r,1} \neq \varepsilon_{r,3}$, the mode remains non-radiative only if the metal film thickness is greater than a cut-off thickness (Berini, 2001).

Following the optical confinement in metal stripe structure, various waveguide configurations such as straight waveguides, S bends, Y junctions, Mach–Zehnder interferometers (MZIs), couplers, and Bragg gratings have been demonstrated (Boltasseva *et al.*, 2005; Charbonneau *et al.*, 2006; Degiron, Cho, Tyler, Jokerst, & Smith, 2009; Jetté-Charbonneau, Charbonneau, Lahoud, Mattiussi, & Berini, 2005; Won *et al.*, 2006). As compared to LRSPP on slabs using prism-coupled geometries (Dostálek, Kasry, & Knoll, 2007; Guo, Keathley, & Hastings, 2008; Joo, Song, & Magnusson, 2010; Slavík & Homola, 2007; Vala, Etheridge, Roach, & Homola, 2009; Wark, Lee, & Corn, 2005), LRSPP on metal stripes can be easily excited via end-fire coupling (butt-coupling) a single-mode fibre (SMF) to the waveguide input and thus leads to the miniaturization of devices. In order to create a symmetric structure for optimum LRSPP propagation, the refractive index around the metal stripe should be homogeneous. Besides, for biosensing application, low index claddings that match the refractive index of the biological compatible fluids ($n \approx 1.33$) are required to maintain the symmetry. Two examples of such materials are Teflon (DuPont) and CYTOP (Asahi Glass). Recent work on the fabrication of metal stripe waveguides and structures on (Daviau, Khan, Lisicka-Skrzek, Tait, & Berini, 2010; Daviau, Lisicka-Skrzek, Tait, & Berini, 2009) or embedded in (Chiu, Lisicka-Skrzek, Tait, & Berini, 2010) CYTOP have been reported. CYTOP is a fluoropolymer which has a refractive index of 1.3348 at operating wavelength $\lambda = 1330$ nm (Takenobu *et al.*, 2008). Previous work on various LRSPP based metal stripe structures with CYTOP claddings (Fan, Buckley, & Berini, 2012; Fan, Charbonneau, & Berini, 2014; Fan, Lisicka-Skrzek, & Berini, 2011; Khan, Chiu, Lisicka-Skrzek, Tait, & Berini, 2010; Khan, Krupin, Lisicka-Skrzek, & Berini, 2011, 2013; Krupin, Asiri, Wang, Tait, & Berini, 2013; Krupin, Wang, & Berini, 2014; Tencer, Krupin, Tezel, & Berini, 2013) forms the fundamental for the biosensing work throughout this thesis.

## 2.3 Surface Functionalization Techniques

One of the main reasons using Au waveguide instead of dielectric waveguide is the availability of good surface chemistries for Au. Besides being a relatively inert material that does not react with most chemicals, Au is the preferred material for surface functionalization because an alkanethiol self-assembled monolayer (SAM) can easily form on Au with high affinity. SAMs of sufficient chain length (n = 12 or more) form a closely packed structure oriented perpendicularly to the metal surface. The alkanethiol terminal groups of SAMs are important for further attachment of biological recognition elements and also for surface resistance towards non-specific adsorption (Holmlin, Chen, Chapman, Takayama, & Whitesides, 2001).

The well-established protocol to prepare SAMs on gold, silver, and other materials is through incubation of a clean substrate into a dilute (~1-10 mM) ethanolic solution of thiols (RSH) for about 12-18 hours at room temperature (Love, Estroff, Kriebel, Nuzzo, & Whitesides, 2005). This procedure originates from early studies of SAMs (Fenter *et al.*, 1991; Nuzzo & Allara, 1983; Porter, Bright, Allara, & Chidsey, 1987) and further literature studies designed to optimize the reproducibility of the SAMs (Bain *et al.*, 1989). The adsorbates (e.g. thiols) saturates the surface quickly (milliseconds to minutes) from millimolar solutions, but time (in the order of hours) is required for a slow reorganization process to obtain a tightly packed SAM with minimum defects (Love *et al.*, 2005). SAMs are stable in air or in contact with water or ethanol for periods of several months (Mrksich & Whitesides, 1995). SAMs desorb at temperatures greater than 70°C or when irradiated with UV light in the presence of oxygen (Mrksich & Whitesides, 1996). The aging effect on the –COOH surface was studied by Hosseini *et al.*, 2015. Formation of the SAM occurs through a covalent bonding of the thiol groups of alkanethiols and gold and it can be clearly demonstrated through Equation 2.1 (Dubois & Nuzzo, 1992; Whitesides *et al.*, 1995) and Figure 2.7 (Motesharei & Myles, 1998).

$$\mathrm{Au + HS\text{-}R \rightarrow Au\text{-}S\text{-}R + ½\,H_2 + e^-} \qquad (2.1)$$

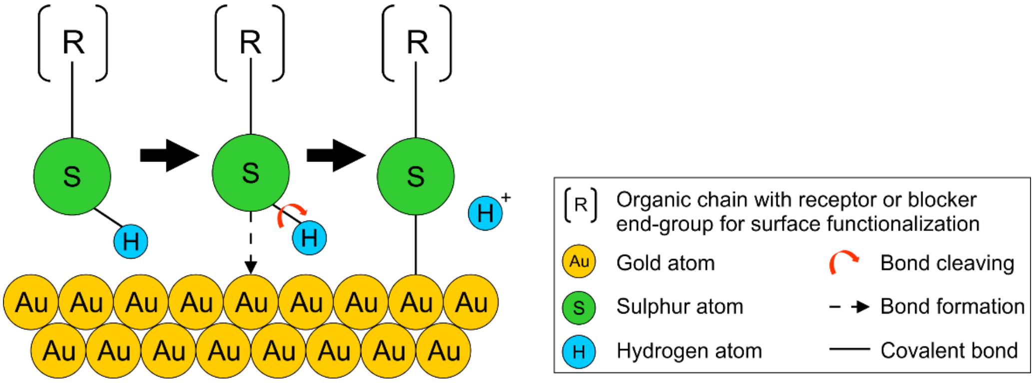

**Figure 2.7: Self-assembled monolayer formation on gold surface through covalent bonding of sulfur end-group (Asiri, 2012; Motesharei & Myles, 1998).**

The main approaches to immobilize biological recognition elements to the functionalized surfaces are based on physical adsorption, formation of covalent bond, and specific interactions involving biochemical affinity reaction (Homola, 2008). Physical adsorption (Figure 2.8a) is the simplest immobilization technique which depends on intermolecular forces (hydrophobic, electrostatic, polar interactions, etc.). However, this approach always results in random orientation and loss of bioactivity (Butler *et al.*, 1992). The most widely-used immobilization technique in surface plasmon biosensing is through covalent coupling (Figure 2.8b). Covalent bond is formed between the functional groups of amino acids (e.g. amino –$NH_2$ groups, thiol –SH groups, carboxyl –COOH groups) of the proteins and the electrophilic groups (e.g. activated carboxyls, aldehydes) on the sensor surface. A common example of the immobilization involving amino groups (–$NH_2$) is through the reaction of N-hydroxysuccinimide sodium salt (NHS) and 1-ethyl-3-(3-dimethylopropyl)3-(3-Dimethylopropyl) (EDC) in an aqueous solvent. Although the covalent immobilization is stable, the proteins might be immobilized in random orientation due to the multiple functional groups in proteins. A more detailed literature review on amine coupling and the mechanism behind this technique will be discussed in Section 5.2.1.

Another protein immobilization approach is based on biochemical affinity reaction (Figure 2.8c). This approach creates a site-specific anchoring point for well-defined and oriented immobilization. For oriented immobilization of antibodies, specific antibody-binding proteins such as protein A and protein G can be used. The Fc fragment of antibodies binds selectively to proteins A or G immobilized on the sensor surface, allowing the binding sites of the antibody (located on Fab variable region) to be accessible for subsequent antigen binding.

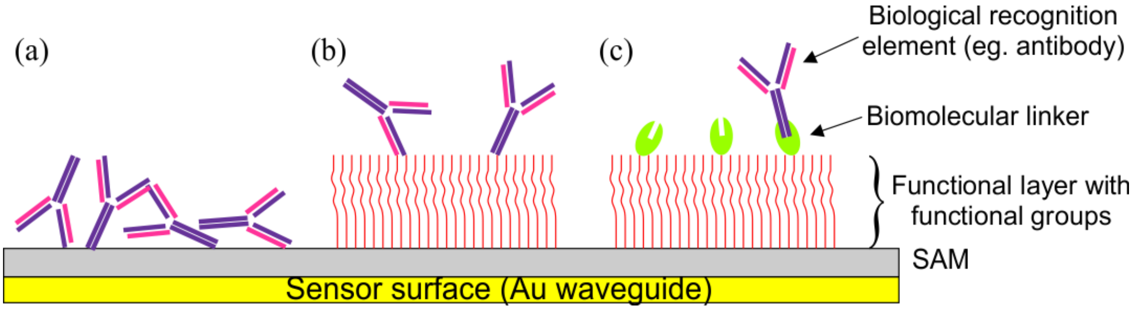

**Figure 2.8: The most common surface functionalization techniques used in surface plasmon biosensing. (a) Physical adsorption. (b) Covalent coupling. (c) Site-specific bioaffinity immobilization. (Adam *et al.*, 2012)**

The advantages and disadvantages of the most common surface functionalization techniques are summarized in Table 2.2.

**Table 2.2: Comparison of the common surface functionalization techniques (Montenegro *et al.*, 2013).**

| Techniques | Advantages | Disadvantages |
|---|---|---|
| **(a) Physical adsorption** | ▪ Facility<br>▪ Versatility | ▪ Reversible attachment |

| | | |
|---|---|---|
| **(b) Covalent coupling**<br>i. Through primary amines<br>ii. Through thiols | ▪ Better reproducibility<br>▪ Stable bond | ▪ Activation of the surface is needed<br>▪ Random binding |
| **(c) Site-specific bioaffinity immobilization**<br>i. Via biotin binding proteins<br>ii. Via secondary antibody<br>iii. Via Fc-binding proteins | ▪ Oriented binding | ▪ Reversible attachment<br>▪ (strept)avidin, protein A and protein G are expensive. |

# CHAPTER 3: DESIGN AND FABRICATION OF LONG RANGE SURFACE PLASMON BASED BIOSENSOR

## 3.1 Introduction

The design and fabrication process of long range surface plasmon based biosensor are described in this chapter. Generally, the LRSPP based waveguide is a thin gold (Au) stripe (~ 5 μm wide, 35 nm thick) embedded in CYTOP claddings (~ 8 μm each). CYTOP which has a refractive index slightly higher than that of water enables the etched channel to be filled with aqueous solutions for biosensing application while maintaining the symmetry of the structure for optimum LRSPP propagation. CYTOP is also an amorphous fluoropolymer with very high light transmittance over deep ultraviolet (DUV) to near infrared (NIR) range. A microfluidic channel is introduced to the biosensor for the sensing fluid to flow across the waveguides.

The fabrication process of the biosensor is almost similar as the previous work done by Asiri, 2012 with some minor modifications for quality improvement. The thin gold stripes are defined on the thick CYTOP claddings through photolithography technique. Using an oxygen plasma etcher, fluidic channels are introduced where portions of the cladded gold stripes are exposed to allow the flow of the sensing fluid.

## 3.2 Literature Review

### 3.2.1 Photolithography

Photolithography is a microfabrication process where patterns can be defined on a substrate using light (Mack, 2008). The process of photolithography consists of a wafer being coated with a light sensitive polymer called photoresist, then the resist is exposed to UV light through a photomask. The exposed regions are removed (positive resist) or non-removable (negative resist) in a developing bath, forming a three-dimensional image on the wafer (Hunsperger, 1984). The size of the features that can be created through photolithography depends on the wavelength of the exposure source. The conventional source for photolithography is ultraviolet (UV, wavelength = 365 nm) and deep ultraviolet (DUV, wavelength = 157 nm) (Ohtsu, 2006).

New fabrication techniques using other sources such as extreme ultraviolet (EUV, wavelength = 13.4 nm), electron-beam (e-beam, wavelength = 0.07 nm), and X-ray (wavelength = 0.8 nm) have been developed to create nanoscale features (Hunsperger, 1984). Table 3.1 summarizes the effect of wavelength on minimum feature size calculated based on Rayleigh criterion. EUV lithography must take place in a vacuum to avoid absorption and scattering of photons (Bjorkholm, 1998). For X-ray lithography, there is no know effective lenses or mirrors for x-rays and thus the beam cannot be collimated. This introduces error in the shape and position of the features that complicates mask design (Campbell, 1996). E-beam lithography is the most widely used method for nanoscale photonic devices fabrication. E-beam exposure is usually performed by direct writing using a focused beam, controlled by pre-programmed computer (Hunsperger, 1984). This technique does not require a mask and thus device design can be frequently changed without additional cost. However, it is a very time-consuming operation and results in low-volume production.

**Table 3.1: Summary of minimum feature size for different exposure sources (Hunsperger, 1984).**

| Exposure Source | Minimum Feature Size (nm) |
|---|---|
| Ultraviolet (UV) | 456 |
| Deep ultraviolet (DUV) | 196 |
| Extreme ultraviolet (EUV) | 16.8 |
| X-ray | 1.0 |
| Electron-beam (e-beam) | 0.09 |

Most of the photonics based planar waveguides are fabricated using photolithography technique because it is a technique derived from the already mature microelectronics industry, resulting in relatively inexpensive production costs. This technique is well suited for mass production where large number of identical devices can be produced, leading to very low price per device (Durandet *et al.*, 1996). The compatibility of silicon wafers with microelectronics also implies that optoelectronic chips such as laser diodes and detectors are readily integrated with the waveguides (Kawachi, 1996). A disadvantages of photolithography is that it needs a flat substrate to start with and is not very effective at creating non-flat shapes. It also needs extremely clean operating conditions hence the modern day clean rooms used (Pease & Chou, 2008). Conventional photolithographic methods using UV can produce patterns that have features down to 1 μm conveniently.

## 3.3 Methodology

### 3.3.1 Modelling of design parameters

The commercial finite element method software COMSOL Multiphysics was used to perform modal analysis of the waveguides. Different design parameters such as the width *w* and thickness *t* of the waveguide were considered for the numerical computation and their performance was evaluated. The waveguides were modelled using a two-dimensional (2D) model where the cross section of the waveguide was used.

The overlap factor $C_i$ for two modes butt-coupled to each other is given by (Buckman, 1992)

$$C_i = \frac{\iint_{A_\infty} E_{y1}\, E_{y2}^{*}\, dA}{\sqrt{\left(\iint_{A_\infty} E_{y1}\, E_{y1}^{*}\, dA\right)\left(\iint_{A_\infty} E_{y2}\, E_{y2}^{*}\, dA\right)}} \tag{3.1}$$

The integrals in Equation 3.1 are taken over the entire computational domain $A_\infty$ at the transverse plane where the modes meet. The coupling loss in decibel (dB) is given by

$$\mathrm{CL} = -20\log_{10}|C_i| \tag{3.2}$$

A single-mode fibre (SMF) is assumed to be purely transverse magnetic (TM) and has a Gaussian field distribution where

$$E_y = \exp(-\frac{x^2+y^2}{r_f^2}) \tag{3.3}$$

The mode field radius $r_f$ is given by

$$r_f = a(0.65 + \frac{1.619}{V^{\frac{3}{2}}} + \frac{2.879}{V^6}) \tag{3.4}$$

where the V parameter is

$$V = \frac{2\pi a}{\lambda_0}\mathrm{NA} \tag{3.5}$$

A standard single-mode fibre (SMF-28) has fiber core radius $a$ = 4.1 µm and the numerical aperture NA = 0.12.

### 3.3.2 Materials for fabrication

CYTOP is an amorphous fluoropolymer developed by Asahi Glass Co (Asahi Glass). It was chosen as the claddings material because it has a refractive index close to that of biologically compatible fluids. In this thesis, S-grade (CTX-809SP2) and M-grade CYTOP (CTL-809M) are used. S-grade CYTOP (no functional group) is the primary choice to build the claddings of the LRSPP biosensor due to its ultra-high light transparency. However, M-grade CYTOP with amino-silane coupling agent is used when adhesion to other materials is required.

MICROPOSIT MF-321, MICROPOSIT S1805, MICROPOSIT REMOVER 1165, MEGAPOSIT SPR 220-7, and MEGAPOSIT MF-24A developer were obtained from Shipley Company. PMGI SFG 2S was bought from MicroChem Corp. 2-isopropanol semiconductor grade (IPA), acetone HPLC grade ≥99.9%, and hydrofluoric acid were obtained from Sigma-Aldrich.

## 3.4 Results and Discussion

### 3.4.1 Design of biosensor

#### 3.4.1.1 Optical waveguides

Several passive elements using the LRSPP based waveguide, including straight waveguides, s-bends, couplers, y-splitters, and Mach-Zehnder interferometers, have been designed (Figure 3.1). The width and thickness of the waveguide as well as the radius of curvature for the bends were determined according to previous theoretical calculations (Berini & Lu, 2006; Charbonneau *et al.*, 2006; Fan *et al.*, 2012). The Au waveguide with $t$ = 35 nm and $w$ = 5 µm produces a confined LRSPP mode with reasonable attenuation and efficient coupling to single-mode fibre at operating wavelength $\lambda_0$ = 1310 nm.

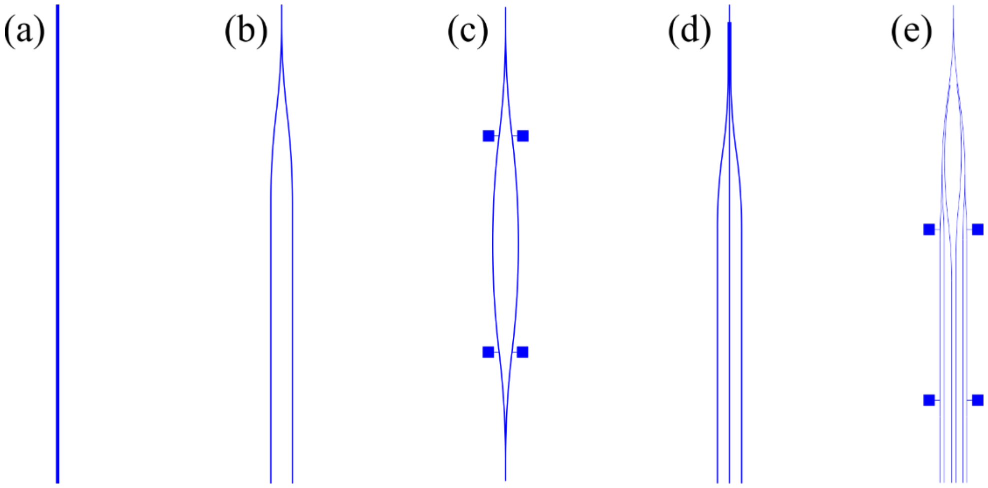

**Figure 3.1: A few examples of the biosensor structures based on LRSPP waveguides. (a) Straight waveguides (b) Y-splitter (c) Mach-Zehnder interferometer (d) Triple coupler (e) Corporate feed y-splitter**

To improve the coupling efficiency between the input fibre and the waveguide facet during optical alignment, an inverse tapered input was also introduced to the design of the biosensor. The coupling loss (in dB/facet) between a standard single-mode fibre (SMF) and the LRSPP waveguide of thickness $t$ = 35 nm was computed for different waveguide widths via overlap integrals (Charbonneau *et al.*, 2006), as shown in Figure 3.2. Besides, the tolerance in misalignment between the SMF and the waveguide was modelled by considering SMF offsets in both x and y directions (Figure 3.3). It can be clearly seen that $w$ = 2 μm produces the least coupling loss with highest tolerance to the offsets while being a confined and non-radiative mode (inset of Figure 3.2b).

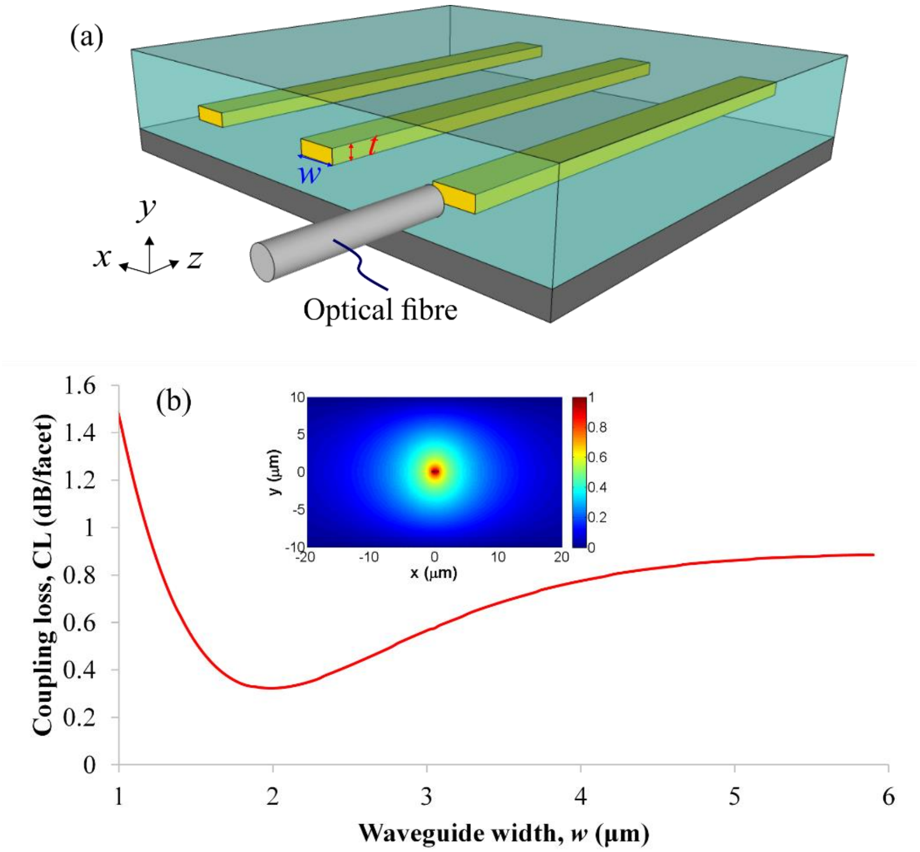

**Figure 3.2: (a) Schematic of the LRSPP biosensor with an optical fibre coupled to the input of the waveguide. The Au stripe (yellow) is of thickness *t* and width *w*. (b) Coupling loss of the LRSPP to a standard single-mode fiber (SMF) as a function of Au waveguide width (*t* = 35 nm). Inset: The transverse electric field distribution, Re{$E_y$} of the LRSPP along a waveguide with *w* = 2 μm.**

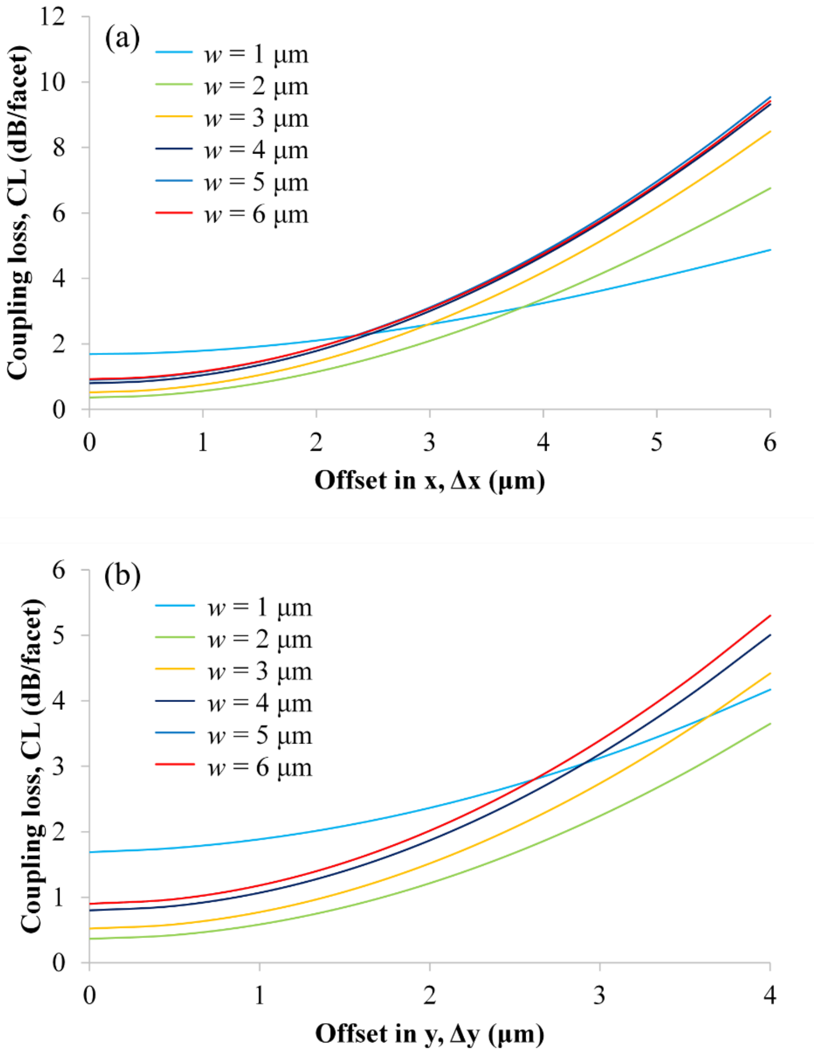

**Figure 3.3: Coupling loss of the LRSPP to a SMF with different offsets in (a) x and (b) y direction.**

Hence, the inverse taper was designed to have an input facet of $w$ = 2 µm and was gradually widened to the target waveguide width ($w$ = 5 µm). In order to make sure the mode is guided non-adiabatically through the taper, the same radius of curvature as the bends ($R$ = 5.5 mm) was considered to connect the input facet to the waveguide (as illustrated in Figure 3.4). A linear inverse taper of length $l$ = 128 µm was implemented as the final design in the mask layout.

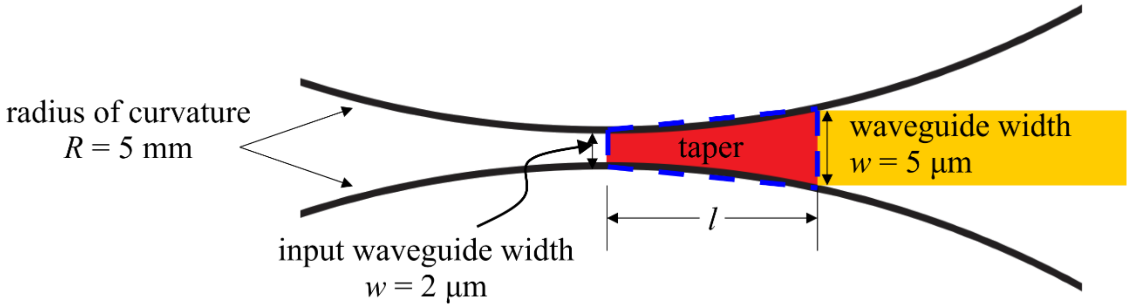

**Figure 3.4: Illustration of how an inverse taper was designed. The blue dotted line represents the final design of the linear taper with $l$ = 128 µm.**

For dengue detection purpose, we aim to perform the antigen-based (NS1 antigen) and serological-based (IgM/IgG antibody) diagnosis at the same time to improve the overall sensitivity (Blacksell *et al.*, 2011; Guzman, Jaenisch, *et al.*, 2010). Therefore, all the designed structures (except for the straight waveguide) have at least two sensing arms for simultaneous biosensing. In certain designs (e.g. Figures 3.1d and e), we even consider a reference arm for signal calibration.

One of the designs for the dengue biosensor is a triple coupler (Figure 3.1d) with its expanded view shown in the inset of Figure 3.6. The input to the triple coupler is a straight waveguide, which also acts as a reference arm. As the input field enters the triple coupler ($z$ = 0), it couples to the two neighbouring waveguides which are 2 µm away at both sides. Three supermodes are supported by such triple coupler (Fan *et al.*, 2014), namely mode (1 1 1), mode (-1 0 1) and mode (1 -1 1). The field distribution of these modes were modelled using finite element method (FEM) and shown in Figure 3.5. The power distributions among the three waveguides were theoretically computed by considering various coupling lengths, CL and the results are presented in Figure 3.6. Since the centre waveguide P2 is used as a reference arm, the power distributions were arranged such that most of the power is transferred to the sensing arms (waveguides P1 and P3). Two coupling lengths, CL = 400 µm and 500 µm, were selected based on this criteria for the design of our biosensor.

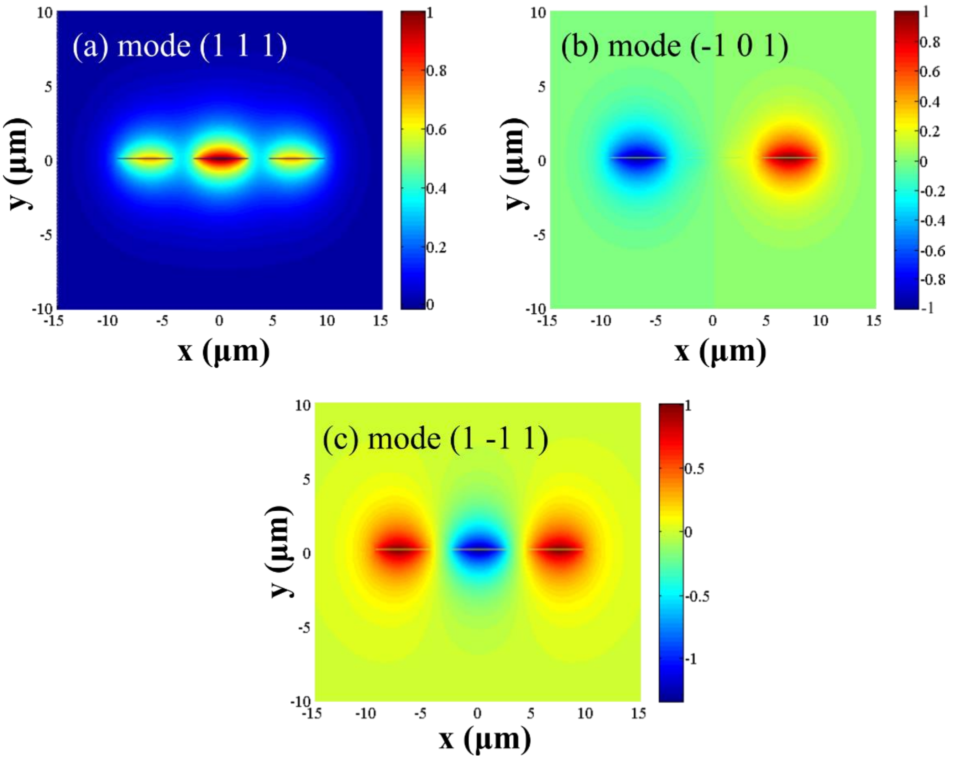

**Figure 3.5: The normalized Re{$E_y$} field distribution of a triple coupler with (a) long-range supermode (1 1 1), (b) long-range supermode (-1 0 1), and (c) long-range supermode (1 -1 1).**

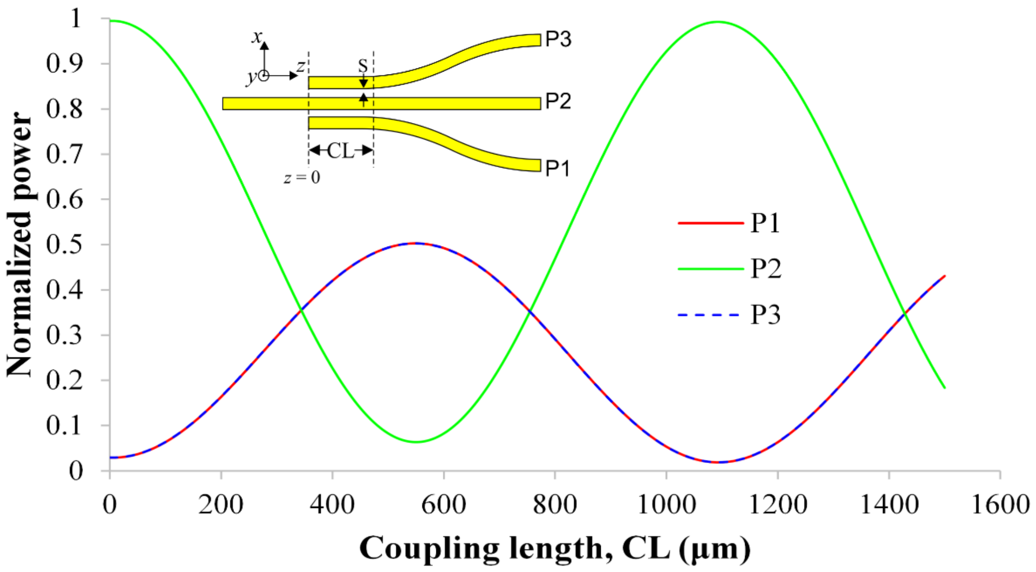

**Figure 3.6: Calculated normalized output power versus coupling length CL for a triple coupler with separation S = 2 μm. The waveguides P1 and P3 have similar output power such that the curves overlap each other. The inset shows the structure of a triple coupler considered for the computation.**

Another design of our dengue biosensor is the corporate feed y-splitter, as illustrated in Figure 3.1e. There are two important variants of this design, which are the coupler and Young's interferometer. The coupler, shown in expanded view in Figure 3.7a, consists of a straight parallel section of length $CL_1$ in between the cascaded y-splitters and a small part of the subsequent s-bend section over the length $CL_2$. The theoretical model for the coupler is similar to that reported in previous work (Charbonneau *et al.*, 2006), where the through port of the coupler is the sensing waveguide P1 and the coupled port is the reference waveguide P2. By using orthogonal symmetric and asymmetric coupler supermodes (Buckman, 1992), the coupled waveguides were modelled using FEM. The field distributions of the symmetric and asymmetric coupler supermodes are shown in Figure 3.8. The normalized optical power in the reference and sensing waveguides was computed for different coupling lengths, shown in Figure 3.7b. Similarly, as most of the power is desired for sensing waveguides, the power transfer coefficient from the input port to the coupled port (reference arm) $T_{\text{coupled}}$ was set to be 0.2 and the coupling length of the straight section $CL_1$ was determined as 200 μm.

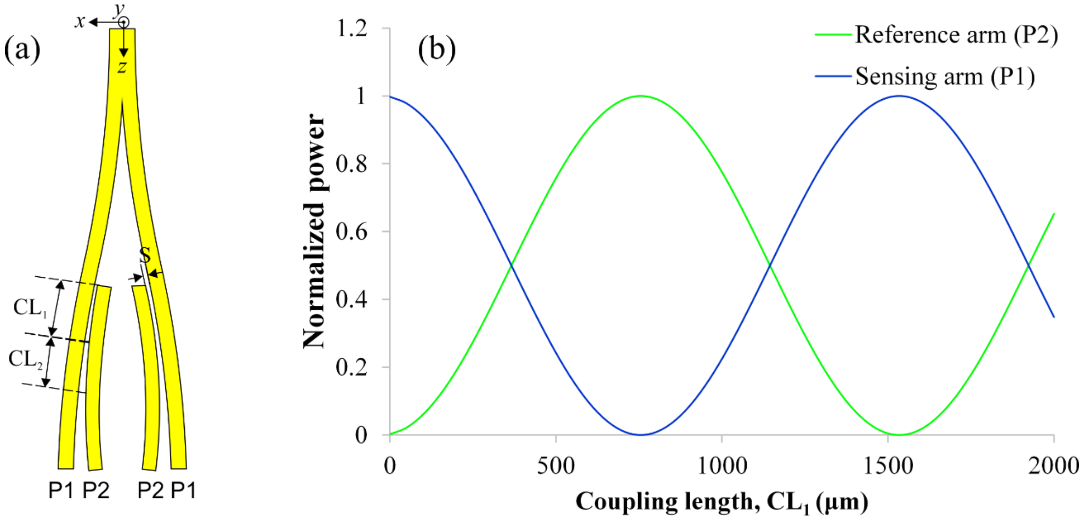

**Figure 3.7: (a) Sketch of the coupler structure in corporate feed y-splitter. (b) Calculated normalized output power versus coupling length $CL_1$ for a coupler with separation S = 2 μm.**

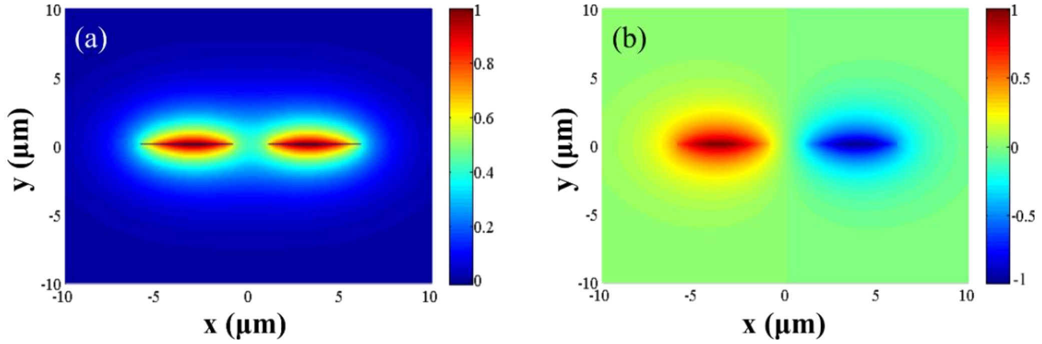

**Figure 3.8: The normalized Re{$E_y$} field distribution of a coupler with (a) symmetric coupler supermode and (b) asymmetric coupler supermode.**

Besides, during the design of corporate feed y-splitter, the distances between the output waveguides were properly arranged so that it can act as a Young's interferometer. The output divergent beams from the corporate feed y-splitter will overlap with each other to form an interference pattern at a distance *L* from the waveguide output. The equations related to multichannel Young's interferometer are given in Ymeti *et al.*, 2003. In brief, the distances between the six output waveguides are $d_{12}$ = 40 μm, $d_{23}$ = 74.44 μm, $d_{34}$ = 44.16 μm, $d_{45}$ = 71.94 μm, and $d_{56}$ = 40 μm where $d_{ij}$ is the distance between *i*th and *j*th waveguides (Figure 3.9). Based on the design, there are thirteen spatial frequencies in the interference pattern which will show up as particular peaks in the amplitude of the Fourier transform of the interference pattern. The phase difference between the waveguides can be extracted from the phase value for each spatial frequency in the phase part of the Fourier transformation.

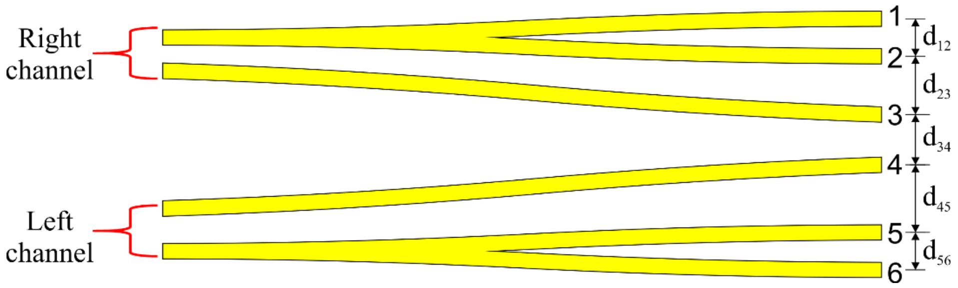

**Figure 3.9: Sketch of the Young's interferometer in corporate feed y-splitter. The different distances between the six output waveguides will appear as thirteen spatial frequencies in the interference pattern.**

The layout of the devices was drawn using a commercial software dw-2000 (Design Workshop Technologies Inc.) before being processed into a photomask. Examples of the photomask layouts are shown in Figure 3.10 where part (a) is the photomask for optical waveguides of different designs and part (b) is the photomask for fluidic channels.

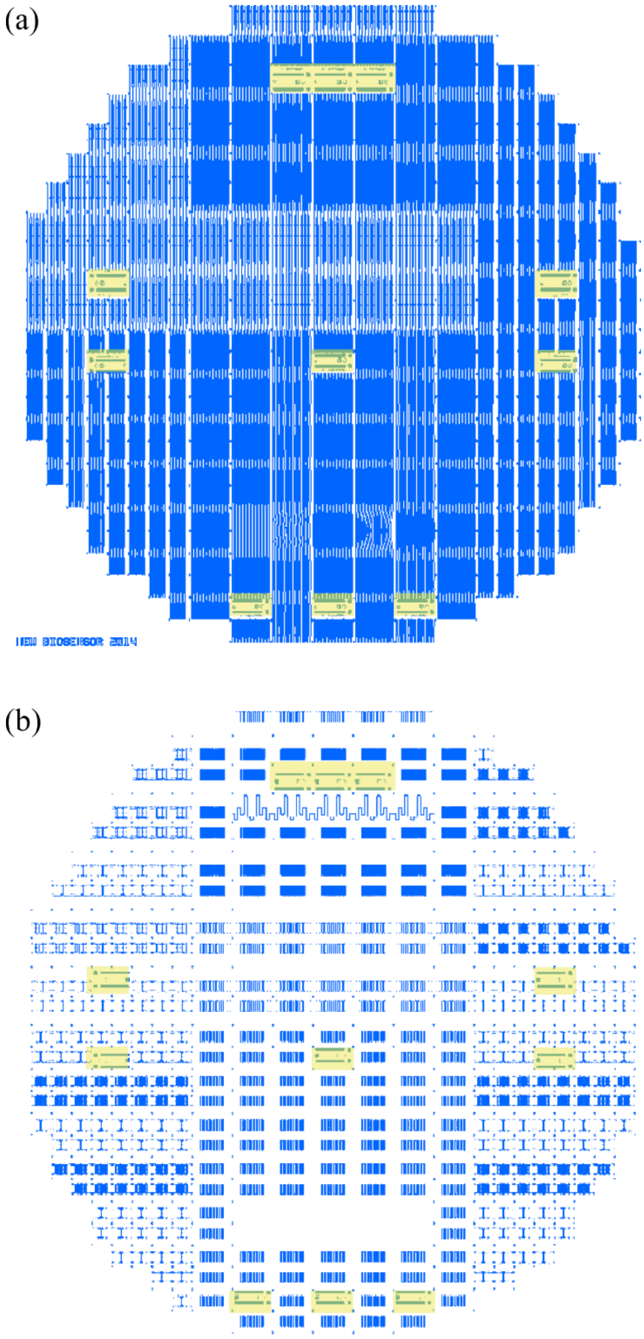

**Figure 3.10: The layout of the photomask for (a) optical waveguides and (b) fluidic channels drawn using dw-2000. The yellow shaded areas indicate the alignment marks (will be discussed in Section 3.4.2.6).**

#### 3.4.1.2 Microfluidic channel

Basically, the microfluidic channel introduced to the biosensor can be either top-access or side-access, depending on the application. It is easier to create a sealed fluidic system with a top-access microfluidic channel. However, if many fluids are to be passed through the biosensor simultaneously, a side-access microfluidic channel provides the convenience to do so.

Figure 3.11 shows the different fluidic architectures designed for LRSPP based biosensor. A simple open channel etch allows the external fluids to be easily introduced onto the sensor die. The etched channel inherits the shape of an O-ring which will be used to seal the microfluidic system. A dedicated channel etch allows only selected waveguides to be etched, especially useful for y-splitters and Mach-Zehnder interferometers (MZIs) where a cladded reference arm can be designed. The width of the dedicated channel is designed to be equal to or larger than 80 μm to ease wetting of the waveguide. In a side-access channel, the fluids can be passed through the selected waveguide at certain flow rate by proper design of the flow channels.

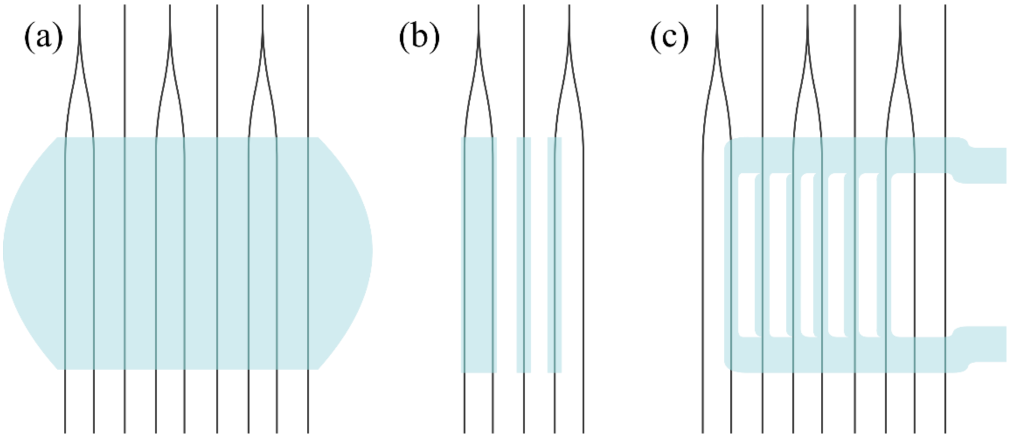

**Figure 3.11: Schematic of the fluidic architectures designed for the LRSPP based biosensor. The blue shaded area represents the etched region where the microfluidic channel is defined. (a) Open channel etch (b) Dedicated channel etch (c) Side-access channel etch**

### 3.4.2 Fabrication process

The fabrication process of the LRSPP biosensor (Figure 3.12) is mainly based on the work done by Asiri, 2012 with some updated adjustments. The gold waveguide fabricated using the protocols developed by Asiri, 2012 has poor adhesion to the CYTOP cladding. In this thesis, the adhesion problem is solved by replacing the last layer of the bottom cladding with 5% M-grade CYTOP. After the whole fabrication process, the wafer is baked for a week to minimize the solvent trapped inside the wafer. More force can be applied to seal the fluidic channel of the hard-baked biosensor without destroying the gold waveguide.

The biosensor fabrication is carried out in the microfabrication cleanroom in University of Carleton, Ottawa, Canada. Briefly, sensors were fabricated by spin-coating CYTOP on a 4-inch silicon wafer as the bottom cladding. Au evaporation and lift-off were performed to define Au features using an optical lithography technique. Subsequently, a top cladding of CYTOP was coated. The top CYTOP cladding was etched down to the Au stripe surface to form a large fluidic channel of sensing length, $L = 1.65$ mm. A thick layer of photoresist was deposited onto the wafer before it was sent for dicing into ~300 dies per wafer. The detailed fabrication process of the sensors will be discussed in the following sections.

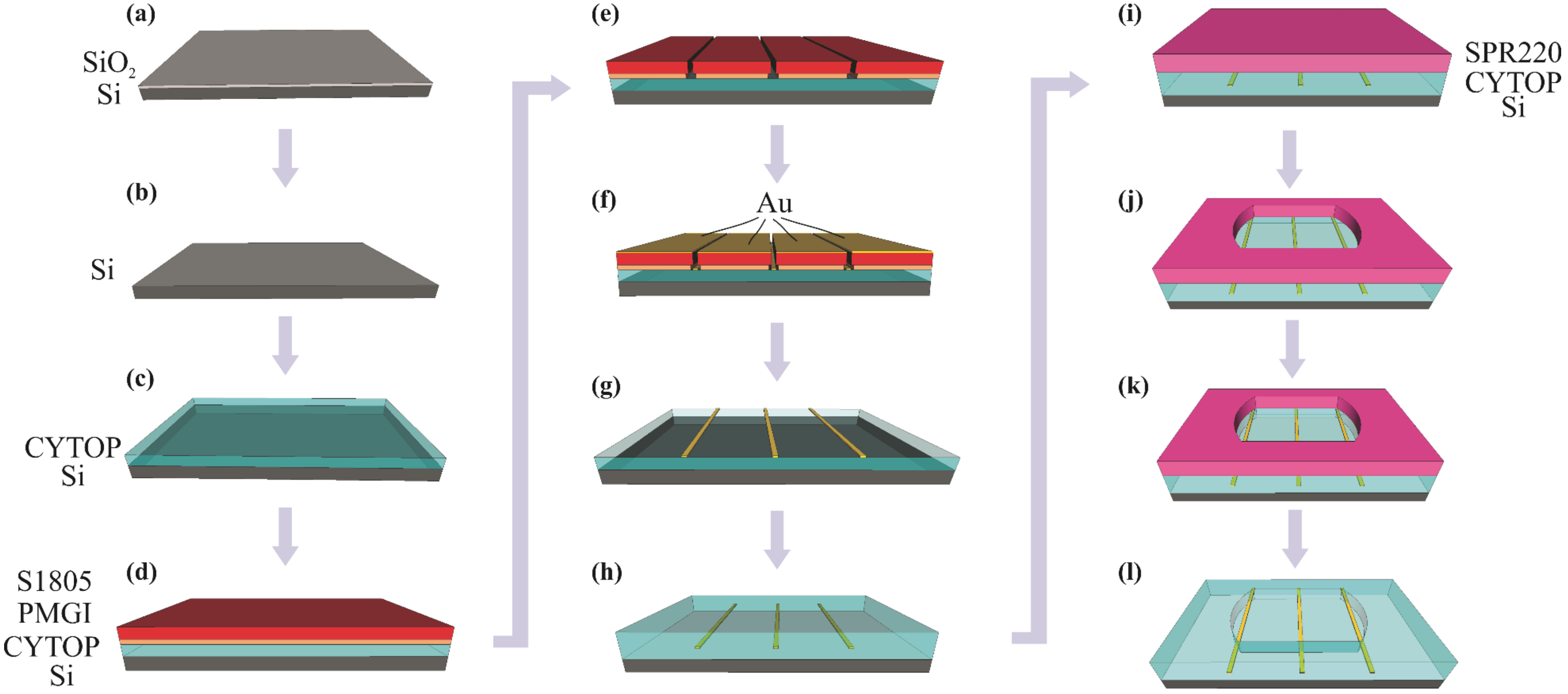

**Figure 3.12: An overall fabrication process flow for long-range surface plasmon based biosensor.**

### 3.4.2.1 Wafer preparation

The wafer preparation process is illustrated in Figures 3.12a-b. All LRSPP biosensor are fabricated on 4-inch silicon wafers with {1 0 0} crystallographic orientation. The crystallographic orientation of the wafer is verified by inspecting the location of the wafer flats. For {1 0 0} wafer, the primary flat (longest flat edge) should be either parallel to (Figure 3.13a) or perpendicular to (Figure 3.13b) the secondary flat (shorter flat edge). The flats at different angles indicate the doping type of the wafer which is not significant to our fabrication process.

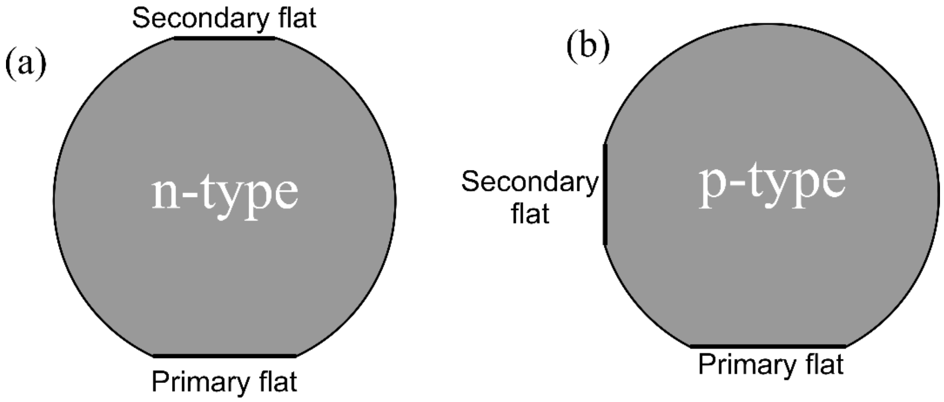

**Figure 3.13: Silicon wafer with {1 0 0} crystallographic orientation. (a) n-type wafer with parallel secondary flat. (b) p-type wafer with perpendicular secondary flat.**

After selecting and scribing a suitable wafer, the wafer was immersed in 10% hydrofluoric (HF) acid for 20s to remove any oxide layer ($SiO_2$) formed on the wafer. After a thorough rinse with deionized water (DI $H_2O$) and dried with nitrogen gas ($N_2$), the wafer was placed in an oxygen ($O_2$) plasma etcher (Plasma Preen II #862) for two consecutive 5-minute runs to dehydrate the surface and to remove any impurities that might survive the HF dip.

### 3.4.2.2 Bottom cladding

The bottom cladding fabrication process is illustrated in Figures 3.12c. The bottom cladding of the sensor is constructed by multiple layers of CYTOP. There are three grades of CYTOP (with different end functional group) available: S-grade, A-grade and M-grade

(AGC Chemicals, 2009). In this thesis, S-grade and M-grade CYTOP are used to form the bottom cladding of our sensor.

The first layer of bottom cladding was formed by spinning a 5% M-grade CYTOP (CTL-809M) at 500 rpm for 10s followed by 1000 rpm for 20s. The thin layer of M-grade CYTOP (~400 nm) acts as an adhesion layer between the silicon wafer and successive CYTOP layers. Three subsequent layers of 9% S-grade CYTOP (CTX-809SP2) were spun at 1000 rpm for 10s then 1500 rpm for an additional 20s to form a bulk bottom cladding of around 7 μm in thickness. 5% M-grade CYTOP was chosen as the last layer of bottom cladding to improve the adhesion between the gold waveguide and CYTOP cladding. The last layer was formed by spinning at 1000 rpm for 20s. M-grade CYTOP was diluted down to 5% using the supplied diluent (CT SOLV 180) to ensure the planarization of the cladding surface. After each spin, a soft-bake at 50 °C for 30 minutes on a hotplate was performed to partially anneal the films. When a complete bottom cladding as illustrated in Figure 3.14 was formed, the wafer which was baked at 50 °C was ramped up to 200 °C at a rate of 150 °C/hour and maintained at 200 °C for 2.5 hours. This hard-bake process which brings the bottom claddings above CYTOP's glass-transition temperature ($T_g$ = 108 °C) is expected to fully evaporate the remaining solvent in the bottom cladding besides smoothing the top surface.

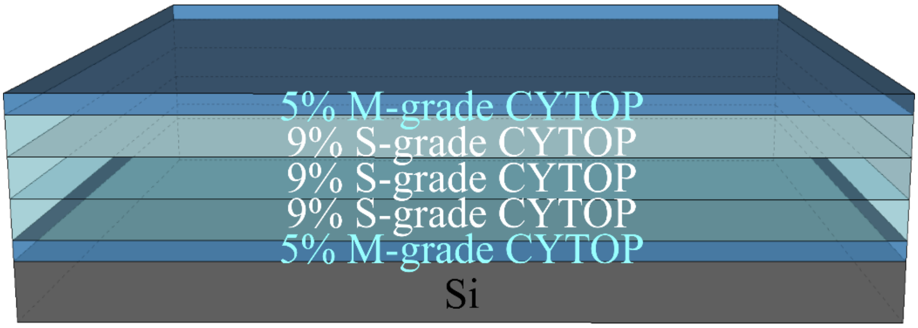

**Figure 3.14: Schematic showing the composition of bottom CYTOP cladding (drawing not to scale).**

### 3.4.2.3 Photolithography

The photolithography process is illustrated in Figures 3.12d-e. After a complete bottom cladding was formed, the desired waveguide patterns were defined on the wafer through photolithography process. Since the hydrophobic CYTOP is highly repellent to water, the surface was activated with a gentle treatment of $O_2$ plasma (March Jupiter II RIE plasma system) for 30s. This 'ashing' step changes the CYTOP surface to hydrophilic and allows the coating of hexamethyldisilazane (HMDS), an adhesion promoter for photoresist. An HMDS vapour prime oven (Yield Engineering Systems) was programmed and run to apply a uniform layer of HMDS on the CYTOP surface.

Bi-layer lithography process was introduced to define the Au stripes and features on the LRSPP biosensor. First, a lift-off resist PMGI SFG 2S (MicroChem Corp.) was spun at 500 rpm for 10s and then at 1000 rpm for 30s to achieve a thickness around 75 nm (MicroChem Corp., 2002). The wafer is then baked on a hotplate at 180°C for 3 minutes to enable precise and reproducible control of undercut during develop process. After that, a layer of around 600 nm positive photoresist MICROPOSIT S1805 (Shipley Company) was spun at 1000 rpm for 10s and then at 4000 rpm for 30s. After spinning, the wafer was baked on a hotplate at 115°C for 3 minutes. The baking time and temperature of both PMGI SFG 2S and MICROPOSIT S1805 have to be controlled precisely because these parameters will affect the develop time (the develop process will be discussed later in this section).

Following the formation of photoresist, the waveguide structures can be defined on the wafer through UV exposure of the photoresist. A photomask with the biosensor structure layouts (e.g. the blue lines in Figure 3.1) has been previously designed and fabricated. MICROPOSIT S1805 is chosen as the photoresist because it is effective for broadband UV exposure, especially for g-line (wavelength at 436 nm) exposure. Exposure was done by using a mask aligner (Karl-Suss MA6) with 350 W mercury (Hg) lamp as light source. The exposure time required for the photoresist to be completely exposed can be calculated from the following equation:

$$\text{Exposure time (s)} = \frac{\text{Exposure dose (mJ/cm2)}}{\text{Measured intensity (mW/cm2)}} \tag{3.1}$$

Before an actual exposure, the Hg lamp intensity was measured to be 10 mW/cm$^2$ at 405 nm (h-line). The suitable exposure dose for MICROPOSIT S1805 was previously determined to be in the range of 80 to 180 mJ/cm$^2$ (Asiri, 2012). Hence, for our fabrication process, the exposure time was set as 12s. Optimum exposure is critical in order to obtain maximum resolution from the photomask.

The wafer was held horizontally on a suitable size chuck by vacuum in the mask aligner with the photoresist facing upwards. The photomask was placed in direct contact on top of the wafer having the patterned side (usually called the "chrome side") facing downwards. After setting the desired exposure time, the wafer was exposed in *Hard Contact* (HP) mode to eliminate any possible air gap between the wafer and photomask for maximum resolution of the features.

After exposure, the wafer was immersed in a developer solution MICROPOSIT MF-321 (Shipley Company) at room temperature. The developer solution will remove the exposed portion of the photoresist MICROPOSIT S1805 and leave behind the desired patterns on the wafer. Since the lift-off resist PMGI SFG 2S is not photosensitive, it will be dissolved by the developer solution isotropically where an undercut profile is formed after sufficient dissolution time. The undercut profile is high desirable for proper lift-off process and good resolution of the Au features. The significance of an undercut will be discussed in the last part of Section 3.4.2.4. For the fabrication of our biosensor, the wafer was developed for 45s with moderate agitation by hand. Next, the wafer was inspected under UV-filtered microscope to make sure all the critical dimensions were properly defined.

#### 3.4.2.4 Metallization and lift-off

The metallization and lift-off process is illustrated in Figures 3.12f-g. Gold deposition was performed using a metal evaporator (BA510, Balzer). Once the wafer was developed, the wafer was loaded to the evaporator and set under vacuum overnight to achieve a pressure below $1 \times 10^{-6}$ Torr absolute. Typically, the pressure of the evaporator will affect the roughness of the Au deposited. A simple schematic of the evaporator is illustrated in Figure 3.15. The wafer was suspended upside down in the evaporator using magnets. A quartz crystal microbalance (QCM) was used as the sensor to determine the deposition rate and film thickness. Before deposition, a gold pellet was added to the tungsten boat. The tungsten boat which is resistively heated by the supplied current will melt the Au pellet. Then, the Au vapour will condense in the form of thin film on the wafer surface. The deposition rate of the evaporator is controlled by the amount of current supplied to the tungsten boat.

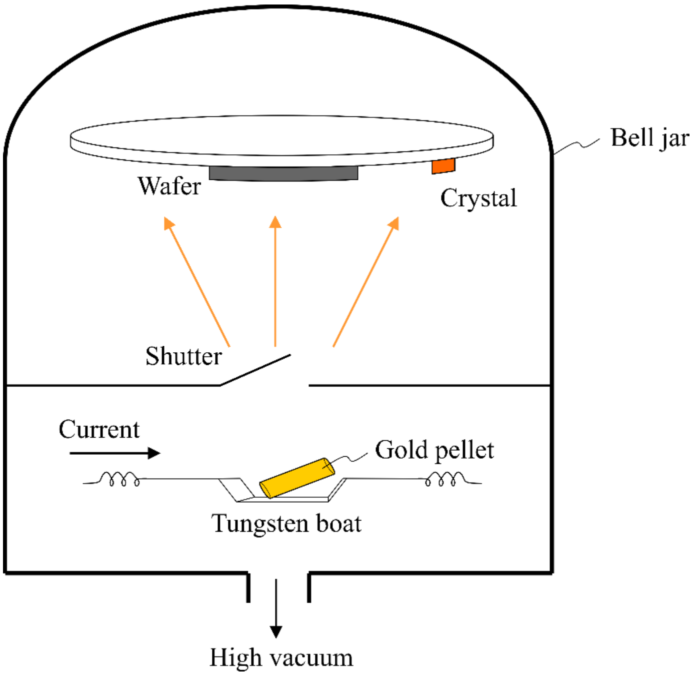

**Figure 3.15: A simplified schematic showing the Balzer BA510 evaporator.**

One of the drawbacks of thermal evaporation is the possibility of contamination. Before opening the shutter of the evaporator for actual deposition, the power was raised above the required level to burn any possible contaminants in the evaporator. Then, the power was brought down low enough that the deposition rate remains zero. Once the current was stabilized for 30s, the shutter was opened and the power was slowly increased to achieve the target deposition rate of 0.2 Å/s. The deposition was performed until a target thickness of 35 nm was achieved. The shutter was closed and the chamber was allowed to cool down for 10 minutes after the deposition was complete. Then, the chamber was vented for another 10 minutes before the wafer was unloaded at atmospheric pressure.

Right after the Au deposition, the lift-off procedure was carried out with two heated baths of MICROPOSIT REMOVER 1165 (Shipley Company). MICROPOSIT REMOVER 1165 will strip off the photoresist and lift-off resist, leaving behind only the Au features on the CYTOP cladding. The two baths were maintained at temperature between 75 – 85 °C. The wafer was immersed in the first bath (dirty bath) for 10 minutes with no agitation. Then, the dirty bath was placed in an ultrasonic bath for 10s to remove most of the resists. Next, the wafer was transferred to the second bath (clean bath) for another 10 minutes, followed by 10-second ultrasonication. After two sequential MICROPOSIT REMOVER 1165 baths, only the defined Au features will remain on the wafer (Figure 3.12g). The wafer was cleaned with 2-isopropanol (IPA) and deionized water (DI $H_2O$) for 10 minutes each to remove any residue of MICROPOSIT REMOVER 1165.

The importance of undercut during develop process can be clearly revealed during the lift-off process. Figure 3.16 represents three possible cases during a develop process, where the wafer is under developed, properly developed, and over developed. When the wafer is under developed, only the lift-off resist under the exposed photoresist is being removed. When Au is deposited, it will slightly cover the sidewalls of resists and thus creates a link to the actual Au stripe deposited. When the lift-off resist is further developed, an undercut will form. Despite the Au deposited on the sidewalls of the resists, the actual Au stripe is isolated due to the bi-layer re-entrant sidewall profile (undercut). However, when the wafer is developed for too long, the photoresist will start sagging down due to insufficient support from the lift-off resist. In this case, we might see the rounded edges and broadening of the features. Besides, the collapsing of the photoresists also causes the Au deposited on the sidewalls to directly attach to the Au stripe.

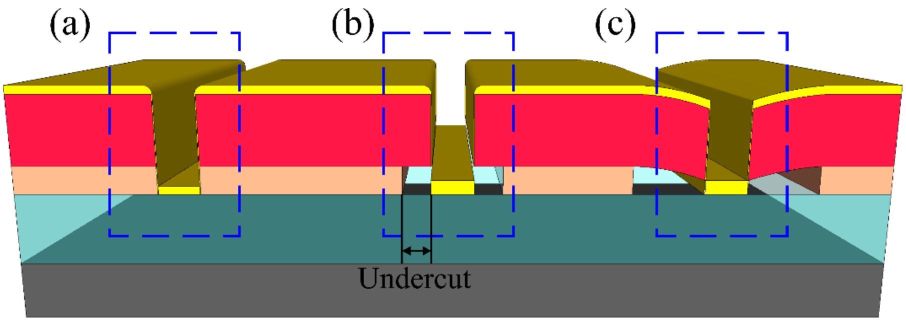

**Figure 3.16: Three possible situations during a develop process. (a) Under-development (b) Proper/good development (c) Over-development.**

If there is a connection between the Au on the sidewalls and Au stripes, part or all of the Au stripe can be washed away during lift-off process. This situation causes “mouse-bite” defect or delamination on the waveguides. Another possible outcome from under- or over-development is the formation of “wing” near the edges of the waveguides. These defects are shown in Figure 3.17.

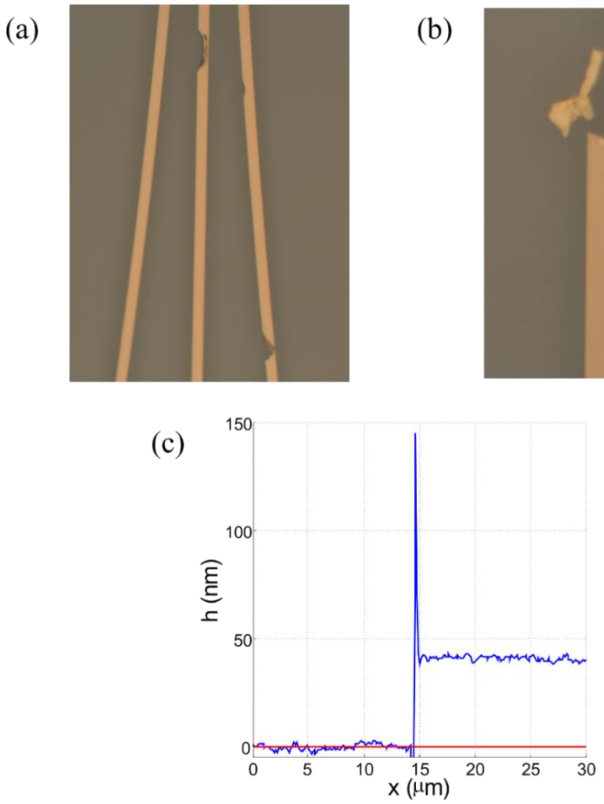

**Figure 3.17: Possible defects on the waveguides due to poor photolithography process. (a) Microscope image showing the "mouse-bite" defect on the waveguides. (b) Microscope image showing the delamination of the waveguides. (c) One-dimensional AFM line scan showing the formation of "wing" near the edges of the waveguides.**

#### 3.4.2.5 Top cladding

The top cladding fabrication process is illustrated in Figure 3.12h. Once the wafer was inspected under microscope and the quality of the Au features was deemed satisfactory, the top CYTOP cladding was spin-coated on the wafer using similar technique as discussed in Section 3.4.2.2. Before spin coating, the wafer was dehydrated by baking on a hotplate at 90 °C for 15 minutes to evaporate any moisture present on the surface of the wafer. Since there is no adhesion required, all layers of the top cladding are constructed using 9% S-grade CYTOP. The spin coater was set to operate at 1000 rpm for 10s followed by 4000 rpm for 20s. The wafer was soft-baked on a hotplate at 50 °C for 30 minutes after a layer of S-grade CYTOP was spun. For the first layer of CYTOP, the wafer was ramped at 5 °C/hour to 100°C and left baking overnight. A slow and long bake is required for the first layer of CYTOP to produce an effective barrier against waveguide deformation (Asiri, 2012). The process of spinning was repeated for an additional 5 times with a soft-bake after each layer was spun on. For the subsequent layers, the wafer was ramped at 25 °C/hour to 100°C and held at this temperature for 1.5 hours. The composition of the top CYTOP cladding is shown in Figure 3.18.

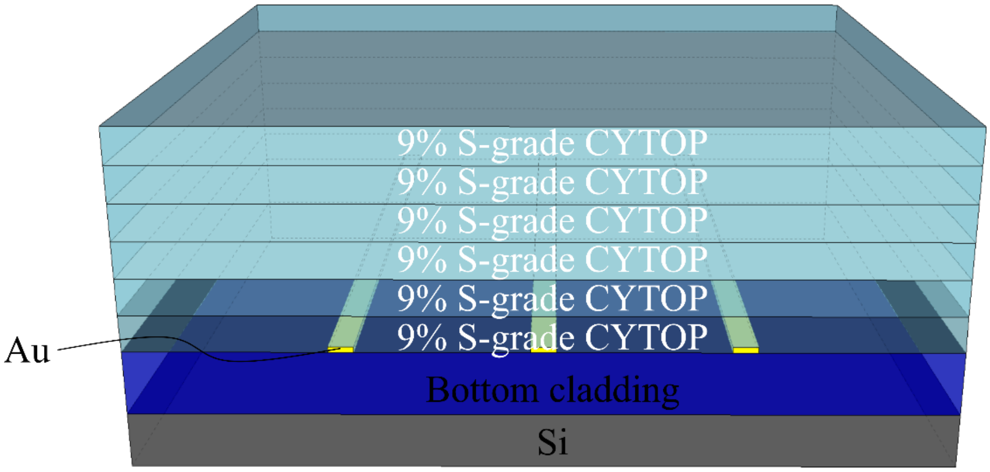

**Figure 3.18: Schematic showing the composition of top CYTOP cladding (drawing not to scale).**

#### 3.4.2.6 Fluidic channel lithography

The fluidic channel lithography process is illustrated in Figures 3.12i-k. The fluidic channels are defined on the wafer using a simpler photolithography technique which requires only a single layer of photoresist. The surface of the wafer was prepared similarly before a layer of photoresist was coated. The fully-cladded wafer was placed into the $O_2$ plasma system for 30s to ‘ash’ the hydrophobic surface. Then, the wafer was coated with HMDS using the HMDS vapour prime oven. MEGAPOSIT SPR 220-7 (Shipley Company) was chosen as the positive photoresist for fluidic channel definition. The highly-viscous photoresist was first spread over the wafer surface at 1000 rpm for 30s and followed by a spin at 2300 rpm for 10s to achieve the target thickness. The thickness of the photoresist was targeted to be around 9 μm so that the thick top CYTOP cladding (~ 8 μm) can be etched (Chiu *et al.*, 2010). After spinning, the wafer was left at room temperature for 30 minutes to allow the resist to outgas. Then, the wafer was placed on a hotplate and ramped from room temperature to 100 °C. The wafer was baked at 100 °C for 15 minutes before being gradually ramped down to room temperature. The gradual ramp during baking in direct contact with the hotplate is essential to avoid any thermal shock or formation of bubbles in the photoresist surface.

Next, the wafer was placed on the mask aligner along with the fluidic channel photomask (e.g. the blue shaded area in Figure 3.11). Precise alignment is crucial during this step to make sure that the fluidic channels are properly overlaid on the optical waveguides. Alignment marks (as shown in Figure 3.19) were added on the both the optical and fluidic channel photomasks to help the alignment process. The exposure time is set to be 99s (corresponding to the required exposure dose of 800 - 1350 mJ/cm$^2$ (Asiri, 2012)). After exposure, the wafer was allowed to rehydrate at room temperature overnight. The thick photoresist needs to be evenly moisturized because water is necessary to complete the photo-reaction.

**Figure 3.19: An example of alignment mark placed on the photomasks. The yellow areas represent the Au deposited on the wafer using the optical photomask and the red shaded areas represent the alignment feature on the fluidic channel photomask (drawing is not to scale).**

A post-exposure bake was carried out by placing the wafer on a hotplate which was ramped from room temperature to 100 °C. The wafer was then transferred to another hotplate at 115 °C for 60s. After that, the wafer was moved back to the hotplate at 100 °C and slowly ramped down to room temperature. The exposed areas of the photoresist were removed using MEGAPOSIT MF-24A developer (Shipley Company). The develop process usually takes around 1 minute 30 seconds with strong agitation in fresh developer solution. However, since there is no lift-off layer and over-development has insignificant effect, the develop time can be extended for longer period to ensure all exposed photoresist is completely removed.

### 3.4.2.7 Fluidic channel etching

The fluidic channel etching process is illustrated in Figure 3.12l. The fluidic channel pattern defined on the photoresist MEGAPOSIT SPR 220-7 can be transferred into the underlying top CYTOP cladding by an $O_2$ plasma etcher (March Jupiter II RIE plasma system) based on high-energy reactive ion etching technology. This directional etch produces fluidic channels having their side walls profile perpendicular to the wafer surface. The settings on the $O_2$ plasma etcher are described in Table 3.2.

**Table 3.2: Settings on the $O_2$ plasma etcher to perform the fluidic channel etching.**

| **March Jupiter II RIE plasma system** | |
|---|---|
| Power (W) | 200 |
| Pressure (mTorr) | 300-340 |
| $O_2$ flow (sccm) | 220 |

The etch rate of CYTOP under $O_2$ plasma at similar conditions was approximated as 0.918 ± 0.017 μm/min (Chiu, 2009). Hence, by considering the approximate thickness of top cladding being 8 μm, a total etch time of 9 minutes was estimated for the Au stripes to be completely exposed. To ensure the full exposure of the waveguides, a slight over-etch which results in a CYTOP pedestal ~ 400 nm high was performed. For more precise etching, the profile of the wafer was checked periodically using a profilometer (Tencor P-1) after 8 minutes of etching. An example of the profilometry scan is shown in Figure 3.20. One point from every region of the wafer (north, south, east, west, and centre) was selected for the profilometry check to make sure all devices on the wafer were properly etched. Additionally, for a more uniform etch across the wafer, the wafer was rotated 90° in the $O_2$ plasma etcher every 2 minutes. After fluidic channels with suitable depth were obtained, the photoresist MEGAPOSIT SPR 220-7 was removed by immersing the wafer into sequential baths of acetone, IPA and DI $H_2O$ for 10 minutes each. Then, the wafer was dried with $N_2$ and loaded into an oven at 100 °C for a week long bake. The final baking step is aimed to minimize the solvent trapped inside the wafer, especially in the CYTOP claddings.

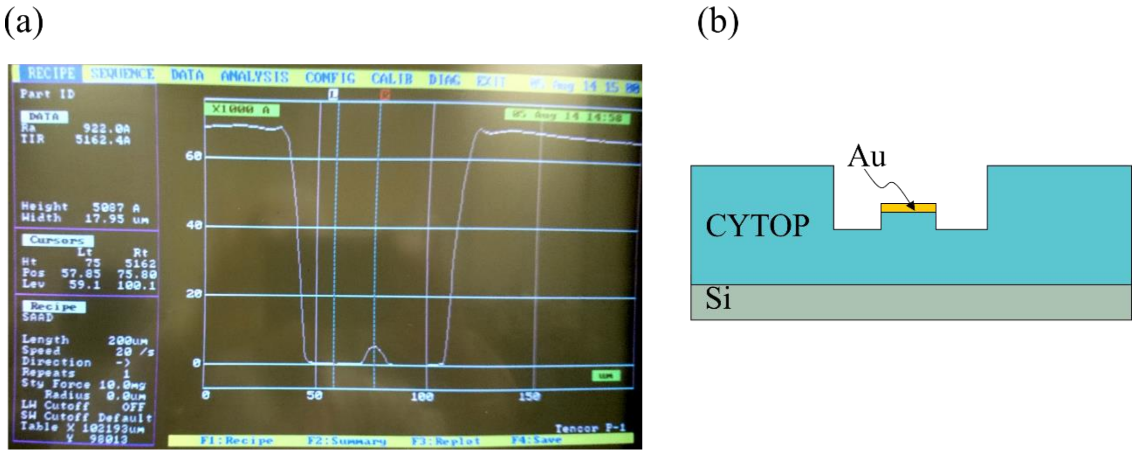

```
Part ID
DATA
Ra        922.0A
TIR      5162.4A

Height    5087 A
Width   17.95 um
Cursors
           Lt      Rt
Ht         75    5162
Pos     57.85   75.80
Lev      59.1   100.1
Recipe
SAAD

Length       200um
Speed         20 /s
Direction       ->
Repeats          1
Sty Force  10.0mg
    Radius   0.0um
LW Cutoff      OFF
SW Cutoff  Default
Table X  102193um
      Y    98013
```

**Figure 3.20: (a) A snapshot of the profilometry scan on an etched wafer. (b) Schematic diagram showing the corresponding configuration of the etched wafer being scanned. Due to slight over-etching, the gold stripe is located on a CYTOP pedestal ~ 500 nm.**

#### 3.4.2.8 Preparation of wafer for dicing

After the long bake, the wafer is ready to be sent for dicing. A 4-inch wafer will be diced into ~300 LRSPP biosensor dies (each die bearing many biosensors). A layer of photoresist was applied to the wafer prior dicing to protect the wafer surface from contamination during dicing process. MEGAPOSIT SPR 220-7 was chosen as the protective film. Similar process as described in Section 3.4.2.6 was applied. The wafer was ‘ashed’ using the $O_2$ plasma system for 30s and coated with HMDS using the HMDS vapour prime oven. MEGAPOSIT SPR 220-7 was spun on the wafer at 1000 rpm for 30s and followed by 2300 rpm for 10s. After spinning, the wafer was allowed to outgas at room temperature for 30 minutes. Then, it was placed directly on a hotplate and ramped from room temperature to 100 °C. The wafer was baked at 100 °C for 20 minutes before being ramped down back to room temperature. The photoresist applied must be cured hard enough such that the diced facets are not contaminated yet soft enough that it will not chip as the dicing saw cuts through the wafer. Figure 3.21 shows an example of a diced wafer coated with MEGAPOSIT SPR 220-7.

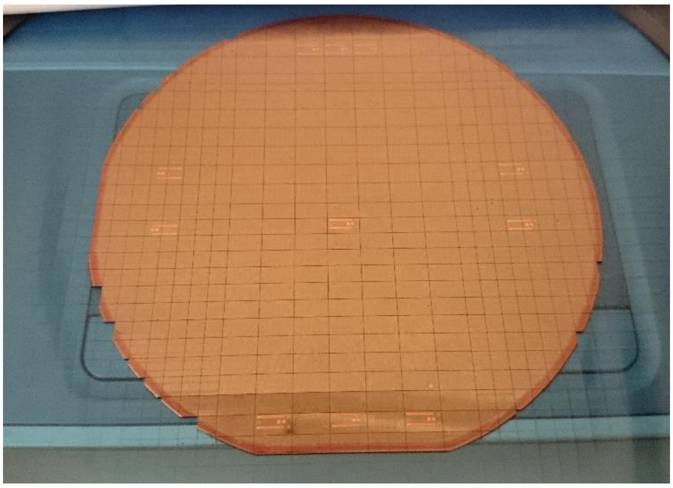

**Figure 3.21: A wafer, coated with MEGAPOSIT SPR 220-7 and placed on a dicing tape, is diced into ~300 LRSPP biosensors (dies).**

### 3.4.3 Atomic Force Microscopy (AFM) Measurements

After the wafer was returned from dicing, a sensor die (diced sample) was randomly selected for atomic force microscopy (AFM) measurements to evaluate the fabrication quality. The important parameters to be obtained from AFM measurements are the waveguide dimensions (thickness and width), gold and CYTOP surface roughness, and over-etch channel depth.

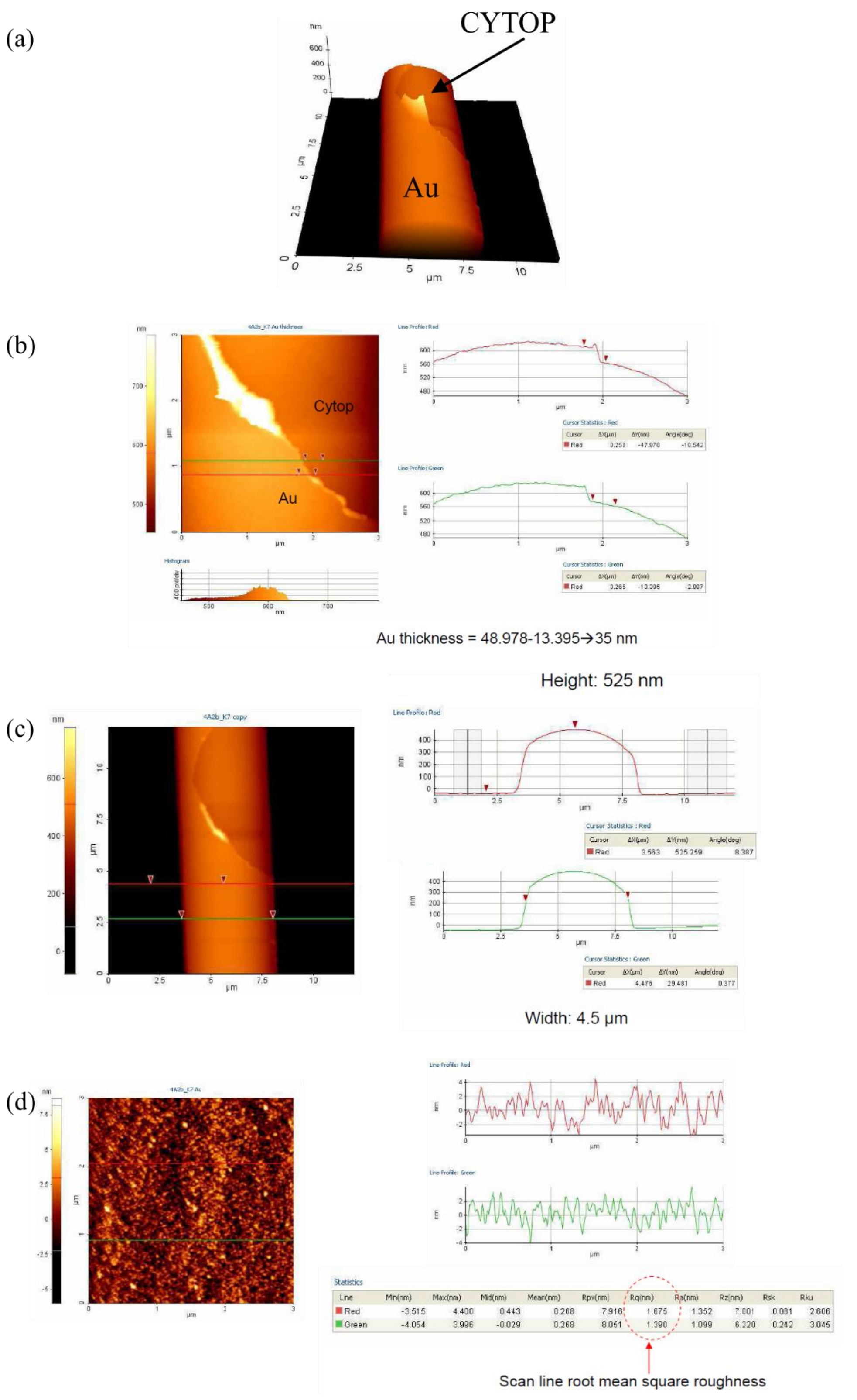

Cursor Statistics : Red

| Cursor | ΔX(µm) | ΔY(nm) | Angle(deg) |
|---|---|---|---|
| Red | 0.253 | -47.878 | -10.542 |

Cursor Statistics : Green

| Cursor | ΔX(µm) | ΔY(nm) | Angle(deg) |
|---|---|---|---|
| Red | 0.265 | -13.395 | -2.887 |

Cursor Statistics : Red

| Cursor | ΔX(µm) | ΔY(nm) | Angle(deg) |
|---|---|---|---|
| Red | 3.563 | 525.259 | 8.387 |

Cursor Statistics : Green

| Cursor | ΔX(µm) | ΔY(nm) | Angle(deg) |
|---|---|---|---|
| Red | 4.478 | 29.481 | 0.377 |

Statistics

| Line | Min(nm) | Max(nm) | Mid(nm) | Mean(nm) | Rpv(nm) | Rq(nm) | Ra(nm) | Rz(nm) | Rsk | Rku |
|---|---|---|---|---|---|---|---|---|---|---|
| Red | -3.515 | 4.400 | 0.443 | 0.268 | 7.916 | 1.675 | 1.352 | 7.001 | 0.081 | 2.606 |
| Green | -4.054 | 3.996 | -0.029 | 0.268 | 8.061 | 1.390 | 1.099 | 6.220 | 0.242 | 3.045 |

**Figure 3.22: AFM measurements on a fabricated sensor. (a) Three-dimensional view of the Au stripe on a CYTOP pedestal (produced by slightly over-etching); the stripe is torn allowing its thickness to be measured. (b) A line scan to estimate the thickness of the Au stripe, which is about 35 nm. (c) The width of the stripe was measured to be 4.5 µm. The over-etch channel depth was determined as 490 nm. (d) The root mean square roughness of the Au stripe is about 1.4 nm.**

In order to measure the thickness of the Au stripe on a CYTOP pedestal, a portion of the waveguide was torn from CYTOP through aggressive ultrasonication. The three-dimensional view of the torn waveguide is illustrated in Figure 3.22a. The gold thickness was estimated by measuring the difference in height between the exposed CYTOP and the residue gold surface (Figure 3.22b). From Figure 3.22c, the over-etch channel was estimated as 525 nm – 35 nm = 490 nm and the waveguide width is around 4.5 μm. The surface roughness of the gold waveguide was ensured to be low enough (~ 1 nm, Figure 3.22d) to avoid optical scattering which will affect the propagation of LRSPP (Berini, Charbonneau, Lahoud, & Mattiussi, 2005).

## 3.5 Conclusion

The design considerations for long range surface plasmon based biosensor were discussed. An inverse taper input, a coupler and a triple coupler were modelled theoretically to predict their optical properties. The detailed fabrication process of the gold waveguides embedded in CYTOP claddings was described. Gold waveguides with improved adhesion which allows the sensor to be reused was fabricated.

In this chapter, original work that has been done includes:

1. Designed two LRSPP waveguide structures for dengue biosensing – triple coupler and corporate feed (Figures 3.1d and e). These structures allows simultaneous detection and signal calibration.
2. Designed an inverse tapered input for LRSPP waveguides which minimizes the coupling loss due to misalignment.
3. Modified the fabrication process developed by Asiri, 2012 to improve the adhesion of the gold waveguides to the CYTOP claddings which allow the biosensors to be reused for many times.

# CHAPTER 4: SURFACE SENSITIVITY AND OPTIMIZATION OF LONG RANGE SURFACE PLASMON WAVEGUIDES FOR ATTENUATION-BASED BIOSENSING

## 4.1 Introduction

The performance of straight long-range surface plasmon waveguides as a biosensor is explored theoretically. The dimensions of the stripe (thickness, width), the sensing length and the refractive index of the sensing buffer are varied in order to understand their impact on sensor performance. The adlayer formation during biosensing is modelled as a growing uniform dielectric film having an effective thickness and refractive index. Optimum designs which maximize attenuation surface sensitivity in biochemical sensing applications leading to compact, sensitive, and cost-effective biosensors are reported.

## 4.2 Literature Review

### 4.2.1 Finite element method (FEM)

The finite element method (FEM) is a numerical technique to find approximate solutions to problems that can be described by partial differential equations (PDEs) (Nikishkov, 2004). This method can be applied to problems involving complex geometries and boundaries with relative ease, making it popular as the simulation tool in the modelling of advanced engineering and scientific problems. The basic idea behind FEM is to partition or discretize the geometry into smaller pieces called finite elements (Jin, 2014). Each element becomes a simple geometry which is easier to be analysed than the actual structure. The solutions are in general an approximation (not exact) and the accuracy is highly dependent on the number of elements (mesh) used. A finer mesh (larger number of elements) will normally yield more accurate results at a cost of greater computational memory required. Therefore, the mesh is usually not uniform across the structure and it is rather finer in regions where the accuracy of the result is critical.

Generally a mesh convergence test is required to ensure the structure is properly meshed and the numerical errors are minimized (Berini & Buckley, 2009).

In recent years, many commercial software products based on FEM have become available to automate the numerical computation, such as COMSOL Multiphysics (Liu & Quek, 2013). COMSOL Multiphysics (previously known as FEMlab) is an interactive environment for modelling and solving scientific and engineering problems based on PDEs. It provides sophisticated tools for geometric modelling and does not require deep understanding of PDEs or numerical analysis from users. There are several modules available in COMSOL that are useful to solve problems in various different field (COMSOL Multiphysics, 2012). Since the work presented in this thesis is to investigate the optical mode properties from LRSPP waveguides, the simulations only make use of the RF module.

#### 4.2.1.1 Discretization and solver

In COMSOL Multiphysics, a 2D model is usually divided into hybrid edge/nodal elements based on linear tangential and quadratic normal vector (Saitoh & Koshiba, 2001). Higher order elements (curvilinear hybrid edge/nodal element) can be defined to model curved boundaries (Saitoh & Koshiba, 2002). COMSOL Multiphysics will assemble a system of equations (a square matrix) based on the physics, material properties, boundary condition, element type, and element shape. The size of this matrix is the number of degrees of freedom (DOFs) of the model, where the number of DOFs is a function of the number of elements, the discretization order used in each physics, and the number of variables solved for (Dhatt, Lefrançois, & Touzot, 2012).

COMSOL is capable of solving nonlinear problems using very general and robust algorithms. At the very core of these algorithms, the software solves for a system of linear equations using either direct or iterative methods (Frei, 2013). The direct solvers in

COMSOL are robust and can handle almost any problem but they require much memory and computational time. Iterative solvers require relatively less memory than the direct solvers, but they require more customization of the settings. Besides, different physics require different iterative methods.

#### 4.2.1.2 Mode analysis

The mode analysis application in COMSOL computes the modes for an electromagnetic wave using an eigenvalue solver. It belongs to the RF module (or Wave Optics module for newer version of COMSOL) and solves the following version of Maxwell's curl equations for non-magnetic materials:

$$\nabla \times \nabla \times \mathbf{E} - \tilde{n}^2(x,y) k_0^2 \mathbf{E} = 0 \tag{4.1}$$

$$\nabla \times \tilde{n}^2(x,y) \nabla \times \mathbf{H} - k_0^2 \mathbf{H} = 0 \tag{4.2}$$

where $\mathbf{H} = \mathbf{H}(x,y)\exp(i(\beta z - \omega t))$, $\mathbf{E} = \mathbf{E}(x,y)\exp(i(\beta z - \omega t))$, $k_0^2 = \omega^2 \mu_0 \epsilon_0$ and $\beta$ is the propagation constant in the *z* direction. Besides the usual boundary conditions to be satisfied in electromagnetic theory, COMSOL's RF module offers several additional boundary conditions to help simplifying the simulation process. These conditions include allowing the boundaries to behave as perfect electric ($\mathbf{n} \times \mathbf{E} = 0$) or magnetic ($\mathbf{n} \times \mathbf{H} = 0$) conductors, and the perfectly matched layer (PML) condition. PMLs are layers that absorbs the incident radiated waves with small reflection (COMSOL Multiphysics, 2012).

## 4.3 Methodology

### 4.3.1 Sensor architecture

A typical LRSPP sensing die based on straight waveguides is illustrated in Figure 4.1. Each waveguide is formed from a Au stripe of width $w$ and thickness $t$ embedded in CYTOP. The structure is supported by a Silicon (Si) wafer. Figure 4.1b shows a longitudinal cross-sectional sketch of the sensing die. The etched channel defines the sensing region where a sensing fluid of refractive index $n_c$ is passed carrying the analyte of interest for adlayer formation on the Au stripe. The higher-index adlayer was modelled as a uniform dielectric layer of thickness $a$ on the top surface of the Au stripe. Due to slight over-etching during the formation of the sensing channels, the Au stripe is located on a CYTOP pedestal ~400 nm in height (Chiu *et al.*, 2010). The lower and upper CYTOP claddings are ~8 and ~6.7 μm thick, respectively.

The modelling was conducted using COMSOL Multiphysics at the free-space wavelength of $\lambda_0$ = 1310 nm. At this wavelength, the refractive index (RI) of CYTOP is 1.3348 (Asahi Glass), the index of Si is 3.5029 (Palik, 1998), and the relative permittivity of Au is -86.06 − j8.322 (Palik, 1998). Three refractive indices for the sensing fluid were chosen for this study, $n_c$ = 1.3303, 1.3348 and 1.3393 (neglecting loss). These refractive indices are slightly below, equal to, and slightly above the refractive index of CYTOP. These sensing solutions can be easily created by mixing glycerol with buffer in different proportions. The refractive index of the adlayer was taken as ($n_a$ = 1.5), which is typical for biochemical matter (Berini, 2008).The propagation loss, coupling loss and insertion loss were computed as a function of the Au stripe dimensions ($w$ and $t$), the length of the sensing channel and the adlayer thickness $a$. From these calculations, optimum designs for straight long-range surface plasmon waveguide biosensors can be determined.

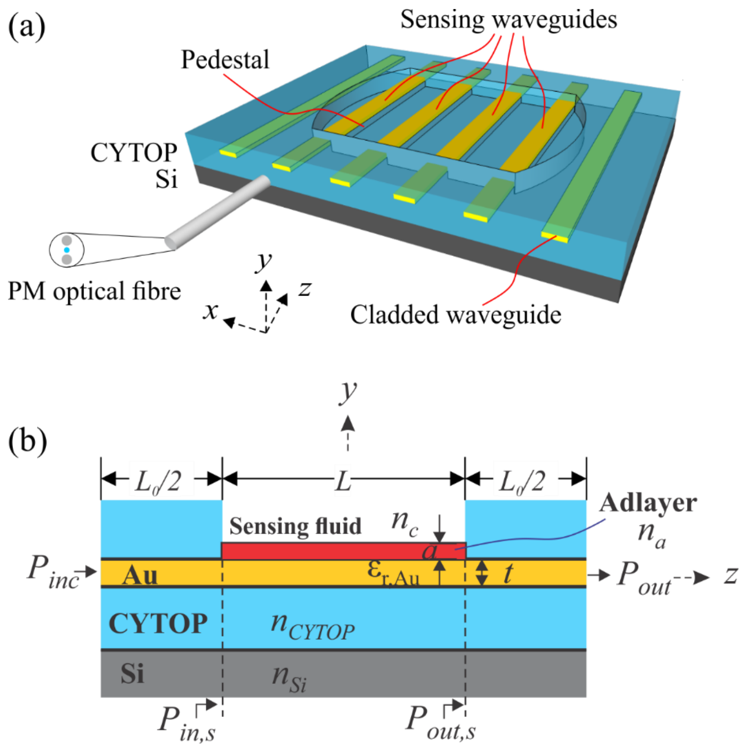

**Figure 4.1: The LRSPP sensing die configuration. (a) 3D illustration of a typical LRSPP sensing die based on straight waveguides. A polarization-maintaining (PM) optical fibre is butt-coupled to the input of the waveguide to excite the LRSPP mode thereon. (b) Longitudinal cross-section of the sensing die with an adlayer of thickness a formed on the Au waveguide.**

### 4.3.2 Steps in FEM simulation using COMSOL Multiphysics

The major steps to simulate the optical behaviour of a LRSPP waveguide are illustrated in Figure 4.2. A fully cladded LRSPP waveguide is illustrated as an example structure. In short, the steps involved include:

1. **Geometrical definition**

   The first step is the definition of the structure of the waveguide (Figure 4.2a). Depending on the waveguide’s symmetry, a smaller sector can be used (half symmetry in this example) to reduce the computational time. The required shapes (rectangles, circles, etc.) are drawn through the settings of the dimensions (height and width) and the positions (x, y).

## 2. Materials definition

Next, the physical properties of the material in each domain has to be set. As shown in Figure 4.2b, the Au waveguide (yellow stripe) is surrounded by CYTOP claddings (blue region) and supported by the silicon wafer (grey layer). An air layer (cyan layer) is also included to see if there is any radiation from the cladding. The common material properties can be found and selected from the COMSOL Multiphysics material database libraries. The electromagnetic properties of a material such as the relative permittivity and refractive index can also be inserted manually.

## 3. Boundary setting

In this example, since a half symmetry structure is employed, a particular boundary condition (BC) has to be applied to find the modes of interest. A detailed discussion on the selection of BC can be found from McIsaac, 1975. For example, in order to look for the fundamental mode of the LRSPP waveguide, a perfect magnetic conductor (PMC) is imposed at the right side of the structure and the remaining sides are imposed with a perfect electric conductor (PEC). PEC and PMC are indicated in black and blue in Figure 4.2c.

## 4. Meshing

Several mesh parameters can be adjusted to discretise the structure into smaller elements. Due to the relatively small dimension of the Au waveguide, a finer mesh is required for that region, as shown in the inset of Figure 4.2d. Usually a mesh convergence test will be carried out (Berini & Buckley, 2009) to ensure the accuracy of the solution.

### 5. Solving

The COMSOL Multiphysics utilizes MUMPS (MUltifrontal Massively Parallel sparse direct Solver) as a direct solver for eigenvalue problems. Once the solver is chosen, the most important parameters to be defined are the guess for the eigenvalue and the number of eigenvalues to be calculated around this value. For example, in the modal analysis of LRSPP waveguide, the estimated effective index $n_{eff}$ is the guess for the eigenvalue.

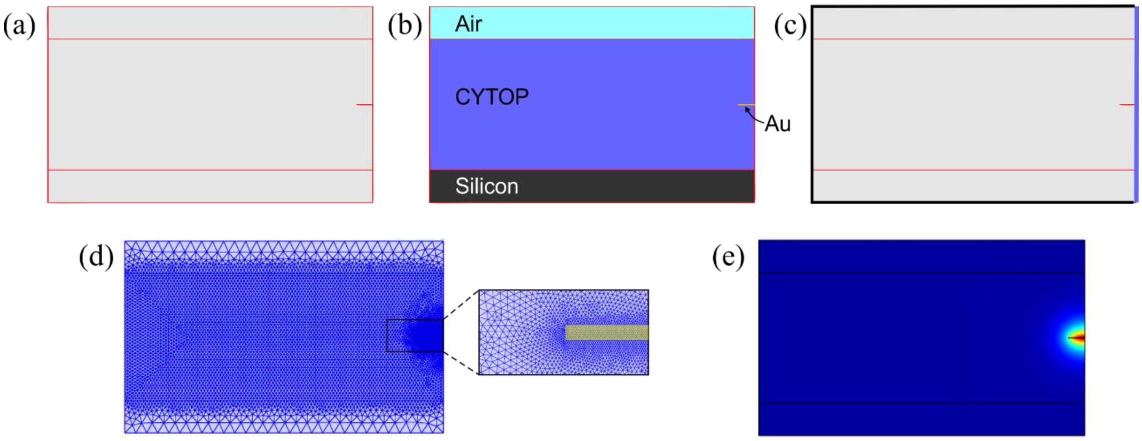

**Figure 4.2: Steps in FEM simulation (a) structural design (b) material definition (c) boundary condition setting (d) mesh generation (e) solution**

## 4.4 Results and Discussion

### 4.4.1 Sensor performance

#### 4.4.1.1 Attenuation and coupling loss

We assume an $e^{+j\omega t}$ time dependence and that the mode propagates in the +z direction according to $e^{-\gamma z}$. The complex propagation constant of the mode γ [m$^{-1}$] is given by $\gamma = \alpha + j\beta$ where α and β are the attenuation and phase constants, respectively. The incident light of power $P_{inc}$ emerges from a polarisation-maintaining single-mode optical fibre aligned to the sensor input, as illustrated in Figure 4.1b. The polarisation of the incident light is aligned to the TM-polarisation of the LRSPP. The LRSPP then propagates in the +z direction along the input access waveguide of length $L_0/2$, the sensing section of length

*L*, and the output access waveguide of length $L_0/2$ (both access waveguides are embedded in CYTOP). The output power from the sensor ($P_{out}$) is then:

$$P_{out}(a) = P_{inc} \cdot |C_i|^2 \exp(-2\alpha L_0) \cdot |C(a)|^4 \exp(-2\alpha_s(a)L) \tag{4.3}$$

where $C_i$ is the overlap factor between the field of the optical fibre and the LRSPP field at the input facet of the sensor (Charbonneau *et al.*, 2006), $\alpha$ is the LRSPP field attenuation coefficient in the cladded sections, $C(a)$ is the overlap factor between the LRSPP fields in the input or output access waveguides and the sensing waveguide, and $\alpha_s(a)$ is the LRSPP field attenuation coefficient along the sensing waveguide. Although not explicitly shown in Equation 4.3, it is noted that $C(a)$ and $\alpha_s(a)$ also depend on the RI of the sensing fluid, $n_c$.

The mode power attenuation (MPA) of the sensing waveguide in dB/mm is computed from the attenuation constant $\alpha_s$ using

$$\mathrm{MPA}(a) = \alpha_s(a) \frac{20}{1000} \log_{10} e \tag{4.4}$$

Figures 4.3 (a-c) plot the attenuation (MPA) and effective index (Re$\{n_{eff}\}$) of the LRSPP ($ss_b^0$ mode (Charbonneau *et al.*, 2006)) as a function of Au stripe thickness in the absence ($a$ = 0 nm) and presence ($a$ = 10 nm) of an adlayer for different refractive indices of the sensing fluid. The width of the stripe was set to $w$ = 5 μm. Generally, the MPA and Re$\{n_{eff}\}$ increase with increasing Au thickness. The effective indices after adlayer formation ($a$ = 10 nm) are always higher than before adlayer formation ($a$ = 0 nm), regardless of the index of sensing fluid.

The overlap factor $C(a)$ between the LRSPP in the etched channel and the LRSPP in the fully-cladded waveguide was computed via overlap integrals (Charbonneau *et al.*, 2006). If there is no material discontinuity, the power coupling efficiency at one interface is given by $|C(a)|^2$. Therefore, the coupling loss (in dB) is:

$$C_{dB}(a) = -20\log_{10}|C(a)| \tag{4.5}$$

Based on the design of our sensing waveguide, the coupling loss to be considered is $2C_{dB}$ due to the existence of two fluidic/cladded interfaces (*i.e.*, 4th power of $|C(a)|$ in Equation 4.3). Considering the same stripe width of $w$ = 5 μm, the coupling losses $2C_{dB}$ versus Au stripe thickness in the absence ($a$ = 0 nm) and presence ($a$ = 10 nm) of an adlayer for different indices of sensing fluid were computed, as shown in Figures 4.3 (d-f).

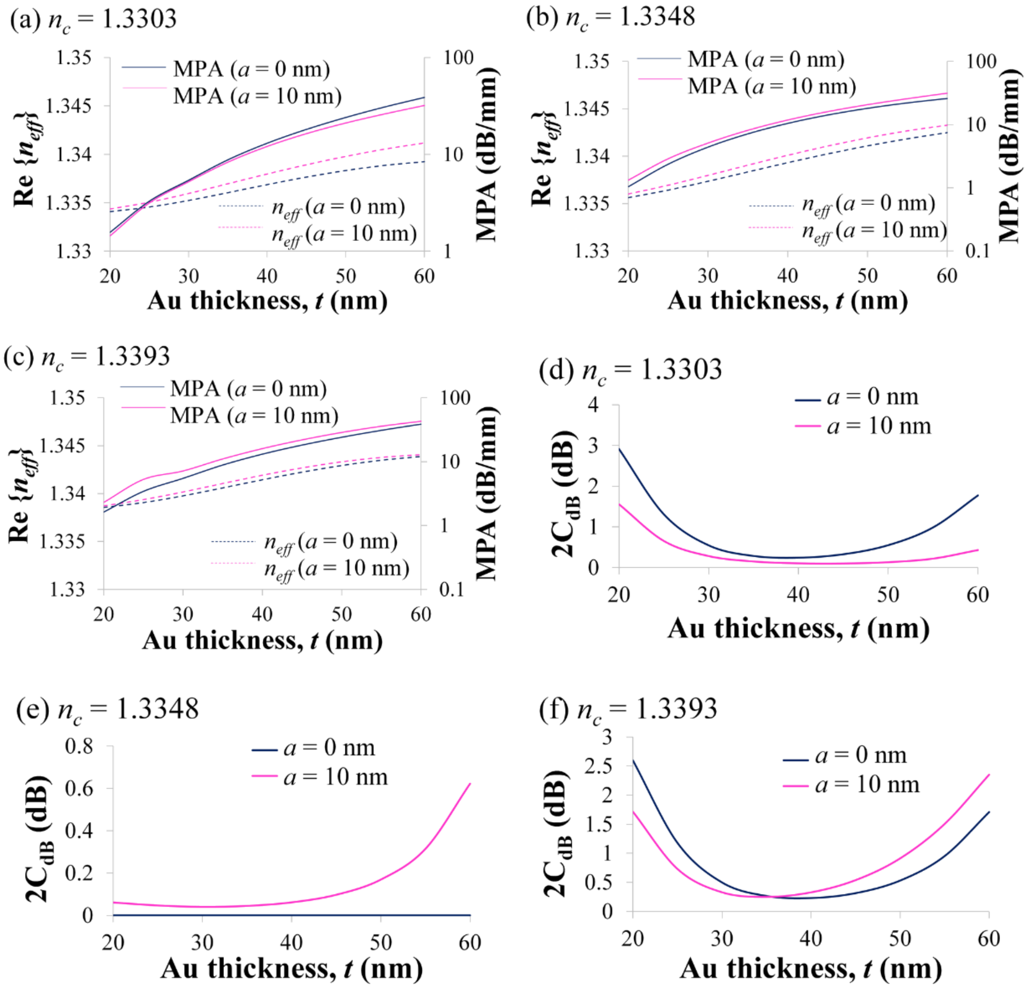

**Figure 4.3: Effective index, mode power attenuation, and coupling loss of the LRSPP as a function of Au stripe thickness for sensing fluids of different refractive indices with and without an adlayer.**

For $n_c$ = 1.3303 (Figure 4.3d), the coupling loss without an adlayer is greater than the coupling loss with an adlayer. The sensing fluid which has an index lower than that of CYTOP causes the waveguide to be asymmetric. The formation of a high-index adlayer pulls the waveguide into symmetry thus lowering its coupling loss. Minimum coupling loss is observed for $t$ ~ 35 - 40 nm. As the Au thickness decreases, the coupling loss increases due to the lower confinement of LRSPP. In the absence of an adlayer, the coupling loss for $n_c$ = 1.3348 (Figure 4.3e) is zero because the sensing waveguide is identical to the fully-cladded waveguide. The coupling loss increases appreciably with adlayer only for $t > 45$ nm. In the case of $n_c$ = 1.3393 (Figure 4.3f), the coupling loss before and after adlayer formation are almost identical when $t = 35$ nm. The sensing fluid has an index higher than that of CYTOP, which causes the waveguide to be asymmetric. When an adlayer is formed, the symmetry of the waveguide is further distorted thus increasing the coupling loss, but only appreciably for $t > 35$ nm.

#### 4.4.1.2 LRSPP mode profiles

The distribution of the vertical transverse electric field component ($E_y$) of the LRSPP ($ss_b^0$ mode (Charbonneau *et al.*, 2006)) for different indices of sensing fluid, with and without an adlayer, is given in Figure 4.4 for an Au stripe of $w = 5$ µm and $t = 45$ nm.

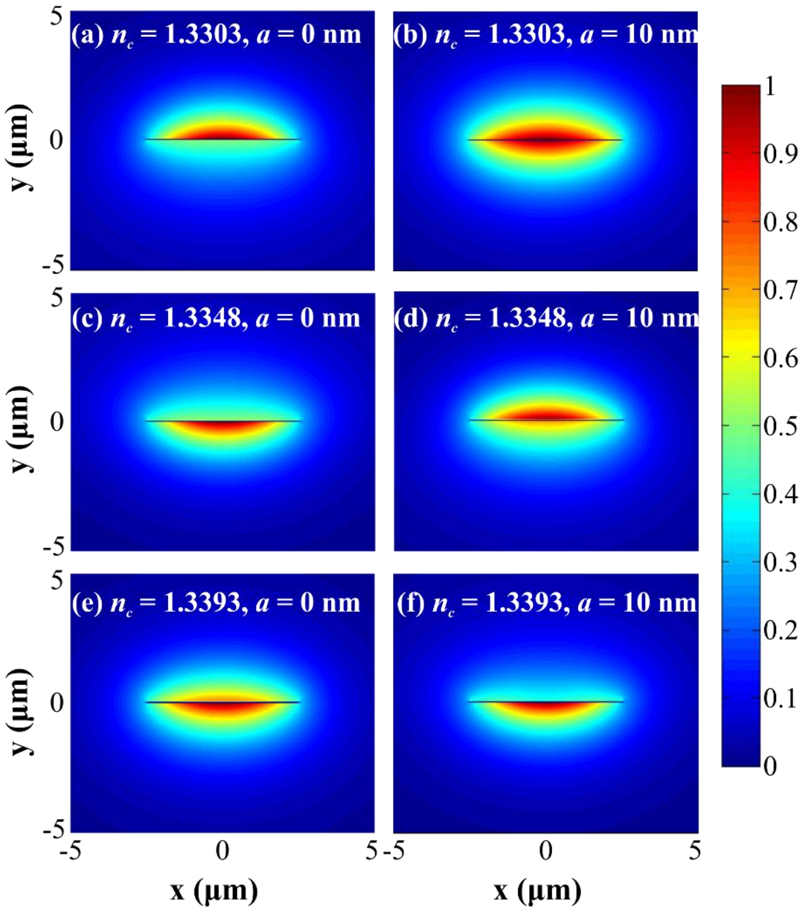

**Figure 4.4: LRSPP mode profiles for (a) $n_c$ = 1.3303, $a$ = 0 nm; (b) $n_c$ = 1.3303, $a$ = 10 nm; (c) $n_c$ = 1.3348, $a$ = 0 nm; (d) $n_c$ = 1.3348, $a$ = 10 nm; (e) $n_c$ = 1.3393, $a$ = 0 nm; (f) $n_c$ = 1.3393, $a$ = 10 nm.**

We first consider a sensing fluid which has an index of $n_c$ = 1.3303, which is lower than that of CYTOP (Figures 4.4a and b). The waveguide is slightly asymmetric due to the mismatch of refractive indices, causing the field distribution to be uneven. In the presence of a higher-index adlayer ($a$ = 10 nm, $n_a$ = 1.5), the effective index increases (Figure 4.3a), and the waveguide becomes more symmetric so the coupling loss decreases, as noted in the previous section. A sensing fluid of index $n_c$ = 1.3348, which is identical to that of CYTOP, is considered next (Figures 4.4c and d). In the absence of an adlayer ($a$ = 0 nm), the structure is similar to a fully-cladded waveguide and the mode is symmetric. The formation of an adlayer causes asymmetry in the waveguide so the field distribution becomes distorted. For the case of a sensing fluid of index higher than that of CYTOP, $n_c$ = 1.3393 (Figures 4.4e and f), the mode profile becomes increasingly asymmetric with adlayer formation, which increases the coupling loss.

Comparing the mode profiles for three different indices of sensing fluid (Figure 4.4), we note that a sensing fluid with an index lower than that of CYTOP is preferred as the buffer in a biosensing experiment, *e.g.*, $n_c$ = 1.3303, because when an adlayer is formed on the surface of the waveguide the mode profile becomes more symmetric (Figures 4.4a and b). Thus the coupling loss drops (Figure 4.3d) and the MPA decreases (Figure 4.3a), so the output power will increase during adlayer formation, rather than decrease, thus continually improving the signal-to-noise during the experiment.

### 4.4.2 Surface sensitivity, mass density and detection limit

It is clear from the previous section that the attenuation and coupling loss of the LRSPP both change with adlayer formation. We seek to better understand how both of these partial sensitivities affect the overall sensitivity of a section of sensing waveguide in attenuation-based biosensing.

The first and second terms in Equation 4.3 remain constant during a sensing experiment. The last term is the transmittance of the sensing channel, $T_s(a)$:

$$T_s(a) \;=\; P_{out,s}(a)/P_{in,s} \;=\; |C(a)|^4 \exp(-2\alpha_s(a)L) \tag{4.6}$$

where $P_{in,s}$ and $P_{out,s}(a)$ are the power incident on, and emerging from, the sensing channel at reference planes just inside the input and output access waveguides (Figure 4.1b). The transmittance of the sensing section depends on $a$.

The surface sensitivity of the sensor is obtained by taking the derivative of the measurand, $P_{out}(a)$, with respect to $a$:

$$\frac{\partial P_{out}(a)}{\partial a} \;=\; P_{inc} \cdot |C_i|^2 \exp(-2\alpha L_0) \cdot \frac{\partial T_s(a)}{\partial a} \tag{4.7}$$

where Equations 4.3 and 4.6 were used. From the above, we note that to increase the sensitivity we should increase the incident power, $P_{inc}$, maximise the overlap factor at the sensor input ($|C_i| \sim 1$), and minimise the loss of the input and output access waveguides, say, by choosing their length ($L_0/2$) as short as is practically possible. Making $|C_i| \sim 1$ is particularly important because any uncoupled light propagates essentially in the forward direction and contributes noise at the power sensor. We also note that we should seek to maximise the sensitivity of the sensing channel, $|\partial T_s(a)/\partial a|$; we have introduced the absolute value because the latter may be positive or negative.

The surface mass density (in g/m$^2$) that accumulates on the surface of the waveguide as binding occurs is related to the adlayer optical model via (De Feijter, Benjamins, & Veer, 1978):

$$\Gamma = \frac{a(n_a - n_c)}{\partial n/\partial c} \tag{4.8}$$

where $\partial n/\partial c$ is the change in RI with analyte concentration (usually $\partial n/\partial c \sim 0.185$ mm$^3$/mg).

The change in surface mass density $\Delta\Gamma$ is related to the change in adlayer thickness $\Delta a$ via the above:

$$\Delta\Gamma = \frac{\Delta a(n_a - n_c)}{\partial n/\partial c} \tag{4.9}$$

Changes in output power $\Delta P_{out}$ are related to $\Delta a$ through:

$$\Delta P_{out} = \frac{\partial P_{out}(a)}{\partial a}\Delta a \tag{4.10}$$

We obtain the detection limit as the smallest detectable change in surface mass density $\Delta\Gamma_{\text{min}}$ by combining Equations 4.9 and 4.10:

$$\Delta\Gamma_{min} = \frac{(n_a - n_c)}{\partial n/\partial c} \frac{1}{|\partial P_{out}(a)/\partial a|} \Delta P_{out,min} \tag{4.11}$$

where $\Delta P_{out,\mathrm{min}}$ is the smallest detectable change in output power which is related to the standard deviation of the baseline output power (often taken as a factor of the latter). The detection limit is observed to decrease as the surface sensitivity $|\partial P_{out}(a)/\partial a|$ increases and as the smallest detectable change in output power $\Delta P_{out,\mathrm{min}}$ decreases.

### 4.4.3 Surface sensitivity of the sensing channel

Based on Equation 4.7, optimising the surface sensitivity of the sensing channel, $\partial T_s(a)/\partial a$, is key. Taking the derivative of Equation 4.6 yields:

$$\frac{\partial T_s(a)}{\partial a} = 2|C(a)|^3 \exp(-2\alpha_s(a)L) \left(2\frac{\partial |C(a)|}{\partial a} - |C(a)|L\frac{\partial \alpha_s(a)}{\partial a}\right) \tag{4.12}$$

We consider two simplifying cases to Equation 4.12. In the first case, the first term dominates:

$$2\left|\frac{\partial |C(a)|}{\partial a}\right| \gg |C(a)|L\left|\frac{\partial \alpha_s(a)}{\partial a}\right| \tag{4.13}$$

so Equation 4.12 simplifies to:

$$\frac{\partial T_s(a)}{\partial a} \cong 4|C(a)|^3 \frac{\partial |C(a)|}{\partial a} \exp(-2\alpha_s(a)L) \tag{4.14}$$

where the coupling sensitivity $\partial|C(a)|/\partial a$ is the key factor determining the sensor performance.

In the second case, the second term dominates:

$$2\left|\frac{\partial |C(a)|}{\partial a}\right| \ll |C(a)|L\left|\frac{\partial \alpha_s(a)}{\partial a}\right| \tag{4.15}$$

so Equation 4.12 simplifies to:

$$\frac{\partial T_S(a)}{\partial a} \cong -2|C(a)|^4 \frac{\partial \alpha_S(a)}{\partial a} L \exp(-2\alpha_s(a)L) \tag{4.16}$$

where the attenuation sensitivity $\partial\alpha_s(a)/\partial a$ and the sensing length $L$ are the key factors determining sensor performance. The sensitivity of the stripe at initial adlayer growth is then given by setting $a = 0$ in Equation 4.16:

$$\frac{\partial T_S(0)}{\partial a} \cong -2|C(0)|^4 \frac{\partial \alpha_S(0)}{\partial a} L \exp(-2\alpha_s(0)L) \tag{4.17}$$

Choosing $L = 1/(2\alpha_s(0))$ maximises the product $L\exp(-2\alpha_s(0)L)$ (following Berini, 2008) so this length is taken as the optimal sensing length $L_{opt}$. Substituting this length into Equation 4.17 yields for the channel sensitivity at $a = 0$:

$$\left.\frac{\partial T_S(0)}{\partial a}\right|_{L=L_{opt}} \cong -|C(0)|^4 \frac{1}{e} \frac{\partial \alpha_S(0)}{\partial a} \frac{1}{\alpha_S(0)} = -|C(0)|^4 \frac{1}{e} K \tag{4.18}$$

where:

$$K = \frac{\partial \alpha_S(0)}{\partial a} \frac{1}{\alpha_S(0)} \tag{4.19}$$

$K$ is analogous to the parameter $G$ that was defined in Berini, 2008 for phase sensing. Maximising the surface sensitivity in this case (*i.e.*, where Equation 4.16 holds) thus requires maximising $|K|$.

We now investigate the channel surface sensitivity numerically, by varying the thickness of the stripe $t$ and the refractive index of the sensing fluid $n_c$, seeking regions where Equation 4.12 must be used or where Equation 4.14 or 4.16 can be used, along with optimal designs. Figure 4.5 plots $\partial|C(0)|/\partial a$, $\partial\alpha_s(0)/\partial a$, and $K$ as a function of $t$ for three sensing fluid RIs.

The values of $\partial|C(0)|/\partial a$ and $\partial\alpha_s(0)/\partial a$ were approximated via $O(h^2)$ equidistant forward-difference formulae (Gerald & Wheatley, 1994):

$$\partial|C(a_i)|/\partial a = (-3|C(a_i)| + 4|C(a_{i+1})| - |C(a_{i+2})|)/2h \tag{4.20}$$

$$\partial\alpha_s(a_i)/\partial a = (-3\alpha_s(a_i) + 4\alpha_s(a_{i+1}) - \alpha_s(a_{i+2}))/2h \tag{4.21}$$

where $h = a_{i+1} - a_i$. In the computations of $\partial|C(0)|/\partial a$ and $\partial\alpha_s(0)/\partial a$, we set $h = 1$ nm and $a_i = 0$, and use the finite-element method to compute the modal properties of the LRSPP for each $a_i$ in Equations 4.20 and 4.21.

In order to assess the inequalities (Equations 4.13 and 4.15), we must assume order-of-magnitude values for $|C(a)|$ and $L$ to be used therein. For this purpose we choose $|C(a)| \sim 1$ and $L \sim 2$ mm, which are typical values, and furthermore allow the inequalities to be assessed by comparing the left axes of Figures 4.4(a-c) directly to the right axes.

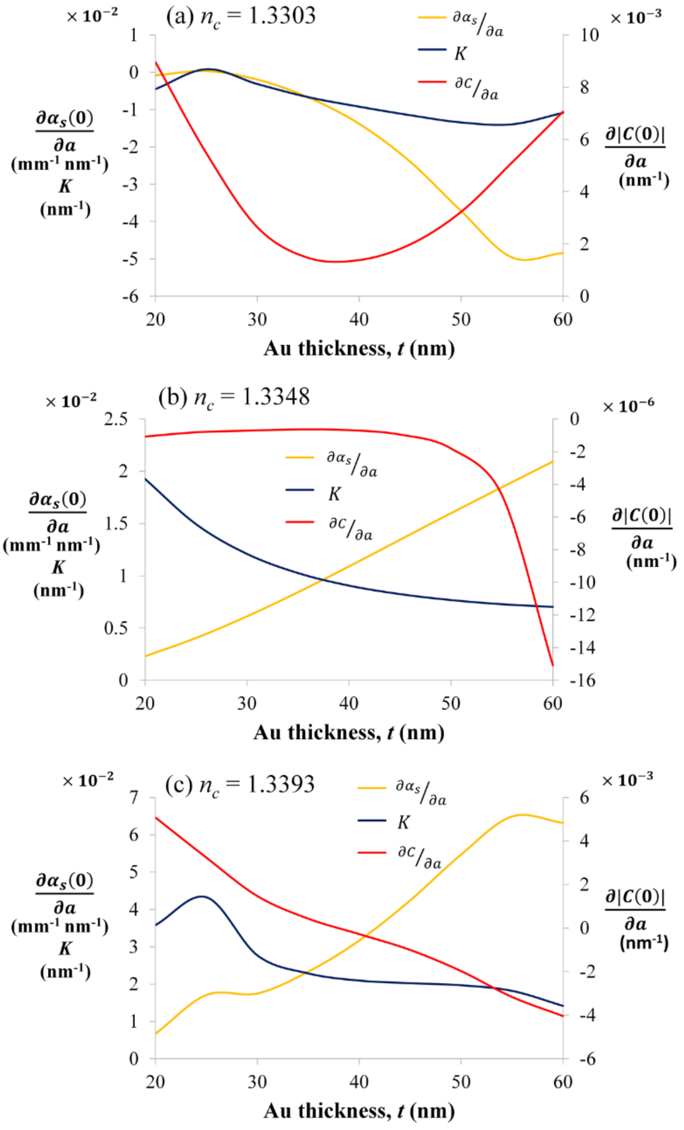

**Figure 4.5: Coupling and attenuation sensitivity as a function of Au stripe thickness for sensing fluids of different refractive indices.**

For $n_c$ = 1.3303 (Figure 4.5a), we find that Equation 4.15 is satisfied for $t \geq 35$ nm so Equation 4.16 can be used. For t < 35 nm, both terms are significant so Equation 4.12 must be used. Due to the signs of the partial derivatives $\partial|C(0)|/\partial a$ and $\partial\alpha_s(0)/\partial a$, the terms are additive and the surface sensitivity (Equation 4.12) is always positive. This result agrees with experimental observations where the output power increases during adlayer formation (Section 5.4.4 and Krupin *et al.*, 2013; Wong *et al.*, 2014).

In the case of $n_c$ = 1.3348 (Figure 4.5b), we find that Equation 4.15 is satisfied over the full range of Au thickness; Equation 4.14 can thus be used throughout.

Similar trends as in $n_c = 1.3303$ are observed for $n_c = 1.3393$ (Figure 4.5c) where Equation 4.15 is satisfied for $t \geq 35$ nm, so Equation 4.16 can be used. Both terms are comparable below this thickness, so Equation 4.12 must be used. As $\partial|C(0)|/\partial a$ crosses over zero at $t \sim 40$ nm, its contribution to the sensor performance goes from subtractive to additive.

We can deduce optimal designs for the biosensor based on the maximum value of $|K|$ while ensuring that the LRSPP remains well-guided throughout the structure (non-radiative with $|C(a)| \sim 1$). For $n_c = 1.3303$, maximum $|K|$ is observed at $t = 55$ nm. For $n_c = 1.3348$, $|K|$ increases with decreasing $t$, so a good Au thickness is taken as $t = 20$ nm (for practical reasons as a high-quality film thinner than 20 nm may be difficult to achieve). For $n_c = 1.3393$, maximum $|K|$ occurs at $t = 25$ nm.

### 4.4.4 Optimal sensing length $L_{opt}$

As discussed in the previous subsection Equation 4.15 is satisfied and the attenuation sensitivity $\partial\alpha_s(a)/\partial a$ dominates the surface sensitivity for a wide range of Au thickness. Thus, Equation 4.16 often holds, and the optimal sensing length $L_{opt} = 1/(2\alpha_s(0)$ should generally be selected. Figure 4.6 plots $L_{opt}$ as a function of Au thickness for three waveguide widths ($w = 4$, 5 and 6 μm) and three RI of the sensing fluid ($n_c = 1.3303$, 1.3348 and 1.3393). For all $n_c$, the sensing length decreases rapidly with increasing stripe thickness. Also, the waveguide width and sensing RI have significant effects on $L_{opt}$ for $t < 30$ nm, but as $t$ increases, $L_{opt}$ tends to ~ 1 mm for $t \sim 30$ nm in all cases. Thicknesses of 25 to 30 nm do not induce too much propagation loss, yet remain suitable for miniaturized biosensors. However, the sensing length must remain long enough to allow radiative modes, if induced by uncoupled light at the input of the sensing waveguide, to spread. $L_{opt}$ for $n_c = 1.3348$ is always greater than for the other sensing RI as the attenuation is lowest when the sensing RI is matched to that of CYTOP.

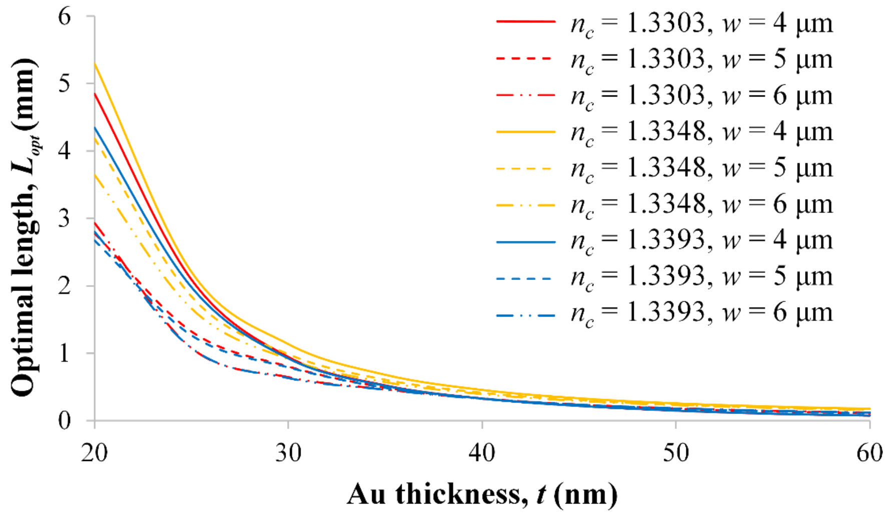

**Figure 4.6: The optimal sensing length as a function of Au stripe thickness for various stripe widths and refractive indices of the sensing fluid.**

Table 4.1 summarizes the performance of some designs for $n_c$ = 1.3303, 1.3348 and 1.3393 using $n_a = 1.5$, $\partial n/\partial c = 0.185$ mm$^3$/mg, $w$ = 5 μm and $L_0$ = 1 mm (selected to allow length for handling and interfacing with external fluidics). The incident power and the minimum detectable power were taken as $P_{inc}$ = 12 mW and $\Delta P_{out,\min}$ = 6.2 nW following typical values observed in experiments (Krupin *et al.*, 2013 and Section 5.4.4). The thickness of the Au stripe was selected in each case to maximise $|K|$ as determined in the previous section, and the corresponding $L_{opt}$ was taken as the length of the sensing channel ($L = L_{opt}$). $\partial P_{out}(a)/\partial a$, $\partial T_s(a)/\partial a$ and $\Delta\Gamma_{\min}$ were computed using Equations 4.7, 4.12 and 4.11.

It is observed from Table 4.1 that the design for $t$ = 55 nm at $n_c$ = 1.3303 has the highest channel surface sensitivity $|\partial T_s(a)/\partial a|$ but the lowest power sensitivity $|\partial P_{out}(a)/\partial a|$ and thus the worst detection limit ($\Delta\Gamma_{\min}$); this is due to attenuation along the access lines, on either side of the sensing channel, which must be fixed to some practical minimum length (*e.g.*, $L_0$ = 1 mm, see Equation 4.7). The other designs in Table 4.1 produce very compelling detection limits of about $\Delta\Gamma_{\min}$ = 0.1 pg mm$^{-2}$.

**Table 4.1: Summary of designs at $n_c$ = 1.3303, 1.3348 and 1.3393.**

| $n_c$ | 1.3303 | 1.3348 | 1.3393 |
|---|---|---|---|
| $t$ (nm) | 55 | 20 | 25 |
| $C_i$ | 0.8179 | 0.9717 | 0.9604 |
| $\alpha$ (mm$^{-1}$) | 2.5370 | 0.1195 | 0.2714 |
| $C(0)$ | 0.9448 | 1.0000 | 0.9344 |
| $\alpha_s(0)$ (mm$^{-1}$) | 3.5584 | 0.1195 | 0.3949 |
| $L_{opt}$ (mm) | 0.1405 | 4.1858 | 1.2661 |
| $\partial\|C(0)\|/\partial a$ (nm$^{-1}$) | $5.119 \times 10^{-3}$ | $-1.0748 \times 10^{-6}$ | $3.2352 \times 10^{-3}$ |
| $\partial\alpha_s(0)/\partial a$ (mm$^{-1}$ nm$^{-1}$) | $-4.9634 \times 10^{-2}$ | $2.3011 \times 10^{-3}$ | $1.7088 \times 10^{-2}$ |
| $\|\partial T_s(a)/\partial a\|$ (nm$^{-1}$) | $1.0441 \times 10^{-2}$ | $7.0884 \times 10^{-3}$ | $8.2497 \times 10^{-3}$ |
| $\|\partial P_{out}(a)/\partial a\|$ (μW nm$^{-1}$) | 0.5245 | 63.2518 | 53.0677 |
| $\Delta\Gamma_{\min}$ (pg mm$^{-2}$) | 10.8438 | 0.0875 | 0.1015 |

### 4.4.5 Linear Model for Sensing Channel Transmittance

In an attenuation-based biosensing experiment, we are interested in monitoring the output power before, during and after the formation of an adlayer, and relating the change to the adlayer thickness. A simple linear model for the transmittance of the sensing channel would be convenient.

A typical binding response of a biomaterial sample (*e.g.* protein) is illustrated in Figure 4.7. Depending on the RI of the sensing fluid, the output power $P_{out}(a)$ can either increase or decrease during adlayer formation (note the sign of the sensitivities plotted in Figure 4.5). If $n_c$ is lower than the RI of CYTOP ($n_c < 1.3348$), the formation of a high-index adlayer causes the field distribution of the waveguide to become increasingly symmetric which increases the sensing channel transmittance and the output power. The opposite situation applies for $n_c \geq 1.3348$, where the field distribution becomes increasingly asymmetric during adlayer formation, decreasing the channel transmittance and output power.

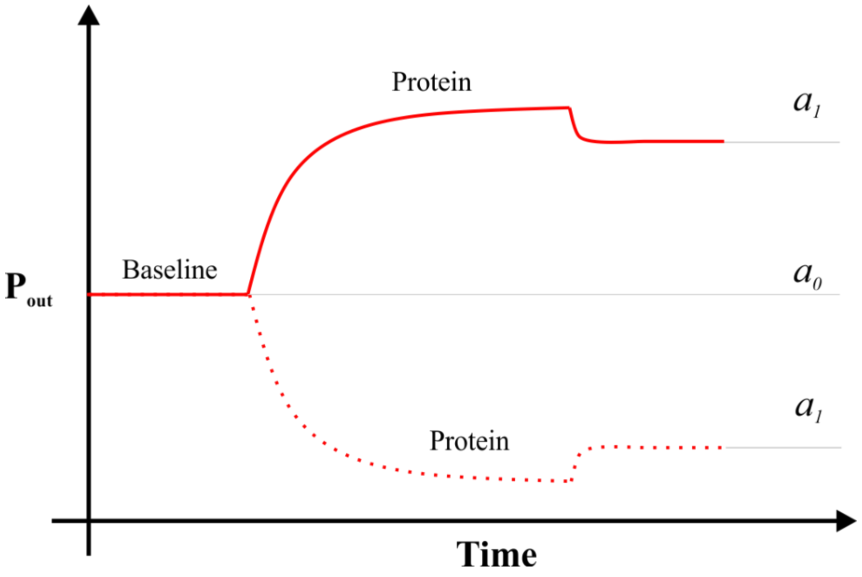

**Figure 4.7: Schematic showing a typical binding response (output power versus time) for protein adsorption where $a_0$ is a nominal thickness prior to adlayer growth (representing say immobilised receptor chemistries) and $a_1$ is the thickness after adlayer formation.**

The sensing channel transmittance $T_s(a)$ depends weakly on $a$ over a small range of $a$ in biochemical sensing (Krupin *et al.*, 2013). We can approximate the exponential in Equation 4.6 as the first two terms of its Taylor series expansion and represent $T_s(a)$ as a linear model:

$$T_s(a) = |C(a)|^4 \exp(-2\alpha_s(a)L) \cong ma + b \tag{4.22}$$

The output power before and after adlayer formation (Figure 4.7) can then be written by substituting the linear model for $T_s(a)$ in Equation 4.3 as:

$$P_{out}(a_0) = k_1(ma_0 + b) \quad \text{and} \quad P_{out}(a_1) = k_1(ma_1 + b) \tag{4.23}$$

where we have defined $k_1 = P_{inc}|C_i|^2\exp(-2\alpha L_0)$. $k_1$ remains constant during a sensing experiment.

The normalised change in output power due to adlayer formation is then written:

$$\frac{P_{out}(a_1)-P_{out}(a_0)}{P_{out}(a_0)} = \frac{m(a_1-a_0)}{ma_0+b} \tag{4.24}$$

If we set $\Delta a = a_1 - a_0$ and $k_2 = m/(ma_0+b)$, then Equation 4.24 becomes:

$$\frac{P_{out}(a_1)-P_{out}(a_0)}{P_{out}(a_0)} = \frac{m\cdot\Delta a}{ma_0+b} = k_2\Delta a \tag{4.25}$$

The thickness of the adlayer formed $\Delta a$ is obtained from the output powers $P_{out}(a_0)$ and $P_{out}(a_1)$ by rearranging Equation 4.25:

$$\Delta a = \frac{1}{k_2}\left(\frac{P_{out}(a_1)}{P_{out}(a_0)} - 1\right) \tag{4.26}$$

Using Equation 4.9 to substitute for $\Delta a$ in Equation 4.26 yields the relationship between the change in surface mass density to the measured output powers before and after adlayer formation:

$$\Delta\Gamma = \frac{1}{k_2}\frac{(n_a-n_c)}{\partial n/\partial c}\left(\frac{P_{out}(a_1)}{P_{out}(a_0)} - 1\right) \tag{4.27}$$

Regardless of the sign of the change in output power, the change in adlayer thickness and surface mass density obtained from Equations 4.26 and 4.27 are always positive for adlayer growth (because $k_2$ and $m$ are correspondingly positive or negative).

The sensing channel transmittance $T_s(a)$ computed using Equation 4.6 with $L = L_{opt}$ is plotted in Figure 4.8 as a function of the adlayer thickness $a$ for $w = 5$ μm, several stripe thicknesses $t$, and different indices of sensing fluid, $n_c$. We also plot the linear model of $T_s(a)$ as the dotted curve for the case of $t$ that maximises $|K|$ and give its equation in inset. As argued above, the sensing channel transmittance is well-represented by the linear model of Equation 4.22, as evidenced by the very good $R^2$ values obtained for each. Figure 4.8 also illustrates the importance of carefully controlling the waveguide thickness during fabrication because an error of ±5 nm will significantly affect the performance of the biosensor.

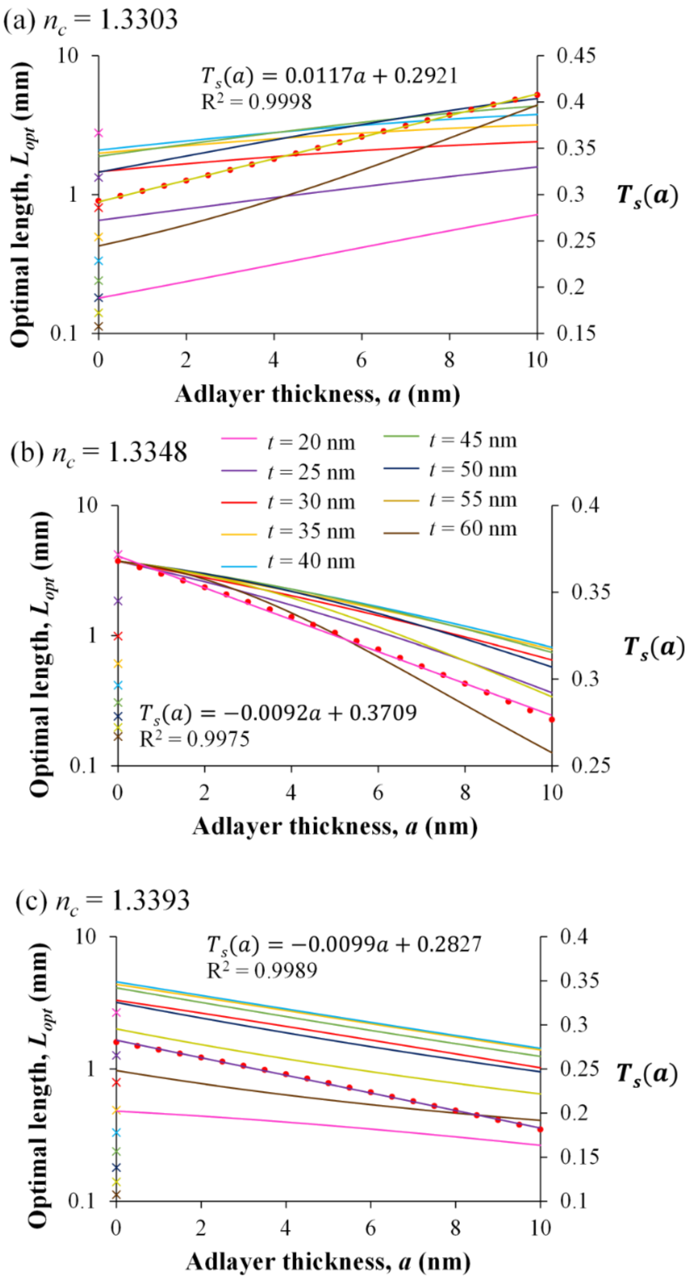

**Figure 4.8: Optimal sensing length $L_{opt}$ (marked as ×) and channel transmittance $T_s(a)$ (solid lines) as a function of the adlayer thickness $a$ for different Au thicknesses $t$ and sensing fluids of RI (a) $n_c$ = 1.3303, (b) $n_c$ = 1.3348 and (c) $n_c$ = 1.3393. The linear fit for $T_s(a)$ is plotted as the red dotted line in each case, for the Au thickness that maximises $|K|$ ((a) $t$ = 55 nm, (b) $t$ = 20 nm, (c) $t$ = 25 nm); the equation of the linear model and $R^2$ goodness of fit are given in inset.**

As discussed previously, the waveguide becomes more symmetric as the adlayer grows for $n_c$ = 1.3303 (Figure 4.8a, sensing fluid RI below CYTOP), causing the transmittance to increase as observed. The trend of the curves for the case $n_c$ = 1.3348 (Figure 4.8b, sensing fluid RI matched to CYTOP) are opposite those of Figure 4.8a because the waveguide is in symmetry in the absence of an adlayer ($a$ = 0), and during adlayer growth, the waveguide becomes asymmetric, reducing its transmittance. The same qualitative behaviour is observed for $n_c$ = 1.3393 (Figure 4.8c, sensing fluid RI above CYTOP).

## 4.5 Conclusion

The surface sensitivity of straight LRSPP waveguides was investigated by considering sensing indices slightly below equal to, and slightly above that of CYTOP, the material used as the claddings. We demonstrated that optimizing the sensor performance involves maximizing |K| where $K = (\partial\alpha_s/\partial a)/\alpha_s$ and selecting the optimal sensing length as $L_{opt} = 1/(2\alpha_s)$. We proposed a linear model for the sensitivity of the sensing channel and demonstrated its applicability over a wide range of designs.

In this chapter, original work that has been done includes:

1. Modelled the attenuation and coupling loss of straight LRSPP waveguides for various gold thicknesses.
2. Modelled the adlayer formation on straight LRSPP waveguides for different sensing indices ($n_c < n_{\text{CYTOP}}$, $n_c = n_{\text{CYTOP}}$, and $n_c > n_{\text{CYTOP}}$,) and the surface sensitivity for each design is predicted.
3. Evaluated the performance of some waveguide designs where the thickness of the Au stripe was selected in each case to maximise $|K|$.
4. Represented the sensing channel transmittance by a linear model.

# CHAPTER 5: CHARACTERIZATION OF LONG RANGE SURFACE PLASMON WAVEGUIDES

## 5.1 Introduction

A LRSPP based sensor should be characterized experimentally after fabrication to verify its capability for biosensing application. In this chapter, we first describe the experimental setup involved which includes the fluidic assembly and optical integration of the sensor die. We also explain the device cleaning and preparation protocols before a sensor die is installed into the setup. A very important step before a sensing experiment is to establish a stable baseline. This is done by checking the stability of the input and output signal to and from the waveguide. Two fundamental sensing experiments are discussed in this chapter: bulk sensing and protein sensing. In bulk sensing, six solutions with different refractive indices are injected sequentially over the sensor surface and an optimally matched refractive index solution is determined as the buffer in biosensing experiments. Protein sensing involves the physisorption of bovine serum albumin (BSA) on carboxyl-terminated surface. The surface mass density of the biomaterial bound on the surface is estimated based on the change in output power measured.

## 5.2 Literature Review

### 5.2.1 Amine coupling

The most versatile and common approach to conjugate biomolecules to sensor surface involves primary amino (–$NH_2$) groups. Lysine residues which provide the nucleophile groups are typically present on the exterior of the protein (Xiao & Bock, 2012). In the case of SAMs, alkanethiols that are ω-terminated with carboxylic group can be used (Löfas & Mcwhirter, 2006). Carboxylic acid can undergo a zero-length coupling to a primary amine using a so-called “carbodiimide chemistry” (Figure 5.1).

To form a covalent bond, the carboxylic groups are first activated with carbodiimide. In aqueous solution, 1-ethyl-3-(3-dimethylopropyl)3-(3-Dimethylopropyl) (EDC) is used to transform the carboxylic group into reactive o-acylisourea intermediate, which can then readily react with primary amines to form amide bonds (Wang *et al.*, 2005). To prevent the reverse transformation of the reactive groups to the carboxylic groups, N-hydroxysuccinimide (NHS) is usually added to the EDC solution forming an active ester that is stable for several minutes to hours (Kim & Herr, 2013).

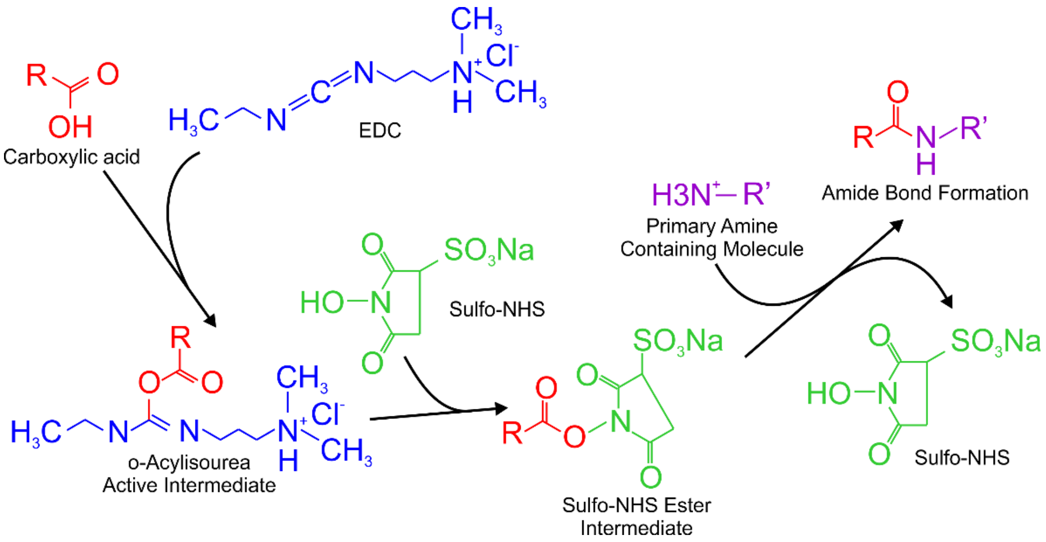

**Figure 5.1: Two-step process of amine-carboxylic acid coupling (Hermanson, 2013).**

Covalent immobilization produces irreversible binding and high surface coverage. The major drawback of covalent coupling is the random orientation of the biomolecules on the surface. The attachment may occur simultaneously through many lysine residues, increasing heterogeneity and restricting conformational flexibility (Rusmini, Zhong, & Feijen, 2007).

When the functional transformation (–COOH group is replaced by –NH2 group) has happened, a slight change in output power can be observed due to the difference in molecular weight of the two functional groups. The change in output power is verified through analytical calculation. Besides, there is two possibilities if the treatment is not successful: 1) the biomolecule is functionalized on the surface through physical adsorption (no covalent binding); or 2) the biomolecule cannot be functionalized on the surface. The second scenario can be easily spotted through real-time measurement where there is no change in output power after passing the biomolecules over the surface. In the first scenario, if the biomolecule is not functionalized through covalent coupling, the surface cannot be regenerated through SDS wash because SDS will break the weak bonding between the biomolecule and the surface. This argument has been verified through experiment.

## 5.3 Methodology

### 5.3.1 Experimental setup

#### 5.3.1.1 Fluidic assembly

In this thesis, all work has been done with only top-access microfluidic channels, either open channel etch or dedicated channel etch (Section 3.4.1.2). An example of the sensor die with open channel etch is shown in Figure 5.2 (top and side view). The sensing fluid is passed from the top of the sensor and flows across the etched waveguides.

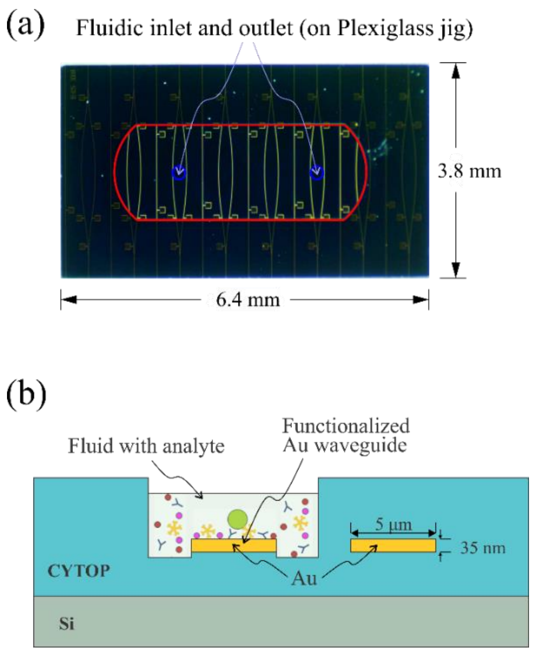

**Figure 5.2: Long range surface plasmon polariton (LRSPP) based sensor. (a) Microscope image of a sensor die with open channel etch. The yellow lines and curves correspond to the Au waveguides. The area bounded in red is the etched region where the waveguides are exposed to sensing fluid. The blue circles indicate the position of the fluidic inlet and outlet on the Plexiglas fluidic jig. (b) Front cross-section of a sensor die showing a functionalized waveguide and a CYTOP-embedded (fully cladded) waveguide.**

Figure 5.3a is a schematic representation of the fluidics setup for top-access microfluidic channels. A sensing die is placed on a metal base and fixed to a Plexiglas fluidic jig with Teflon screws. The rationale of using Teflon screws is to provide sufficient pressure for good seal and fluidic exchange in the etched channel without being too harsh to destroy the Au waveguide (since CYTOP cladding is relatively soft). Two holes (fluidic inlet and outlet) are machined on the Plexiglas jig for fluidic tubing and an O-ring that matches the dimensions of the etched region is attached to the bottom face of the jig. The fluid is supplied through pico tubing (550 µm outer diameter, 250 µm inner diameter) by a syringe pump (PicoPlus, Harvard Apparatus) into the cavity formed between the etched channel and the O-ring.

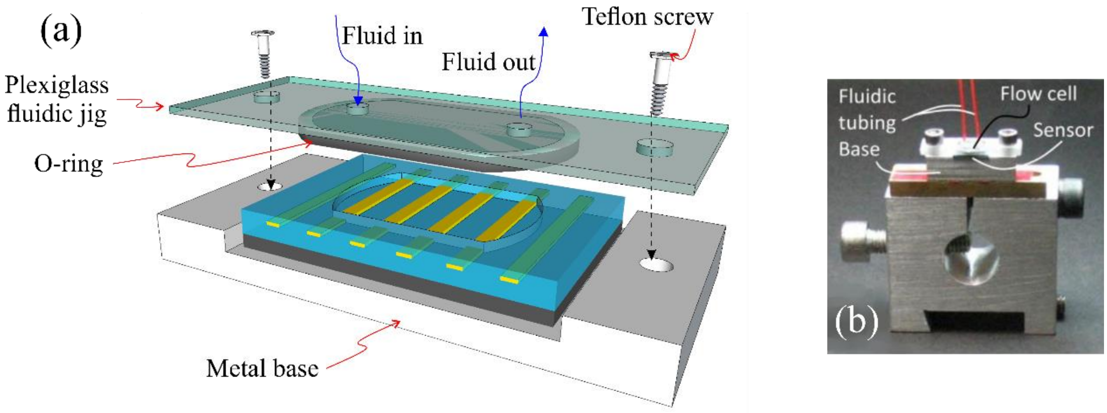

**Figure 5.3: Sensor die with integrated fluidics. (a) Schematic of a sensor die sandwiched between a metal base and a Plexiglas jig. (b) Image of the fluidic assembly of the LRSPP based sensor.**

#### 5.3.1.2 Optical interrogation

Sensors were interrogated by coupling a polarization-maintaining (PM) optical fiber to the input, thereby launching light generated by a semiconductor laser diode at operating wavelength, $\lambda_0 = 1310$ nm into the sensor as propagating LRSPPs. The output power of the laser diode was controlled by a precision current source (LDX-3220, ILX Lightwave). The PM optical fiber (PMJ-3AX-1300-7/125-1-1-1, OZ Optics) has a core diameter of 7 μm. One multi-axis positioning stage (Newport Corporation) was used to butt-couple the fiber to the sensor, which is also resting on a positioning stage. A 20× objective lens (M-20X, Newport) was placed after the positioning stages to magnify and collimate the optical output from the sensing waveguide. The background radiation of the output signal was minimized using a pinhole aperture before the output signal was passed through a 50:50 beam splitter (BSW12, Thorlabs). One portion of the output beam was sent to an infrared (IR) camera (7290A, MicronViewer) to visually monitor the emerging mode for ease of alignment, and the other portion was sent to a power meter (PM100D, Thorlabs) to observe changes in output signal during an experiment. Labview software was used to perform data acquisition at a specific time interval. An example of the Labview script to read the power meter (HP8153A, Agilent Technologies) measurement is attached in Appendix C. The setup is shown is Figure 5.4.

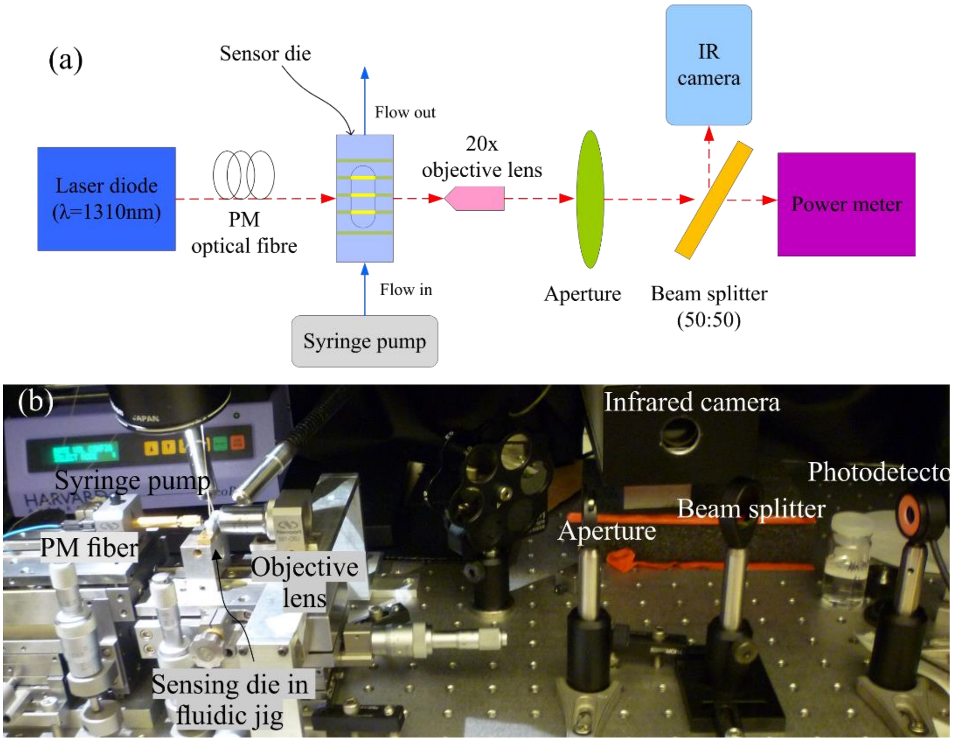

**Figure 5.4: (a) Schematic representation and (b) photo of the optical setup with the sensing die installed. Red lines represent the optical path while the blue lines indicate the fluidic flow.**

### 5.3.2 Chemicals and reagents

16-Mercaptohexadecanioc acid (16-MHA), phosphate buffered saline (PBS) 0.01 M, pH 7.4, bovine serum albumin (BSA), 2-isopropanol semiconductor grade (IPA), acetone HPLC grade ≥99.9%, octane, and glycerol (electrophoresis grade) were obtained from Sigma-Aldrich. Distilled water was deionized using Millipore filtering membranes (Millipore, Milli-Q water system at 16 MΩ cm).

### 5.3.3 Device preparation

During dicing of a wafer, the waveguide facets are covered with debris, as shown in Figure 5.5a. Therefore, the facets need to be cleaned through ultrasonication for efficient optical input and output coupling. The optimized settings of the ultrasonic cleaner (FB-11201, Fisher Scientific) were determined as: frequency = 37 kHz and power = 50 % to provide sufficient agitation to remove the debris without destroying the Au waveguides.

A fresh sensor die was cleaned by ultrasonication in octane for 5 minutes. Octane was chosen because the dicing photoresist (MEGAPOSIT SPR 220-7) is not soluble in octane and thus is able to act as a protection layer during ultrasonication.

The sensor die was then left immersed in two sequential acetone baths for 5 minutes and 30 minutes, respectively to completely remove the dicing photoresist. After a thorough washing in IPA and drying with nitrogen gas ($N_2$), the sensor die was placed in a UV/ozone chamber (PSD-UV, Novascan) to remove any possible organic matter from the Au surface. The die was then washed intensely with distilled/deionized water (DDI $H_2O$) and IPA, followed by $N_2$ drying. A cleaned sensor die was incubated in a 1 mM IPA solution of 16-MHA overnight to allow self-assembled monolayer (SAM) formation. The SAM-modified sensor die was rinsed with IPA and dried with $N_2$ before being placed into the fluidic jig. An example of a cleaned sensor die ready to be used for biosensing experiments is shown in Figure 5.5b.

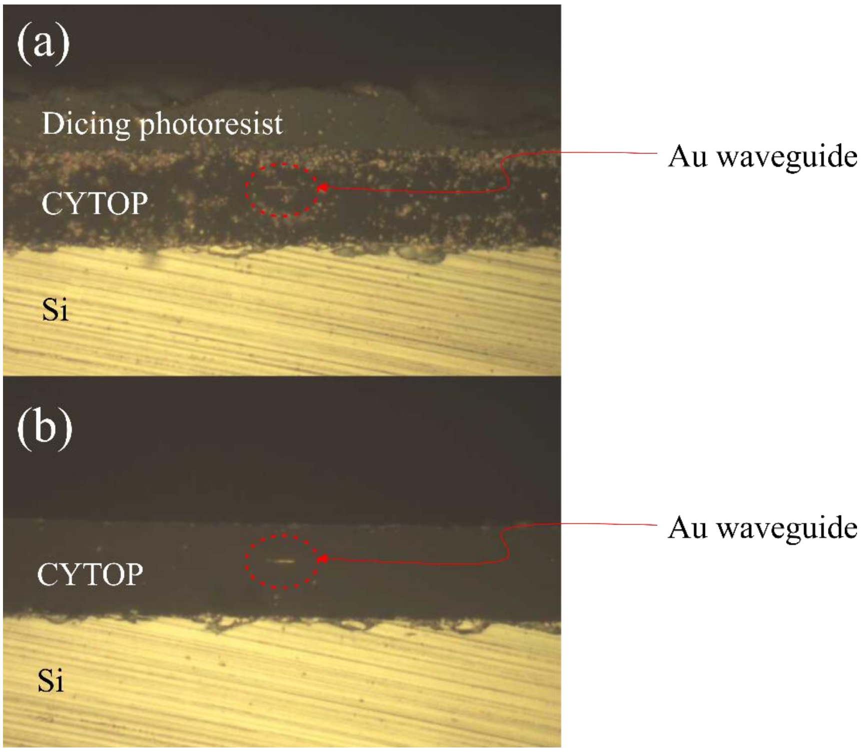

**Figure 5.5: The facet of the sensor die (a) before and (b) after cleaning.**

Upon completion of an experimental cycle, the Au surface of the sensor die was fully regenerated by placing it in a UV/ozone chamber. After that, the sensor die was washed with plenty of DDI $H_2O$, IPA and dried with $N_2$. The regenerated sensor die was again incubated in a 2 mM IPA solution of 16-MHA overnight to prepare the die for another experimental cycle.

## 5.4 Results and Discussion

### 5.4.1 Cutback measurements

The attenuation and coupling loss of a LRSPP straight waveguide can be characterized experimentally and compared to the theoretical predictions by using a cutback technique. Considering constant input power, the output power of fully cladded sensor dies with length $L_{die}$ = 2 mm, 2.6 mm, 3.5 mm and 4.6 mm was recorded using the experimental setup described in section 5.3.1.2. Then, the insertion loss (in dB) of the sensor dies was computed using a simple equation IL (dB) = $P_{in}$ (dBm) – $P_{out}$ (dBm) and plotted as a function of the die length (Figure 5.6). As mentioned in previous chapter (Equation 4.18), the insertion loss in dB can be expressed as IL (dB) = MPA · $L_{die}$ + $C_{dB}$. Hence, by creating a linear model for the measurements, the measured mode power attenuation and coupling loss at the input facet can be determined. The measurements are very close to the theoretical computation using COMSOL Multiphysics, as presented in Table 5.1. The coupling loss is higher than that of the theoretical value due to the diced facet quality and slight misalignment due to human error.

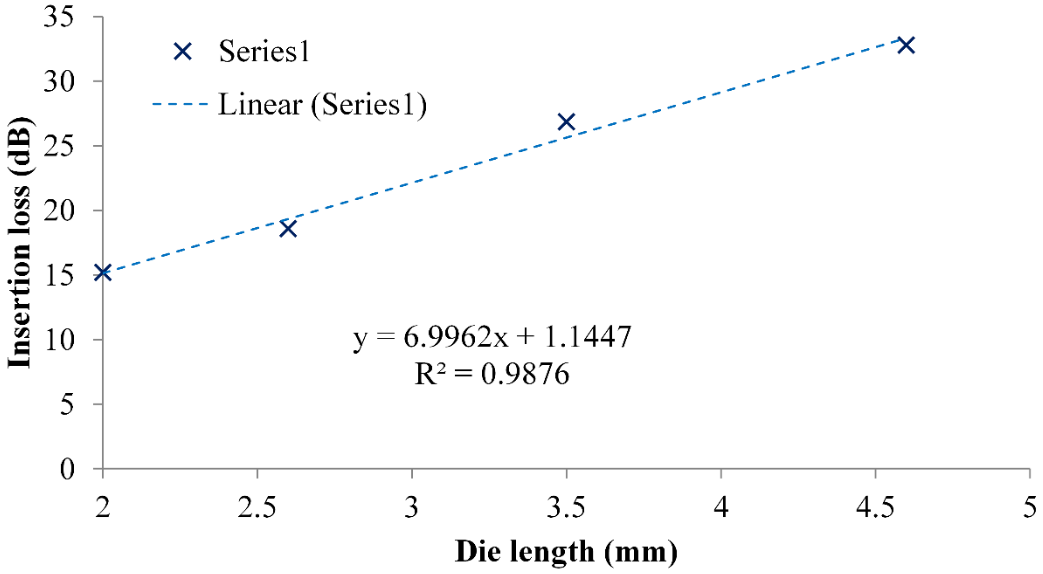

**Figure 5.6: Cutback measurements for fully cladded straight Au waveguides at $\lambda_0$ = 1310 nm. The crosses represent the experimental results and the dotted line corresponds to the linear fit.**

**Table 5.1: Theoretical and experimental values of the attenuation and coupling loss for a fully cladded straight waveguide.**

| | **Theoretical values** | **Experimental values** | **Error (%)** |
|---|---|---|---|
| Attenuation (dB/mm) | 7.1 | 6.9962 | 1.46 |
| Coupling loss (dB/facet) | 0.89 | 1.1447 | 28.6 |

### 5.4.2 Stability test

Each time before an experiment, a laser-to-lens stability test (without installation of sensor die) was performed to ensure the absence of a physical drift in the optical setup. Besides, a distortion in the signal might occur when the PM fibre is placed too tightly in the fibre chuck. A real-time measurement of the output power from the PM fibre was recorded over a period of ~20 minutes, as shown in Figure 5.7.

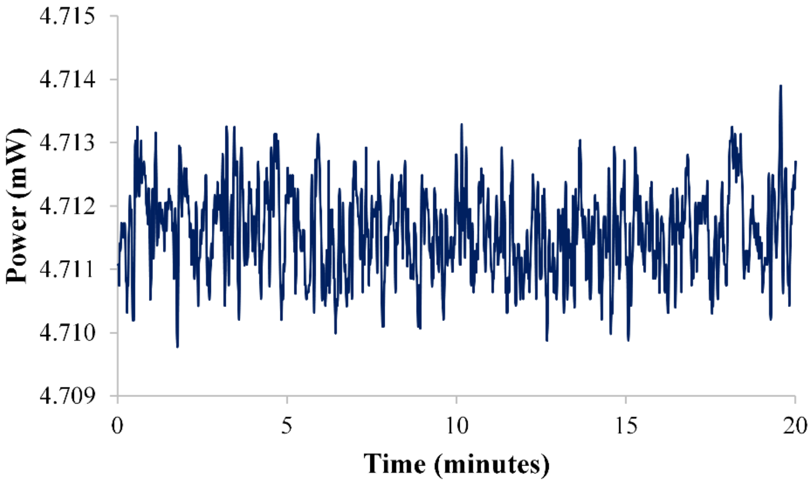

**Figure 5.7: Power measurement of the laser-to-lens stability test showing that the system is having a stable output signal without any significant drift or distortion over a period of 20 minutes.**

After obtaining a stable laser-to-lens signal, the sensing die was installed and the signal stability was again determined. A precise alignment is crucial to establish a stable power baseline for sensing application. Figure 5.8a shows different power signal patterns which correspond to the quality of butt-coupling between the input fibre and the waveguide. A low-noise signal corresponds to a high signal-to-noise ratio ($\Delta S/\sigma$), and thus improves (lowers) the detection limit of the system. As compared to the blue curve in Figure 5.8 which has a standard deviation of the optical output power $\sigma$ = 13.7 nW, the red curve has a relatively low noise level ($\sigma$ = 3.7 nW). Besides, the magenta curve shows a worse case where the noisy signal ($\sigma$ = 15.5 nW) has sudden spike at t = 1 min and minor drift after t = 5 mins. Sudden spike is often caused by a sudden disturbance within or to the system (usually mechanical such as vibration) while a drift in the signal is often related to the misalignment in the setup. A good baseline signal for biosensing experiment with $\sigma$ = 1.4 nW is also shown as the orange curve in Figure 5.8. Apart from analysing the signal measurement, a visual inspection on the mode output is required. An output mode from the Au waveguide should be bright and clear with minimum surrounding radiation, as shown in the inset of Figure 5.8.

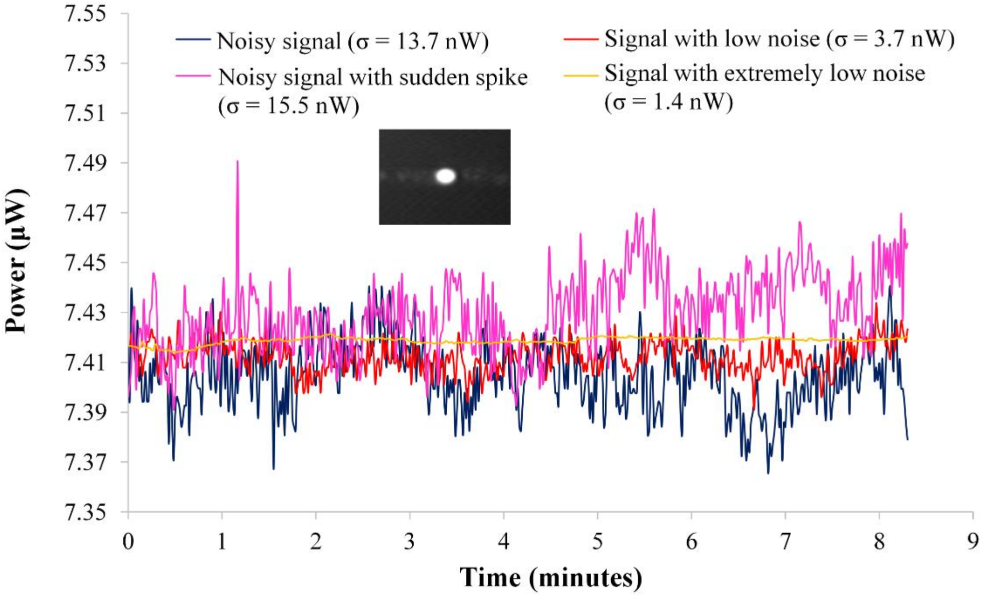

**Figure 5.8: Power measurement with the sensing die installed. Inset: the image of a mode output with closed aperture.**

Generally, the limiting noise sources in the detection are the noise from the laser source, the stability of the translational stages and the quality of butt-coupling between the input fibre and the waveguide.

### 5.4.3 Bulk sensing

In order to observe how the index of a solution affects LRSPP propagation in our fabricated sensor, six solutions of varying refractive indices were prepared and sequentially injected into the sensor under a continuous flow rate of 20 µl/min (Figure 5.9). The sensor die was previously cleaned and prepared using the protocols as discussed in Section 5.3.3. The refractive index is adjusted by starting off with phosphate buffer saline (PBS) solution with a base refractive index of 1.32136 and adding glycerol (n = 1.4631) to it (PBS/Gly). The refractive index of each solution was measured at $\lambda_0$ = 1312 nm using a prism-coupler based instrument (Model 2010, Metricon, Prism 200-P1). The refractive indices of the solutions measured were: 1.32842, 1.33046, 1.33258, 1.33499, 1.33722 and 1.34149 respectively.

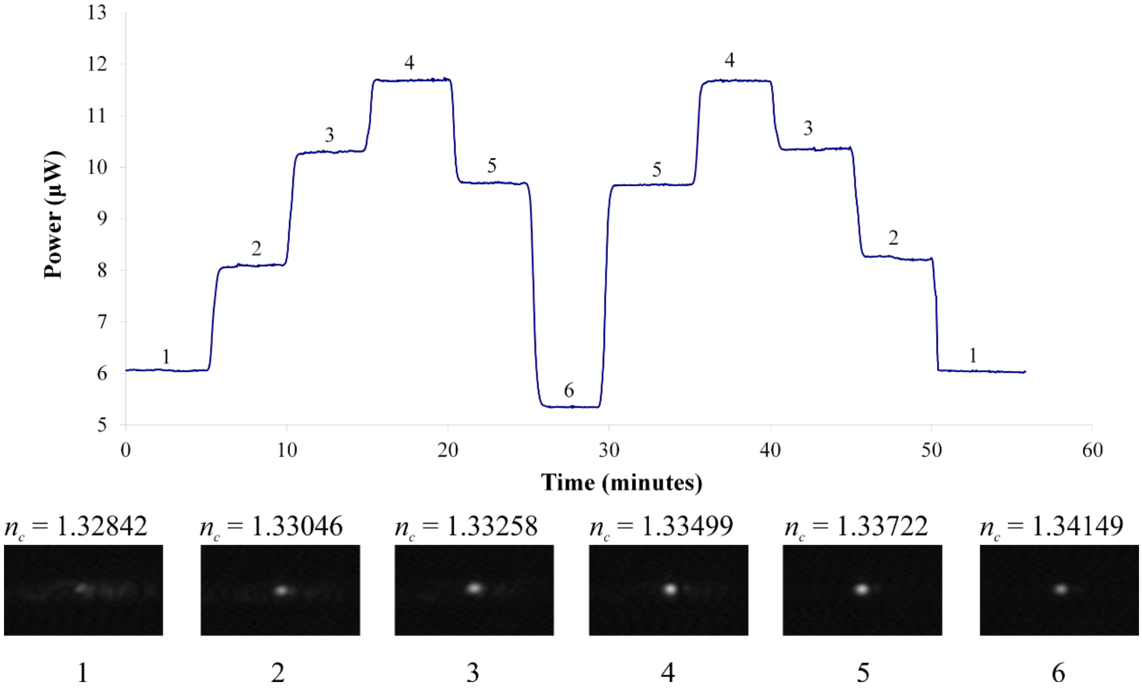

**Figure 5.9: Real-time measurement showing PBS/Glycerol solutions of different refractive indices were injected over a Au stripe sensor functionalized with 16-MHA. A corresponding mode output was taken for each solution for visual comparison.**

The aim of bulk sensing is to determine an optimally matched refractive index solution (buffer) which is suitable to carry out biosensing experiments and to determine the fluid exchange time in our system. During every injection, a mode image was captured to visually compare the mode intensity and its relative background. It is shown that the change in output power does not correspond directly to the constant change in refractive index (Krupin *et al.*, 2013). The maximum output power was observed for the solutions with n = 1.33499 which is very close to the refractive index of CYTOP (n = 1.3348). This observation is consistent with the symmetric waveguide case discussed previously (Breukelaar, Charbonneau, & Berini, 2006). The largest signal change was observed from $n_c$ = 1.33046 to 1.33258 where ΔS = 2.2 µW. Considering the standard deviation of the output power σ = 6.15 nW, the corresponding signal-to-noise ratio was calculated as ΔS/σ = 358. From this value, we can determine the detection limit of the sensor die near $n_c$ = 1.33046 as $5.92 \times 10^{-6}$ RIU (for ΔS/σ = 1) although a detection limit as low as $2.3 \times 10^{-6}$ RIU was reported previously (Krupin *et al.*, 2013).

From this experiment, it was also observed that the fluid exchange in the channel took about 1.5 minutes. The fluid exchange time is calculated from the change of solutions in the syringe pump to the actual change in signal observed due to the solution. It is important to estimate the fluid exchange time in order to differentiate the bulk effect from the binding response during a biosensing experiment. The fluid exchange time can be shortened by reducing the length of the fluidic tubing. However, the tubing length has to be long enough for the syringe pump to be isolated from the experimental setup so that the exchange of solutions can take place during a biosensing experiment.

### 5.4.4 Protein sensing

The capability of straight LRSPP waveguides for sensing small biochemical entities such as proteins was demonstrated through bovine serum albumin (BSA) physisorption. A gold stripe sensor was functionalized with 16-MHA using the same protocols as Section 5.3.3. The refractive index of the PBS/Gly buffer was chosen as $n_c$ = 1.3303 (Krupin *et al.*, 2013). The optimum concentration of BSA was determined as 100 µg/ml since this value causes a minimum bulk refractive index change in the buffer while being high enough to avoid diffusion.

A baseline under PBS/Gly flow at 20 µl/min was established for 10 minutes followed by the injection of BSA solution (Figure 5.10a). The power increased gradually as BSA adsorbed onto the sensor surface. After the excess BSA was washed with PBS/Gly, a mild decrease in signal is observed which can be caused by both protein dissociation and a slight bulk refractive index change.

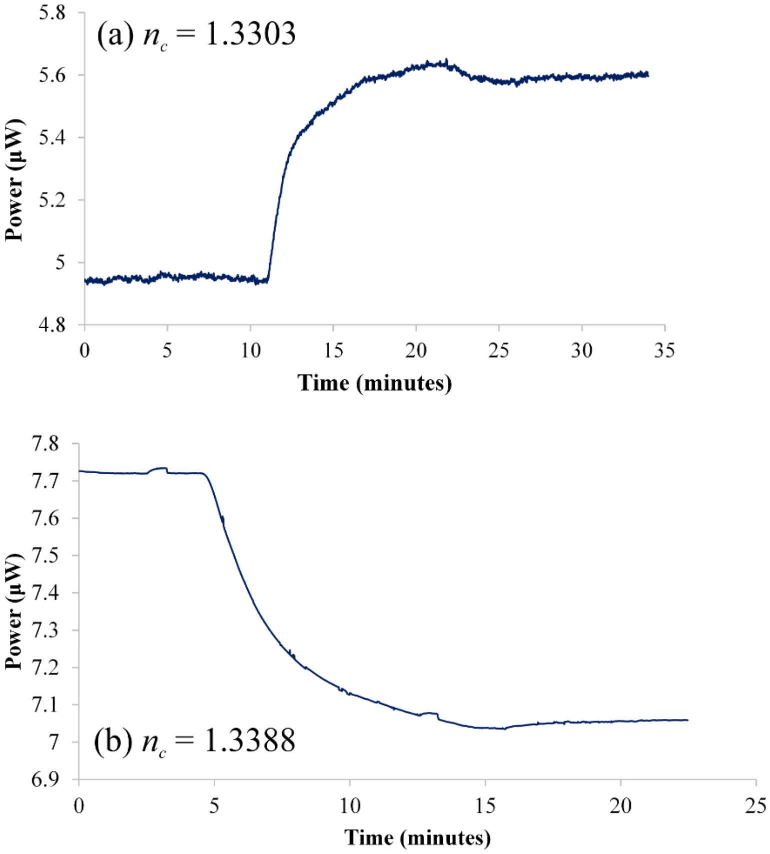

**Figure 5.10: Response of a Au stripe sensor to BSA physisorption on a carboxyl-terminated SAM for sensing buffer with indices (a) $n_c$ = 1.3303 and (b) $n_c$ = 1.3388.**

For attenuation-based biosensing, the difference in power measured before and after protein injection is proportional to the mass of biomaterial bound to the waveguide surface. As discussed in Section 4.4.5, we can relate the surface mass density of the biomaterial on the sensor surface (in g/m$^2$) to its equivalent optical parameters ($n_a$, $P_{out}$) through:

$$\Gamma = \frac{1}{k_2}\frac{(n_a - n_c)}{\partial n/\partial c}\left(\frac{P_{out}(a_1)}{P_{out}(a_0)} - 1\right) \tag{5.1}$$

where $n_a$ and $n_c$ are the refractive indices of the adlayer formed and the sensing buffer respectively, $\partial n/\partial c$ is the partial change of refractive index relative to a change in concentration of the adlayer, $P_{out}\ (a_0)$ is the power measured before protein injection, and $P_{out}\ (a_1)$ is the power measured after protein injection. $k_2$ is a constant related to the characteristics of the waveguide which is affected by slight variations during fabrication. Hence, for every batch of sensor dies fabricated and different refractive indices of buffer used, $k_2$ is determined from a BSA physisorption experiment. Assuming a close-packed monolayer of BSA is adsorbed on the sensor surface ($\Gamma$ = 3669 pg/mm$^2$) (Krupin *et al.*, 2013), $n_c$ = 1.3303, $n_a$ = 1.5, and $\partial n/\partial c$ = 0.185 mm$^3$/mg (De Feijter *et al.*, 1978), the $k_2$ value can be calculated from the result in Figure 5.10a:

$$\Gamma = \frac{(n_a - n_c)}{k_2 \partial n/\partial c}\left(\frac{P_{out}(a)}{P_{out}(a_0)} - 1\right)$$

$$3669 = \frac{(1.5 - 1.3303)}{k_2\ (0.185)}\left(\frac{5.585\ \mu W}{4.955\ \mu\mathrm{W}} - 1\right) \tag{5.2}$$

$$\mathrm{k}_2 = 0.0318\ \mathrm{nm}^{-1} \tag{5.3}$$

This $k_2$ value was further used to estimate the surface mass density based on the change in power measured for biosensing experiment in Chapter 6, using Equation 5.1.

For the biosensing experiments in Chapter 7, an improved experimental setup and a new refractive index of PBS/Gly ($n_c$ = 1.3388) were used (Figure 7.2). Hence, another BSA physisorption experiment was carried out to determine the new $k_2$ value. The result is shown in Figure 5.10b and the trend of the response agrees qualitatively with the sketch of Figure 4.7 and the results of Figure 4.8. From Figure 5.10, we can observe that the transmittance increases during adlayer formation for a sensing fluid RI below that of CYTOP and decreases for a sensing fluid RI matched to or above that of CYTOP. The $k_2$ value for $n_c$ = 1.3388 is computed as following:

$$\Gamma = \frac{(n_a - n_c)}{k_2 \partial n/\partial c}\left(\frac{P_{out}(a)}{P_{out}(a_0)} - 1\right)$$

$$3669 = \frac{(1.5 - 1.3388)}{k_2\ (0.185)}\left(\frac{7.06\ \mu W}{7.72\ \mu\mathrm{W}} - 1\right) \tag{5.4}$$

$$\mathrm{k}_2 = -0.0203\ \mathrm{nm}^{-1} \tag{5.5}$$

Given that the BSA physisorption experiment for $n_c$ = 1.3388 was detected with a signal-to-noise ratio of $\Delta S/\sigma = 390$, the detection limit of the new experimental setup is estimated as 9.42 pg/mm$^2$ (for $\Delta S/\sigma = 1$).

## 5.5 Conclusion

The LRSPP waveguides were shown to have a propagation loss of 7 dB/mm and a coupling loss of 0.9dB/facet. The straight waveguide responded to the changes in the bulk refractive index of a solution with a detection limit of $5.92 \times 10^{-6}$ RIU. Protein sensing was demonstrated through physisorption of BSA on carboxyl-terminated surface. The detection limit for surface mass density was found to be ~ 9 pg/mm$^2$.

In this chapter, original work that has been done includes:

1. Assembled the experimental setup and fluidic jig for biosensing application.
2. Prepared the LRSPP sensor die for biosensing experiments which includes cleaning of the sensor die and chemical functionalization of the sensor surface.
3. Performed cutback measurements to determine the coupling and propagation loss of the fabricated LRSPP waveguides.
4. Checked the stability of the experimental setup to ensure the noise of the system is low enough to define the detection limit.
5. Demonstrated bulk and protein sensing using straight LRSPP waveguides.

# CHAPTER 6: SEROLOGICAL-BASED DENGUE DETECTION IN BLOOD PLASMA USING LONG-RANGE SURFACE PLASMON WAVEGUIDES

## 6.1 Introduction

To date, the most widely used dengue diagnosis method is serological-based, where dengue-specific antibodies are detected in patients' blood samples. In particular, identification of dengue-specific immunoglobulin M (IgM) antibody is normally chosen as the preferred serological test because dengue-specific IgM is detectable earlier than dengue-specific IgG. In this chapter, two surface functionalization approaches are proposed for the detection of dengue-specific immunoglobulin M (IgM) antibody in actual patient blood plasma samples. The results obtained via these two surface functionalization approaches are comparable to, or of greater quality, than those collected by conventional IgM Antibody Capture Enzyme Linked Immunosorbent Assay (MAC-ELISA). Our second functionalization approach was found to minimize non-specific binding, thus improving the sensitivity and accuracy of the test. We also demonstrate re-use of the biosensors by regenerating the sensing surface down to the virus (or antibody) level, or down to the bare Au.

## 6.2 Literature Review

### 6.2.1 Serological based dengue detection

Serological tests are more commonly used in laboratory diagnosis of dengue infection because they are more easily and cheaply implemented. In particular, identification of dengue-specific immunoglobulin M (IgM) antibody is normally chosen as the preferred serological test because dengue-specific IgM is detectable earlier than dengue-specific IgG (Rathakrishnan & Sekaran, 2013). Many immunoassay kits based on IgM Antibody Capture Enzyme Linked Immunosorbent Assay (MAC-ELISA) are commercially available (Hunsperger *et al.*, 2009), but they usually require long assay times and labour-intensive sample processing. Several rapid IgM-based dengue diagnostic tests have been developed for use at point of care but they generally have lower sensitivity than the ELISA assay, and so have limited clinical use (Peeling *et al.*, 2010).

Previous work reported detection of the dengue antibody using a commercial SPR instrument, but not in a patient sample and using a complex sensing protocol involving dengue antigen-BSA conjugate (Kumbhat *et al.*, 2010). A broader literature search reveals that very little work has been done, in general, on the detection of antibodies in complex fluids such as patient blood samples using SPR techniques (Avramis, Avramis, Hunter, & Long, 2009; Gomara, Ercilla, Alsina, & Haro, 2000; Nagel, Gajovic-Eichelmann, Tobisch, Schulte-Spechtel, & Bier, 2008), and that additional pre-processing steps and features on the sensor (such as a reference channel) to minimize non-specific binding are suggested (Rodriguez-Emmenegger *et al.*, 2011; Springer, Bockova, & Homola, 2013; Vaisocherová *et al.*, 2009).

## 6.3 Methodology

### 6.3.1 Sensing device and experimental system

The sensor die (3.8 mm × 6.4 mm) which consists of 16 alternating straight Au waveguides and Mach-Zehnder interferometers (MZIs), was fabricated by following the procedures as described in Chapter 3. In this chapter, only a single straight Au waveguide (~5 μm wide, 35 nm thick) located in the middle of a sensor die was used throughout to ensure the consistency in measurements. The experimental system and device preparation were described in Chapter 5.

### 6.3.2 Chemicals and reagents

16-Mercaptohexadecanioc acid (16-MHA), phosphate buffered saline (PBS) 0.01 M, pH 7.4, bovine serum albumin (BSA), sodium dodecyl sulfate (SDS), 2-isopropanol semiconductor grade (IPA), acetone HPLC grade ≥99.9%, sulfuric acid ($H_2SO_4$) 99.999%, hydrogen peroxide ($H_2O_2$) solution ≥30%, octane, and glycerol (electrophoresis grade) were obtained from Sigma-Aldrich. N-Hydroxysuccinimide sodium salt (NHS) and 1-ethyl-3-(3-dimethylaminopropyl)carbodiimide hydrochloride, ≥99% (EDC) were purchased from Chem-Impex International, Inc. Distilled water was deionized using Millipore filtering membranes (Millipore, Milli-Q water system at 16 MΩ cm). All the solutions except for the dengue virus serotype 2 (DENV-2) and plasma samples were filtered through Millex-GP filters (PES membrane 0.22 μm).

### 6.3.3 Dengue virus serotypes 2 (DENV-2)

Dengue virus serotype 2 (DENV-2) strain New Guinea C (NGC) was obtained from the Department of Medical Microbiology, Faculty of Medicine, University of Malaya, Malaysia. Briefly, virus was propagated in African green monkey kidney cells (VERO) in growth medium (20 mM hepes buffered RPMI 1640 with 10 mM nonessential amino acid, 2 mM glutamine, 10% fetal calf serum (FCS), 100 U/ml penicillin G sodium and 100 μg/ml of streptomycin sulfate) by inoculating 1 ml of virus stock solution into a 50 $cm^2$ tissue culture flasks. The infected cells were then maintained at 37 $^oC$ in 5% $CO_2$. The monolayer was harvested when 70% cytopathic effect (CPE) was seen. The cells were then trypsinized, pelleted by low speed centrifugation, washed with 0.01 M phosphate buffered saline (PBS), (Dulbecco “A” from Oxiod, U.K.) at pH 7.4 and aliquoted into 15 ml Falcon tubes at $5\times10^7$ cells per tube. The virus stock which has a viral concentration of $1\times10^6$ PFU/ml was stored at -20 °C until use.

### 6.3.4 Plasma samples

#### 6.3.4.1 Dengue Positive Samples

Three patient plasma samples laboratory-confirmed as dengue positive were obtained from the Department of Medical Microbiology, Faculty of Medicine, University of Malaya, Malaysia (Ethical Clearance No. 782.90 from the University Malaya Medical Centre). The samples were collected and tested for dengue using a combination of hemagglutination inhibition (HI), NS1 capture ELISA, IgG capture ELISA and IgM capture ELISA prior to experimentation (Rathakrishnan & Sekaran, 2013).

#### 6.3.4.2 Dengue Negative Sample (Negative Control)

A non-infected human plasma in K3 EDTA (lot no. PLE050412) was purchased from Zen-Bio, Inc. to serve as a negative control. The donor is of U.S. origin, male, African American and 49 years old.

### 6.3.5 Experimental procedures

#### 6.3.5.1 Dengue virus serotype 2 (DENV-2) functionalized surface

Rapid dengue diagnosis requires single-step detection in clinical blood samples with a pre-functionalized sensor surface. We first present results relevant for this case, where dengue virus serotype 2 (DENV-2) was immobilized on the sensor surface to capture dengue-specific IgM antibody present in plasma samples. The functionalization process is illustrated in Figure 6.1a along with a sensing and regeneration run.

A sensor die was cleaned and functionalized with 1 mM IPA solution of 16-mercaptohexadecanioc acid (16-MHA). The die was then placed into a fluidic jig with PBS/Gly buffer (a mixture of standard phosphate buffered saline (PBS) with glycerol 7.235% w/w) filling the etched channel. At the beginning of an experiment a baseline signal level was established while flowing PBS/Gly buffer for 10 min to ensure signal stability and low noise. The carboxyl group of 16-MHA was then activated *in situ* by injecting a mixture of 0.1 M N-hydroxysuccinimide (NHS) and 0.1 M 1-ethyl-3-(3-dimethylaminopropyl) carbodiimide hydrochloride (EDC) in PBS/Gly buffer for 15 min. Next, the fluidic cell was flushed with PBS/Gly buffer to recover the baseline signal. DENV-2 diluted with PBS/Gly buffer in 1:10 ratio was then injected for 10 min to be covalently attached to the sensor surface. The drop in signal immediately after DENV-2 injection (Figure 6.1b) is caused by a bulk change in refractive index, but the virus binding in real-time still can be observed over the time frame of 35–45 min. After the sensor was washed with PBS/Gly buffer to remove excess DENV-2, a new baseline power level corresponding to the formation of a DENV-2 adlayer on the surface was established (Figure 6.1b). Preliminary experiments with patient samples indicated that nonspecific binding can be significant for this functionalization approach and that it can affect the determination of results (data not shown). Thus, a 10-min flow of bovine serum albumin (BSA) solution was introduced to mitigate potential nonspecific binding - no measurable change in signal is observed in this case (Figure 6.1b) suggesting saturation of the surface with DENV-2. A clinical plasma sample diluted in a 1:10 ratio with PBS/Gly buffer was then injected and the flow was stopped after 5 min to allow reaction with DENV-2 on the surface. Stopping the flow reduces the consumption of plasma. The immunoreaction between immobilized DENV-2 and dengue-specific IgM antibody in the plasma sample was then followed by a PBS/Gly wash for 10 min to eliminate any loosely bound compounds. The same DENV-2 surface was reused to produce several measurements for the same patient sample (repeats). This was accomplished by washing away the associated antibody through an injection of 0.5% sodium dodecyl sulfate (SDS). It has been shown previously (Dutra, Mendes, Lins da Silva, & Kubota, 2007) that a sensor surface can be regenerated in this manner without affecting immunoreactivity. After the SDS flow, followed by a PBS/Gly wash, the signal level returned close to that prior to plasma injection, remaining slightly higher, indicating that some material remained bound to the surface (Figure 6.1b). Three binding/regeneration cycles were carried out in this manner for each patient plasma sample. The binding capacity of the DENV-2 surface was observed to drop slightly after every cycle, probably because some material remained bound after SDS injection; however, the sensor produced consistent results for all patients after three repeats for each.

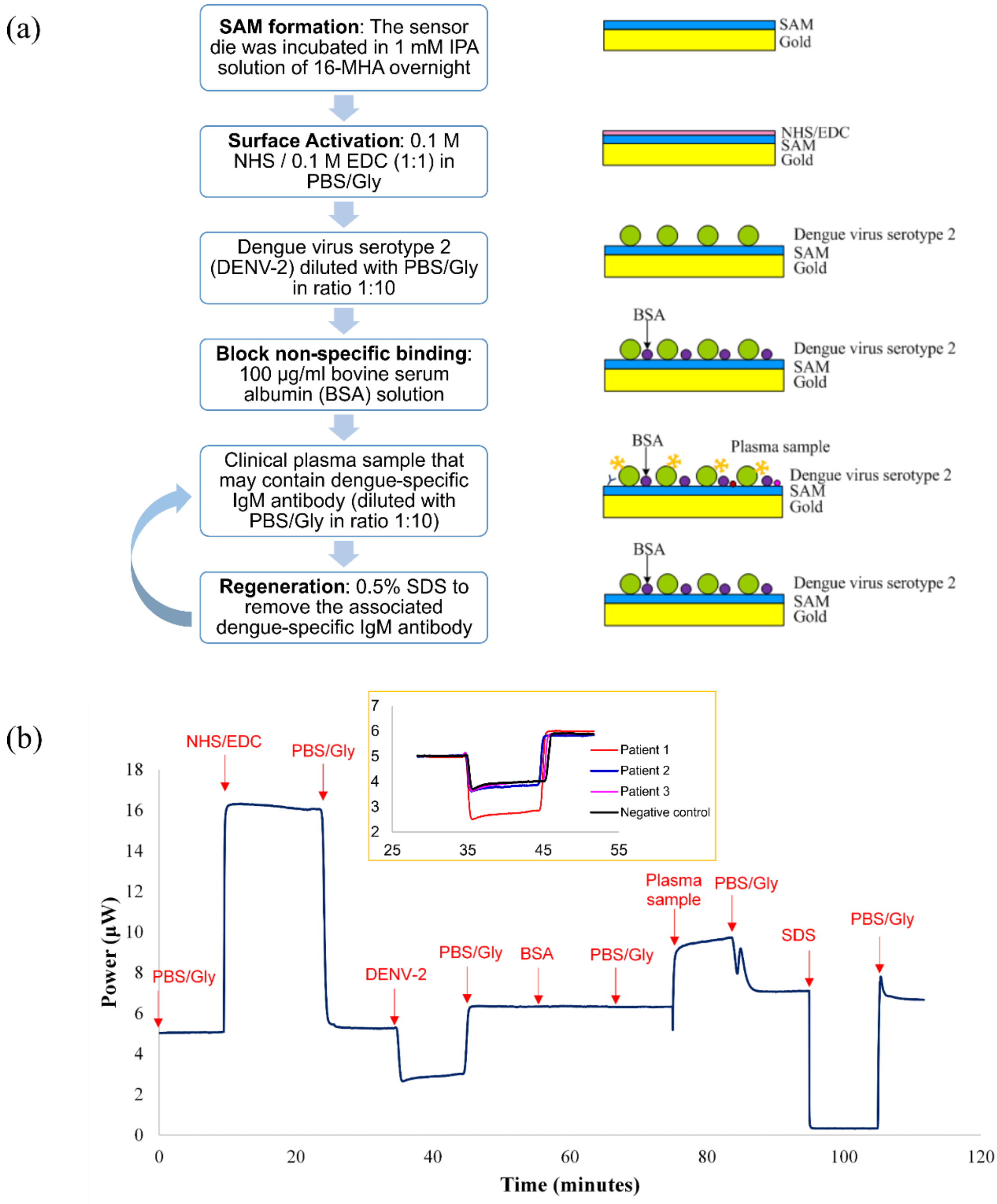

**Figure 6.1: Surface functionalization of Au waveguide with dengue virus serotype 2 (DENV-2). (a) Schematic illustrating the functionalization of the sensor and a sensing run. (b) Real-time measurement showing the immobilization of DENV-2 onto the 16-MHA modified Au waveguide through a NHS/EDC reaction followed by the injection and capture of dengue-specific IgM antibodies. Inset: The zoom-in image shows the responses during DENV-2 attachment after fully regenerating a waveguide (down to the Au surface) between patient plasma samples.**

Three positive samples with different concentrations of dengue-specific IgM antibody and normal plasma (negative control) were tested using the same Au waveguide on a sensor die. After a complete experimental cycle with one plasma sample (including repeats), the sensor surface was fully regenerated, down to the bare Au waveguide, by placing it in a UV/ozone chamber. The fully regenerated sensor die was then incubated in 16-MHA and another functionalization and experimental cycle was carried out with a different patient plasma sample. The inset to Figure 6.1b shows an expanded view of the responses observed during immobilization of DENV-2 onto the sensor surface after each full regeneration cycle. The power level measured before and after DENV-2 injection varies only very slightly from regeneration to regeneration, indicating that the sensor surface was not significantly degraded due to UV/ozone and that essentially the same virus coverage was achieved in all cases. This implies that the sequence in which the patients' plasma is investigated should be irrelevant. Nevertheless, we performed the first experimental run for each patient with the negative control.

#### 6.3.5.2 Plasma functionalized surface

The observation of nonspecific binding in the case of the negative control observed in using DENV-2 functionalized surface led us to our second immobilization approach, which is inspired by the standard protocol in dengue diagnosis using conventional MAC-ELISA, where the plasma sample is immobilized onto the surface and the dengue virus is injected thereon. Figure 6.2a illustrates the functionalization and experimental procedures applied to the same sensor die as used in the previous section (after full regeneration via UV/ozone and piranha (3:1 solution of concentrated sulfuric acid ($H_2SO_4$) and 30% hydrogen peroxide ($H_2O_2$) cleaning).

After establishing a stable baseline with PBS/Gly buffer, the carboxyl groups of the SAM on the Au waveguide were activated by a flow of NHS/EDC. The refractive index mismatch between PBS/Gly buffer and NHS/EDC in PBS/Gly resulted in a sudden rise in signal as observed in Figure 6.2b. The baseline signal level recovered after a PBS/Gly wash and plasma samples were injected into the flow cell for covalent attachment to the sensor surface. Next, DENV-2 was introduced over the surface for 10 min. If there exists any dengue-specific IgM antibody on the sensor surface, DENV-2 will be captured resulting in a gradual rise in signal. Finally, PBS/Gly buffer was injected to wash away any loosely bound material. To regenerate the plasma surface for repeated measurements, the bound DENV-2 was washed away via a 10-min flow of SDS. Once the baseline signal level recovered to that observed before virus injection, DENV-2 was again introduced. Three repeats were obtained in this manner for each surface functionalized with different plasma samples (three positive samples with different concentrations of dengue-specific IgM antibody and a negative control). The experiments were performed in a similar sequence as in the previous section, starting with the negative control sample, to ensure consistency in the measurement process.

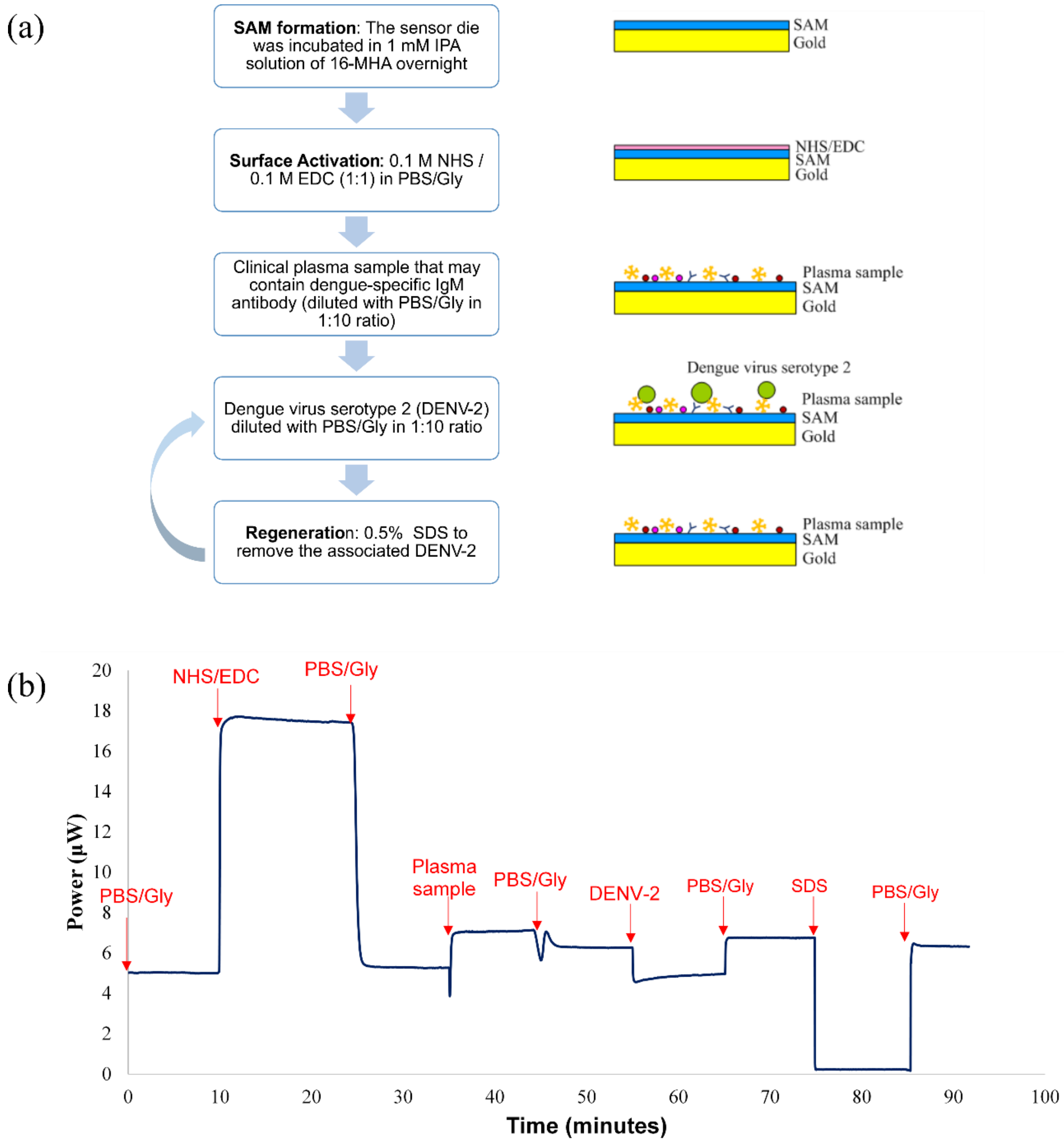

**Figure 6.2: Surface functionalization of Au waveguide with a plasma sample. (a) Schematic illustrating the functionalization of the sensor and a sensing run. (b) Real-time measurement showing the immobilization of a plasma sample onto the 16-MHA modified Au waveguide through a NHS/EDC reaction, followed by the injection and capture of DENV-2 by dengue-specific IgM antibody on the surface. The surface was regenerated at the plasma level with 0.5% SDS for repeated measurements.**

## 6.4 Results

### 6.4.1 Dengue virus serotype 2 (DENV-2) functionalized surface

Figure 6.3 summarizes the sensor responses of the three iterations carried out for each plasma sample. During the injection of plasma samples, a spike in signal was observed due to the exchange of solution from PBS/Gly buffer to the more viscous plasma sample. The gradual increase in power after plasma injection indicates the real time binding of biomaterial to the DENV-2 surface. After 10 min, PBS/Gly buffer was injected to dissociate loosely bound biomaterial. The difference in power measured before and after plasma injection is proportional to the mass of biomaterial bound to the DENV-2 surface. Using Equation 5.1, the surface mass density of bound biomaterial is computed and plotted against time in Figures 6.3 (b, d, f); the zero of surface mass density was set to the baseline level before the injection of plasma (if the power measured after plasma injection equals that before injection, then no additional biomaterial was bound to the surface).

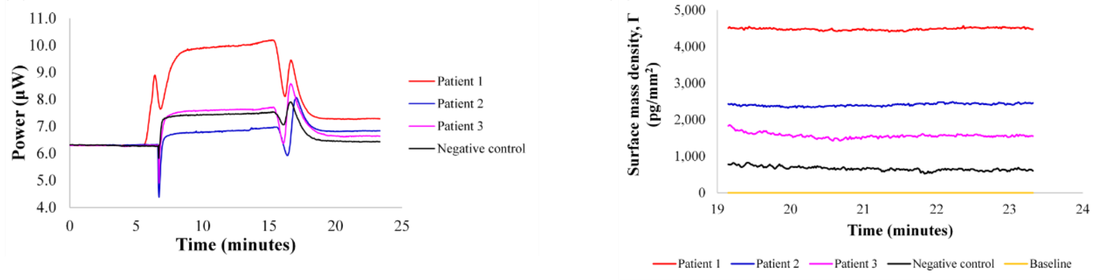
(a) Iteration 1

(b) Iteration 1

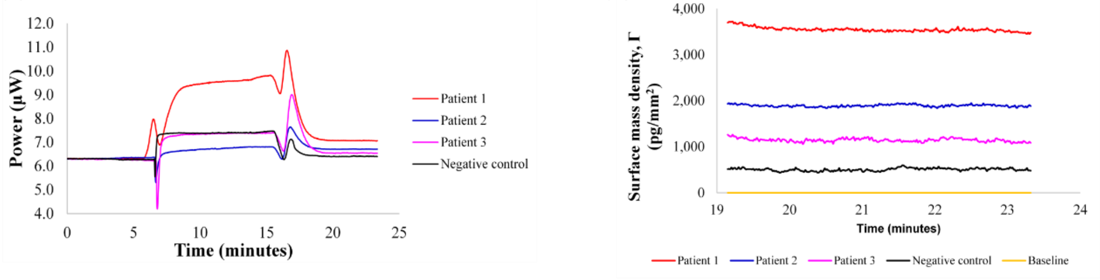
(c) Iteration 2

(d) Iteration 2

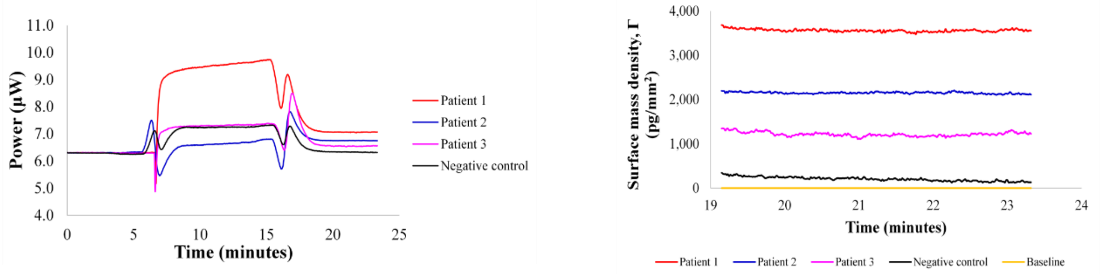
(e) Iteration 3

(f) Iteration 3

**Figure 6.3: Dengue detection using a DENV-2 functionalized surface. (a, c, e) Real-time response data summarized for different plasma samples (patient 1, patient 2, patient 3, and negative control) injected over the DENV-2 surface. (b, d, f) Surface mass density adsorbed onto the sensor surface after plasma injection.**

We observe in Figures 6.3 (b, d, f) the accumulation of mass for the case of the negative control (surface mass density of 663 pg/mm$^2$ in Figure 6.3b). We attribute this accumulation to residual non-specific binding (due to the rather complex composition of plasma), which could not be completely mitigated by the BSA injection in our protocol. The increase in surface mass density for the three patient samples, relative to the negative control, is attributed to the binding of dengue-specific IgM antibody to the DENV-2 surface.

### 6.4.2 Plasma functionalized surface

Figure 6.4 summarizes the sensor responses of the three iterations of DENV-2 injection on each plasma-functionalized sample. Generally, the solution of DENV-2 has a lower refractive index than PBS/Gly buffer which leads to a drop in power level during the solution exchange. As DENV-2 was captured by the dengue-specific IgM antibody on the sensor surface, the signal increased gradually. A new power level was established when PBS/Gly buffer was passed through the flow cell to wash away loosely bound material.  The difference in power measured before and after DENV-2 injection is proportional to the mass of DENV-2 bound to the surface, which in turn is correlated to the actual amount of dengue-specific IgM antibody immobilized on the surface. Using Equation 5.1, the surface mass density of the DENV-2 bound to the plasma surface was computed and plotted over time as Figures 6.4 Figure 6.4 (b, d, f). The surface mass density of the negative control in this case (Figures 6.4 Figure 6.4 (b, d, f)) is about 3 times lower than in the previous case (Figures 6.3 (b, d, f)) indicating less nonspecific binding. The surface mass density on the positive plasma samples is also comparatively lower but not by a factor of 3, implying higher accuracy for this sensing approach.

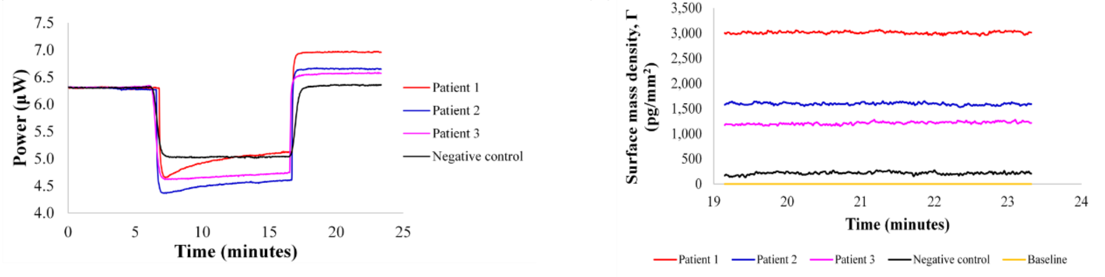
(a) Iteration 1

(b) Iteration 1

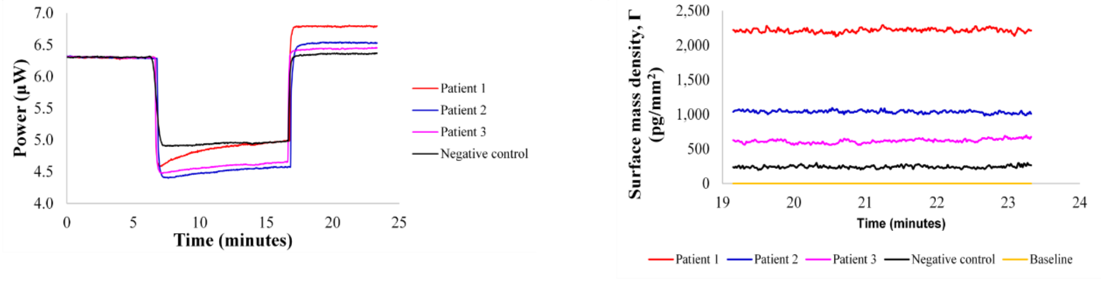
(c) Iteration 2

(d) Iteration 2

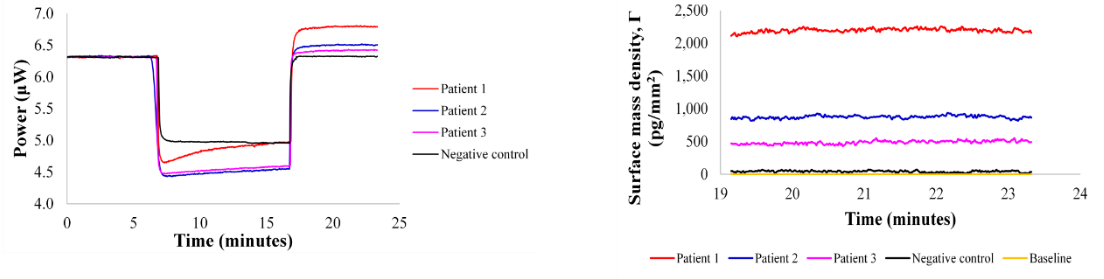
(e) Iteration 3

(f) Iteration 3

**Figure 6.4: Dengue detection using a plasma functionalized surface. (a, c, e) Real-time response data summarized for different plasma samples (patient 1, patient 2, patient 3, and negative control) on the surface, during injection of DENV-2. (b, d, f) Surface mass density adsorbed onto the sensor surface after DENV-2 injection.**

### 6.5 Discussion

In order to evaluate the performance of our approaches, we compare our results with those obtained by MAC-ELISA (Lam, Devi, & Pang, 1987). In an ELISA assay, a positive-to-negative (P/N) ratio in terms of the optical density (OD) values obtained for a patient and a negative sample is generated. The OD (or absorbance) of a sample is a logarithmic ratio of the intensity of light that has passed through the sample to the intensity of the light incident thereon. According to Beer's law, the OD of a sample is proportional to its concentration in solution. A result with a P/N ratio greater than or equal to 2.0 is considered positive. The same figure of merit was applied to our experimental results. The time-averaged surface mass density of a positive sample was divided by the time-averaged value of the negative control to obtain a P/N ratio:

$$P/N = \frac{\langle \Gamma_p \rangle}{\langle \Gamma_n \rangle} \tag{6.1}$$

where $\langle \Gamma_p \rangle$ is the time-averaged surface mass density of the positive sample and $\langle \Gamma_n \rangle$ is the time-averaged surface mass density of the negative control. The P/N ratios of the results using MAC-ELISA and our sensing approaches are summarized in Table 6.1. In general, higher surface mass densities are obtained on the DENV-2 functionalized surface than on a plasma functionalized surface. The plasma functionalized surface is again shown to reduce the nonspecific binding, probably due to the much less complex composition of the DENV-2 solution. Assuming independent and random Gaussian noises for the measurements, the error on the P/N ratio $\sigma_{P/N}$ can be computed as (Taylor, 1997)

$$\sigma_{P/N} = \frac{\langle \Gamma_p \rangle}{\langle \Gamma_n \rangle} \cdot \sqrt{\left(\frac{\sigma_p}{\langle \Gamma_p \rangle}\right)^2 + \left(\frac{\sigma_n}{\langle \Gamma_n \rangle}\right)^2} \tag{6.2}$$

where $\langle \Gamma_p \rangle$ is the time-averaged surface mass density of the positive sample, $\langle \Gamma_n \rangle$ is the time-averaged surface mass density of the negative control, $\sigma_p$ is the error in surface mass density of the positive sample, and $\sigma_n$ is the error in surface mass density of the negative sample. These errors were added to the data in Table 6.1.

The P/N ratios versus iteration number are summarized in **Figure** 6.5 for all patients, as measured using both surface functionalization approaches, and the results obtained using MAC-ELISA are indicated as the horizontal lines, for reference. In general, the P/N ratios obtained using our approaches are comparable to or greater than those obtained from ELISA. The P/N of the third iteration for the plasma functionalized surface is extremely high compared to the previous ones because the surface mass density of the negative control is very close to the baseline level (Figure 6.4f), suggesting very low nonspecific binding in this case.

**Table 6.1: Summary of results in terms of P/N ratio using MAC-ELISA, DENV-2 functionalized surface and plasma functionalized surface.**

| **P/N** | **MAC-ELISA** | **iteration 1** | | **iteration 2** | | **iteration 3** | |
|---|---|---|---|---|---|---|---|
| | | **DENV-2 surface** | **plasma surface** | **DENV-2 surface** | **plasma surface** | **DENV-2 surface** | **plasma surface** |
| **patient 1** | 7.71 | 6.77 ± 0.58 | 13.88 ± 1.67 | 6.99 ± 0.60 | 9.21 ± 1.11 | 17.19 ± 1.63 | 52.83 ± 6.42 |
| **patient 2** | 4.20 | 3.63 ± 0.22 | 7.35 ± 0.57 | 3.74 ± 0.23 | 4.31 ± 0.34 | 10.39 ± 0.71 | 21.02 ± 1.87 |
| **patient 3** | 3.82 | 2.36 ± 0.55 | 5.59 ± 1.77 | 2.26 ± 0.52 | 2.56 ± 0.81 | 5.88 ± 1.38 | 11.71 ± 3.76 |
| **negative control** | 1.00 | 1.00 ± 0.12 | 1.00 ± 0.17 | 1.00 ± 0.08 | 1.00 ± 0.11 | 1.00 ± 0.33 | 1.00 ± 0.45 |

Although the P/N ratios for the DENV-2 functionalized surface are slightly lower than those of MAC-ELISA, a dengue positive result is easily concluded for all positive patients given the small standard deviation of the measured optical output power (σ = 6.3 nW). This functionalization approach has the advantage that sensor surfaces can be prepared in advance and detection of dengue-specific IgM antibody in plasma carried out in a single step. Label-free and real-time single-step detection is promising as a rapid IgM-based dengue diagnostic tool for use at point-of-care.

The second functionalization approach (plasma immobilization) exhibits almost twofold higher P/N ratios compared to the MAC-ELISA results, suggesting improved sensitivity and accuracy over the latter. Although very simple, this approach is probably better-suited to laboratory use given the multiple steps involved, but is still quicker to carry out than MAC-ELISA, significantly reducing the time for dengue virus detection. Furthermore, only a very small amount of plasma (~10 μl) is required, even for repeated measurements to confirm a diagnosis. It is difficult, but not impossible (Vazquez *et al.*, 2005), to identify dengue serotypes through the immunoreaction between dengue virus and dengue-specific antibodies. Thus, there is also a possibility that the same plasma surface can be reused to identify the serotype of dengue virus infection.

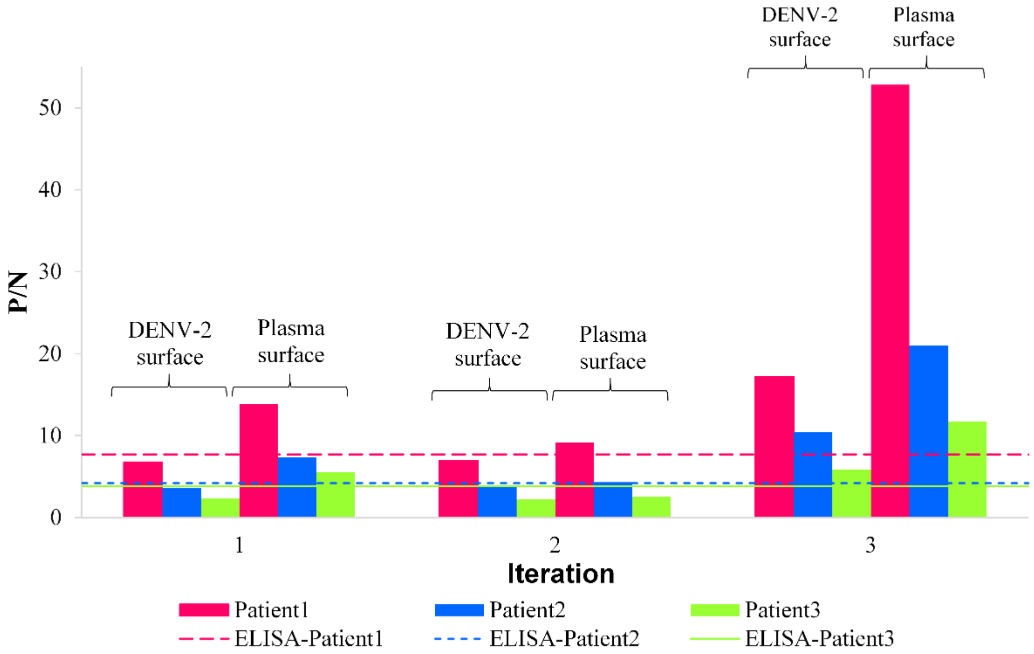

**Figure 6.5: P/N versus iteration number for all patients, measured using MAC-ELISA, DENV-2 functionalized surface, and plasma functionalized surface**

Considering the largest signal change of $\Delta S = 0.66$ μW due the plasma sample of patient 1 using the second surface functionalization approach, the corresponding signal-to-noise ratio ($\Delta S/\sigma$) is ~135. The standard deviation of the surface mass density calculated indicates the detection limit of dengue diagnosis using our setup, which is $\Delta\Gamma$ ~22 pg/mm$^2$. The determination of the detection limit is dependent on the dengue-specific IgM concentration in plasma sample. Therefore, it does not represent the ultimate detection limit of our setup. In fact, we estimated the detection limit of our setup as $\Delta\Gamma$ ~12 pg/mm$^2$ in previous work (Krupin *et al.*, 2013).

## 6.6 Conclusion

The detection of dengue-specific IgM antibody in real-world complex samples of patient blood plasma was demonstrated using long-range surface plasmon waveguides. Two different surface functionalization protocols were presented: immobilized virus or immobilized plasma. The identification of positives by immobilizing virus (and flowing plasma) is almost as conclusive as using MAC-ELISA, whereas the identification of positives by immobilizing plasma (and flowing virus) is more conclusive by a factor of 2. Our proposed approaches can thus be used for the identification of dengue-specific IgM in complex media (plasma), in the presence of background interference (such as nonspecific binding).

In this chapter, original work that has been done includes:

1. Demonstrated the detection of dengue-specific antibodies in patient's blood plasma.
2. Proposed two surface functionalization approaches: a dengue virus serotype 2 (DENV-2) functionalized surface to capture dengue-specific IgM antibody in blood plasma and the reverse, a blood plasma functionalized surface to capture DENV-2.
3. Analysed the detection results in terms of positive-to-negative ratio (P/N) and they are comparable to, or of greater quality, than those collected by MAC-ELISA.

# CHAPTER 7: ANTIGEN-BASED DENGUE DETECTION USING LONG-RANGE SURFACE PLASMON WAVEGUIDES

## 7.1 Introduction

During early stage of dengue infection, dengue-specific antibodies are not found in all patient blood samples. The detection of dengue non-structural 1 (NS1) antigen (one of the non-structural proteins in the dengue virus) in blood samples is another important diagnosis method for dengue infection. This chapter describes the detection of dengue NS1 in clean fluid (pure NS1 glycoprotein in buffer) and in blood plasma using anti-NS1 monoclonal antibody (MAb). Plasma functionalized surface was used during the detection of dengue NS1 antigen in blood plasma to minimize non-specific binding. Using the plasma functionalized surface, both dengue NS1 antigen and dengue-specific antibodies are able to be detected within a single experiment. The results obtained for antigen-based dengue diagnosis agree with those collected by conventional Enzyme Linked Immunosorbent Assay (ELISA).

## 7.2 Literature Review

### 7.2.1 Antigen-based dengue detection

Non-structural 1 (NS1) protein, which is approximately 45 kDa in molecular weight (Allonso, da Silva Rosa, Coelho, da Costa, Nogueira, Bozza, Dos Santos, *et al.*, 2011; Zhao *et al.*, 1987), is secreted from dengue virus infected cells. Dengue serotypes can be identified by using serotype-specific anti-NS1 monoclonal antibody (Ding *et al.*, 2011). Much of the research on biosensors has been done on the detection of purified dengue NS1 antigen in buffer (Camara *et al.*, 2013; Figueiredo *et al.*, 2015; Hu *et al.*, 2013; Mishra, Patel, Kumari, & Mishra, 2014; Silva *et al.*, 2014; Singh, 2012; Su *et al.*, 2003; Tai *et al.*, 2005) or on spiked NS1 antigen in serum samples (Cecchetto, Carvalho, Santos, Fernandes, & Bueno, 2015; Dias *et al.*, 2013; Silva *et al.*, 2014; Yen *et al.*, 2015). The detection of naturally occurring dengue NS1 antigen in serum was reported using electrochemical (I. T. Cavalcanti *et al.*, 2012; Parkash, Yean, & Shueb, 2014), fluorescence (Linares, Pannuti, Kubota, & Thalhammer, 2013) and quart crystal microbalance (Wu *et al.*, 2005) biosensors. The detection of dengue NS1 in blood plasma is more challenging than the detection of dengue-specific antibodies (Wong *et al.*, 2014) because NS1 has a smaller molecular weight and occurs in lower concentration in blood (0.01 – 2 μg/ml (Alcon *et al.*, 2002)).

## 7.3 Methodology

### 7.3.1 Modifications to experimental setup and materials

After a careful study and experiments on the long range surface plasmon based biosensors, a few modifications were made to improve the sensitivity and repeatability of the biosensors. Two adjustments were made before carrying out the experiments in this chapter. First, from the theoretical study in Chapter 4 and the protein sensing experiment in Chapter 5, it was shown that a sensing buffer (PBS/Gly) with higher refractive index will result in higher response for protein binding. The theoretical prediction of the change in insertion loss due to adlayer formation (protein attachment on sensor surface) for different sensing indices is shown in Figure 7.1. The refractive index of the sensing buffer used throughout this chapter was chosen as 1.3388. The sensing index was chosen to be high enough to exhibit sensitive response to protein binding but also to be low enough to be below the cut-off of the mode.

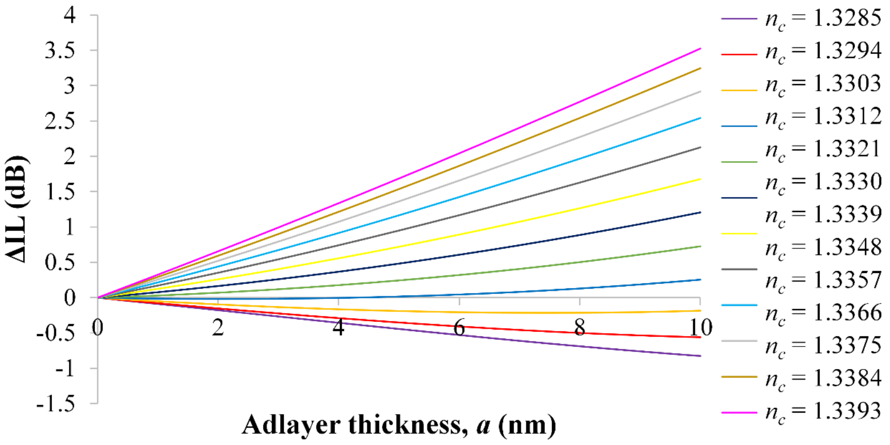

**Figure 7.1: The change in insertion loss ΔIL as a function of the adlayer thickness *a* for different indices of sensing buffer $n_c$. The Au waveguide which is 35 nm thick and 5 µm wide has a sensing channel of 1.65 mm.**

Second, it was observed that the stability of the output power is greatly dependent on the polarization of the input optical fiber. As described in Chapter 5, the input power was initially launched through a cleaved polarization-maintaining optical fiber (PM fiber) held by a fiber chuck. While mechanical force was applied to hold the fiber, any excessive force will introduce pressure to the stress rod in the PM fiber which causes fluctuation in the output power. Hence, to reduce the noise in the measured power and thus lowering the detection limit of the biosensors, a lensed polarization-maintaining optical fiber was used to replace the cleaved PM fiber. The lensed PM fiber (LPF-D1-1300-7/125-P-0.44-1.1-3.2GR,1.4AS-50-3A-1-1, OZ Optics) has similar core and cladding sizes as the cleaved PM fiber (7 µm and 125 µm, respectively) with a collimating lens of 4 mm outer diameter. The lensed PM fiber has a beam of diameter ~ 8 µm when it is placed about 1.2 mm away from the input of the biosensor (verified using beam profiler). Figure 7.2 shows the new biosensing experimental setup.

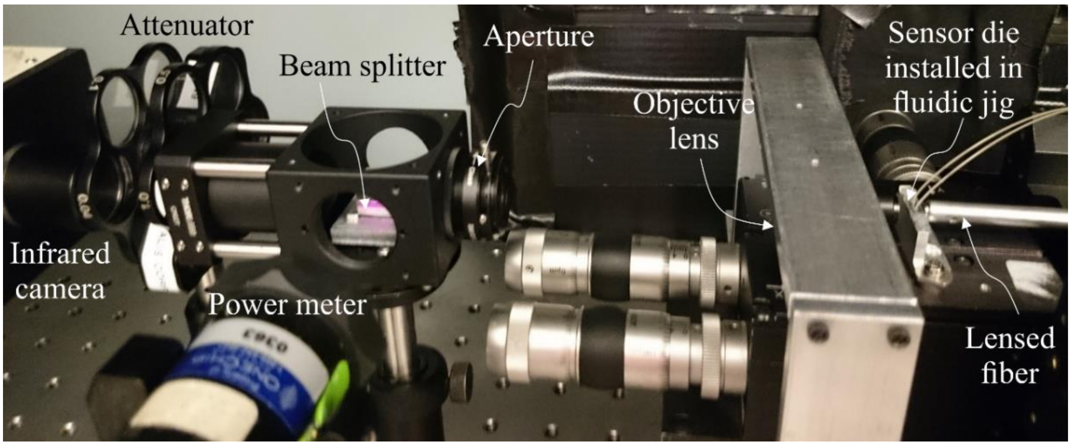

**Figure 7.2: Improved experimental setup for long rang surface plasmon biosensing.**

### 7.3.2 Sensing device

The sensor die used in this chapter (3.5 mm × 6.4 mm) consists of 24 alternating straight waveguides and y-splitters, as shown in Figure 7.3. A straight Au waveguide (~5 μm wide, 35 nm thick) located in the middle of a sensor die was used for all the experiments.

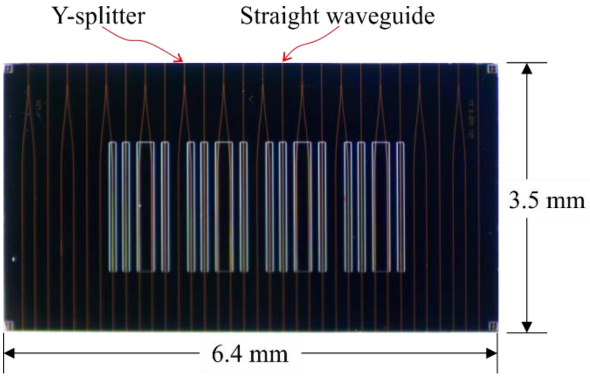

**Figure 7.3: Microscope image of the sensor die used for antigen-based dengue biosensing experiments.**

### 7.3.3 Chemicals and reagents

16-Mercaptohexadecanioc acid (16-MHA), phosphate buffered saline (PBS) 0.01 M, pH 7.4, sodium dodecyl sulfate (SDS), 2-isopropanol semiconductor grade (IPA), and glycerol (electrophoresis grade), N-Hydroxysuccinimide sodium salt (NHS) and 1-ethyl-3-(3-dimethylaminopropyl)carbodiimide hydrochloride, ≥99% (EDC) were obtained from Sigma-Aldrich. Dengue virus anti-NS1 glycoprotein antibody, clone D2N3 was purchased from Vivantis Technologies. Dengue virus NS1 glycoprotein full length protein (ab64456) was purchased from Abcam. Distilled water was deionized using Millipore filtering membranes (Millipore, Milli-Q water system at 16 MΩ cm). The sensing buffer (PBS/Gly, refractive index of 1.3388) and the deionized water were filtered through Millex-GP filters (PES membrane 0.22 μm).

Dengue virus serotype 2 (DENV-2) strain New Guinea C (NGC) and a patient plasma sample laboratory-confirmed as dengue positive (both NS1-positive and IgM-positive) were obtained from the Department of Medical Microbiology, Faculty of Medicine, University of Malaya, Malaysia (Ethical Clearance No. 782.90 from the University Malaya Medical Centre). The plasma sample was collected and tested for dengue using a combination of hemagglutination inhibition (HI), NS1 capture ELISA, IgG capture ELISA and IgM capture ELISA prior to experimentation. Normal human plasma in K3 EDTA (lot no. PLE050412) was purchased from Zen-Bio, Inc. to serve as a negative control. The donor is of U.S. origin, male, African American and 49 years old.

### 7.3.4 Experimental procedures

#### 7.3.4.1 Dengue non-structural 1 (NS1) antigen in clean fluid

Before proceeding to the detection of dengue non-structural 1 (NS1) antigen in patient plasma sample, a biosensing experiment in clean fluid was carried out. Clean fluid refers to the pure biomaterial solution (usually stored in buffer and some preservatives/stabilizers) without any other proteins or antibodies in the background. In this case, dengue virus NS1 full length protein purchased from Abcam was used.

Figure 7.4a illustrates the functionalization process of the clean fluid experiment. The sensor die was cleaned and prepared following a similar process described in Chapter 5. Then, it was immersed in 1 mM 2-isopropanol (IPA) solution of 16-mercaptohexadecanioc acid (16-MHA) overnight before being placed together with the fluidic jig into the experimental setup. After establishing a stable baseline signal with the sensing buffer PBS/Gly, the carboxyl surface was activated by 0.1 M NHS/EDC for 15 min. After washing the surface with PBS/Gly, the dengue NS1 antigen (20 μg/ml) was passed through the fluidic channel to be covalently attached to the sensor surface. Human IgG kappa antibody (10 μg/ml) was first injected over the sensor surface as a negative control and also as a blocking agent of any unreacted site. A slight binding response was observed during the flow of human IgG kappa antibody but the baseline signal was recovered after washing with PBS/Gly. This observation indicates the response was mainly due to the loosely bound antibody on the sensor surface which dissociated after the wash with buffer. When anti-NS1 monoclonal antibody (MAb) was injected, a significant binding response was recorded after the fluid exchange which resulted in the change in baseline signal. In order to regenerate the surface for repeated measurements, the surface was washed with 0.5% SDS in PBS/Gly. The flow of human IgG kappa antibody and anti-NS1 MAb were repeated sequentially.

The sensorgram of the clean fluid experiment is presented in Figure 7.4b. To reduce the consumption of biomaterials, the flow of NHS/EDC, dengue NS1 protein, human IgG kappa antibody, and anti-NS1 MAb were stopped after 5 min of fluid exchange. However, due to the change in pressure during the restarting of the syringe pump, the slope of the binding response curve differs at t ~ 40, 60 and 80 min. After the first wash with SDS, the baseline signal returns to a level which is slightly higher that that after the functionalization of dengue NS1 antigen. This is because some of the loosely bound dengue NS1 antigen on the sensor surface was washed away by SDS. We can also support this explanation through the results plotted in Figure 7.6. The non-specific binding shown by the negative control is slightly higher during the second and third iterations.

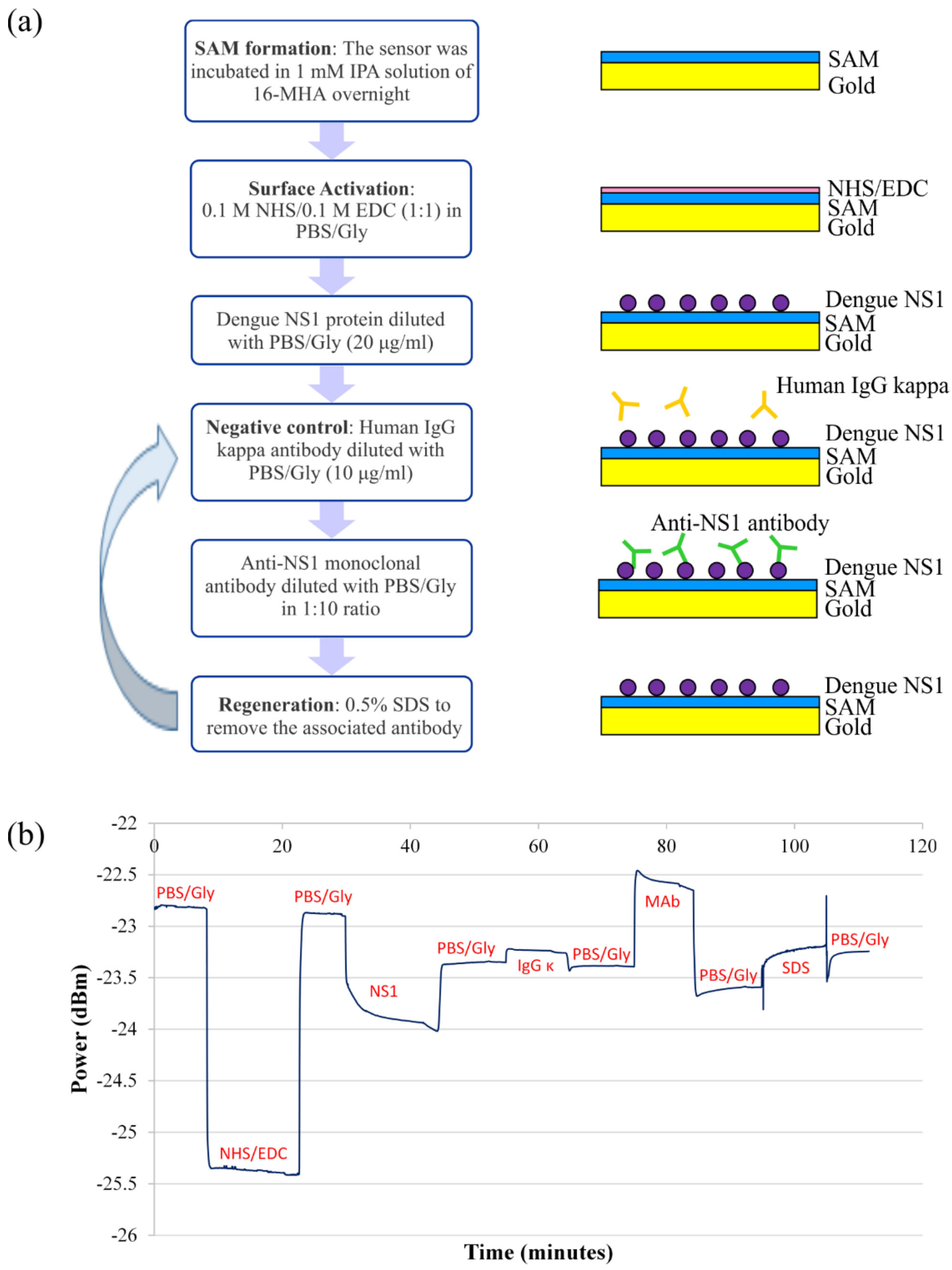

**Figure 7.4: Surface functionalization of Au waveguide with pure dengue NS1 protein. (a) Schematic illustrating the functionalization of the sensor and a sensing run. (b) Real-time measurement showing the immobilization of pure dengue NS1 protein onto the 16-MHA modified Au waveguide through a NHS/EDC reaction followed by the injection of negative control (human IgG kappa) and positive sample (anti-NS1 MAb).**

### 7.3.4.2 Dengue antigen and antibodies detection in blood plasma sample

The detection of dengue NS1 in blood plasma sample is more challenging as compared to the detection of dengue-specific antibodies described in previous chapter. Antibodies (IgG or IgM) are large molecules with molecular weight of hundreds of kilodaltons (kDa) as compared to the NS1 antigen which is 48 kDa in molecular weight (Allonso, da Silva Rosa, Coelho, da Costa, Nogueira, Bozza, Dos Santos, *et al.*, 2011; Zhao *et al.*, 1987).

Similar surface functionalization approach as described in previous section (clean fluid experiment) was applied for the detection of dengue NS1 in blood plasma sample, illustrated in Figure 7.5a. Once the sensor surface was prepared with carboxylated self-assembled monolayer (SAM), the patient blood plasma was immobilized on the surface through amine coupling (using NHS/EDC). Anti-NS1 monoclonal antibody (MAb) was injected to recognise any possible NS1 antigen that might exist in the blood plasma. 0.5% SDS in PBS/Gly was passed through the fluidic channel to regenerate the plasma functionalized surface for repeated measurements. Besides, the regenerated surface can also be used for the detection of dengue-specific antibodies by injecting the dengue virus (will be discussed later). Figure 7.5b presents the sensorgram of the biosensing experiment for the detection of dengue NS1 antigen in blood plasma sample.

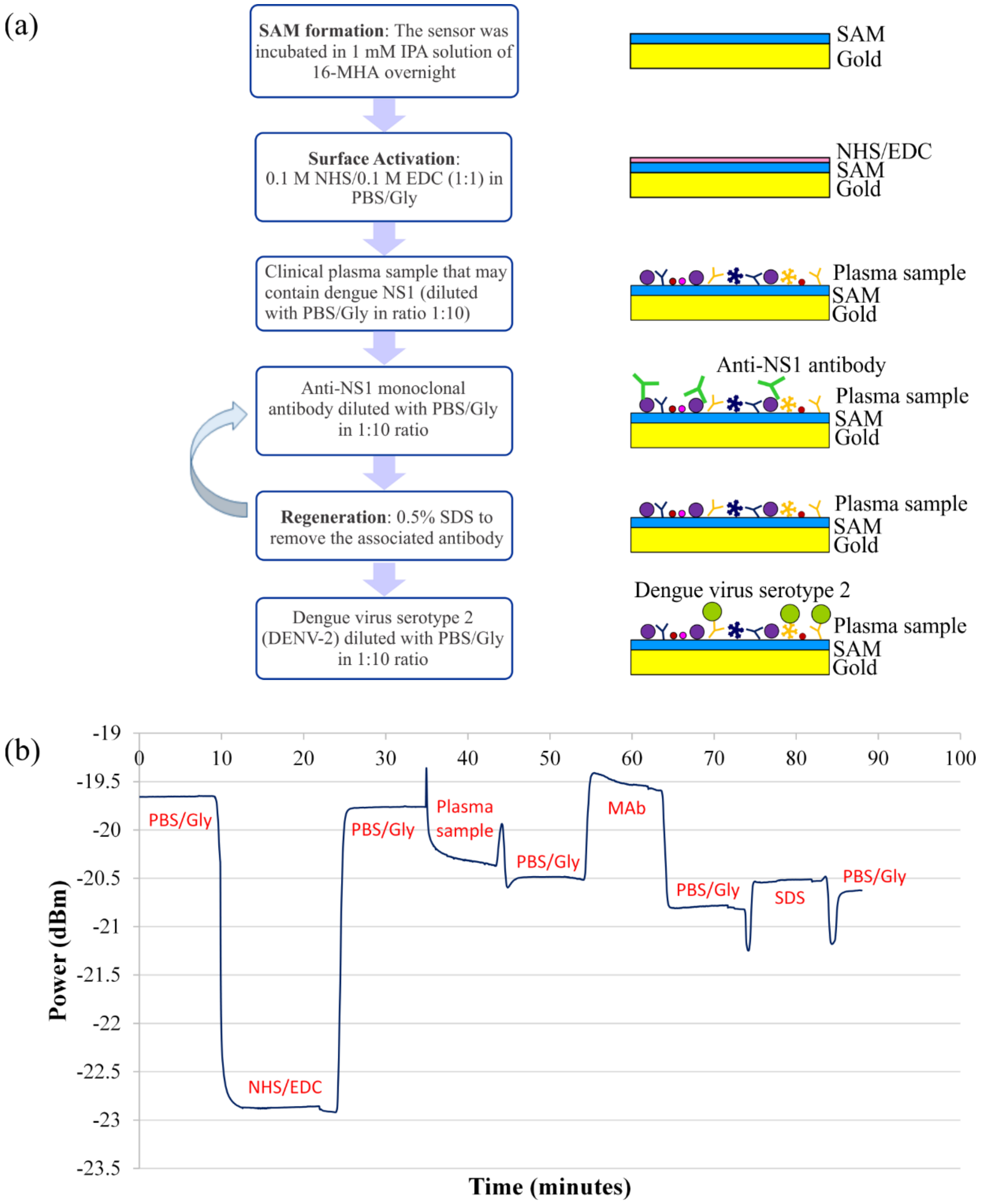

**Figure 7.5: Surface functionalization of Au waveguide with a plasma sample. (a) Schematic illustrating the functionalization of the sensor and a sensing run. (b) Real-time measurement showing the immobilization of a plasma sample onto the 16-MHA modified Au waveguide through a NHS/EDC reaction, followed by the injection and capture of anti-NS1 MAb by dengue NS1 antigen on the surface.**

After three repeated measurements were obtained for the detection of dengue NS1 antigen in plasma samples, the plasma functionalized surface was again regenerated using 0.5% SDS. Instead of anti-NS1 MAb, dengue virus serotype 2 (DENV-2) was injected over the surface (Figure 7.5a). The envelope (E) protein in DENV-2 will recognize the presence of dengue-specific antibodies in the plasma samples. This serological-based biosensing experiment has been previously described in details in Chapter 6. In this section, the experiment was carried out to demonstrate that it is possible on a plasma functionalized surface to detect both the dengue NS1 antigen and dengue-specific antibodies within a single experiment.

## 7.4 Results

### 7.4.1 Dengue non-structural 1 (NS1) antigen in clean fluid

The measurements obtained for the detection of NS1 antigen in clean fluid were summarized in Figure 7.6. From Figure 7.6a, we can clearly differentiate the change in power level due to the binding of anti-NS1 MAb to the dengue NS1 antigen immobilized on the waveguide, as compared to the negative control. The measured power (in μW) was normalized by considering the baseline signal before the injection of analyte (human IgG kappa antibody or anti-NS1 MAb) to be equal to 1. As discussed in Chapter 4, for sensing buffer with refractive index above CYTOP, the waveguide becomes more asymmetric during adlayer growth and thus having lower output power after the binding of analyte. We also analysed the surface mass density of the biomaterials bound to the dengue NS1 antigen surface by using Equation 5.1 and $k_2$ value calculated from Chapter 5. The surface mass density over time for the clean fluid experiment is plotted in Figure 7.6b. The zero of surface mass density was set to the baseline level before the injection of analyte. Despite the low non-specific binding for the negative control, the binding of the anti-NS1 MAb to the dengue NS1 antigen immobilised on the waveguide is relatively consistent among the iterations.

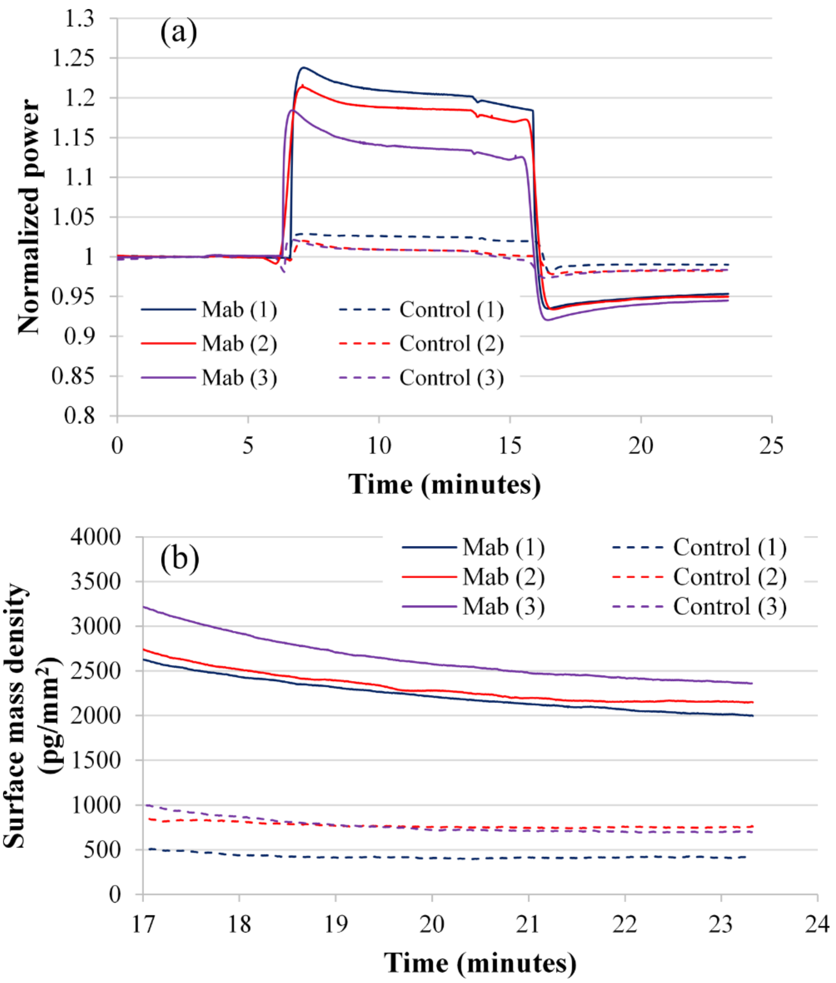

**Figure 7.6: Detection of dengue NS1 antigen in clean fluid. (a) Real-time normalized response data during injection of anti-NS1 MAb and human IgG kappa as a negative control (control). The number in parentheses indicates the iteration number. (b) Surface mass density adsorbed onto the sensor surface after injection of anti-NS1 MAb and human IgG kappa (control) (the zero was set to the baseline level before injection).**

### 7.4.2 Dengue detection in blood plasma sample

#### 7.4.2.1 Dengue non-structural 1 (NS1) antigen

Figure 7.7 summarizes the sensor responses for the detection of dengue NS1 antigen carried out for positive and negative plasma samples. The binding between the dengue NS1 antigen in blood plasma and the dengue anti-NS1 MAb is reflected through the difference in power measured before and after MAb injection, shown in Figure 7.7a. The mass of anti-NS1 MAb bound to the plasma functionalized surface corresponds to the amount of dengue NS1 antigen present in the blood plasma. From the surface mass density plot in Figure 7.7b, the non-specific binding shown by the negative plasma sample is higher than that by the negative control in the clean fluid experiment due to the complex composition of the plasma samples. However, the presence of dengue NS1 antigen in plasma samples is distinguishable based on the calculated surface mass density. After every surface regeneration with SDS, the mass density of the bound biomaterials increases which is possibly due to the removal of some loosely bound material on the sensor surface (Dutra *et al.*, 2007). Nevertheless, the sensor produced consistent results which easily differentiate the positive and negative samples.

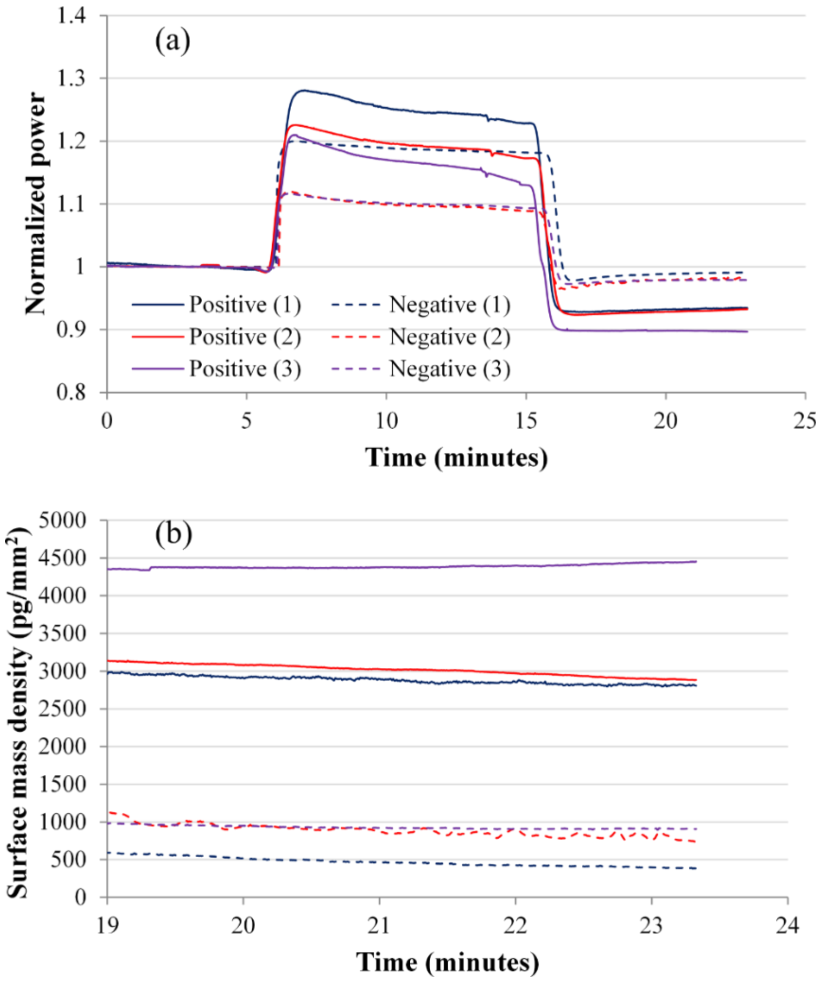

**Figure 7.7: Detection of dengue NS1 antigen in blood plasma. (a) Real-time normalized response data summarized for positive and negative plasma samples on the surface, during injection of anti-NS1 MAb. The number in parentheses indicates the iteration number. (b) Surface mass density adsorbed onto the sensor surface after anti-NS1 MAb injection (the zero was set to the baseline level before injection).**

#### 7.4.2.2 Dengue-specific antibodies (serological detection)

Figure 7.8 shows the measured power and the corresponding surface mass density for the detection of dengue-specific antibodies in positive and negative plasma samples. The difference in power measured before and after DENV-2 injection is proportional to the mass of DENV-2 bound to the surface, which in turn is correlated to the actual amount of dengue-specific antibodies immobilized thereon.

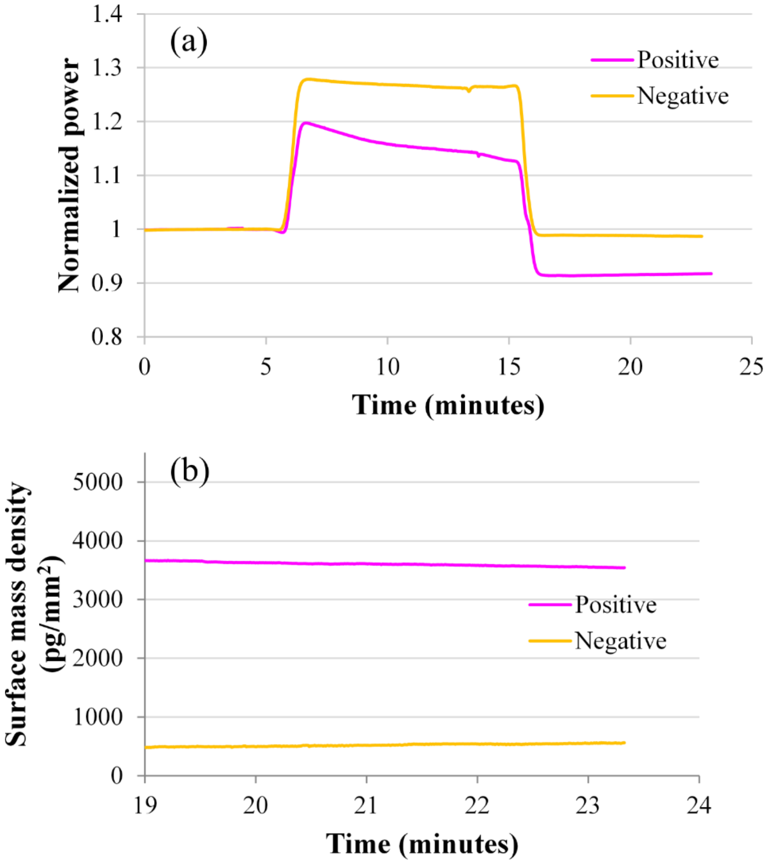

**Figure 7.8: Detection of dengue-specific antibodies in blood plasma. (a) Real-time response data summarized for positive and negative plasma samples on the surface, during injection of DENV-2. (b) Surface mass density adsorbed onto the sensor surface after DENV-2 injection (the zero was set to the baseline level before injection).**

### 7.5 Discussion

We evaluated dengue biosensing experimental results through a positive-to-negative (P/N) ratio in Chapter 6. Similar figure of merit was applied to analyse the results in this chapter. The time-averaged surface mass density from all measurements were used for the result analysis. Table 7.1 summarizes the P/N ratios for all the results obtained in this chapter. The detection method in ELISA assay where a P/N ratio greater than or equal to 2.0 is considered positive agrees very well with our results. A dengue positive result is easily concluded from the calculation in Table 7.1.

**Table 7.1: Summary of results in terms of P/N ratio for detection of dengue NS1 antigen in clean fluid and detection of dengue NS1 antigen and dengue-specific antibodies in plasma sample.**

| | **Detection Approach** | **ELISA** | **Iteration 1** | **Iteration 2** | **Iteration 3** |
|---|---|---|---|---|---|
| **Clean fluid** | Dengue NS1 antigen | - | 4.98 ± 0.12 | 2.90 ± 0.03 | 3.44 ± 0.06 |
| **Plasma sample** | Dengue NS1 antigen | Positive | 6.69 ± 0.39 | 3.55 ± 0.19 | 4.83 ± 0.04 |
| | Dengue-specific antibodies | Positive | 6.65 ± 0.15 | - | - |

The baseline noise observed during the experiments varies from 0.2 nW to 13.6 nW with a typical value of 3 nW. The variation in σ is mostly due to a slight misalignment of the input fibre in our setup, which can easily be corrected. The largest signal-to-noise ratio (ΔS/σ) is found to be 356. The lowest detection limit of our setup in terms of surface mass density is estimated as 5.73 pg/mm$^2$ (for $\Delta S/\sigma = 1$).

## 7.6 Conclusion

The detection of dengue NS1 antigen has been demonstrated in both clean fluid and blood plasma. Using plasma functionalized surface, the sensor surface can be used to detect both the dengue NS1 antigen and antibodies by regenerating the surface with SDS wash. Although the positive-to-negative ratio of our results is not as high as those measured using ELISA, our biosensor is able to identify the dengue NS1 antigen in clinical plasma samples with high reliability and in real-time.

In this chapter, original work that has been done includes:

1. Demonstrated the detection of purified dengue NS1 antigen in clean fluid (buffer).
2. Demonstrated the detection of natural-occurring dengue NS1 antigen in patient’s blood plasma.
3. Analysed the detection results in terms of positive-to-negative ratio (P/N) and they agree with those collected by ELISA.

# CHAPTER 8: CONCLUSION AND FUTURE WORK

The main findings related to the research objectives are summarised in this chapter. General conclusions are drawn based on the findings and the strengths and limitations of the work done throughout this thesis are discussed. Furthermore, a few suggestions for future research are also presented.

## 8.1 Conclusion

This study aimed to develop a compact, cost-effective, label-free, and real-time biosensor for dengue diagnosis, which can lead to affordable, point-of-care detection of dengue fever. The research is focused on the design, fabrication, characterization and implementation of long range surface plasmon polariton (LRSPP) based waveguides to achieve these requirements.

To improve the overall sensitivity of dengue diagnosis through the detection of both dengue antigen and antibodies, several passive structures using the LRSPP based waveguide were designed for simultaneous biosensing. Finite element method (FEM) was applied to model the designed structures in order to ensure the LRSPP mode is well-confined, non-radiative, and with acceptable losses. The sensing gold stripe waveguides embedded in CYTOP (a fluoropolymer having a refractive index close to that of biologically compatible fluids) were fabricated on a 4-inch silicon wafer using photolithography technique. In order to produce sensing structures with designed dimensions, the fabrication process was optimized through the manipulation of the fabrication variables (such as the bake time, exposure time, and develop time of photoresists).

The surface sensitivity of straight LRSPP waveguides was investigated by considering sensing fluids of refractive index slightly below, equal to, and slightly above that of

CYTOP, the material used as the claddings. The sensor performance was optimized through maximizing $|K|$ where $K = (\partial\alpha_s/\partial a)/\alpha_s$ and selecting the optimal sensing length as $L_{opt} = 1/(2\alpha_s)$. Optimal designs were predicted to produce very compelling detection limits of $\Delta\Gamma_{\mathrm{min}} < 0.1$ pg mm$^{-2}$. A linear model for the sensitivity of the sensing channel was proposed and its applicability was demonstrated over a wide range of designs.

A typical waveguide alignment system was set up to launch light operating at wavelength $\lambda_0 = 1310$ nm through a polarization-maintaining (PM) optical fiber into the sensor as propagating LRSPPs. The straight LRSPP waveguide was characterized through cutback measurements to estimate the insertion loss and the measurements agreed well with the theoretical computations. Through proper butt-coupling between the input fibre and the waveguide, a baseline signal with standard deviation in output power as low as 1.4 nW was achieved. Different refractive indices of PBS/Gly solutions were injected over the LRSPP waveguide to observe its response towards bulk changes. During the bulk experiment, the fluid exchange time of the fluidic system was determined to be ~ 1.5 minutes. The ability of straight LRSPP waveguides to perform protein sensing was demonstrated through the BSA physisorption on carboxyl-terminated surface.

The detection of dengue-specific IgM antibody in real-world complex samples of patient blood plasma using long-range surface plasmon waveguides was demonstrated through two different surface functionalization protocols: immobilized virus or immobilized plasma. The identification of positives by immobilizing virus (and flowing plasma) is almost as conclusive as using conventional MAC-ELISA method, whereas the identification of positives by immobilizing plasma (and flowing virus) is more conclusive by a factor of 2. The plasma functionalized surface was found to minimize the background interference (such as nonspecific binding) in complex media (plasma), thus improving the sensitivity and accuracy of the test. The reuse of the biosensors by regenerating the sensing surface down to the virus (or antibody) level or down to the bare Au was also presented.

The straight long-range surface plasmon waveguides were also used to detect the dengue NS1 antigen, another biomarker for dengue diagnosis. The detection of NS1 antigen was carried out both in clean fluid (pure NS1 protein in buffer) and complex blood plasma sample. The positives can be clearly identified from the negative controls and the results for plasma samples agree with those obtained from ELISA. The plasma functionalized surface was demonstrated to be able to detect both dengue NS1 antigen and dengue-specific antibodies within a single experiment.

In short, the objectives of this thesis were achieved where the long range surface plasmon based biosensor was demonstrated to be a promising tool for rapid dengue diagnosis. The comparison of the work in this thesis with recent literature of dengue biosensor is summarized in Table 8.1. To simplify the comparison, the work chosen for comparison is mostly using clinical blood samples. Although more clinical trials and engineering problems need to be solved before this biosensor can be introduced for point-of-care diagnosis, it has a great potential to provide a competitive (low-cost, compact, user-friendly) solution to the major health problem. Besides, the sensor and functionalization approaches presented can likely be applied to improve the diagnosis of other virus-induced infections.

**Table 8.1: Comparison of the work done in this thesis with recent literature.**

| Author(s) | Solution | Detection target | Transduction mechanism | Label-free? | Real-time? | Amount of solution required | Assay time | Detection limit (LOD) |
|---|---|---|---|---|---|---|---|---|
| Fang, Tan, Tse, & Ooi, 2010 | Clinical serum | Antibodies | Electrochemical | √ | X | - | 2 hours | 50,000 dilutions |
| Lee, Lien, Lei, & Lee, 2009 | Clinical serum | | Fluorescence | X | X | 100 µL | 30 mins | 21 pg |
| Jahanshahi *et al.*, 2014 | Clinical serum | | Surface plasmon | √ | √ | 1 µL | 30 mins | - |
| **Wong *et al.*, 2014** | **Clinical plasma** | | **Surface plasmon** | √ | √ | **10 µL or less** | **30 mins** | **22 pg mm$^{-2}$** |
| Camara *et al.*, 2013 | Buffer | NS1 | Surface plasmon | √ | X | - | 1 hour | 0.074 µg mL$^{-1}$ |
| Silva *et al.*, 2014 | Spike serum | | Electrochemical | X | X | - | 1 hour | 0.035 µg mL$^{-1}$ |
| Yen *et al.*, 2015 | Spike serum | | Lateral flow chromatography | √ | √ | - | - | 150 ng mL$^{-1}$ |
| Wu *et al.*, 2005 | Clinical serum | | Quartz crystal microbalance | √ | √ | 1 mL | - | 0.740 µg mL$^{-1}$ |
| **Wong *et al.*, 2015** | **Clinical plasma** | | **Surface plasmon** | √ | √ | **10 µL or less** | **30 mins** | **5.73 pg mm$^{-2}$** |

## 8.2 Future Work

### 8.2.1 Clinical verification and other tests of dengue diagnosis

In order to verify the sensitivity and repeatability of our biosensor for clinical use, a larger size of patient blood samples have to be tested. My colleague, Peyman Jahanshahi has shown that the commercial surface plasmon resonance (SPR) instrument, BIAcore 3000 is able to detect dengue serologically with 30 positive samples (Jahanshahi *et al.*, 2014). Similar experiments has to be conducted for our long range surface plamon based biosensor. The numbers of false positive and false negative have to be considered to determine the reliability of the biosensor. The specificity of the biosensor has to be deduced from the cross-reaction of dengue with other flaviviruses (e.g. West Nile, Yellow Fever) and other illnesses.

Besides identifying the positives and negatives from the patient samples, biosensing experiments can be done to identify dengue serotypes and to differentiate primary and secondary infection. The serotype of dengue infection can be identified through the immunoreaction between dengue virus and dengue-specific antibodies. By quantifying the amount of dengue-specific IgM and IgG in the plasma samples, primary or secondary dengue infection can be concluded. All this information will be helpful and allows proper management and treatment of the illness.

### 8.2.2 Different sensing structures

#### 8.2.2.1 Side-access fluidic channel

As described in Section 3.4.1.2, biosensors with side-access fluidic channels were designed and fabricated. An example of such sensor die is shown in Figure 8.1. With side-access channels, two independent solutions can be passed through the waveguides at the same time where simultaneous biosensing is possible. However, the fluidic assembly for the sensor die with side-access fluidic channels are more challenging. Figure 8.2

shows the parts for the side-access fluidic jig. Currently, the fluidic jig is still unable to provide good seal at both sides for fluid exchange. More mechanical modifications have to be done so that the jig is user-friendly.

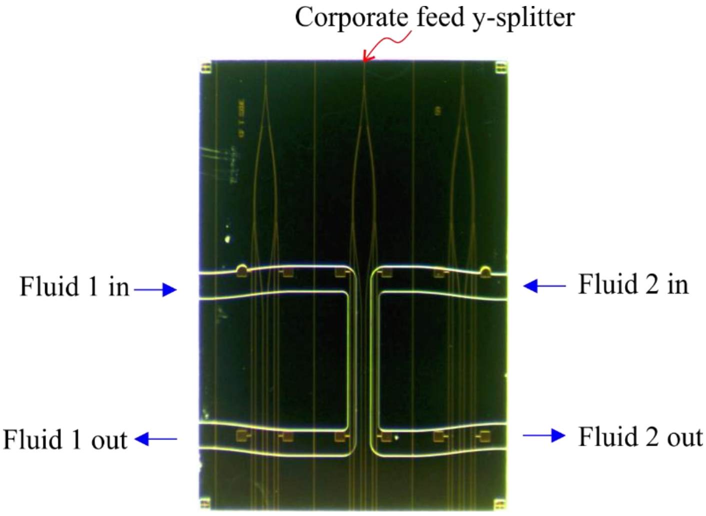

**Figure 8.1: Microscope image of next-generation long-range surface plasmon based dengue biosensor which has corporate feed y-splitter waveguides and side-access fluidic channels.**

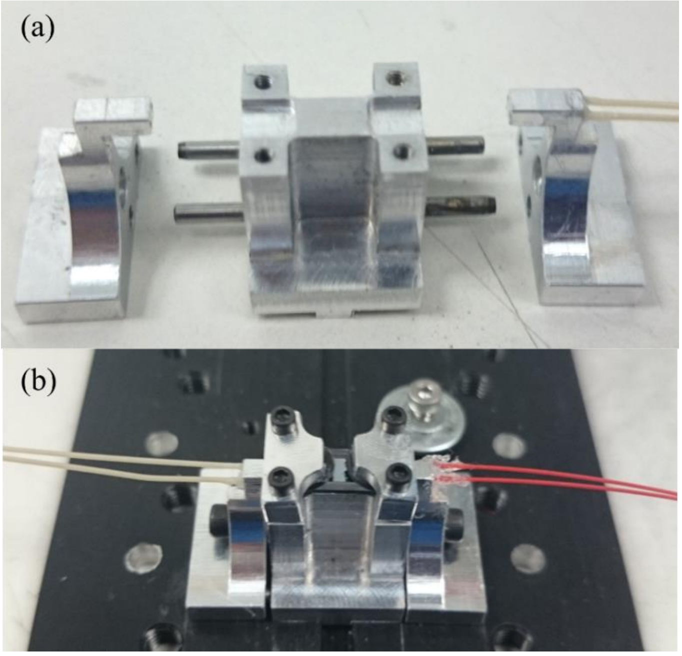

**Figure 8.2: The fluidic jig for LRSPP biosensor with side-access fluidic channels (a) before and (b) after assembly.**

#### 8.2.2.2 Different designs of optical structures

In this thesis, biosensing experiments were demonstrated only with straight LRSPP waveguides. Further characterization and biosensing experiments of other designed structures have to be performed. For those structures with a reference waveguide, the instability and noise in the output signal can be eliminated and the biosensor is expected to have lower detection limit. Mach-Zehnder interferometers and Young's interferometer which are based on phase interrogation will be demonstrated to be more sensitive biosensors.

#### 8.2.2.3 Multilayer bottom cladding

The current fabrication process is limited by the glass transition temperature of CYTOP. Since CYTOP has a glass transition temperature of 108 °C, the baking temperature of the top cladding is limited to 100 °C to avoid the deformation of gold structures. As a result, there is still a small amount of solvent trapped in the top CYTOP cladding and it is not cured hard enough where sometimes too much force on the fluidic jig will destroy the gold waveguide.

One of the solutions to overcome the problems caused by CYTOP is to replace the bottom cladding with multilayer structure (1-dimensional photonic crystal structure). Figure 8.3 shows the proposed biosensor structure with the bottom cladding composed of alternating silica ($SiO_2$) and tantalum pentoxide ($Ta_2O_5$). The structure was designed and modelled theoretically with the help of Dr Marco Liscidini and his student, Matteo Menotti from University of Pavia, Italy. Chromium (Cr) is used as the adhesion layer between the Au waveguide and the $SiO_2$ layer. Using FEM, the field distribution of the vertical transverse electric field component, Re{$E_y$} of the LRSPP supported by this new structure is given in Figure 8.4. Besides having slightly higher propagation loss, the waveguides supported by this new structure are expected to perform similarly as the typical LRSPP waveguides with CYTOP claddings.

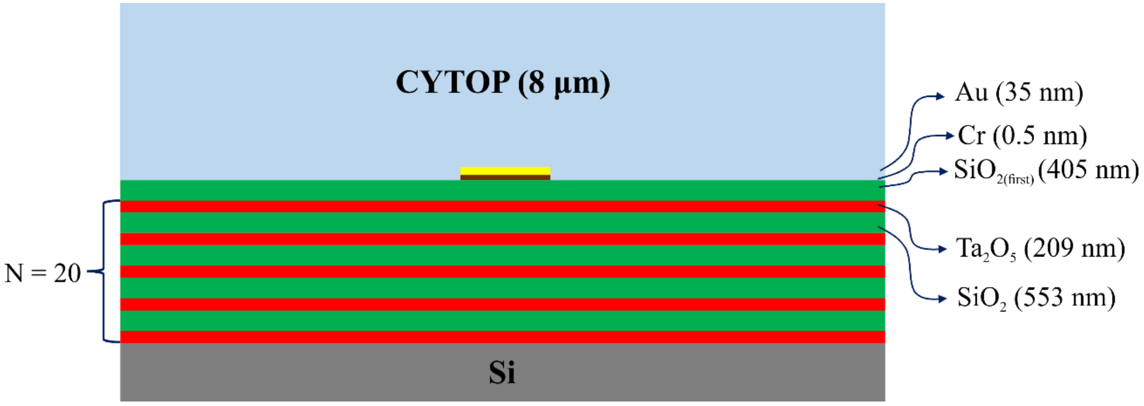

**Figure 8.3: Schematic illustration of the LRSPP waveguide structure with multilayer bottom cladding.**

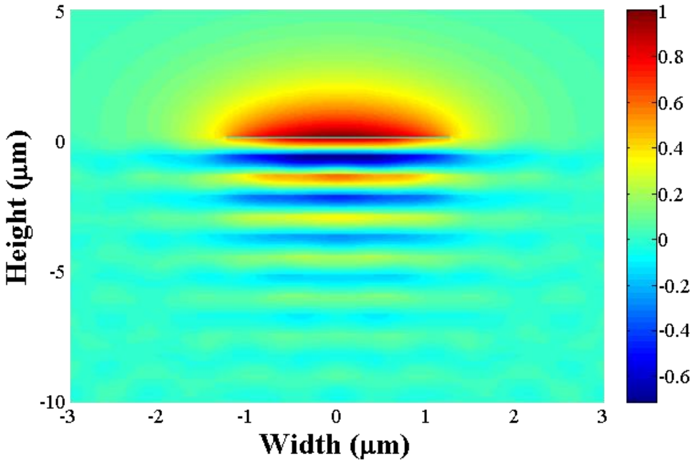

**Figure 8.4: The transverse electric field distribution, Re{Ey} of the LRSPP along a waveguide with *w* = 5 µm. The thicknesses of gold (Au) and chromium (Cr) are 35 nm and 0.5 nm, respectively.**

Two major problems from current biosensor can be solved using this multilayer bottom cladding. First, the top CYTOP cladding can be baked at higher temperature (> 108 °C) to ensure all solvents are evaporated and the claddings are fully cured. Second, the over-etching problem (Au waveguide located on CYTOP pedestal) during the introduction of fluidic channel can be avoided. With the new structure, the bottom cladding will not be etched by the oxygen plasma etcher and the fluidic channel depth does not require precise control of the etch time.

# REFERENCES

Adam, P., Piliarik, M., Šípová, H., Špringer, T., Vala, M., & Homola, J. (2012). Surface plasmons for biodetection. In G. Xiao & W. J. Bock (Eds.), *Photonic sensing: Principles and applications for safety and security monitoring* (pp. 1-58). New Jersey: John Wiley & Sons.

AGC Chemicals. (2009). CYTOP: Amorphous fluoropolymer (pp. 1-18). Tokyo, Japan: Asahi Glass.

Alcon, S., Talarmin, A., Debruyne, M., Falconar, A., Deubel, V., & Flamand, M. (2002). Enzyme-linked immunosorbent assay specific to dengue virus type 1 nonstructural protein NS1 reveals circulation of the antigen in the blood during the acute phase of disease in patients experiencing primary or secondary infections. *Journal of Clinical Microbiology, 40*(2), 376-381.

Allonso, D., da Silva Rosa, M., Coelho, D. R., da Costa, S. M., Nogueira, R. M. R., Bozza, F. A., . . . Mohana-Borges, R. (2011). Polyclonal antibodies against properly folded dengue virus NS1 protein expressed in E. coli enable sensitive and early dengue diagnosis. *Journal of Virological Methods, 175*(1), 109-116.

Allonso, D., da Silva Rosa, M., Coelho, D. R., da Costa, S. M., Nogueira, R. M. R., Bozza, F. A., . . . Mohana-Borges, R. (2011). Polyclonal antibodies against properly folded dengue virus NS1 protein expressed in E. coli enable sensitive and early dengue diagnosis. *Journal of Virological Methods, 175*(1), 109-116. doi: http://dx.doi.org/10.1016/j.jviromet.2011.04.029

Andrade, C. A., Oliveira, M. D., De Melo, C. P., Coelho, L. C., Correia, M. T., Nogueira, M. L., . . . Zeng, X. (2011). Diagnosis of dengue infection using a modified gold electrode with hybrid organic–inorganic nanocomposite and *bauhinia monandra* lectin. *Journal of Colloid and Interface Science, 362*(2), 517-523.

Asahi Glass. (2009). CYTOP technical brochure. from https://www.agc.com

Asiri, H. (2012). *Fabrication of surface plasmon biosensors in Cytop.* (Master's thesis), University of Ottawa, Ottawa, Canada. Available from https://www.ruor.uottawa.ca/handle/10393/23286

Atias, D., Liebes, Y., Chalifa-Caspi, V., Bremand, L., Lobel, L., Marks, R. S., & Dussart, P. (2009). Chemiluminescent optical fiber immunosensor for the detection of IgM antibody to dengue virus in humans. *Sensors and Actuators B: Chemical, 140*(1), 206-215.

Avelino, K., Andrade, C., de Melo, C., Nogueira, M., Correia, M., Coelho, L., & Oliveira, M. (2014). Biosensor based on hybrid nanocomposite and CramoLL lectin for detection of dengue glycoproteins in real samples. *Synthetic Metals, 194,* 102-108.

Avramis, V. I., Avramis, E. V., Hunter, W., & Long, M. C. (2009). Immunogenicity of native or pegylated E. coli and erwinia asparaginases assessed by ELISA and surface plasmon resonance (spr-biacore) assays of IgG antibodies (ab) in sera from patients with acute lymphoblastic leukemia (all). *Anticancer Research, 29*(1), 299-302.

Aytur, T., Foley, J., Anwar, M., Boser, B., Harris, E., & Beatty, P. R. (2006). A novel magnetic bead bioassay platform using a microchip-based sensor for infectious disease diagnosis. *Journal of Immunological Methods, 314*(1), 21-29.

Baeumner, A. J., Schlesinger, N. A., Slutzki, N. S., Romano, J., Lee, E. M., & Montagna, R. A. (2002). Biosensor for dengue virus detection: Sensitive, rapid, and serotype specific. *Analytical Chemistry, 74*(6), 1442-1448.

Bain, C. D., Troughton, E. B., Tao, Y. T., Evall, J., Whitesides, G. M., & Nuzzo, R. G. (1989). Formation of monolayer films by the spontaneous assembly of organic thiols from solution onto gold. *Journal of the American Chemical Society, 111*(1), 321-335.

Beatty, M. E., Stone, A., Fitzsimons, D. W., Hanna, J. N., Lam, S. K., Vong, S., . . . Letson, G. W. (2010). Best practices in dengue surveillance: A report from the Asia-Pacific and Americas dengue prevention boards. *PLoS Neglected Tropical Diseases, 4*(11), e890.

Berini, P. (1999). Plasmon polariton modes guided by a metal film of finite width. *Optics Letters, 24*(15), 1011-1013.

Berini, P. (2001). Plasmon-polariton waves guided by thin lossy metal films of finite width: Bound modes of asymmetric structures. *Physical Review B, 63*(12), 125417.

Berini, P. (2008). Bulk and surface sensitivities of surface plasmon waveguides. *New Journal of Physics, 10*(10), 105010.

Berini, P. (2009). Long-range surface plasmon polaritons. *Advances in Optics and Photonics, 1*(3), 484-588.

Berini, P., & Buckley, R. (2009). On the convergence and accuracy of numerical mode computations of surface plasmon waveguides. *Journal of Computational and Theoretical Nanoscience, 6*(9), 2040-2053.

Berini, P., Charbonneau, R., Lahoud, N., & Mattiussi, G. (2005). Characterization of long-range surface-plasmon-polariton waveguides. *Journal of Applied Physics, 98*(4), 043109. doi: http://dx.doi.org/10.1063/1.2008385

Berini, P., & Lu, J. (2006). Curved long-range surface plasmon-polariton waveguides. *Optics Express, 14*(6), 2365-2371.

Bhatt, S., Gething, P. W., Brady, O. J., Messina, J. P., Farlow, A. W., Moyes, C. L., . . . Sankoh, O. (2013). The global distribution and burden of dengue. *Nature, 496*, 504-507.

Bjorkholm, J. E. (1998). EUV lithography—the successor to optical lithography? *Intel Technology Journal, 3*, 98.

Blacksell, S. D., Jarman, R. G., Bailey, M. S., Tanganuchitcharnchai, A., Jenjaroen, K., Gibbons, R. V., . . . Lalloo, D. G. (2011). Evaluation of six commercial point-of-care tests for diagnosis of acute dengue infections: The need for combining NS1 antigen and IgM/IgG antibody detection to achieve acceptable levels of accuracy. *Clinical and Vaccine Immunology, 18*(12), 2095-2101.

Boltasseva, A., Nikolajsen, T., Leosson, K., Kjaer, K., Larsen, M. S., & Bozhevolnyi, S. I. (2005). Integrated optical components utilizing long-range surface plasmon polaritons. *Journal of Lightwave Technology, 23*(1), 413-422.

Bozhevolnyi, S. I., Volkov, V. S., Devaux, E., Laluet, J.-Y., & Ebbesen, T. W. (2006). Channel plasmon subwavelength waveguide components including interferometers and ring resonators. *Nature, 440*(7083), 508-511.

Breukelaar, I., Charbonneau, R., & Berini, P. (2006). Long-range surface plasmon-polariton mode cutoff and radiation in embedded strip waveguides. *Journal of Applied Physics, 100*(4), 043104. doi: http://dx.doi.org/10.1063/1.2244479

Buckman, A. B. (1992). *Guided-wave photonics*: Saunders College Pub.

Butler, J., Ni, L., Nessler, R., Joshi, K., Suter, M., Rosenberg, B., . . . Cantarero, L. (1992). The physical and functional behavior of capture antibodies adsorbed on polystyrene. *Journal of Immunological Methods, 150*(1), 77-90.

Camara, A. R., Gouvêa, P. M., Dias, A. C., Braga, A., Dutra, R. F., de Araujo, R. E., & Carvalho, I. (2013). Dengue immunoassay with an LSPR fiber optic sensor. *Optics Express*, *21*(22), 27023-27031.

Campbell, S. A. (1996). The science and engineering of microelectronic fabrication: Oxford University Press, USA.

Cavalcanti, I., Silva, B., Peres, N., Moura, P., Sotomayor, M., Guedes, M., & Dutra, R. (2012). A disposable chitosan-modified carbon fiber electrode for dengue virus envelope protein detection. *Talanta, 91*, 41-46.

Cavalcanti, I. T., Guedes, M. I., Sotomayor, M. D., Yamanaka, H., & Dutra, R. F. (2012). A label-free immunosensor based on recordable compact disk chip for early diagnostic of the dengue virus infection. *Biochemical Engineering Journal, 67*, 225-230.

Cecchetto, J., Carvalho, F. C., Santos, A., Fernandes, F. C., & Bueno, P. R. (2015). An impedimetric biosensor to test neat serum for dengue diagnosis. *Sensors and Actuators B: Chemical, 213*, 150-154.

Chang, W.-S., Shang, H., Perera, R. M., Lok, S.-m., Sedlak, D., Kuhn, R. J., & Lee, G. U. (2008). Rapid detection of dengue virus in serum using magnetic separation and fluorescence detection. *Analyst, 133*(2), 233-240.

Charbonneau, R., Scales, C., Breukelaar, I., Fafard, S., Lahoud, N., Mattiussi, G., & Berini, P. (2006). Passive integrated optics elements based on long-range surface plasmon polaritons. *Journal of Lightwave Technology, 24*(1), 477.

Chen, S.-H., Chuang, Y.-C., Lu, Y.-C., Lin, H.-C., Yang, Y.-L., & Lin, C.-S. (2009). A method of layer-by-layer gold nanoparticle hybridization in a quartz crystal microbalance DNA sensing system used to detect dengue virus. *Nanotechnology, 20*(21), 215501.

Cheng, M. S., Ho, J. S., Tan, C. H., Wong, J. P. S., Ng, L. C., & Toh, C.-S. (2012). Development of an electrochemical membrane-based nanobiosensor for ultrasensitive detection of dengue virus. *Analytica Chimica Acta, 725*, 74-80.

Chiu, C. (2009). *Fabrication of surface plasmon waveguide devices in CYTOP with microfluidic channels.* (Master's thesis), University of Ottawa, Ottawa, Canada. Available from https://www.ruor.uottawa.ca/handle/10393/28516

Chiu, C., Lisicka-Skrzek, E., Tait, R. N., & Berini, P. (2010). Fabrication of surface plasmon waveguides and devices in Cytop with integrated microfluidic channels. *Journal of Vacuum Science & Technology B, 28*(4), 729-735.

Clark, L. C. (1956). Monitor and control of blood and tissue oxygen tensions. *ASAIO Journal, 2*(1), 41-48.

COMSOL Multiphysics. (2012). Comsol multiphysics user guide (version 4.3 a).

Darwish, N. T., Alias, Y. B., & Khor, S. M. (2015). An introduction to dengue-disease diagnostics. *TrAC Trends in Analytical Chemistry, 67*, 45-55.

Daviau, R., Khan, A., Lisicka-Skrzek, E., Tait, R. N., & Berini, P. (2010). Fabrication of surface plasmon waveguides and integrated components on Cytop. *Microelectronic Engineering, 87*(10), 1914-1921.

Daviau, R., Lisicka-Skrzek, E., Tait, R. N., & Berini, P. (2009). Broadside excitation of surface plasmon waveguides on Cytop. *Applied Physics Letters, 94*(9), 091114.

De Feijter, J. A., Benjamins, J., & Veer, F. A. (1978). Ellipsometry as a tool to study the adsorption behavior of synthetic and biopolymers at the air–water interface. *Biopolymers, 17*(7), 1759-1772. doi: 10.1002/bip.1978.360170711

Degiron, A., Cho, S.-Y., Tyler, T., Jokerst, N. M., & Smith, D. R. (2009). Directional coupling between dielectric and long-range plasmon waveguides. *New Journal of Physics, 11*(1), 015002.

Deng, J., & Toh, C.-S. (2013). Impedimetric DNA biosensor based on a nanoporous alumina membrane for the detection of the specific oligonucleotide sequence of dengue virus. *Sensors, 13*(6), 7774-7785.

Dhatt, G., Lefrançois, E., & Touzot, G. (2012). *Finite element method*: John Wiley & Sons.

Dias, A. C., Gomes-Filho, S. L., Silva, M., & Dutra, R. F. (2013). A sensor tip based on carbon nanotube-ink printed electrode for the dengue virus NS1 protein. *Biosensors and Bioelectronics, 44*, 216-221.

Ding, X., Hu, D., Chen, Y., Di, B., Jin, J., Pan, Y., . . . Wang, M. (2011). Full serotype- and group-specific NS1 capture enzyme-linked immunosorbent assay for rapid differential diagnosis of dengue virus infection. *Clinical and Vaccine Immunology, 18*(3), 430-434.

Director General of Health. (2015). Situasi semasa deman denggi di Malaysia [Press release]. Retrieved from http://www.moh.gov.my/index.php/database_stores/attach_download/337/621

Ditlbacher, H., Krenn, J., Schider, G., Leitner, A., & Aussenegg, F. (2002). Two-dimensional optics with surface plasmon polaritons. *Applied Physics Letters, 81*(10), 1762-1764.

Dostálek, J., Kasry, A., & Knoll, W. (2007). Long range surface plasmons for observation of biomolecular binding events at metallic surfaces. *Plasmonics, 2*(3), 97-106.

Drezet, A., Hohenau, A., Stepanov, A. L., Ditlbacher, H., Steinberger, B., Aussenegg, F. R., . . . Krenn, J. R. (2006). Surface plasmon polariton mach–zehnder interferometer and oscillation fringes. *Plasmonics, 1*(2-4), 141-145.

Dubois, L. H., & Nuzzo, R. G. (1992). Synthesis, structure, and properties of model organic surfaces. *Annual review of physical chemistry, 43*(1), 437-463.

DuPont. Teflon® AF properties. from http://www.dupont.com/

Durandet, A., Perry, A., Boswell, R., Ladouceur, F., Love, J., Faith, M., . . . Austin, M. (1996). Silica buried channel waveguides fabricated at low temperature using pecvd. *Electronics Letters, 32*(4), 326-327.

Dutra, R. F., Mendes, R. K., Lins da Silva, V., & Kubota, L. T. (2007). Surface plasmon resonance immunosensor for human cardiac troponin T based on self-assembled monolayer. *Journal of Pharmaceutical and Biomedical Analysis, 43*(5), 1744-1750.

Fan, H., Buckley, R., & Berini, P. (2012). Passive long-range surface plasmon-polariton devices in Cytop. *Applied Optics, 51*(10), 1459-1467.

Fan, H., Charbonneau, R., & Berini, P. (2014). Long-range surface plasmon triple-output Mach-Zehnder interferometers. *Optics Express, 22*(4), 4006-4020.

Fan, H., Lisicka-Skrzek, E., & Berini, P. (2011). *Measurement of long-range surface plasmon-polariton devices in Cytop.* Paper presented at the Photonics North 2011.

Fang, X., Tan, O. K., Tse, M. S., & Ooi, E. E. (2010). A label-free immunosensor for diagnosis of dengue infection with simple electrical measurements. *Biosensors and Bioelectronics, 25*(5), 1137-1142.

Fenter, P., Eisenberger, P., Li, J., Camillone III, N., Bernasek, S., Scoles, G., . . . Liang, K. (1991). Structure of octadecyl thiol self-assembled on the silver (111) surface: An incommensurate monolayer. *Langmuir, 7*(10), 2013-2016.

Figueiredo, A., Vieira, N. C., Dos Santos, J. F., Janegitz, B. C., Aoki, S. M., Junior, P. P., . . . Guimarães, F. E. (2015). Electrical detection of dengue biomarker using egg yolk immunoglobulin as the biological recognition element. *Scientific reports, 5*.

Frei, W. (2013). Solutions to linear systems of equations: Direct and iterative solvers. Retrieved from http://www.comsol.com/blogs/solutions-linear-systems-equations-direct-iterative-solvers/

Gerald, C. F., & Wheatley, P. O. (1994). *Applied numerical analysis* (5th ed.). Reading, MA: Addison-Wesley Publishing Company.

Gomara, M., Ercilla, G., Alsina, M., & Haro, I. (2000). Assessment of synthetic peptides for hepatitis a diagnosis using biosensor technology. *Journal of Immunological Methods*, *246*(1), 13-24.

Gubler, D. J. (1998). Dengue and dengue hemorrhagic fever. *Clinical Microbiology Reviews, 11*(3), 480-496.

Gubler, D. J. (2002). Epidemic dengue/dengue hemorrhagic fever as a public health, social and economic problem in the 21st century. *Trends in Microbiology, 10*(2), 100-103.

Gubler, D. J., & Meltzer, M. (1999). Impact of dengue/dengue hemorrhagic fever on the developing world. *Advances in Virus Research, 53*, 35-70.

Guo, J., Keathley, P. D., & Hastings, J. (2008). Dual-mode surface-plasmon-resonance sensors using angular interrogation. *Optics Letters*, *33*(5), 512-514.

Guzman, M. G., Halstead, S. B., Artsob, H., Buchy, P., Farrar, J., Gubler, D. J., . . . Martínez, E. (2010). Dengue: A continuing global threat. *Nature Reviews Microbiology, 8*, S7-S16.

Guzman, M. G., Jaenisch, T., Gaczkowski, R., Hang, V. T. T., Sekaran, S. D., Kroeger, A., . . . Mercado, J. C. (2010). Multi-country evaluation of the sensitivity and specificity of two commercially-available NS1 ELISA assays for dengue diagnosis. *PLoS Neglected Tropical Diseases, 4*(8), e811.

Halstead, S. B. (1988). Pathogenesis of dengue: Challenges to molecular biology. *Science, 239*(4839), 476-481.

Hermanson, G. T. (2013). Chapter 4 - zero-length crosslinkers. In G. T. Hermanson (Ed.), *Bioconjugate techniques (third edition)* (pp. 259-273). Boston: Academic Press.

Holmlin, R. E., Chen, X., Chapman, R. G., Takayama, S., & Whitesides, G. M. (2001). Zwitterionic SAMs that resist nonspecific adsorption of protein from aqueous buffer. *Langmuir, 17*(9), 2841-2850.

Homola, J. (2008). Surface plasmon resonance sensors for detection of chemical and biological species. *Chemical Reviews*, *108*(2), 462-493.

Homola, J., Vaisocherová, H., Dostálek, J., & Piliarik, M. (2005). Multi-analyte surface plasmon resonance biosensing. *Methods, 37*(1), 26-36.

Hosseini, S., Ibrahim, F., Rothan, H. A., Yusof, R., van der Marel, C., Djordjevic, I., & Koole, L. H. (2015). Aging effect and antibody immobilization on cooh exposed surfaces designed for dengue virus detection. *Biochemical Engineering Journal, 99*, 183-192.

Hu, D., Fry, S. R., Huang, J. X., Ding, X., Qiu, L., Pan, Y., . . . Buechler, J. (2013). Comparison of surface plasmon resonance, resonant waveguide grating biosensing and enzyme linked immunosorbent assay (ELISA) in the evaluation of a dengue virus immunoassay. *Biosensors, 3*(3), 297-311.

Huang, M. C., Mateus, C. F., Foley, J. E., Beatty, R., Cunningham, B. T., & Chang-Hasnain, C. J. (2008). VCSEL optoelectronic biosensor for detection of infectious diseases. *IEEE Photonics Technology Letters, 20*(6), 443-445.

Hunsperger, E. A., Yoksan, S., Buchy, P., Nguyen, V. C., Sekaran, S. D., Enria, D. A., . . . Drebot, M. (2009). Evaluation of commercially available anti–dengue virus immunoglobulin m tests. *Emerging Infectious Diseases, 15*(3), 436.

Hunsperger, R. G. (1984). *Integrated optics: Theory and technology* (Vol. 2): Springer.

Jahanshahi, P., Zalnezhad, E., Sekaran, S. D., & Adikan, F. R. M. (2014). Rapid immunoglobulin M-based dengue diagnostic test using surface plasmon resonance biosensor. *Scientific Reports, 4*(3851). doi: 10.1038/srep03851

Jetté-Charbonneau, S., Charbonneau, R., Lahoud, N., Mattiussi, G., & Berini, P. (2005). Demonstration of Bragg gratings based on long-ranging surface plasmon polariton waveguides. *Optics Express, 13*(12), 4674-4682.

Jin, J.-M. (2014). The finite element method in electromagnetics: John Wiley & Sons.

Joo, Y. H., Song, S. H., & Magnusson, R. (2010). Demonstration of long-range surface plasmon-polariton waveguide sensors with asymmetric double-electrode structures. *Applied Physics Letters, 97*(20), 201105.

Jorgenson, R., & Yee, S. (1993). A fiber-optic chemical sensor based on surface plasmon resonance. *Sensors and Actuators B: Chemical, 12*(3), 213-220.

Kawachi, M. (1996). Recent progress in silica-based planar lightwave circuits on silicon. *IEE Proceedings-Optoelectronics, 143*(5), 257-262.

Kelly, K. L., Coronado, E., Zhao, L. L., & Schatz, G. C. (2003). The optical properties of metal nanoparticles: The influence of size, shape, and dielectric environment. *The Journal of Physical Chemistry B, 107*(3), 668-677.

Khan, A., Chiu, C., Lisicka-Skrzek, E., Tait, R. N., & Berini, P. (2010). *Characterization of biosensing waveguides on Cytop.* Paper presented at the Photonics North.

Khan, A., Krupin, O., Lisicka-Skrzek, E., & Berini, P. (2011). Sensing of bacteria immobilised under static conditions using long-range surface plasmon waveguides in Cytop. Paper presented at the Photonics North.

Khan, A., Krupin, O., Lisicka-Skrzek, E., & Berini, P. (2013). Mach-Zehnder refractometric sensor using long-range surface plasmon waveguides. *Applied Physics Letters, 103*(11), 111108.

Kim, D., & Herr, A. E. (2013). Protein immobilization techniques for microfluidic assays. *Biomicrofluidics, 7*(4), 041501.

Klar, T., Perner, M., Grosse, S., Von Plessen, G., Spirkl, W., & Feldmann, J. (1998). Surface-plasmon resonances in single metallic nanoparticles. *Physical Review Letters, 80*(19), 4249.

Kottmann, J., Martin, O., Smith, D., & Schultz, S. (2000). Spectral response of plasmon resonant nanoparticles with a non-regular shape. *Optics Express, 6*(11), 213-219.

Kretschmann, E. (1971). Determination of optical constants of metals by excitation of surface plasmons. *Zeitschrift für Physik, 241*(4), 313.

Krupin, O., Asiri, H., Wang, C., Tait, R. N., & Berini, P. (2013). Biosensing using straight long-range surface plasmon waveguides. *Optics Express, 21*(1), 698-709.

Krupin, O., Wang, C., & Berini, P. (2014). Selective capture of human red blood cells based on blood group using long-range surface plasmon waveguides. *Biosensors and Bioelectronics, 53*, 117-122.

Kuhn, R. J., Zhang, W., Rossmann, M. G., Pletnev, S. V., Corver, J., Lenches, E., . . . Strauss, J. H. (2002). Structure of dengue virus. Retrieved June 23, 2014, from Protein Data Bank http://www.rcsb.org/pdb/explore/explore.do?structureId=1K4R

Kumbhat, S., Sharma, K., Gehlot, R., Solanki, A., & Joshi, V. (2010). Surface plasmon resonance based immunosensor for serological diagnosis of dengue virus infection. *Journal of Pharmaceutical and Biomedical Analysis, 52*(2), 255-259.

Kwakye, S., Goral, V. N., & Baeumner, A. J. (2006). Electrochemical microfluidic biosensor for nucleic acid detection with integrated minipotentiostat. *Biosensors and Bioelectronics, 21*(12), 2217-2223.

Lam, S., Devi, S., & Pang, T. (1987). Detection of specific IgM in dengue infection. *Southeast Asian Journal of Tropical Medicine and Public Health, 18*(4), 532-538.

Lavers, C., & Wilkinson, J. (1994). A waveguide-coupled surface-plasmon sensor for an aqueous environment. *Sensors and Actuators B: Chemical, 22*(1), 75-81.

Law, J. W.-F., Ab Mutalib, N.-S., Chan, K.-G., & Lee, L.-H. (2014). Rapid methods for the detection of foodborne bacterial pathogens: Principles, applications, advantages and limitations. *Frontiers in Microbiology, 5*.

Lee Han, L., Vasan, S., Birgelen, L., Murtola, T., Gong, H., Field, R. W., . . . Murad, S. (2010). Immediate cost of dengue to Malaysia and thailand: An estimate.

Lee, Y.-F., Lien, K.-Y., Lei, H.-Y., & Lee, G.-B. (2009). An integrated microfluidic system for rapid diagnosis of dengue virus infection. *Biosensors and Bioelectronics, 25*(4), 745-752.

Liedberg, B., Nylander, C., & Lunström, I. (1983). Surface plasmon resonance for gas detection and biosensing. *Sensors and Actuators, 4*(0), 299-304. doi: http://dx.doi.org/10.1016/0250-6874(83)85036-7

Linares, E. M., Pannuti, C. S., Kubota, L. T., & Thalhammer, S. (2013). Immunospot assay based on fluorescent nanoparticles for dengue fever detection. *Biosensors and Bioelectronics, 41*, 180-185.

Liu, G.-R., & Quek, S. S. (2013). *The finite element method: A practical course*: Butterworth-Heinemann.

Löfas, S., & Mcwhirter, A. (2006). The art of immobilization for spr sensors *Surface plasmon resonance based sensors* (pp. 117-151): Springer.

Love, J. C., Estroff, L. A., Kriebel, J. K., Nuzzo, R. G., & Whitesides, G. M. (2005). Self-assembled monolayers of thiolates on metals as a form of nanotechnology. *Chemical Reviews, 105*(4), 1103-1170.

Lum, L. C., Suaya, J. A., Tan, L. H., Sah, B. K., & Shepard, D. S. (2008). Quality of life of dengue patients. *The American journal of tropical medicine and hygiene, 78*(6), 862-867.

Luna, D., Oliveira, M. D., Nogueira, M. L., & Andrade, C. A. (2014). Biosensor based on lectin and lipid membranes for detection of serum glycoproteins in infected patients with dengue. *Chemistry and Physics of Lipids, 180*, 7-14.

Mack, C. (2008). Fundamental principles of optical lithography: The science of microfabrication: John Wiley & Sons.

Mandal, S., Akhmechet, R., Chen, L., Nugen, S., Baeumner, A., & Erickson, D. (2007). *Nanoscale optofluidic sensor arrays for dengue virus detection.* Paper presented at the NanoScience+ Engineering.

Mateus, C. F., Huang, M. C., Parekh, D., Chang-Hasnain, C. J., Foley, J. E., Lim, W., . . . Cunningham, B. (2004). *Ultra sensitive and compact VCSEL-based biosensor for detection of protein interactions and dengue antibodies.* Paper presented at the Biophotonics/Optical Interconnects and VLSI Photonics/WBM Microcavities, 2004 Digest of the LEOS Summer Topical Meetings.

Matsumura, T., Stollar, V., & Schlesinger, R. W. (1971). Studies on the nature of dengue viruses: V. Structure and development of dengue virus in vero cells. *Virology, 46*(2), 344-355.

McIsaac, P. (1975). Symmetry-induced modal characteristics of uniform waveguides-i: Summary of results. *Microwave Theory and Techniques, IEEE Transactions on, 23*(5), 421-429.

MicroChem Corp. (2002). Nano PMGI resists. http://www.first.ethz.ch/infrastructure/Chemicals/Ebeam_lithography/Data_PMGI.pdf

Mishra, V., Patel, P., Kumari, S., & Mishra, G. (2014). Dengue NS1 detection used chemically modified porous silicon microcavity (psmc). *Silicon*, 1-7.

Montenegro, J.-M., Grazu, V., Sukhanova, A., Agarwal, S., Jesus, M., Nabiev, I., . . . Parak, W. J. (2013). Controlled antibody/(bio-) conjugation of inorganic nanoparticles for targeted delivery. *Advanced Drug Delivery Reviews, 65*(5), 677-688.

Motesharei, K., & Myles, D. C. (1998). Molecular recognition on functionalized self-assembled monolayers of alkanethiols on gold. *Journal of the American Chemical Society, 120*(29), 7328-7336.

Mouvet, C., Harris, R., Maciag, C., Luff, B., Wilkinson, J., Piehler, J., . . . Ismail, G. (1997). Determination of simazine in water samples by waveguide surface plasmon resonance. *Analytica Chimica Acta, 338*(1), 109-117.

Mrksich, M., & Whitesides, G. M. (1995). Patterning self-assembled monolayers using microcontact printing: A new technology for biosensors? *Trends in Biotechnology, 13*(6), 228-235.

Mrksich, M., & Whitesides, G. M. (1996). Foodborne pathogens and diseaseusing self-assembled monolayers to understand the interactions of man-made surfaces with proteins and cells. *Annual Review of Biophysics and Biomolecular Structure, 25*(1), 55-78.

Nagel, T., Gajovic-Eichelmann, N., Tobisch, S., Schulte-Spechtel, U., & Bier, F. F. (2008). Serodiagnosis of lyme borreliosis infection using surface plasmon resonance. *Clinica Chimica Acta, 394*(1), 110-113.

Nascimento, H. P., Oliveira, M. D., de Melo, C. P., Silva, G. J., Cordeiro, M. T., & Andrade, C. A. (2011). An impedimetric biosensor for detection of dengue serotype at picomolar concentration based on gold nanoparticles-polyaniline hybrid composites. *Colloids and Surfaces B: Biointerfaces, 86*(2), 414-419.

Nguyen, B. T. T., Gan, V. C. H., Leo, Y. S., Finkc, K., & Toha, C.-S. (2013). *Electrochemical identification of unlabelled virus using a capture-and-probe strategy with a nanoporous membrane sensor*. India: World Health Organization South-East Asia Region.

Nguyen, B. T. T., Peh, A. E. K., Chee, C. Y. L., Fink, K., Chow, V. T., Ng, M. M., & Toh, C.-S. (2012). Electrochemical impedance spectroscopy characterization of nanoporous alumina dengue virus biosensor. *Bioelectrochemistry, 88*, 15-21.

Nikishkov, G. (2004). Introduction to the finite element method. *University of Aizu*.

Nuzzo, R. G., & Allara, D. L. (1983). Adsorption of bifunctional organic disulfides on gold surfaces. *Journal of the American Chemical Society, 105*(13), 4481-4483.

Ohtsu, M. (2006). Progress in nano-electro-optics v: Springer.

Oliveira, M. D., Correia, M. T., & Diniz, F. B. (2009). A novel approach to classify serum glycoproteins from patients infected by dengue using electrochemical impedance spectroscopy analysis. *Synthetic Metals, 159*(21), 2162-2164.

Oliveira, M. D., Nogueira, M. L., Correia, M. T., Coelho, L. C., & Andrade, C. A. (2011). Detection of dengue virus serotypes on the surface of gold electrode based on *cratylia mollis* lectin affinity. *Sensors and Actuators B: Chemical, 155*(2), 789-795.

Otto, A. (1968). Excitation of nonradiative surface plasma waves in silver by the method of frustrated total reflection. *Zeitschrift für Physik, 216*(4), 398-410.

Palik, E. D. (1998). *Handbook of optical constants of solids* (Vol. 3): Academic Press.

Parkash, O., Yean, C. Y., & Shueb, R. H. (2014). Screen printed carbon electrode based electrochemical immunosensor for the detection of dengue NS1 antigen. *Diagnostics, 4*(4), 165-180.

Pease, R. F., & Chou, S. Y. (2008). Lithography and other patterning techniques for future electronics. *Proceedings of the IEEE, 96*(2), 248-270.

Peeling, R. W., Artsob, H., Pelegrino, J. L., Buchy, P., Cardosa, M. J., Devi, S., . . . Guzman, M. G. (2010). Evaluation of diagnostic tests: Dengue. *Nature Reviews: Microbiology, 8,* S30-S37.

Peh, A. E. K., & Li, S. F. Y. (2013). Dengue virus detection using impedance measured across nanoporous aluminamembrane. *Biosensors and Bioelectronics, 42,* 391-396.

Porter, M. D., Bright, T. B., Allara, D. L., & Chidsey, C. E. (1987). Spontaneously organized molecular assemblies. 4. Structural characterization of n-alkyl thiol monolayers on gold by optical ellipsometry, infrared spectroscopy, and electrochemistry. *Journal of the American Chemical Society, 109*(12), 3559-3568.

Rai, V., Hapuarachchi, H. C., Ng, L. C., Soh, S. H., Leo, Y. S., & Toh, C.-S. (2012). Ultrasensitive cDNA detection of dengue virus RNA using electrochemical nanoporous membrane-based biosensor. *PloS One, 7*(8), e42346.

Rathakrishnan, A., & Sekaran, S. D. (2013). New development in the diagnosis of dengue infections. *Expert Opinion on Medical Diagnostics, 7*(1), 99-112.

Rechberger, W., Hohenau, A., Leitner, A., Krenn, J., Lamprecht, B., & Aussenegg, F. (2003). Optical properties of two interacting gold nanoparticles. *Optics Communications, 220*(1), 137-141.

Ribeiro Teles, F. R., França dos Prazeres, D. M., & de Lima-Filho, J. L. (2007). Electrochemical detection of a dengue-related oligonucleotide sequence using ferrocenium as a hybridization indicator. *Sensors, 7*(11), 2510-2518.

Rigau-Pérez, J. G., Clark, G. G., Gubler, D. J., Reiter, P., Sanders, E. J., & Vance Vorndam, A. (1998). Dengue and dengue haemorrhagic fever. *Lancet, 352*(9132), 971-977.

Rodriguez‐Emmenegger, C., Brynda, E., Riedel, T., Houska, M., Šubr, V., Alles, A. B., . . . Huck, W. T. (2011). Polymer brushes showing non‐fouling in blood plasma challenge the currently accepted design of protein resistant surfaces. *Macromolecular Rapid Communications, 32*(13), 952-957.

Ronot-Trioli, C., Trouillet, A., Veillas, C., & Gagnaire, H. (1996). Monochromatic excitation of surface plasmon resonance in an optical-fibre refractive-index sensor. *Sensors and Actuators A: Physical, 54*(1), 589-593.

Rusmini, F., Zhong, Z., & Feijen, J. (2007). Protein immobilization strategies for protein biochips. *Biomacromolecules, 8*(6), 1775-1789.

Saitoh, K., & Koshiba, M. (2001). Full-vectorial finite element beam propagation method with perfectly matched layers for anisotropic optical waveguides. *Journal of Lightwave Technology, 19*(3), 405.

Saitoh, K., & Koshiba, M. (2002). Full-vectorial imaginary-distance beam propagation method based on a finite element scheme: Application to photonic crystal fibers. *Quantum Electronics, IEEE Journal of, 38*(7), 927-933.

Schasfoort, R. B., & Tudos, A. J. (2008). *Handbook of surface plasmon resonance*: Royal Society of Chemistry.

Shepard, D. S., Lees, R., Ng, C. W., Undurraga, E. A., Halasa, Y., & Lum, L. (2013). Burden of dengue in Malaysia. Report from a collaboration between universities and the Ministry of Health of Malaysia. *Unpublished report*.

Shepard, D. S., Undurraga, E. A., Lees, R. S., Halasa, Y., Lum, L. C. S., & Ng, C. W. (2012). Use of multiple data sources to estimate the economic cost of dengue illness in Malaysia. *The American journal of tropical medicine and hygiene, 87*(5), 796-805.

Silva, M., Dias, A. C., Silva, B. V., Gomes‐Filho, S. L., Kubota, L. T., Goulart, M. O., & Dutra, R. F. (2014). Electrochemical detection of dengue virus NS1 protein with a poly (allylamine)/carbon nanotube layered immunoelectrode. *Journal of Chemical Technology and Biotechnology*.

Singh, M. (2012). *Dengue NS1 detection using chemically modified silicon micropillars.* (Master of Science), University of Alberta, Edmonton, Alberta.

Slavík, R., & Homola, J. (2007). Ultrahigh resolution long range surface plasmon-based sensor. *Sensors and Actuators B: Chemical, 123*(1), 10-12.

Slavík, R., Homola, J., Čtyroký, J., & Brynda, E. (2001). Novel spectral fiber optic sensor based on surface plasmon resonance. *Sensors and Actuators B: Chemical, 74*(1), 106-111.

Souza, E., Nascimento, G., Santana, N., Ferreira, D., Lima, M., Natividade, E., . . . Lima-Filho, J. (2011). Label-free electrochemical detection of the specific oligonucleotide sequence of dengue virus type 1 on pencil graphite electrodes. *Sensors, 11*(6), 5616-5629.

Springer, T., Bockova, M., & Homola, J. (2013). Towards label-free biosensing in complex media: A novel referencing approach. *Analytical Chemistry, 85*, 5637–5640.

Su, C.-C., Wu, T.-Z., Chen, L.-K., Yang, H.-H., & Tai, D.-F. (2003). Development of immunochips for the detection of dengue viral antigens. *Analytica Chimica Acta, 479*(2), 117-123.

Suaya, J. A., Shepard, D. S., Siqueira, J. B., Martelli, C. T., Lum, L. C., Tan, L. H., . . . Montoya, R. (2009). Cost of dengue cases in eight countries in the Americas and asia: A prospective study. *The American journal of tropical medicine and hygiene, 80*(5), 846-855.

Tai, D.-F., Lin, C.-Y., Wu, T.-Z., & Chen, L.-K. (2005). Recognition of dengue virus protein using epitope-mediated molecularly imprinted film. *Analytical Chemistry, 77*(16), 5140-5143.

Tai, D.-F., Lin, C.-Y., Wu, T.-Z., Huang, J.-H., & Shu, P.-Y. (2006). Artificial receptors in serologic tests for the early diagnosis of dengue virus infection. *Clinical Chemistry, 52*(8), 1486-1491.

Takenobu, S., Kuwana, Y., Takayama, K., Sakane, Y., Ono, M., Sato, H., . . . Grote, N. (2008). *All-polymer 8x8 awg wavelength router using ultra low loss polymer optical waveguide material (CYTOP$^{TM}$).* Paper presented at the Optical Fiber Communication Conference/National Fiber Optic Engineers Conference, San Diego, California.

Taylor, J. R. (1997). An introduction to error analysis: The study of uncertainties in physical measurements (2nd ed.). Sausalito, CA: University Science Books.

Teles, F. S. R. R. (2011). Biosensors and rapid diagnostic tests on the frontier between analytical and clinical chemistry for biomolecular diagnosis of dengue disease: A review. *Analytica Chimica Acta, 687*(1), 28-42.

Tencer, M., Krupin, O., Tezel, B., & Berini, P. (2013). Electrochemistry of Au-SAM-protein stacks. *Journal of The Electrochemical Society, 160*(1), H22-H27.

Undurraga, E. A., Halasa, Y. A., & Shepard, D. S. (2013). Use of expansion factors to estimate the burden of dengue in southeast asia: A systematic analysis. *PLoS Neglected Tropical Diseases, 7*(2), e2056.

Vaisocherová, H., Zhang, Z., Yang, W., Cao, Z., Cheng, G., Taylor, A. D., . . . Jiang, S. (2009). Functionalizable surface platform with reduced nonspecific protein adsorption from full blood plasma—material selection and protein immobilization optimization. *Biosensors and Bioelectronics, 24*(7), 1924-1930. doi: http://dx.doi.org/10.1016/j.bios.2008.09.035

Vala, M., Etheridge, S., Roach, J., & Homola, J. (2009). Long-range surface plasmons for sensitive detection of bacterial analytes. *Sensors and Actuators B: Chemical, 139*(1), 59-63.

Vazquez, S., Perez, A., Ruiz, D., Rodriguez, R., Pupo, M., Calzada, N., . . . Serrano, T. (2005). Serological markers during dengue 3 primary and secondary infections. *Journal of Clinical Virology, 33*(2), 132-137.

Wang, B., & Wang, G. P. (2004). Surface plasmon polariton propagation in nanoscale metal gap waveguides. *Optics Letters, 29*(17), 1992-1994.

Wang, Y., Lai, H.-H., Bachman, M., Sims, C. E., Li, G., & Allbritton, N. L. (2005). Covalent micropatterning of poly (dimethylsiloxane) by photografting through a mask. *Analytical Chemistry, 77*(23), 7539-7546.

Wark, A. W., Lee, H. J., & Corn, R. M. (2005). Long-range surface plasmon resonance imaging for bioaffinity sensors. *Analytical Chemistry, 77*(13), 3904-3907.

Whitesides, G. M., Simanek, E. E., Mathias, J. P., Seto, C. T., Chin, D., Mammen, M., & Gordon, D. M. (1995). Noncovalent synthesis: Using physical-organic chemistry to make aggregates. *Accounts of Chemical Research, 28*(1), 37-44.

Won, H. S., Kim, K. C., Song, S. H., Oh, C.-H., Kim, P. S., Park, S., & Kim, S. I. (2006). Vertical coupling of long-range surface plasmon polaritons. *Applied Physics Letters, 88*(1), 011110-011110-011113.

Wong, W. R., Krupin, O., Sekaran, S. D., Mahamd Adikan, F. R., & Berini, P. (2014). Serological diagnosis of dengue infection in blood plasma using long-range surface plasmon waveguides. *Analytical Chemistry, 86*(3), 1735-1743.

World Health Organization. (2014). Dengue, countries or areas at risk, 2013. Retrieved June 25, 2014, from http://gamapserver.who.int/mapLibrary/Files/Maps/Global_DengueTransmission_ITHRiskMap.png

World Health Organization and the Special Programme for Research and Training in Tropical Diseases. (2009). *Dengue: Guidelines for diagnosis, treatment, prevention and control* (pp. 147). Retrieved from http://www.who.int/tdr/publications/documents/dengue-diagnosis.pdf

World Health Organization Western Pacific Region. (2014, June 3). Dengue situation updates. *Emerging disease surveillance and response.* Retrieved June 23, 2014, from http://www.wpro.who.int/emerging_diseases/DengueSituationUpdates/en/

Wu, T.-Z., Su, C.-C., Chen, L.-K., Yang, H.-H., Tai, D.-F., & Peng, K.-C. (2005). Piezoelectric immunochip for the detection of dengue fever in viremia phase. *Biosensors and Bioelectronics, 21*(5), 689-695.

Xiao, G., & Bock, W. J. (2012). Photonic sensing: Principles and applications for safety and security monitoring (Vol. 227): John Wiley & Sons.

Yellow Springs Instruments. A brief history of YSI. Retrieved February 18, 2015, from http://www.ysi.com/history.php

Yen, C.-W., de Puig, H., Tam, J. O., Gómez-Márquez, J., Bosch, I., Hamad-Schifferli, K., & Gehrke, L. (2015). Multicolored silver nanoparticles for multiplexed disease diagnostics: Distinguishing dengue, yellow fever, and ebola viruses. *Lab on a Chip, 15*(7), 1638-1641.

Ymeti, A., Kanger, J. S., Greve, J., Lambeck, P. V., Wijn, R., & Heideman, R. G. (2003). Realization of a multichannel integrated young interferometer chemical sensor. *Applied Optics, 42*(28), 5649-5660.

Yusof, N., Ibrahim, F., Rahman, H., Adwan, S., & Harun, S. (2015). Tapered plastic optical fiber sensor for dengue non-structural protein 1 (ns1) detection. *Optoelectronics and Advanced Materials -Rapid Communications, 9*(1-2), 75-78.

Zaytseva, N. V., Montagna, R. A., & Baeumner, A. J. (2005). Microfluidic biosensor for the serotype-specific detection of dengue virus RNA. *Analytical Chemistry, 77*(23), 7520-7527.

Zaytseva, N. V., Montagna, R. A., Lee, E. M., & Baeumner, A. J. (2004). Multi-analyte single-membrane biosensor for the serotype-specific detection of dengue virus. *Analytical and Bioanalytical Chemistry, 380*(1), 46-53.

Zhang, G.-J., Zhang, L., Huang, M. J., Luo, Z. H. H., Tay, G. K. I., Lim, E.-J. A., . . . Chen, Y. (2010). Silicon nanowire biosensor for highly sensitive and rapid detection of dengue virus. *Sensors and Actuators B: Chemical, 146*(1), 138-144.

Zhang, Y., Bahns, J. T., Jin, Q., Divan, R., & Chen, L. (2006). Toward the detection of single virus particle in serum. *Analytical Biochemistry, 356*(2), 161-170.

Zhao, B., Prince, G., Horswood, R., Eckels, K., Summers, P., Chanock, R., & Lai, C.-J. (1987). Expression of dengue virus structural proteins and nonstructural protein NS1 by a recombinant vaccinia virus. *Journal of Virology, 61*(12), 4019-4022.

# LIST OF PUBLICATIONS AND PAPERS PRESENTED

## A. Published Papers

1. **Wong, W. R.**, Krupin, O., Sekaran, S. D., Mahamd Adikan, F. R., & Berini, P. (2014). Serological diagnosis of dengue infection in blood plasma using long-range surface plasmon waveguides. *Analytical chemistry*, *86*(3), 1735-1743.
2. **Wong, W. R.**, Mahamd Adikan, F. R., & Berini, P. (2014). Surface sensitivity of straight long-range surface plasmon waveguides for attenuation-based biosensing. *Applied Physics A*, *117*(2), 527-535.
3. **Wong, W. R.**, Krupin, O., Mahamd Adikan, F. R., & Berini, P. (2015). Optimization of long-range surface plasmon waveguides for attenuation-based biosensing. *Journal of Lightwave Technology*, *33*(15), 3234-3242.
4. **Wong, W. R.**, Sekaran, S. D., Mahamd Adikan, F. R., & Berini, P. (2015). Detection of dengue NS1 antigen using long-range surface plasmon waveguides. *Submitted.*

## B. Papers Presented at Conferences, Seminars, Symposiums, etc.

1. **Wong, W. R**., Krupin, O., Mahamd Adikan, F. R., & Berini, P. (2013). *Dengue detection with long-range surface plasmon polariton (LRSPP) waveguides*. Poster presented at the BiopSys 9th All Network Meeting (ANM-9), Toronto, Canada.
2. **Wong, W.R.**, Sandoghchi, S., & Mahamd Adikan, F. (2013). *Surface plasmon in slab waveguide: A verification test-bed*. Paper presented at the IEEE 4th International Conference on Photonics (ICP), Melaka, Malaysia.
3. **Wong, W. R.**, Krupin, O., Sekaran, S. D., Mahamd Adikan, F. R., & Berini, P. (2014). *Serological diagnosis of dengue infection in blood plasma using long-range surface plasmon waveguides*. Poster presented at the META'14, the 4th

International Conference on Metamaterials, Photonic Crystals and Plasmonics, Singapore.

4. Krupin, O., **Wong, W. R.**, Wang, C., & Berini, P. (2014). *Long-range surface plasmon polariton (LRSPP) waveguides as (bio)chemical and biological sensors*. Poster presented at the Schawlow-Townes Symposium on Photonics Ottawa, Canada.
5. **Wong, W. R.**, Krupin, O., Sekaran, S. D., Mahamd Adikan, F. R., & Berini, P. (2015). *Long range surface plasmon based biosensor for dengue diagnosis*. Poster presented at the 8th Edition of the Engineering and Computer Science Graduate Poster Competition, University of Ottawa, Canada.
6. **Wong, W. R.**, Krupin, O., Sekaran, S. D., Mahamd Adikan, F. R., & Berini, P. (2015). *Long-range surface plasmon polariton (LRSPP) waveguides as dengue biosensors*. Oral presentation at the 7th International Conference on Surface Plasmon Photonics (SPP7), Jerusalem, Israel.

# APPENDIX A: COPYRIGHT AND PERMISSION FROM JOURNALS

## A.1 Figure 2.1

**NATURE PUBLISHING GROUP LICENSE**
**TERMS AND CONDITIONS**

Jun 22, 2014

This is a License Agreement between Wei Ru Wong ("You") and Nature Publishing Group ("Nature Publishing Group") provided by Copyright Clearance Center ("CCC"). The license consists of your order details, the terms and conditions provided by Nature Publishing Group, and the payment terms and conditions.

**All payments must be made in full to CCC. For payment instructions, please see information listed at the bottom of this form.**

| | |
|---|---|
| License Number | 3414290112296 |
| License date | Jun 22, 2014 |
| Licensed content publisher | Nature Publishing Group |
| Licensed content publication | Nature Reviews Microbiology |
| Licensed content title | Dengue: a continuing global threat |
| Licensed content author | Maria G. Guzman, Scott B. Halstead, Harvey Artsob, Philippe Buchy, Jeremy Farrar et al. |
| Licensed content date | Dec 1, 2010 |
| Volume number | 8 |
| Issue number | 12 |
| Type of Use | reuse in a dissertation / thesis |
| Requestor type | academic/educational |
| Format | print and electronic |
| Portion | figures/tables/illustrations |
| Number of figures/tables/illustrations | 1 |
| High-res required | no |
| Figures | Figure 2 : The dengue virus genome |
| Author of this NPG article | no |
| Your reference number | None |
| Title of your thesis / dissertation | Long-range surface plasmon based biosensor for dengue diagnosis |
| Expected completion date | Feb 2015 |
| Estimated size (number of pages) | 100 |
| Total | 0.00 USD |
| Terms and Conditions | |

Terms and Conditions for Permissions

Nature Publishing Group hereby grants you a non-exclusive license to reproduce this material for this purpose, and for no other use,subject to the conditions below:

## A.2 Figure 2.2

### NATURE PUBLISHING GROUP LICENSE
### TERMS AND CONDITIONS

Jun 22, 2014

This is a License Agreement between Wei Ru Wong ("You") and Nature Publishing Group ("Nature Publishing Group") provided by Copyright Clearance Center ("CCC"). The license consists of your order details, the terms and conditions provided by Nature Publishing Group, and the payment terms and conditions.

**All payments must be made in full to CCC. For payment instructions, please see information listed at the bottom of this form.**

| | |
|---|---|
| License Number | 3414371115421 |
| License date | Jun 22, 2014 |
| Licensed content publisher | Nature Publishing Group |
| Licensed content publication | Nature Reviews Microbiology |
| Licensed content title | Evaluation of diagnostic tests: dengue |
| Licensed content author | Rosanna W. Peeling, Harvey Artsob, Jose Luis Pelegrino, Philippe Buchy, Mary J. Cardosa et al. |
| Licensed content date | Dec 1, 2010 |
| Volume number | 8 |
| Issue number | 12 |
| Type of Use | reuse in a dissertation / thesis |
| Requestor type | academic/educational |
| Format | print and electronic |
| Portion | figures/tables/illustrations |
| Number of figures/tables/illustrations | 1 |
| High-res required | no |
| Figures | Figure 2 : major diagnostic markers for dengue infection |
| Author of this NPG article | no |
| Your reference number | None |
| Title of your thesis / dissertation | Long-range surface plasmon based biosensor for dengue diagnosis |
| Expected completion date | Feb 2015 |
| Estimated size (number of pages) | 100 |
| Total | 0.00 USD |
| Terms and Conditions | |

Terms and Conditions for Permissions

Nature Publishing Group hereby grants you a non-exclusive license to reproduce this material for this purpose, and for no other use,subject to the conditions below:

## A.3 Chapter 4

Wong, W. R., Mahamd Adikan, F. R., & Berini, P. (2014). Surface sensitivity of straight long-range surface plasmon waveguides for attenuation-based biosensing. *Applied Physics A*, *117*(2), 527-535

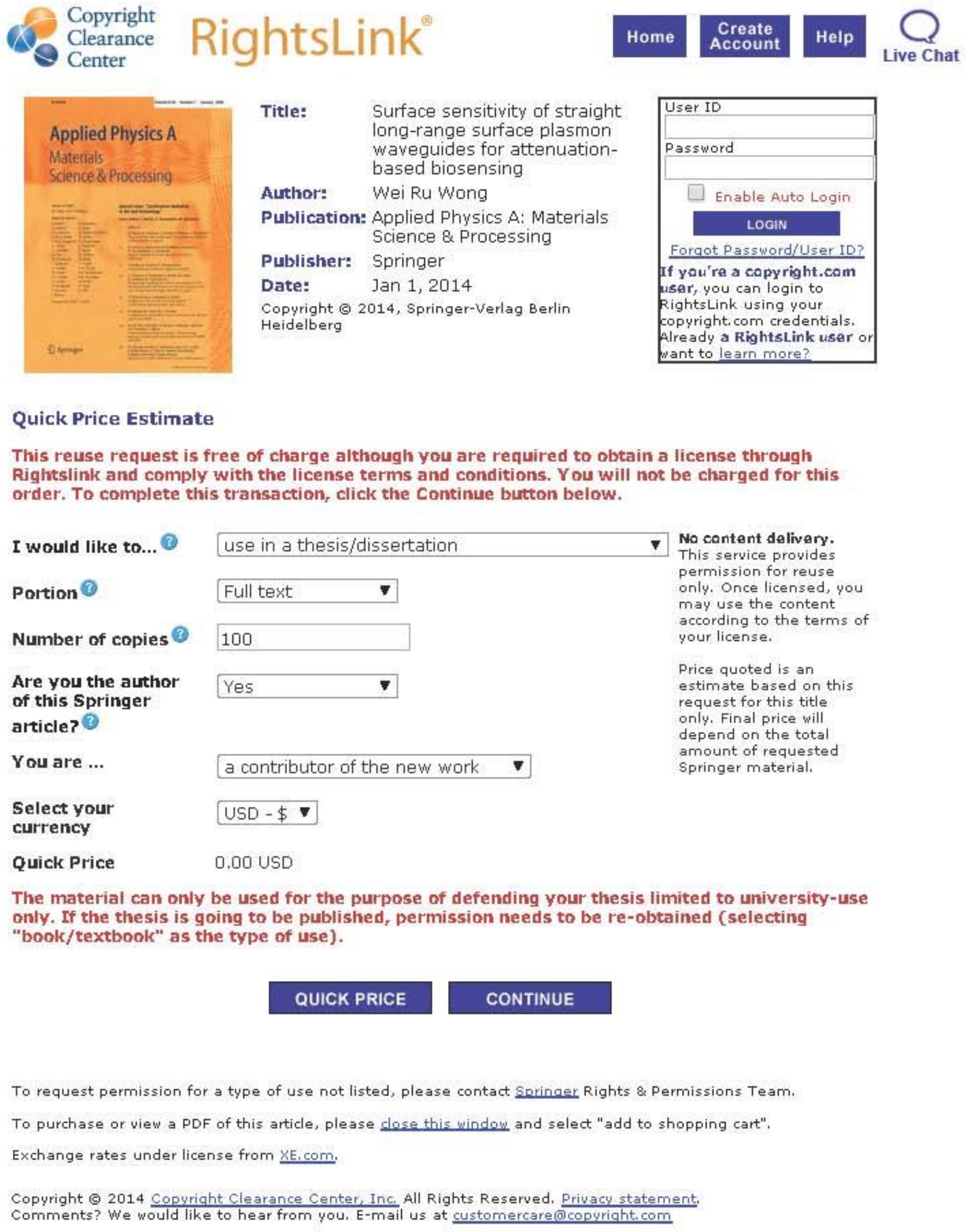

**Title:** Surface sensitivity of straight long-range surface plasmon waveguides for attenuation-based biosensing
**Author:** Wei Ru Wong
**Publication:** Applied Physics A: Materials Science & Processing
**Publisher:** Springer
**Date:** Jan 1, 2014

Copyright © 2014, Springer-Verlag Berlin Heidelberg

User ID

Password

☐ Enable Auto Login

LOGIN

Forgot Password/User ID?

**If you're a copyright.com user,** you can login to RightsLink using your copyright.com credentials. Already **a RightsLink user** or want to learn more?

**Quick Price Estimate**

**This reuse request is free of charge although you are required to obtain a license through Rightslink and comply with the license terms and conditions. You will not be charged for this order. To complete this transaction, click the Continue button below.**

| | |
|---|---|
| **I would like to...** | use in a thesis/dissertation |
| **Portion** | Full text |
| **Number of copies** | 100 |
| **Are you the author of this Springer article?** | Yes |
| **You are ...** | a contributor of the new work |
| **Select your currency** | USD - $ |
| **Quick Price** | 0.00 USD |

**No content delivery.** This service provides permission for reuse only. Once licensed, you may use the content according to the terms of your license.

Price quoted is an estimate based on this request for this title only. Final price will depend on the total amount of requested Springer material.

**The material can only be used for the purpose of defending your thesis limited to university-use only. If the thesis is going to be published, permission needs to be re-obtained (selecting "book/textbook" as the type of use).**

QUICK PRICE CONTINUE

To request permission for a type of use not listed, please contact Springer Rights & Permissions Team.

To purchase or view a PDF of this article, please close this window and select "add to shopping cart".

Exchange rates under license from XE.com.

Copyright © 2014 Copyright Clearance Center, Inc. All Rights Reserved. Privacy statement.
Comments? We would like to hear from you. E-mail us at customercare@copyright.com

## A.4 Chapter 4

Wong, W. R., Krupin, O., Mahamd Adikan, F. R., & Berini, P. (2015). Optimization of long-range surface plasmon waveguides for attenuation-based biosensing. *Journal of Lightwave Technology*, *33*(15), 3234-3242

**Title:** Optimization of Long-Range Surface Plasmon Waveguides for Attenuation-Based Biosensing
**Author:** Wei Ru Wong; Krupin, O.; Mahamd Adikan, F.R.; Berini, P.
**Publication:** Lightwave Technology, IEEE/OSA Journal of
**Publisher:** IEEE
**Date:** Aug.1, 1 2015
Copyright © 2015, IEEE

**If you're a copyright.com user**, you can login to RightsLink using your copyright.com credentials. Already **a RightsLink user** or want to learn more?

**Thesis / Dissertation Reuse**

**The IEEE does not require individuals working on a thesis to obtain a formal reuse license, however, you may print out this statement to be used as a permission grant:**

*Requirements to be followed when using any portion (e.g., figure, graph, table, or textual material) of an IEEE copyrighted paper in a thesis:*

1) In the case of textual material (e.g., using short quotes or referring to the work within these papers) users must give full credit to the original source (author, paper, publication) followed by the IEEE copyright line © 2011 IEEE.
2) In the case of illustrations or tabular material, we require that the copyright line © [Year of original publication] IEEE appear prominently with each reprinted figure and/or table.
3) If a substantial portion of the original paper is to be used, and if you are not the senior author, also obtain the senior author's approval.

*Requirements to be followed when using an entire IEEE copyrighted paper in a thesis:*

1) The following IEEE copyright/ credit notice should be placed prominently in the references: © [year of original publication] IEEE. Reprinted, with permission, from [author names, paper title, IEEE publication title, and month/year of publication]
2) Only the accepted version of an IEEE copyrighted paper can be used when posting the paper or your thesis on-line.
3) In placing the thesis on the author's university website, please display the following message in a prominent place on the website: In reference to IEEE copyrighted material which is used with permission in this thesis, the IEEE does not endorse any of [university/educational entity's name goes here]'s products or services. Internal or personal use of this material is permitted. If interested in reprinting/republishing IEEE copyrighted material for advertising or promotional purposes or for creating new collective works for resale or redistribution, please go to http://www.ieee.org/publications_standards/publications/rights/rights_link.html to learn how to obtain a License from RightsLink.

If applicable, University Microfilms and/or ProQuest Library, or the Archives of Canada may supply single copies of the dissertation.

## A.5 Chapter 6

Wong, W. R., Krupin, O., Sekaran, S. D., Mahamd Adikan, F. R., & Berini, P. (2014). Serological diagnosis of dengue infection in blood plasma using long-range surface plasmon waveguides. *Analytical chemistry*, 86(3), 1735-1743.

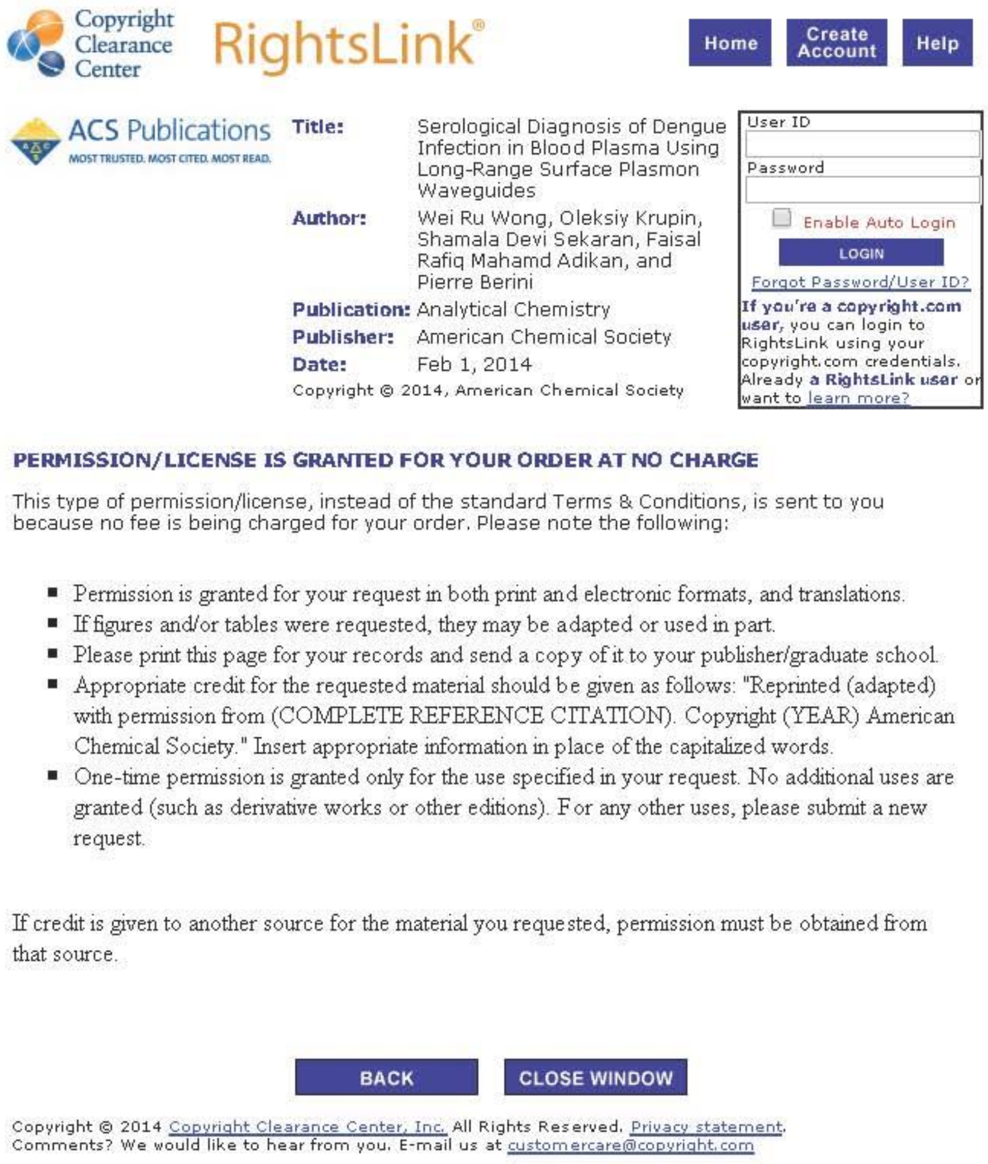

**Title:** Serological Diagnosis of Dengue Infection in Blood Plasma Using Long-Range Surface Plasmon Waveguides

**Author:** Wei Ru Wong, Oleksiy Krupin, Shamala Devi Sekaran, Faisal Rafiq Mahamd Adikan, and Pierre Berini

**Publication:** Analytical Chemistry

**Publisher:** American Chemical Society

**Date:** Feb 1, 2014

Copyright © 2014, American Chemical Society

**If you're a copyright.com user,** you can login to RightsLink using your copyright.com credentials. Already **a RightsLink user** or want to learn more?

**PERMISSION/LICENSE IS GRANTED FOR YOUR ORDER AT NO CHARGE**

This type of permission/license, instead of the standard Terms & Conditions, is sent to you because no fee is being charged for your order. Please note the following:

- Permission is granted for your request in both print and electronic formats, and translations.
- If figures and/or tables were requested, they may be adapted or used in part.
- Please print this page for your records and send a copy of it to your publisher/graduate school.
- Appropriate credit for the requested material should be given as follows: "Reprinted (adapted) with permission from (COMPLETE REFERENCE CITATION). Copyright (YEAR) American Chemical Society." Insert appropriate information in place of the capitalized words.
- One-time permission is granted only for the use specified in your request. No additional uses are granted (such as derivative works or other editions). For any other uses, please submit a new request.

If credit is given to another source for the material you requested, permission must be obtained from that source.

Copyright © 2014 Copyright Clearance Center, Inc. All Rights Reserved. Privacy statement.
Comments? We would like to hear from you. E-mail us at customercare@copyright.com

# APPENDIX B: LABVIEW SCRIPT TO READ HP8153A POWER METER

## C.1 Front Panel

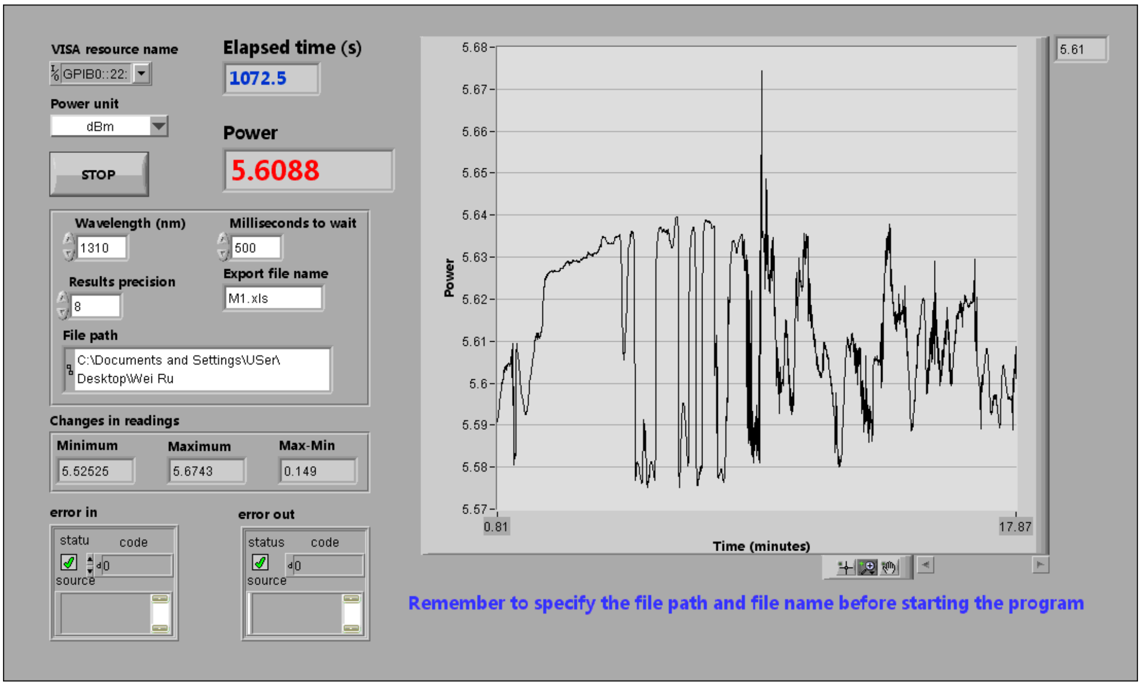

VISA resource name: GPIB0::22:

Power unit: dBm

Elapsed time (s): 1072.5

Power: 5.6088

Wavelength (nm): 1310

Milliseconds to wait: 500

Results precision: 8

Export file name: M1.xls

File path: C:\Documents and Settings\USer\Desktop\Wei Ru

Changes in readings

| Minimum | Maximum | Max-Min |
|---|---|---|
| 5.52525 | 5.6743 | 0.149 |

error in: statu ☑ code 0 source

error out: status ☑ code 0 source

Remember to specify the file path and file name before starting the program

## C.2 Block Diagram

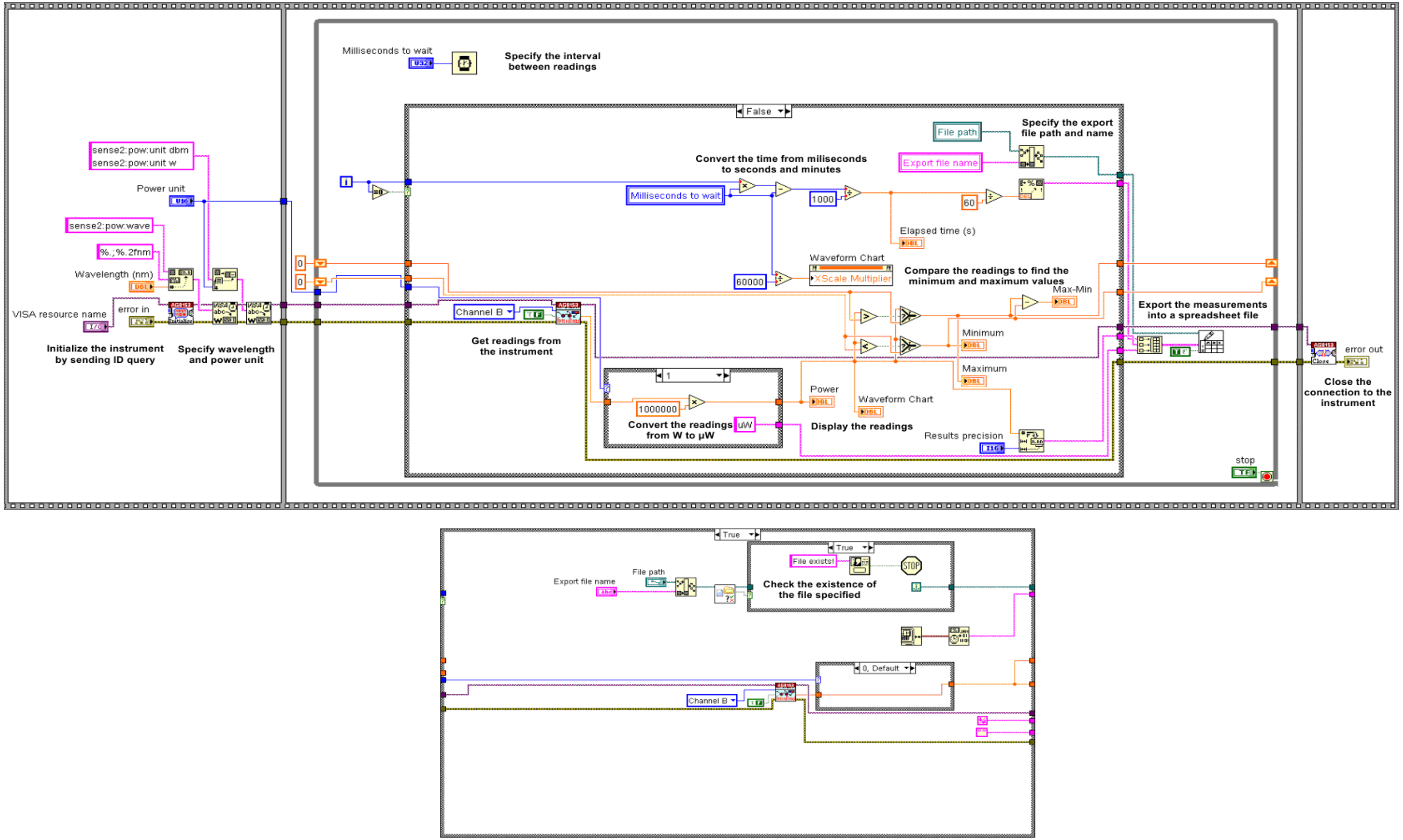

# APPENDIX C: PRESS COVERAGE ON THE RESEARCH WORK

## C.1 News Coverage

1. Dengue diagnosis made simple with optical detection (2014, December 30). *PRWeb*. Retrieved from http://www.prweb.com/releases/2015/01/prweb12419405.htm

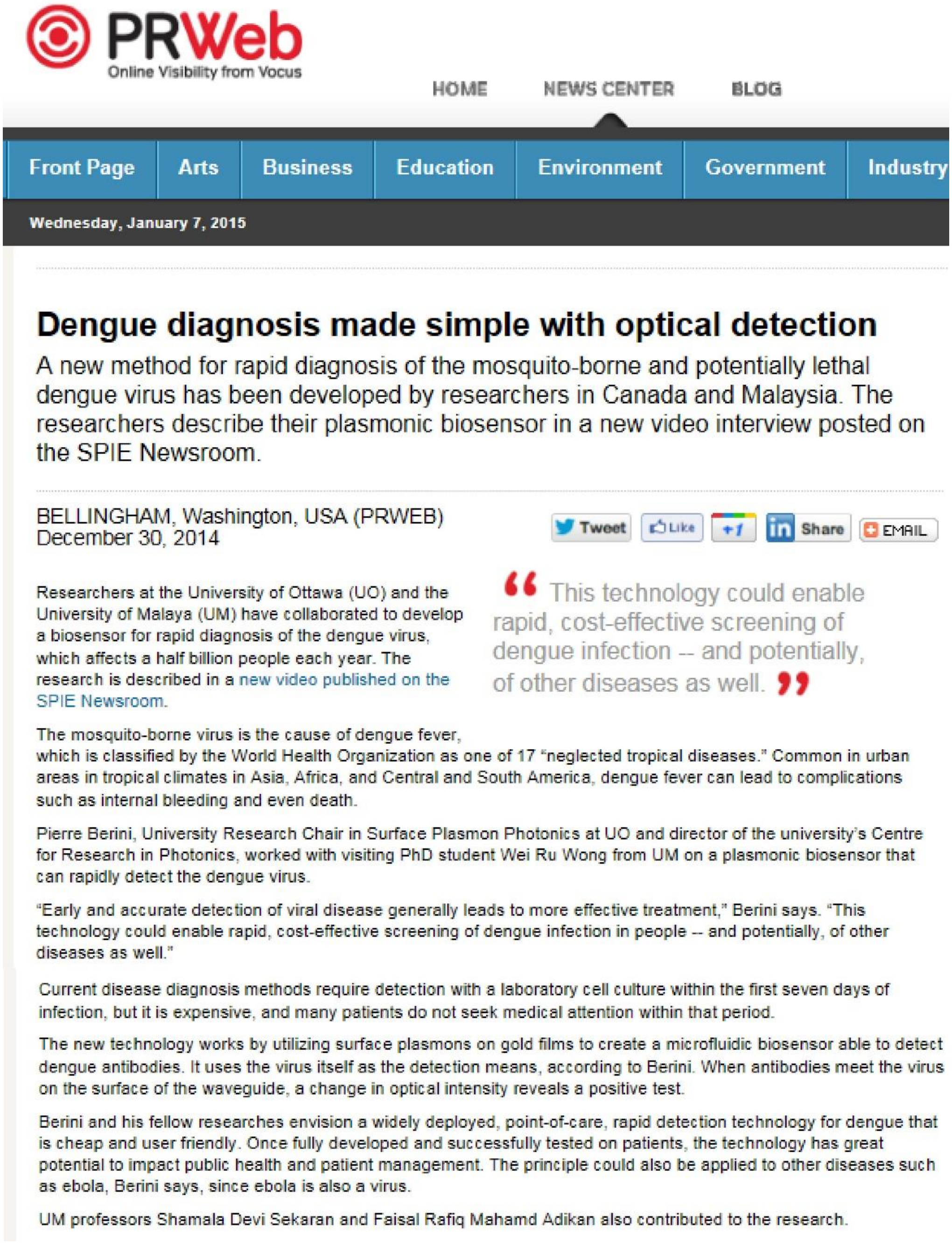

Wednesday, January 7, 2015

**Dengue diagnosis made simple with optical detection**

A new method for rapid diagnosis of the mosquito-borne and potentially lethal dengue virus has been developed by researchers in Canada and Malaysia. The researchers describe their plasmonic biosensor in a new video interview posted on the SPIE Newsroom.

BELLINGHAM, Washington, USA (PRWEB)
December 30, 2014

> “This technology could enable rapid, cost-effective screening of dengue infection -- and potentially, of other diseases as well.”

Researchers at the University of Ottawa (UO) and the University of Malaya (UM) have collaborated to develop a biosensor for rapid diagnosis of the dengue virus, which affects a half billion people each year. The research is described in a new video published on the SPIE Newsroom.

The mosquito-borne virus is the cause of dengue fever, which is classified by the World Health Organization as one of 17 “neglected tropical diseases.” Common in urban areas in tropical climates in Asia, Africa, and Central and South America, dengue fever can lead to complications such as internal bleeding and even death.

Pierre Berini, University Research Chair in Surface Plasmon Photonics at UO and director of the university’s Centre for Research in Photonics, worked with visiting PhD student Wei Ru Wong from UM on a plasmonic biosensor that can rapidly detect the dengue virus.

“Early and accurate detection of viral disease generally leads to more effective treatment,” Berini says. “This technology could enable rapid, cost-effective screening of dengue infection in people -- and potentially, of other diseases as well.”

Current disease diagnosis methods require detection with a laboratory cell culture within the first seven days of infection, but it is expensive, and many patients do not seek medical attention within that period.

The new technology works by utilizing surface plasmons on gold films to create a microfluidic biosensor able to detect dengue antibodies. It uses the virus itself as the detection means, according to Berini. When antibodies meet the virus on the surface of the waveguide, a change in optical intensity reveals a positive test.

Berini and his fellow researches envision a widely deployed, point-of-care, rapid detection technology for dengue that is cheap and user friendly. Once fully developed and successfully tested on patients, the technology has great potential to impact public health and patient management. The principle could also be applied to other diseases such as ebola, Berini says, since ebola is also a virus.

UM professors Shamala Devi Sekaran and Faisal Rafiq Mahamd Adikan also contributed to the research.

**Similar articles are also featured in:**

i. Lifestyle-KSTV-TV (United States)
http://lifestyle.kstc45.com/story/27733410/dengue-diagnosis-made-simple-with-optical-detection

ii. StamfordAdvocate.com | United States
http://www.stamfordadvocate.com/business/press-releases/article/Dengue-diagnosis-made-simple-with-optical-5986347.php

iii. Chron.com | United States |
http://www.chron.com/business/press-releases/article/Dengue-diagnosis-made-simple-with-optical-5986347.php

iv. San Antonio Express-News | United States |
http://www.mysanantonio.com/business/press-releases/article/Dengue-diagnosis-made-simple-with-optical-5986347.php

v. Seattlepi.com | United States |
http://www.seattlepi.com/business/press-releases/article/Dengue-diagnosis-made-simple-with-optical-5986347.php

vi. KFXL Fox Nebraska | United States |
http://www.foxnebraska.com/story/27733410/dengue-diagnosis-made-simple-with-optical-detection

vii. KAUZ-TV: NewsChannel 6 Now | United States |
http://www.newschannel6now.com/story/27733410/dengue-diagnosis-made-simple-with-optical-detection

viii. ABC 40 KRHD-TV | United States |
http://www.abc40.com/story/27733410/dengue-diagnosis-made-simple-with-optical-detection

ix. CW GA-BAMA | United States |
http://www.cw-gabama.com/story/27733410/dengue-diagnosis-made-simple-with-optical-detection

x. KFMB-TV CBS-8 | United States |
http://www.cbs8.com/story/27733410/dengue-diagnosis-made-simple-with-optical-detection

xi. KTEN.com | United States |
http://www.kten.com/story/27733410/dengue-diagnosis-made-simple-with-optical-detection

xii. KYTX CBS 19 | United States |
http://www.cbs19.tv/story/27733410/dengue-diagnosis-made-simple-with-optical-detection

2. Wallace, J. (2015, Jan 2). Video: Surface-plasmon-based biosensor enables point-of-care detection of dengue-fever virus. *Laser Focus World*. Retrieved from http://www.laserfocusworld.com/articles/2015/01/surface-plasmon-based-biosensor-enables-point-of-care-detection-of-dengue-fever-virus.html

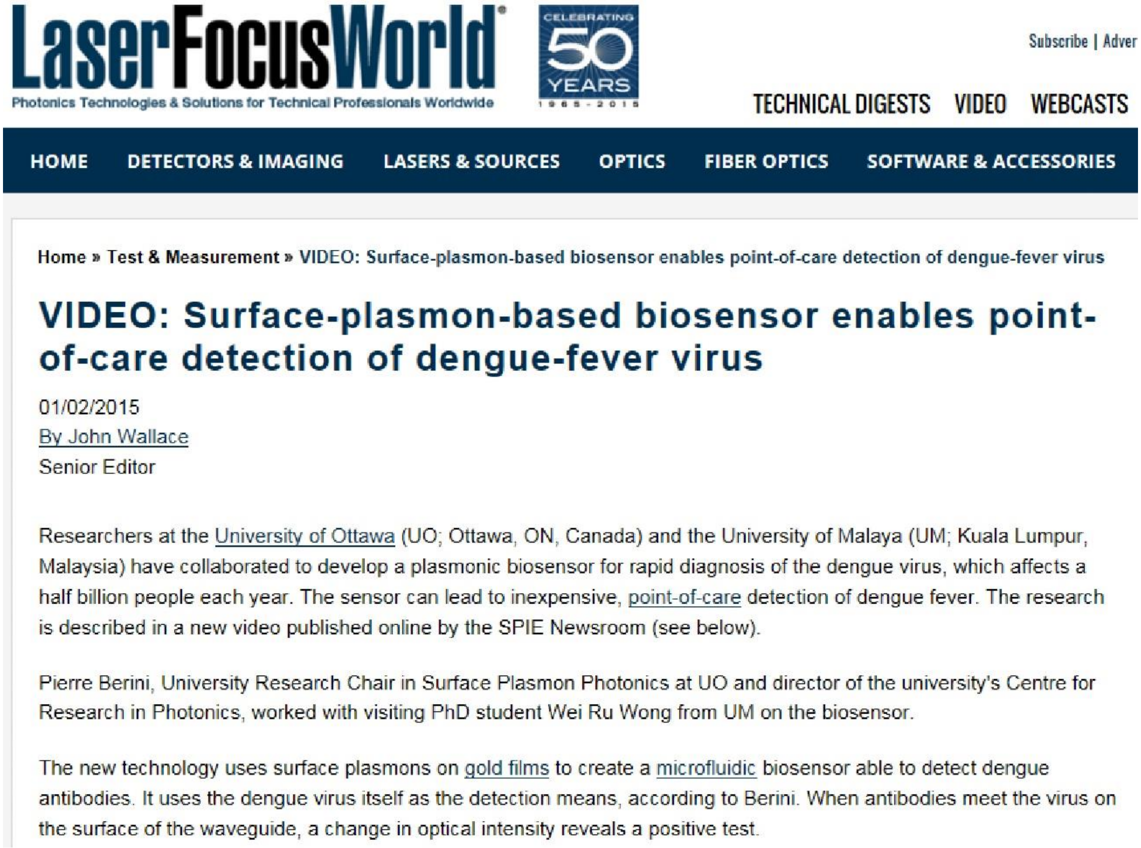

## VIDEO: Surface-plasmon-based biosensor enables point-of-care detection of dengue-fever virus

01/02/2015
By John Wallace
Senior Editor

Researchers at the University of Ottawa (UO; Ottawa, ON, Canada) and the University of Malaya (UM; Kuala Lumpur, Malaysia) have collaborated to develop a plasmonic biosensor for rapid diagnosis of the dengue virus, which affects a half billion people each year. The sensor can lead to inexpensive, point-of-care detection of dengue fever. The research is described in a new video published online by the SPIE Newsroom (see below).

Pierre Berini, University Research Chair in Surface Plasmon Photonics at UO and director of the university's Centre for Research in Photonics, worked with visiting PhD student Wei Ru Wong from UM on the biosensor.

The new technology uses surface plasmons on gold films to create a microfluidic biosensor able to detect dengue antibodies. It uses the dengue virus itself as the detection means, according to Berini. When antibodies meet the virus on the surface of the waveguide, a change in optical intensity reveals a positive test.

3. Spears, T. (2015, January 19). Photonics eliminates weeklong wait for dengue diagnosis. *Ottawa Citizen*. Retrieved from http://ottawacitizen.com/news/local-news/photonics-eliminates-weeklong-wait-for-dengue-diagnosis

   Spears, T. (2015, January 20). U of O prof helps find dengue quickly. *Ottawa Citizen* (print edition).

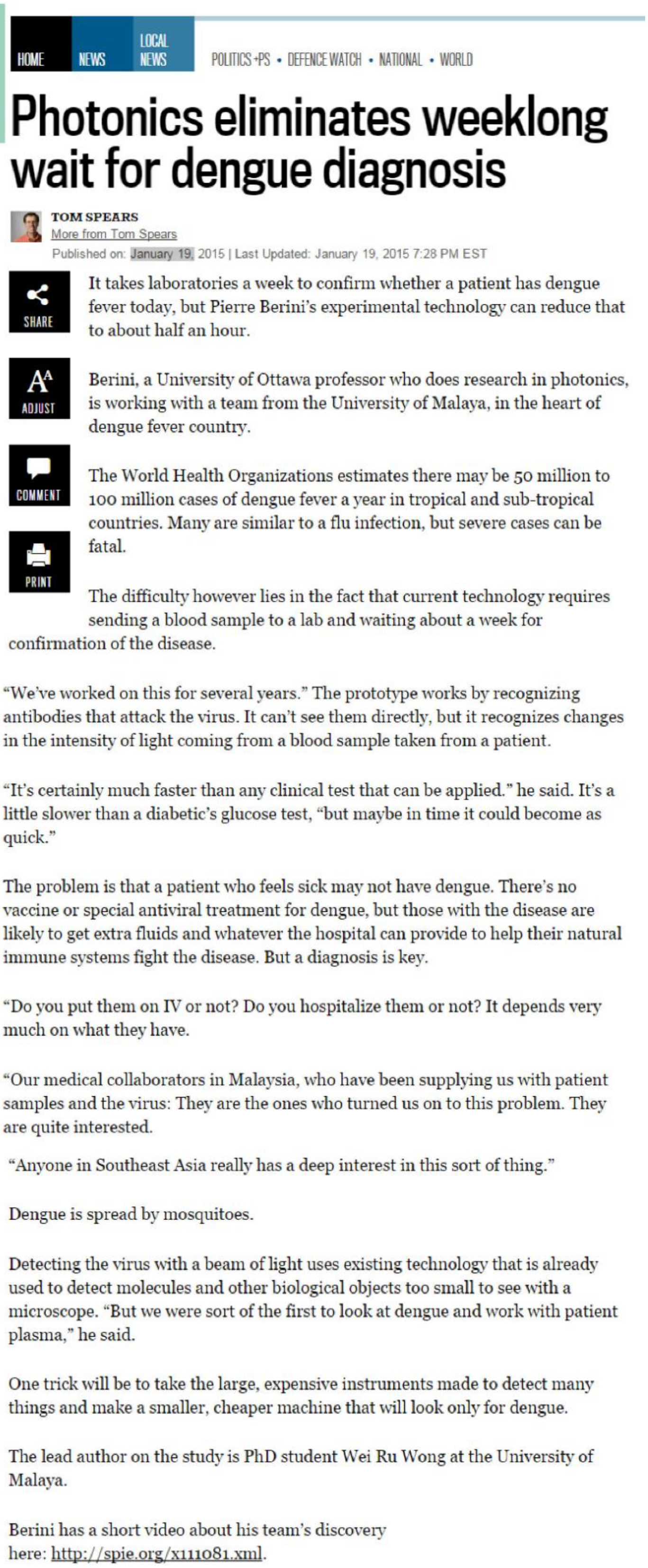

# Photonics eliminates weeklong wait for dengue diagnosis

**TOM SPEARS**
More from Tom Spears
Published on: January 19, 2015 | Last Updated: January 19, 2015 7:28 PM EST

It takes laboratories a week to confirm whether a patient has dengue fever today, but Pierre Berini's experimental technology can reduce that to about half an hour.

Berini, a University of Ottawa professor who does research in photonics, is working with a team from the University of Malaya, in the heart of dengue fever country.

The World Health Organizations estimates there may be 50 million to 100 million cases of dengue fever a year in tropical and sub-tropical countries. Many are similar to a flu infection, but severe cases can be fatal.

The difficulty however lies in the fact that current technology requires sending a blood sample to a lab and waiting about a week for confirmation of the disease.

"We've worked on this for several years." The prototype works by recognizing antibodies that attack the virus. It can't see them directly, but it recognizes changes in the intensity of light coming from a blood sample taken from a patient.

"It's certainly much faster than any clinical test that can be applied." he said. It's a little slower than a diabetic's glucose test, "but maybe in time it could become as quick."

The problem is that a patient who feels sick may not have dengue. There's no vaccine or special antiviral treatment for dengue, but those with the disease are likely to get extra fluids and whatever the hospital can provide to help their natural immune systems fight the disease. But a diagnosis is key.

"Do you put them on IV or not? Do you hospitalize them or not? It depends very much on what they have.

"Our medical collaborators in Malaysia, who have been supplying us with patient samples and the virus: They are the ones who turned us on to this problem. They are quite interested.

"Anyone in Southeast Asia really has a deep interest in this sort of thing."

Dengue is spread by mosquitoes.

Detecting the virus with a beam of light uses existing technology that is already used to detect molecules and other biological objects too small to see with a microscope. "But we were sort of the first to look at dengue and work with patient plasma," he said.

One trick will be to take the large, expensive instruments made to detect many things and make a smaller, cheaper machine that will look only for dengue.

The lead author on the study is PhD student Wei Ru Wong at the University of Malaya.

Berini has a short video about his team's discovery here: http://spie.org/x111081.xml.

# U of O prof helps find dengue quickly

***TOM SPEARS***
OTTAWA CITIZEN

It takes laboratories a week to confirm whether a patient has dengue fever today, but Pierre Berini's experimental technology can reduce that to about half an hour.

Berini, a University of Ottawa professor who does research in photonics, is working with a team from the University of Malaya, in the heart of dengue fever country.

The World Health Organization estimates there may be 50 million to 100 million cases of dengue fever a year in tropical and sub-tropical countries. Many are similar to a flu infection, but severe cases can be fatal.

The difficulty, however, lies in the fact that current technology requires sending a blood sample to a lab and waiting about a week for confirmation of the disease.

"We've worked on this for several years," he said. The prototype works by recognizing antibodies that attack the virus. It can't see them directly, but it recognizes changes in the intensity of light coming from a blood sample taken from a patient.

Pierre Berini

"It's certainly much faster than any clinical test that can be applied," Berini said. It's a little slower than a diabetic's glucose test, "but maybe in time it could become as quick."

The problem is that a patient who feels sick may not have dengue. There's no vaccine or special antiviral treatment for dengue, but those with the disease are likely to get extra fluids and whatever the hospital can provide to help their natural immune systems fight the disease. But a diagnosis is key.

"Do you put them on IV or not? Do you hospitalize them or not? It depends very much on what they have."

Dengue is spread by mosquitoes.

Detecting the virus with a beam of light uses existing technology that is already used to detect molecules and other biological objects too small to see with a microscope. "But we were sort of the first to look at dengue and work with patient plasma," he said.

One trick will be to take the large, expensive instruments made to detect many things and make a smaller, cheaper machine that will look only for dengue.

The lead author on the study is PhD student Wei Ru Wong at the University of Malaya.

*tspears@ottawacitizen.com*
*twitter.com/TomSpears1*

4. Gibney, E. (2015). Optics: Leading lights. *Nature*, *518*(7538), 154-157.

# LEADING LIGHTS

*Shape it, squeeze it, energize it or tie it into knots. Scientists are taking light to new extremes.*

| BY ELIZABETH GIBNEY |

FEATURE NEWS

| SQUEEZING LIGHT |

## *Pierre Berini*

PETER THORNTON/UNIV. OTTAWA

Pierre Berini knows a bargain when he sees one; the evidence is in his lab, which is cluttered with lasers, oscillators and other components that he bought at auctions after local companies folded. The University of Ottawa physicist often buys in batches, after spotting essential items in a job lot that otherwise looks like junk. "There are lots of surprises," he says.

Berini has a certain sympathy for the failed companies. He is a leader in plasmonics, a way of manipulating electrons with light that could be used to transmit information in super-fast computers. Months after launching a venture-backed firm, Spectalis, to market plasmonics circuitry to the communications industry in the early 2000s, he began to feel the effects of the dot-com bubble bursting. He ended up hosting an auction of his own and closing shop. Unperturbed, he plans to try again this year, launching a company to apply his technology to tiny sensors in handheld devices that detect diseases rapidly and with extreme sensitivity.

The devices use a peculiar kind of light that emerges from waves of electrons propagating across a metal surface in contact with an insulator, such as air or glass. When excited with a laser, these charges, or plasmons, generate fluctuating electric and magnetic fields that flow just above the metal surface. Trapped at the interface, the waves can be funnelled into structures that confine their wavelengths to a few tens of nanometres — as little as one-tenth of the laser's wavelength. The squeezed waves travel more slowly than laser light, so can retain the same frequency.

Berini backed into studying plasmonics while looking for ways to improve normal electrical components and photo detectors in the late 1990s. Light travels much faster than electrical signals, so using it to connect silicon chips would massively speed up calculations. But light is limited by its wavelength: although electronic devices can be shrunk to a few tens of nanometres, the infrared light used in telecommunications cannot focus to spots much smaller than a micrometre. "It's a fundamental incompatibility," says Berini. The smaller wavelengths available with plasmons looked promising, but plasmonic light does not always behave. The waves, created by the movement of electrons, decay quickly as a result of resistance in the metal, and they travel only micrometres.

Berini used tools that can craft nanoscale structures, which were becoming cheaper and more readily available, to create the first plasmonic waves that could travel for centimetres (ref. 8). His lab made whole circuits, guiding plasmons down metal strips less than 30 nanometres thick.

But allowing the waves to travel farther increases the light's wavelength. Although plasmonic waves are still smaller than conventional light waves, the compromise lessened their advantage and Berini found it tough to crack the telecommunications industry, where each component in use had been honed over decades. So he and others have been busy developing other techniques to deal with the short range of plasmonic light, either branching out into applications that turn the loss into an advantage, such as photodetectors, or by using nanostructures to amplify the waves. Physicists are now developing an assortment of nanoshapes — stars, rods and crescents — in a range of materials that could harness these waves for applications such as capturing solar energy, killing cancer cells and creating chip-integrated lasers, known as spasers.

Henry Schriemer, a physicist at the University of Ottawa, calls Berini a "quintessential experimentalist with a deep appreciation for the theory". But Berini says that it is applications that turn his lab on; he attributes this entrepreneurial bent to his parents, who ran their own businesses in Timmins, the Ontario mining and logging community where he grew up.

Today, Berini is recycling the efforts made in long-range circuits to make a detector for dengue fever. The device, a handheld biosensor developed last year with researchers at the University of Malaya in Kuala Lumpur, sends plasmon waves down a chip scattered with dengue virus particles. A blood sample is placed on the chip; if the donor has the infection, the sample will contain antibodies that bind to the virus, disrupting the wave and producing a signal[9]. Berini says that the sensors could speed up diagnosis, which normally involves sending samples away to a lab.

A new company is now in the works to commercialize a range of similar biosensors. But Berini believes that the application is just one of many that squeezed light will have in the future. "With plasmonics, there is a lot of new physics to be uncovered," he says. All of which means that some of the random equipment that litters the lab might find a new use. ■

5. Stockman, M. I. (2015). Nanoplasmonic sensing and detection. *Science*, *348*(6232), 287-288.

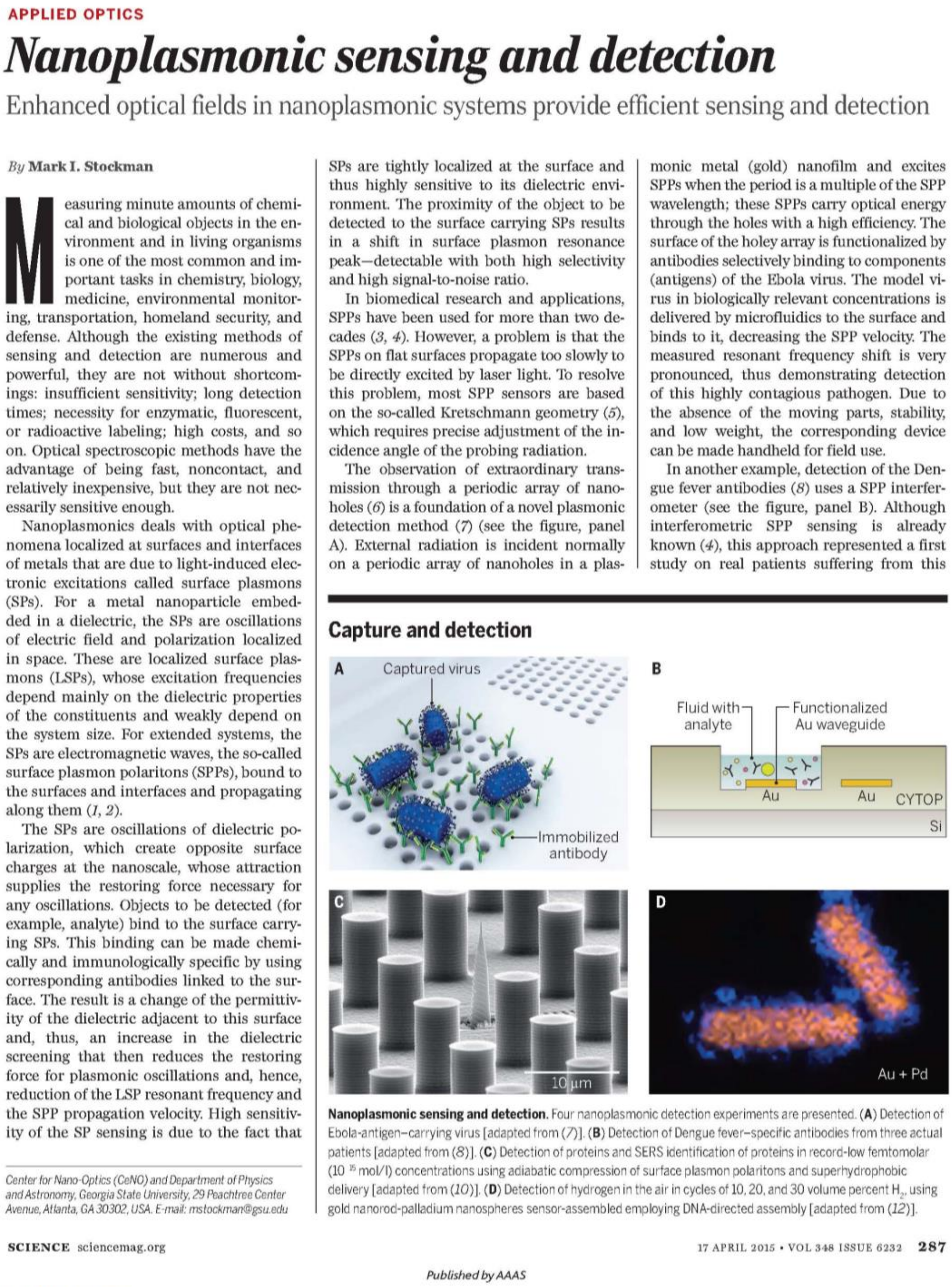

APPLIED OPTICS

# Nanoplasmonic sensing and detection

## Enhanced optical fields in nanoplasmonic systems provide efficient sensing and detection

*By* **Mark I. Stockman**

Measuring minute amounts of chemical and biological objects in the environment and in living organisms is one of the most common and important tasks in chemistry, biology, medicine, environmental monitoring, transportation, homeland security, and defense. Although the existing methods of sensing and detection are numerous and powerful, they are not without shortcomings: insufficient sensitivity; long detection times; necessity for enzymatic, fluorescent, or radioactive labeling; high costs, and so on. Optical spectroscopic methods have the advantage of being fast, noncontact, and relatively inexpensive, but they are not necessarily sensitive enough.

Nanoplasmonics deals with optical phenomena localized at surfaces and interfaces of metals that are due to light-induced electronic excitations called surface plasmons (SPs). For a metal nanoparticle embedded in a dielectric, the SPs are oscillations of electric field and polarization localized in space. These are localized surface plasmons (LSPs), whose excitation frequencies depend mainly on the dielectric properties of the constituents and weakly depend on the system size. For extended systems, the SPs are electromagnetic waves, the so-called surface plasmon polaritons (SPPs), bound to the surfaces and interfaces and propagating along them (*1*, *2*).

The SPs are oscillations of dielectric polarization, which create opposite surface charges at the nanoscale, whose attraction supplies the restoring force necessary for any oscillations. Objects to be detected (for example, analyte) bind to the surface carrying SPs. This binding can be made chemically and immunologically specific by using corresponding antibodies linked to the surface. The result is a change of the permittivity of the dielectric adjacent to this surface and, thus, an increase in the dielectric screening that then reduces the restoring force for plasmonic oscillations and, hence, reduction of the LSP resonant frequency and the SPP propagation velocity. High sensitivity of the SP sensing is due to the fact that SPs are tightly localized at the surface and thus highly sensitive to its dielectric environment. The proximity of the object to be detected to the surface carrying SPs results in a shift in surface plasmon resonance peak—detectable with both high selectivity and high signal-to-noise ratio.

In biomedical research and applications, SPPs have been used for more than two decades (*3*, *4*). However, a problem is that the SPPs on flat surfaces propagate too slowly to be directly excited by laser light. To resolve this problem, most SPP sensors are based on the so-called Kretschmann geometry (*5*), which requires precise adjustment of the incidence angle of the probing radiation.

The observation of extraordinary transmission through a periodic array of nanoholes (*6*) is a foundation of a novel plasmonic detection method (*7*) (see the figure, panel A). External radiation is incident normally on a periodic array of nanoholes in a plasmonic metal (gold) nanofilm and excites SPPs when the period is a multiple of the SPP wavelength; these SPPs carry optical energy through the holes with a high efficiency. The surface of the holey array is functionalized by antibodies selectively binding to components (antigens) of the Ebola virus. The model virus in biologically relevant concentrations is delivered by microfluidics to the surface and binds to it, decreasing the SPP velocity. The measured resonant frequency shift is very pronounced, thus demonstrating detection of this highly contagious pathogen. Due to the absence of the moving parts, stability, and low weight, the corresponding device can be made handheld for field use.

In another example, detection of the Dengue fever antibodies (*8*) uses a SPP interferometer (see the figure, panel B). Although interferometric SPP sensing is already known (*4*), this approach represented a first study on real patients suffering from this

### Capture and detection

**Nanoplasmonic sensing and detection.** Four nanoplasmonic detection experiments are presented. (**A**) Detection of Ebola-antigen–carrying virus [adapted from (*7*)]. (**B**) Detection of Dengue fever–specific antibodies from three actual patients [adapted from (*8*)]. (**C**) Detection of proteins and SERS identification of proteins in record-low femtomolar ($10^{-15}$ mol/l) concentrations using adiabatic compression of surface plasmon polaritons and superhydrophobic delivery [adapted from (*10*)]. (**D**) Detection of hydrogen in the air in cycles of 10, 20, and 30 volume percent $H_2$, using gold nanorod-palladium nanospheres sensor-assembled employing DNA-directed assembly [adapted from (*12*)].

*Center for Nano-Optics (CeNO) and Department of Physics and Astronomy, Georgia State University, 29 Peachtree Center Avenue, Atlanta, GA 30302, USA. E-mail: mstockman@gsu.edu*

*Published by AAAS*

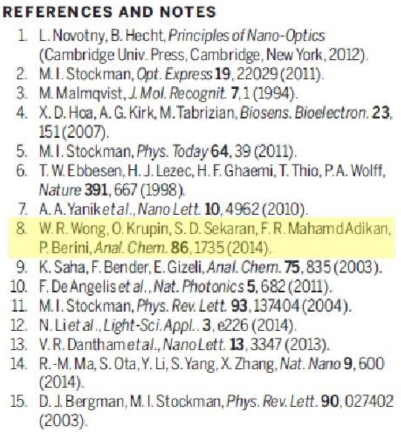

**REFERENCES AND NOTES**

1. L. Novotny, B. Hecht, *Principles of Nano-Optics* (Cambridge Univ. Press, Cambridge, New York, 2012).
2. M. I. Stockman, *Opt. Express* **19**, 22029 (2011).
3. M. Malmqvist, *J. Mol. Recognit.* **7**, 1 (1994).
4. X. D. Hoa, A. G. Kirk, M. Tabrizian, *Biosens. Bioelectron.* **23**, 151 (2007).
5. M. I. Stockman, *Phys. Today* **64**, 39 (2011).
6. T. W. Ebbesen, H. J. Lezec, H. F. Ghaemi, T. Thio, P. A. Wolff, *Nature* **391**, 667 (1998).
7. A. A. Yanik *et al.*, *Nano Lett.* **10**, 4962 (2010).
8. W. R. Wong, O. Krupin, S. D. Sekaran, F. R. Mahamd Adikan, P. Berini, *Anal. Chem.* **86**, 1735 (2014).
9. K. Saha, F. Bender, E. Gizeli, *Anal. Chem.* **75**, 835 (2003).
10. F. De Angelis *et al.*, *Nat. Photonics* **5**, 682 (2011).
11. M. I. Stockman, *Phys. Rev. Lett.* **93**, 137404 (2004).
12. N. Li *et al.*, *Light-Sci. Appl.*. **3**, e226 (2014).
13. V. R. Dantham *et al.*, *Nano Lett.* **13**, 3347 (2013).
14. R.-M. Ma, S. Ota, Y. Li, S. Yang, X. Zhang, *Nat. Nano* **9**, 600 (2014).
15. D. J. Bergman, M. I. Stockman, *Phys. Rev. Lett.* **90**, 027402 (2003).

## C.2 Videos

1. University of Ottawa. (2013, January 30). University of Ottawa professor thinks “big” about seeing the small picture. [Motion picture] Retrieved from http://www.gazette.uottawa.ca/en/2013/01/university-of-ottawa-professor-thinks-big-about-seeing-the-small-picture/

2. Berini, P. (2014, December 12). Plasmonic detection of dengue could address major world health problem. [Motion Picture] Retrieved from http://spie.org/x111081.xml. doi: 10.1117/2.3201412.02

## C.3 Others

The research in this thesis was featured in the Undergraduate Studies Viewbook 2015-2016, Faculty of Engineering, University of Ottawa.

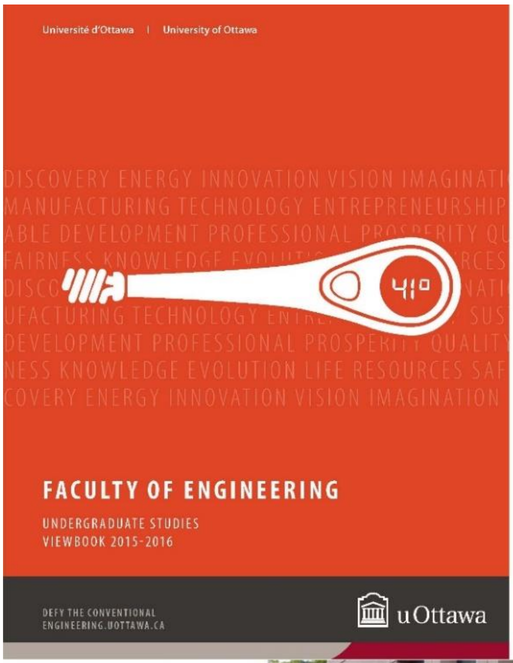

Université d'Ottawa | University of Ottawa

FACULTY OF ENGINEERING

UNDERGRADUATE STUDIES
VIEWBOOK 2015-2016

DEFY THE CONVENTIONAL
ENGINEERING.UOTTAWA.CA

uOttawa

USING LIGHT TO DIAGNOSE DISEASE

Faculty of Engineering professor **Pierre Berini** worked with partners in Malaysia to develop a blood test for dengue fever, a serious tropical disease. An expert in photonics, Berini studies how light interacts with matter. His biosensor uses light to help detect the presence of potentially deadly viruses.

TABLE OF CONTENTS

KEEP IN TOUCH

Facebook.com/uOttawa.Engineering

Twitter.com/uOttawaGenie

Youtube.com/FacultyofEngineering

02 ENGINEERING.UOTTAWA.CA